

TAS measurements for neutrino physics and nuclear structure

study of the beta decays of ^{150}Er, ^{152,156}Yb and ^{188,190,192}Pb

PhD Thesis

Author:
Maria Esther
Estevez Aguado

Supervisor:
Dr. Alejandro
Algora

Dep. de Física Atómica, molecular y nuclear
Instituto de Física Corpuscular
Valencia, 2012

Universidad de Valencia
Instituto de Física Corpuscular
Dep. de Física Experimental

TAS measurements for neutrino physics and nuclear structure:

study of the beta decays of ^{150}Er, $^{152,\ 156}$Yb and ^{188,190,192}Pb

Por

Maria Esther Estevez Aguado

Tesis para optar al grado de
Doctora en Física

Director: Alejandro Algora

Este proyecto ha recibido apoyo de: MEC FPA 2002-04181-004-03, FPA 2005-03993, FPA 2008-02878, FPA2008-06419-C02-01 y PROMETEO 2008/004. Apoyo parcial: Ramón y Cajal y contrato Marie Curie RTN-MRTNCT-2006-035505.

VALENCIA
2012

.

Alejandro Algora, Científico Titular del CSIC (Consejo Superior de Investigaciones Científicas),

CERTIFICA:
Que la presente Memoria **"TAS measurements for neutrino physics and nuclear structure: study of the beta decays of ^{150}Er, ^{152,156}Yb and ^{188,190,192}Pb"** ha sido realizada bajo su dirección en el Departamento de Física Experimental del Instituto de Física Corpuscular (Centro Mixto Universidad de Valencia - CSIC) por **Maria Esther Estevez Aguado** y constituye su Tesis para obtener el grado de Doctora en Física.

Valencia, Febrero de 2012

Y para que así conste presenta la referida Memoria, firmando el presente certificado.

Fdo: Alejandro Algora

To my friends, for being my family.

Acknowledgments

"One sees clearly only with the heart.
What is essential is invisible to the eye."

Antoine de Saint-Exupéry, The Little Prince.

"Every one of us is, in the cosmic
perspective, precious. If a human
disagrees with you, let him live.
In a hundred billion galaxies, you
will not find another."

Carl Sagan, Cosmos.

This is the very important place where one has their acknowledgments written down so that they are not forgotten. I will start saying that it is sad for me to leave the Gamma Spectroscopy group. My endless thanks to Ale, for his patience, good advice and support, and for always having time for me despite his busy schedule. He accepted to work with me in hard times and trusted in me. I hope his secret wish comes true[1]. Jose Luis and Berta are not only amazing physicists but also some of the greatest people I have met in this profession. Special thanks to the people who participated in the measurements and to Prof. José Bernabéu, Pedro Sarriguren and Oscar Moreno, since without them this thesis would never exist. Also big thanks to the rest of the team for the good moments and laughs. The lab time and the "*darts and beer*" sessions after 18 daily hours of work at the ISOLDE hall were epic and are just one of the things I will always remember. Experiments, detectors building, physics, adventures... those were good times! (B.T. or "Before Thesis")

I would also like to thank all the people with whom I have collaborated at many different levels, not only in experiments but also in other activities. The people in the FRS at GSI, the Surrey group, people in ISOLDE and n-ToF at CERN, in YFL at Jyväskylä and in the RCNP at Osaka. A lot of things have to work well for an experiment to succeed, and a lot of hours of hard work and effort were devoted by all these people for that purpose.

[1] "*...Ondear la melena al viento en un acantilado...*"

I don't forget about my teachers in the Interuniversitary Course on Nuclear Physics for their effort and availability in such intensive courses. Also, this course gave me the opportunity to be a teacher in my field (I had always taught a lot of things but not nuclear physics) and meet many wonderful nuclear-physics grasshoppers, with whom I have shared so many conferences, pilgrimages to Santiago, adventures, trips, beers and good times in general. Without them these years would surely be lacking something, and I hope we will still keep in touch in the future.

How not to mention the *Subnormales*. I haven't stopped mentioning them to everybody and transmitting their legend. *V. el Inmortal*, *Negro*, *DENTINI*, *Wes*, *AfricanoH*, *Cl.*, *JarJar Binks*, *Piltrafa*, *Marranica*, *Elber G. T.*, and all the new acquisitions. Thanks to them, my days in Valencia were great, and *Subnormality* is considered a religion, although banned in almost every planet and parallel universe in the spacetime. Our lives are changing now (my grandma would call it "to mature") and one of them will turn us into uncles soon. Among my "normal" (but not less important) friends: Joel ("el P.A."), who took the trouble to read and correct one of the chapters of this thesis, and who gave me the greatest honor one can receive: to be *one of his pillars*. Pauliña "Pe. Tu." (or "Te. Mu." ?) who always helps me or gives me good advice. Felip for his help with LaTeX, Mathematica and computers in general, and for always reminding me how viking I am, Anabel, my DEAR dear Anabel, and in general all the people that made me laugh and forget about my problems (so many people to mention): Aoude and Franziska "cabras suaves", "the family" from La Flama (Ana "Anuska", Lidia, Saray, etc. and specially those who are gone), Yoko "Maria Yoquia" who is actually Spanish, Clarita, Willy, my "uncle" Juanito, Juanito 2, Luna, Marco "Merluzconi", Bibi, Eva, Lotfi, Nuria, Vincent, Neil for turning my broken English into nice British English, Nayelita my favorite coagulum ("vikings love blood"), Lore, Luisda, Edu and Aurorita, the "catrachos" and the Latin Front in general, Lucho and Scott, Nathalie and Marijke the "duddas" (godverdomme!), Marthe "smartie" (moréname!), Carsten "the cowboy" and Martin, Javi, Mery, the girls of ALAHAS and Amparo "la tórtola que danza", Moni who can speak *frangaleñol*, Miky, Pedrito and Ana in Sevilla, Alfredo "Freddy Turbina" (viva Viña!) and those who have already left Valencia. Thanks to all these awesome people from a trillion different nationalities and to those I may have forgotten.

Before I finish, I would like to thank those who were there in the very beginning. When I left home to study physics, I went through hard times economically, physically and psychologically, but I found the support of these people, most of them dead now, or far away, or no longer in my life for other reasons. They don't want to appear here, but I consider them my other family. They saw me at my worst, lent me a hand selflessly, and pulled me out of many holes. If I finished a career and this PhD is only thanks to their help in those first years. And finally, going even further back in time, I thank my old friends in Panama, far away but very present. Among them are my closest friends who were always there in one way or the other during all these years: Ramses "mi pana", Hugo, Gorda, Marita, Mely and specially Evelyn, who is always there lately, through thick and thin, despite the distance.

Thanks also to J. Cham who reminded me I was not alone.

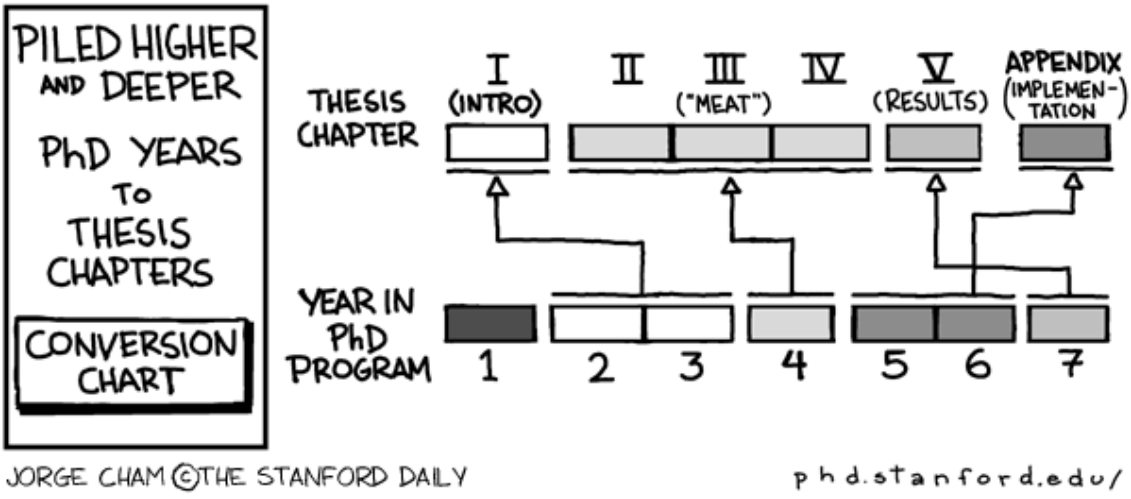

Contents

I Introduction 1

1 General Introduction 3

2 General Aspects 5
2.1 About the measurement technique . . . 5
2.1.1 What do we want to measure . . . 5
2.1.2 The Pandemonium effect . . . 6
2.1.3 Total Absorption Spectroscopy . . . 7
2.2 About the data analysis . . . 10
2.2.1 Calculating the branching ratios . . . 11
2.2.2 Simulating the response . . . 12
2.2.3 Extracting the feedings . . . 13

II Neutrino Physics 17

3 Motivation 19
3.1 Beta, EC and hybrid beam facilities . . . 23
3.2 Proton rich nuclei . . . 25
3.3 Neutrino beam facilities from proton rich nuclei . . . 27

4 Experiments 33
4.1 GSI Facility . . . 33
4.2 TAS measuring station . . . 34
4.3 Mass A = 152 measurement . . . 35
4.4 Mass A = 150,156 measurements . . . 36

5 Analysis and Results 41
5.1 Mass A = 152 . . . 41
5.2 Mass A = 150 . . . 51
5.3 Mass A = 156 . . . 57

6 Discussion and Conclusions 63

III Nuclear Deformation 73

7 Motivation 75
7.1 A new signature of deformation . . . 78
7.1.1 Brief description of the theoretical formalism . . . 79

8 Experiment 83
8.1 ISOLDE facility . . . 83
8.2 *Lucrecia* measuring station . . . 85
8.3 The measurement . . . 87

9 Analysis and Results 89
9.1 Mass A = 192 . . . 89
9.2 Mass A = 190 . . . 106
9.3 Mass A = 188 . . . 120

10 Discussion and Conclusions 131

IV General Conclusions 143

V Resumen en español 149

VI Appendixes 155

A Summary: general steps of the analysis 157

B Preparation of the data for Part II 161

C Preparation of the data for Part III 167
C.1 Alignment . . . 169
C.2 Calibrations . . . 172
C.2.1 Energy calibrations . . . 172
C.2.2 Width calibration . . . 177
C.3 Efficiencies . . . 180
C.4 Sources . . . 182

References 186

List of Tables

3.1 Latest global fit of the neutrino oscillation parameters. 21
3.2 Relevant nuclear data for the studied candidates. 29
3.3 Comparison of production yields at ISOLDE. 31

4.1 Details of the measurements of masses 152, 150 and 156. 38

5.1 Known levels used in the analysis of the EC decay of ^{152}Yb. 42
5.2 Giant resonance parameters for ^{152}Tm. 43
5.3 Normalization factors of all the contributions to the ^{152}Yb decay. . . 47
5.4 Deduced $I_{EC+\beta^+}$ values for ^{152}Yb. 50
5.5 Known levels used in the analysis of the EC decay of ^{150}Er. 51
5.6 Giant resonance parameters for ^{150}Ho. 51
5.7 Normalization factors of all the contributions to the ^{150}Er decay. . . 55
5.8 Deduced $I_{EC+\beta^+}$ values for ^{150}Er. 56
5.9 Known levels used in the analysis of the EC decay of ^{156}Yb. 57
5.10 Giant resonance parameters for ^{156}Tm. 57
5.11 Normalization factors of all the contributions to the ^{156}Yb decay. . . 60
5.12 Deduced $I_{EC+\beta^+}$ values for ^{156}Yb. 61

6.1 Summary of the TAS results for the feedings. 65
6.2 Summary of the TAS results for the strength. 66
6.3 Summary of the TAS results for the strength in the ^{146}Gd region. . . 70

7.1 Energies of the intruder states in the Pb isotopes. 76
7.2 Relevant nuclear data for the neutron deficient Pb nuclei. 80

8.1 Details of the Pb measurements at ISOLDE. 88

9.1 Giant resonance parameters for ^{192}Tl. 90
9.2 Normalization factors of the contributions to the ^{192}Pb decay. 96
9.3 Peaks seen in TAS spectra of mass 192. 98
9.4 Deduced $I_{EC+\beta^+}$ values for ^{192}Pb. 104
9.5 Giant resonance parameters for ^{190}Tl. 107
9.6 Normalization factors of the contributions to the ^{190}Pb decay. 110
9.7 Peaks seen in TAS spectra of mass 190. 112
9.8 Deduced $I_{EC+\beta^+}$ values for ^{190}Pb. 118
9.9 Giant resonance parameters for ^{188}Tl. 121

9.10 Normalization factors of the contributions to the ^{188}Pb decay. 124
9.11 Peaks seen in TAS spectra of mass 188. 125
9.12 Deduced $I_{EC+\beta^+}$ values for ^{188}Pb. 128

10.1 Energy and strength of the most strongly populated levels. 136
10.2 Total strength lying inside the Q_{EC} window. 136
10.3 Mixing of the ground state in the lead nuclei studied in this work. . 138

B.1 Details of the data files used in Part II. 164

C.1 Peaks used for the energy calibration of the TAS detector. 173
C.2 Peaks used for the energy calibration of the planar germanium. . . . 174
C.3 Peaks used for the energy calibration of the coaxial germanium. . . . 174
C.4 Peaks used for the energy calibration of the MC simulation. 176
C.5 Calibration coefficients of Eq. C.5 for the detectors. 177
C.6 Peaks used for the width calibration of the TAS detector. 178
C.7 Peaks used for the width calibration of the simulation. 178
C.8 Calibration coefficients of Eq. C.6 for the data and the MC. 178
C.9 Peaks used for the efficiency calibration of the Ge detectors. 181
C.10 Calibration coefficients of Eq. C.10 for the Ge detectors. 181
C.11 Information available for the ISOLDE sources. 182

List of Figures

2.1 Schematic diagram showing the Pandemonium effect 8
2.2 Germanium gamma spectrum vs. TAS gamma spectrum 9
2.3 Comparison of I_β's obtained with HR and TAS technique. 9

3.1 Example of a Beta Beam facility. 23
3.2 Decay of ^{6}He. 24
3.3 Decay of ^{18}Ne. 24
3.4 Different energy regions of $P(\nu_e \rightarrow \nu_\mu)$ covered by a hybrid facility. . 26
3.5 The nuclei above ^{146}Gd. 28
3.6 ^{152}Tm known level scheme from HR measurements. 29
3.7 ^{150}Ho known level scheme from HR measurements. 30
3.8 ^{156}Tm known level scheme from HR measurements. 30

4.1 Layout of UNILAC and the low energy hall at the GSI facility. . . . 34
4.2 TAS Measuring Station installed at GSI. 35
4.3 Setup and ancillary detectors used in mass A = 152 measurement. . 39
4.4 Setup and ancillary detectors used in mass A = 150,156 measurements. 39

5.1 Schematic diagram of the Q values in the decay chain of ^{152}Yb. . . . 42
5.2 Average branching ratio matrix for the EC decay of ^{152}Yb. 44
5.3 Gamma response matrix for the EC decay of ^{152}Yb. 44
5.4 X-ray spectra showing the gates for the analysis of mass A = 152. . 45
5.5 Gates of the isobars produced in the EC decay chain of ^{152}Yb. 46
5.6 Alpha branch contamination in the ^{152}Tm gate. 48
5.7 Pileup calculation for mass A = 152. 49
5.8 Decay with contaminants for mass A = 152. 49
5.9 Final results of the analysis of the EC decay of ^{152}Yb. 50
5.10 Gamma response matrix for the EC decay of ^{150}Er. 52
5.11 X-ray spectra showing the gates for the analysis of mass A = 150. . 53
5.12 Gates of the isobars produced in the EC decay chain of ^{150}Er. . . . 54
5.13 Pulse measured for mass A = 150 and 156. 55
5.14 Decay with contaminants for mass A = 150. 55
5.15 Final results of the analysis of the EC decay of ^{150}Er. 56
5.16 Gamma response matrix for the EC decay of ^{156}Yb. 58
5.17 X-ray spectra showing the gates for the analysis of mass A = 156 . . 58
5.18 Gates of the isobars produced in the EC decay chain of ^{156}Yb. 59

5.19 Decay with contaminants for mass A = 156. 60
5.20 Final results of the analysis of the EC decay of ^{156}Yb. 61

6.1 Comparison of the TAS results and HR data. 64
6.2 Ground state configurations for N = 82 and N = 83. 67
6.3 Systematics of the region above ^{146}Gd. 68
6.4 Systematics of the decays when adding neutrons. 69
6.5 Evolution of the strength with the occupation number. 71

7.1 Energies of the intruder states in the Pb isotopes. 76
7.2 Theoretical results for the normal and accumulated strength. 81

8.1 CERN accelerator complex. 84
8.2 Schematic view of RILIS at ISOLDE. 84
8.3 *Lucrecia* measuring station. 86

9.1 Known level scheme of ^{192}Tl. 90
9.2 *Lucrecia* geometry implemented in the MC simulation. 91
9.3 Comparison between measured and simulated sources. 92
9.4 *Lucrecia*'s gamma response for monoenergetic gammas 93
9.5 X-ray spectra showing the gates for the analysis of mass A = 192. . 93
9.6 Gates of the isobars produced in the EC decay chain of ^{192}Pb. . . . 95
9.7 Pulse measured for masses A = 192, 190 and 188. 95
9.8 TAS, GeG and GeX background measurement for mass 192. 96
9.9 ^{192}Pb decay with contaminants. 97
9.10 Results of the first analysis of mass 192. 98
9.11 GeG detector gated on ^{192}Tl x rays 99
9.12 Ge planar detector spectrum for ^{192}Tl. 100
9.13 Different analysis tests for the known level scheme of mass 192. . . . 103
9.14 Comparison between raw, chosen and reference analysis. 104
9.15 Results of the first analysis of mass 192. 105
9.16 Comparison of ΣB(GT), selected and reference analysis, A = 192. . 105
9.17 Known level scheme of ^{190}Tl. 106
9.18 X-ray spectra showing the gates for the analysis of mass A = 190. . 108
9.19 Gates of the isobars produced in the EC decay chain of ^{190}Pb. . . . 109
9.20 TAS, GeG and GeX background measurement for mass 190. 110
9.21 ^{190}Pb decay with contaminants. 111
9.22 Results of the first analysis of mass 190. 112
9.23 GeG detector gated on ^{190}Tl x rays 113
9.24 Ge planar detector spectrum for ^{190}Tl. 113
9.25 Different analysis tests for the known level scheme of mass 190. . . . 116
9.26 Comparison between raw, chosen and reference analysis. 117
9.27 Results of the first analysis of mass 190. 119
9.28 Comparison of ΣB(GT), selected and reference analysis, A = 190. . 119
9.29 Known level scheme of ^{188}Tl. 120

9.30 X-ray spectra showing the gates for the analysis of mass A = 188. . 122
9.31 Gates of the isobars produced in the EC decay chain of ^{188}Pb. 123
9.32 ^{188}Pb decay with contaminants. 124
9.33 Results of the first analysis of mass 188. 125
9.34 GeG detector gated on ^{188}Tl x rays 126
9.35 Ge planar detector gated on ^{188}Tl x rays 126
9.36 Different analysis tests for the known level scheme of mass 188. . . . 127
9.37 Comparison between raw, chosen and reference analysis. 127
9.38 Results of the first analysis of mass 188. 128
9.39 Comparison of ΣB(GT), selected and reference analysis, A = 188. . 129
9.40 Systematics of the lead isotopes studied in this work. 129

10.1 Comparison between TAS results and HR data for ^{192}Pb. 132
10.2 Comparison between TAS results and HR data for ^{190}Pb and ^{188}Pb. 133
10.3 Comparison between TAS results and calculations for ^{192}Pb. 134
10.4 Comparison between TAS results and calculations for ^{190}Pb. 135
10.5 Comparison between TAS results and calculations for ^{188}Pb. 135
10.6 Accumulated strength, comparison between data and theory. 137
10.7 Accumulated strength, comparison with weighted theory. 138
10.8 Results of the widening of the theoretical calculations for mass 192. 140
10.9 Accumulated strength, comparison with widened theory. 140
10.10 Systematics of the even-mass Tl levels populated in β decay. 141
10.11 Mean square charge radii for lead, mercury and platinum. 141

B.1 GOOSY structure of event and subevent type 10, subtype 1. 162
B.2 Dump of two `lmd` files showing the parameters identification. 163
B.3 Data structure of ROOT files generated from 2000 `lmd` files. 165
B.4 Data structure of ROOT files generated from 1996 `lmd` files. 166

C.1 Tree structure of the ROOT data files. 168
C.2 Gain drift of the TAS spectra. 169
C.3 Results of the fit of some peaks with function C.4. 171
C.4 Comparison between the raw spectra and the aligned spectra. 172
C.5 Energy calibration plots for the detectors used in the analysis. . . . 175
C.6 Comparison of low and high energy MC peaks. 176
C.7 Width calibration plots. 179
C.8 Function for the instrumental resolution distribution. 180
C.9 Efficiency calibration plots. 182
C.10 ^{22}Na level scheme. 183
C.11 ^{24}Na level scheme. 183
C.12 ^{60}Co level scheme. 184
C.13 ^{137}Cs level scheme. 184
C.14 ^{152}Eu level scheme, Gd branch. 185
C.15 ^{152}Eu level scheme, Sm branch. 185

Part

I

Introduction

1

General Introduction

"If you want to make an apple pie from scratch, you must first create... ...the universe".

Carl Sagan

Nuclear physics is a strongly phenomenological field: a large amount of what we know comes mainly from measurements. Even the most advanced theoretical models use experimental inputs, effective potentials and other parameterizations taken from measurements. The fact that the nucleus, made of Z protons and N neutrons (in total $A = Z + N$ nucleons), is a many-body system, makes it difficult to find a coherent theoretical formulation able to describe any nuclear behaviour along the whole chart of nuclides. To give an example, what is fine to describe a group of observations in a determined zone of the nuclear chart may fail to explain another set of observations or phenomena taking place in another region of the chart. A theoretical formulation in terms of quarks is also not able to predict all the nuclear properties. These facts put in evidence our poor knowledge of the nuclear potential, and underline the need for more and better measurements with new techniques and to further improve our theoretical understanding of the atomic nucleus.

These measurements can include nuclear reactions, which allow the "artificial" production of a wide variety of species (some of them called"exotic") that give important information about their nuclear properties. Another kind of measurement is to let nature act and wait for a special kind of decay to occur. In this work, the second experimental approach is selected, to measure the beta decay of 6 different nuclear species.

This work is organized as follows: there is a first and introductory part that includes all the general information that is common to the other two parts of the work. An introduction to the nuclear properties measured in this work is presented in Chapter 2. However, the basis of beta decay can be found in any good reference book and it is not the aim to reproduce them here. The mentioned beta decay properties were measured with a special technique, the Total Absorption Spectroscopy (TAS) technique, that is introduced and explained in Subs. 2.1.2 and 2.1.3. The analysis method used to analyze the TAS data is complex. The correct way to do this analysis for the data of parts II and III of this work is explained in a general way in Sec. 2.2, and in a more detailed way in Appendix A.

Two applications of the TAS technique are presented in Part II and Part III of this work. In Part II an application to neutrino physics is presented, consisting of the measurement, with the TAS technique, of the beta decay of heavy nuclei that could be used as neutrino sources in neutrino beta beam and electron capture facilities. Specifically, the beta feedings of ^{152}Yb, ^{150}Er and ^{156}Yb are determined from measurements made at GSI in 1996 and 2000. These measurements are also important from the nuclear structure point of view for the problem of the "missing strength", that will be explained in the motivation (Chapter 3). Part III is an application of the TAS technique to nuclear structure, in which the deformation of the ground state of lead nuclei is deduced from the data taken with the TAS spectrometer. These measurements profit from the use of RILIS, a laser ionization ion source installed at ISOLDE (CERN) that allows a cleaner selection of the isotopes of interest. In this Part, the study of the beta strength produced in the decay of $^{188,190,192}Pb$ nuclei measured at the end of 2008 at CERN is used as an alternative technique for ground state shape determination.

2 General Aspects

2.1. About the measurement technique

2.1.1. What do we want to measure

In beta decay studies, one of the many quantities of interest is the strength, which is related to the distribution of the beta decay probabilities in a nucleus. Basically, this distribution reflects the overlap of the wave functions of states in the parent and daughter nuclei, which is of fundamental interest for many reasons:

- To test nuclear structure theoretical models, and in this way make more accurate predictions of half-lives, etc.
- Deduce nuclear structure properties, for example, the shape of a nucleus.
- Calculate the mean energy of the radiation emitted in the decay, which can be important for some applications such as reactor decay-heat studies.
- Calculate the parameters of importance for ν-oscillation experiments.
- Understand the synthesis of elements in astrophysical processes.
- Understand the problem of the missing strength, etc.

The Gamow-Teller strength $B(\mathrm{GT})$ can be defined as in Eq. 2.1:

$$B(\mathrm{GT}) = \frac{1}{2J_i+1}\left|\left\langle \psi_i \left| \sum_k \sigma_k \tau_k^{\pm} \right| \psi_f \right\rangle\right|^2 = \langle \sigma\tau \rangle^2 \tag{2.1}$$

where J_i is the spin of the level i, and $\sigma\tau$ is the (GT) operator that connects the ψ_i and ψ_f states. On the experimental side, the analogous expression is the experimental strength function, which is calculated from the measured beta intensity or feeding probability, the beta-decay half-life $t_{1/2}$ and the mass difference Q_β, and is defined *for each energy bin* as in Eq. 2.2:

$$S_\beta(E) = \frac{I_\beta(E)}{f(Q_\beta - E)t_{1/2}} \tag{2.2}$$

where S_β is the strength function, E is the excitation energy, I_β is the beta feeding per energy bin (ΔE) and $f(Q_\beta - E)$ is the Fermi function, (where $Q_\beta - E$ is the energy available in the decay). $S_\beta(E)$, as defined in Eq. 2.2, is an average quantity and can be understood as the mean value of the B(GT) for transitions occurring to levels inside the bin ΔE.

These two magnitudes, theoretical (B(GT)) and experimental ($S_\beta(E)$), are related by the expression:

$$S_\beta = \frac{1}{6147 \pm 7}\left(\frac{g_A}{g_V}\right)^2 \sum_{E_f \in \Delta E} \frac{1}{\Delta E} B(\mathrm{GT})_{i\to f} \tag{2.3}$$

where 6147 ± 7 is a constant defined by $2ln2\pi^3\hbar^7/m_e^5c^4g_V^2$, g_A and g_V are axial and vector coupling constants, and B(GT) is given in units of $g_A^2/4\pi$. This expression will allow the comparison between the theoretical calculations and the measured strength.

For the experiments discussed here, in Eq. 2.2, Q_β and $t_{1/2}$ are supposed to be known or measurable, and the only quantity to be determined in the present experimental work is the beta intensity (I_β). Very often the only information available about the beta intensity has been measured with high-resolution (HR) gamma detectors, that can suffer from the Pandemonium effect. This problem and its solution is discussed in the following subsections.

2.1.2. The Pandemonium effect

The *Pandemonium effect* [Har77] is a problem that may appear when HR detectors (usually germanium detectors) are used in beta decay studies. It can affect the correct determination of the feeding probabilities to the different levels of the daughter nucleus in beta decay studies.

When a parent nucleus decays into its daughter, the levels in the daughter can be populated in two ways:

- either by direct feeding from the decay (beta intensity I_β),
- or by de-excitation of higher energy levels also beta-populated in the decay (gamma intensity ΣI_i).

When a level decays, the total gamma intensity emitted by the level (I_T) should be equal to the sum of these two contributions[1]. Since the quantities that can be

[1]Neglecting internal conversion for simplicity.

measured are the gamma intensities (ΣI_i and I_T), the beta feeding (that is, how many times a level is populated by direct feeding) can be extracted indirectly by subtracting the contribution from de-excitations of higher energy levels (ΣI_i) to the total gamma intensity that leaves the level (I_T), that is, $I_\beta = I_T - \Sigma I_i$.

Sometimes the decay has a large Q value, allowing the existence of many levels. This means that the total feeding can be fragmented, as it could spread over all of them (with a certain distribution determined by the strength, the level density, decay selection rules, etc). Then, the gamma intensity emitted from the less populated levels will be weak, and it will be weaker as we go to higher energies where the level density can be very high. Also, the energy of the gammas de-excitating this high density level zone at high excitation can be large. Measuring these γ rays with HR detectors may present two problems related with these two situations: First, these detectors have little sensitivity to weak radiation in most of the cases. Second, the efficiency curve drops to very low values as it goes to higher energies, starting from energies of the order of 1-2 MeV, meaning that most of the information coming from the high energy γ rays will be lost (see [Har77] and Fig. C.9 in this work for examples of typical efficiency curves of these detectors).

The consequence of these two effects is that much of the beta feeding at high excitation energy is not detected and less ΣI_i is subtracted from the I_T, so the low lying levels are incorrectly assigned more I_β than they really have. This is schematically shown in the diagram of Fig. 2.1.

One possible solution to this experimental problem is to use a calorimeter like detector, which will be introduced in the next section. Even with a high efficiency array of Germanium detectors in a very close geometry, it has been shown [Alg03] that about 55 % of the total B(GT) observed with the TAS technique can be lost, although this depends heavily on the case.

2.1.3. Total Absorption Spectroscopy

The Total Absorption Spectrometer or TAS is a concept of gamma detector that can be perfectly suited for beta feeding measurements *within the full decay energy window* for nuclei far from stability. It is made of a scintillator material that almost completely surrounds the activity to be measured, as it covers a solid angle of approximately 4π. Also, in an ideal case, it should be insensitive to any other type of radiation and thick enough to have a peak efficiency close to 100 % (in this way its total efficiency is also very close to 100 %).

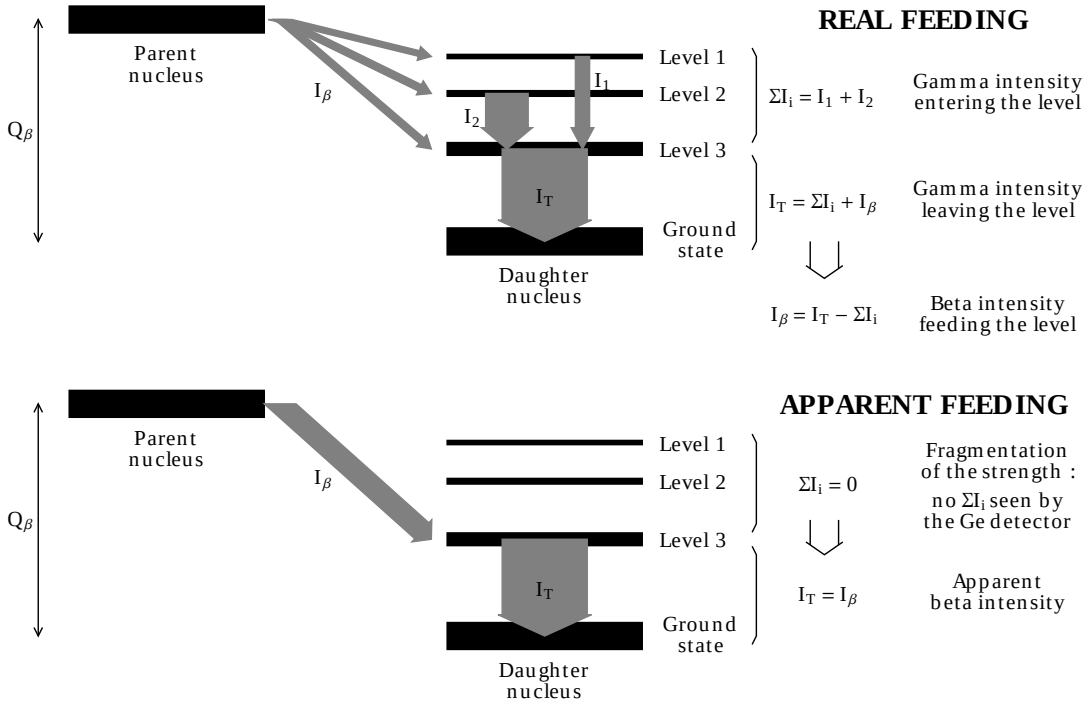

Figure 2.1: Schematic diagram showing how the Pandemonium effect can affect the results in an imaginary decay to a nucleus that has 3 levels. If this effect is large, feeding to high lying levels is not detected, and more beta feeding is assigned to the low-lying energy levels

There is a change in philosophy when measuring with a TAS. It will detect the gamma cascades emitted in the decay instead of the individual γ rays. Then, the final energy spectrum will not be a collection of different energy peaks coming from the different transitions (as can be expected in the case of a germanium detector), but a collection of peaks situated at an energy of the fed levels, that is the sum of the different energies of all the gammas of the cascade emitted from each level. This means that the energy spectrum measured with a TAS will be in reality a spectrum of levels, where each peak is a level populated in the decay (see Fig. 2.2). Since the efficiency is close to 100 %, it is possible to see the feeding to the high excitation levels that usually can not be seen with HR detectors. This makes Total Absorption Spectroscopy the best method to measure beta feedings and provide accurate I_β distributions for complex decay schemes (Fig. 2.3).

As with other detectors, if nuclei with short half-lives are measured, the gamma energy spectrum will be contaminated with the gamma cascades of the nuclei produced in the decay chain. The two TAS detectors used for the measurements presented in this work have the possibility to place ancillary detectors inside them to measure secondary radiation like x rays, electrons or positrons. In this way it is possible to tag the components of the decay during the analysis, allowing to separate the contributions coming from all the different nuclei (isobaric separation) in the electron capture cases.

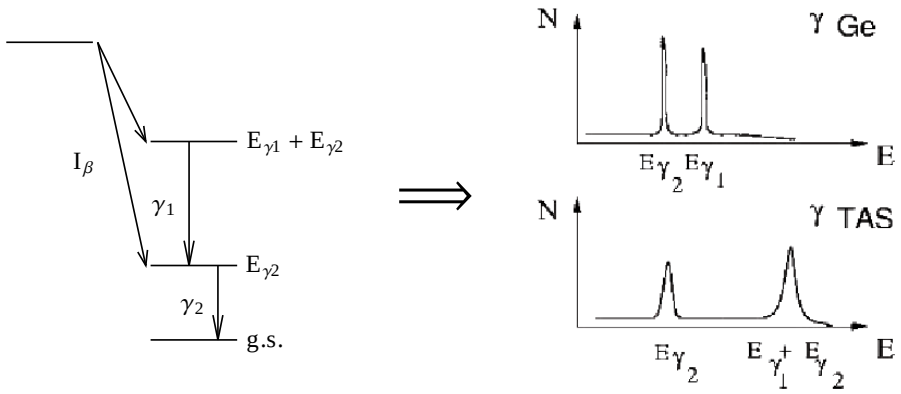

Figure 2.2: Hypothetical β decay seen by germanium and TAS detectors. With a germanium detector, (Ge) the energy peaks corresponding to individual gammas are seen, but the TAS detector gives a spectrum of the levels populated in the decay (ideal TAS). The TAS detector has less resolution but higher efficiency.

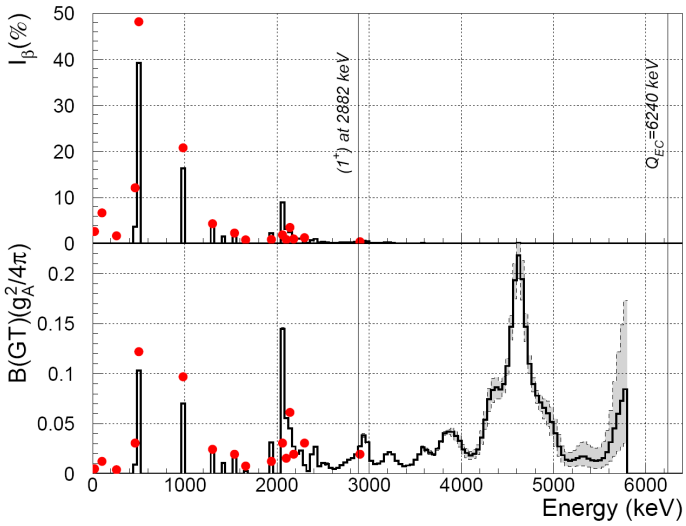

Figure 2.3: Comparison between the high-resolution technique (dots) and the total absorption technique (line) showing that some strength (B(GT)) is missed with the HR technique. The vertical line marks the last level seen by the HR technique. Taken from [Nac04a].

In an ideal case, the measured TAS spectrum would be proportional to the I_β. But a real TAS has limited efficiency, so the beta intensity has to be extracted from the analysis of the measured spectrum which depends on the spectrometer response. To obtain the strength shown in Fig. 2.3 from the measured data, a deconvolution process should be applied, as will be explained in the following section.

2.2. About the data analysis

The complex analysis of the data measured with the TAS can be reduced to the solution of a linear problem, that is, by solving Eq. 2.4, which relates the measured data (d) with the feedings (f) from which the beta intensity distribution I_β (see Eq. 2.2) can be obtained:

$$\mathbf{d} = \mathbf{R}\mathbf{f} \qquad or \qquad d_i = \sum_{i=1,\, j=0}^{i_{max},\, j_{max}} R_{ij} f_j \tag{2.4}$$

Here i is the index for data bins and j the index for energy levels, d_i is the content of bin i in the decay spectrum free of contaminants, R_{ij} is the response matrix of the detector (it represents the probability that a decay that feeds the level j gives a count in bin i of the spectrum), and f_j is the feeding to the level j. The function R depends on the detector but also on the particular level scheme of the daughter nucleus that is being measured.

To be able to extract the value of f_j from the data d_i the equation has to be inverted. Unfortunately this can not be easily done because there is similar response to the feeding of adjacent levels at high excitation energies where the level density is high. In other words, this is one of the so-called "*ill-posed*" problems, for which several sets of parameters can reproduce closely the same data set.

In an hypothetical case were only gamma responses are involved, as is the case for the decays studied in this work[2], the response $\mathbf{R}$ of the detector can be calculated recursively as:

$$R_j = \sum_{k=0}^{j-1} b_{jk} g_{jk} \otimes R_k \tag{2.5}$$

where b_{jk} are the branching ratios[3] from level j to level k and g_{jk} is the response to an emitted γ ray connecting levels j and k. Now, the unknowns in our problem are the feedings and the branching ratios. But, the higher the efficiency of the TAS used, the lower the dependence of the response on the branching ratios. Then it is possible to introduce the unknown branching ratios by hand from a plausible guess. A good guess can be calculated by means of the Statistical Model, as will be explained in Sub. 2.2.1. The responses g_{jk} are calculated with a Monte Carlo (MC) simulation as explained in Sub. 2.2.2.

Then the procedure to find the feedings is iterative: using the best method that can be found to solve the inverse problem, the feedings are extracted; if they don't

[2] All of them are electron-capture decays. In the other cases (β^+, β^-, etc.) it will be necessary to calculate also the response to the other particles emitted in the decay.

[3] A branching ratio here is the percentage of the total γ rays leaving the level j that are emitted in the transition from level j to level k.

reproduce the experimental data, it means that the initial guess of the branching ratios is wrong and has to be changed (of course, it is also possible to play with other parameters of the analysis). Repeating this procedure iteratively in a hopefully reduced number of steps, the data are finally reproduced.

For consistency in the calculations, the energy is calculated as:

$$(\text{number of bin}) \times (\text{size of bin})$$

that is, the energy corresponding to the end of the bin (for all the analysis, a bin size of 40 keV was used). In this way, the sum of the energy of two γ rays is equal to the energy of one γ ray whose energy is equal to the sum of both. This won't be true if, for example, the center of the bin is used instead.

In the following subsections, the details of the steps to solve the inverse problem are described. The calculation of the branching ratios is covered in Sub. 2.2.1. The way to obtain the responses is presented in Sub. 2.2.2 and finally, the extraction of the feedings is explained in Sub. 2.2.3. This general procedure has been followed to analyze the TAS data of both Part II and Part III of this work. A detailed description of the procedure is provided also in Appendix A.

2.2.1. Calculating the branching ratios

The best way to handle this problem is to keep a set of discrete levels at low excitation energies and a set of binned levels at high energies. The set at low energies is supposed to be known and can be taken from databases (for example, the [ENSDF] database, which has information from what has been already measured with the HR technique). The set at high energies is unknown and does not overlap with the known part. At the end of this calculation, the whole region of levels inside the Q value window (known and unknown) is binned.

At this stage of the analysis it is important to know the internal conversion coefficients for the transitions connecting the known levels. The internal conversion coefficient is defined as the number of de-excitations via e^- emission over those via γ emission. If internal conversion takes place, the EM multipole fields of the nucleus do not result in the emission of a photon, instead, the fields interact with the atomic electrons and cause one of the electrons to be emitted from the atom. The gamma that would be emitted after the beta decay is missed, and the γ intensity decreases accordingly: $I_T = I_\gamma + I_{e^-} = I_\gamma(1 + \alpha_e)$, so this phenomenon has to be taken into account in the calculation. Also, the x rays will be contaminated with those coming from the electron conversion process. This is important in electron capture decay, as it can affect the results of any x-ray gated spectra if the internal conversion is strong. Its probability is higher for lower energies and high multipolarities.

To obtain the whole branching ratio matrix b_{jk}, the Statistical Nuclear Model is used. This model generates a binned branching ratio matrix from *average level densities* and *average gamma strength functions*. For the unknown part, average branching ratios can be calculated, for which several parameterizations may be chosen, while for the known part the information in the databases is used. The parameterization of the Back-Shifted Fermi Gas Model [Dil73] was used for the calculation of the parameters of the average level densities. For the average gamma strength functions, the parameterization of a generalized Lorentzian found in [Kop90] was implemented to obtain its Giant Resonance parameters. See Appendix A, part 1 for details.

Two outputs are generated once this part of the analysis is finished:

1. The branching ratio matrix.
2. A level list file, that allows to fix the feeding of a specific level or its exclusion for later use in the analysis.

These two outputs are used in the next step: the convolution of the simulation with the branching ratios.

2.2.2. Simulating the response

For this part of the analysis the measured sources and Monte Carlo (MC) simulations are used.

It is not possible to have gamma sources that emit all the energies needed to calculate accurately the response of a TAS detector. For this reason, it is better to make a MC simulation of the response. For this simulation to be reliable, the interactions of all the particles emitted in the decay (γ, e^-/e^+, Auger e, x rays, etc.) have to be modeled accurately, and the geometry and materials in the way of these particles have to be well reproduced. Also, the light production of the scintillator has to be included. The way to perform this simulation is explained in detail in references [Can99a] and [Can00]. GEANT3 and GEANT4 [Geant] are well suited for these kind of simulations.

If the scintillator material of the TAS detector suffers from a *non proportionality* in the light production[4], the peaks produced by a cascade will be displaced further for every increment in the multiplicity[5] and the width of these peaks will be different from the width of single peaks with the same energy. This effect can be introduced

[4] An example of this are the NaI scintillators [Eng56]. The two TAS detectors presented in this work are made of NaI.

[5] The multiplicity is the number of gammas produced in the cascade de-excitating a level. For example, the multiplicity of the main level populated in the decay of ^{137}Cs is 1 (661.7 keV), but the multiplicity of the main level populated in the decay of ^{60}Co is 2 (1173.2 keV + 1332.5 keV).

in the simulation by means of a hyperbolic scintillation efficiency [Can98, Sec. 3.2].

The simulation of the light production will widen the peaks of the TAS spectrum; however, this still does not reproduce the real width of the experimental peaks. During the measurement there are additional statistical processes that affect the energy collection and are not included in the MC, as those related with the electronic chain converting a physical event in the crystal into digital data. The effect of this is an extra widening of the TAS experimental peaks. As the peaks reproduced with the MC do not have the correct width, a convolution with an empirical instrumental resolution distribution has to be applied to the simulated response. For this, a calibration in energy and width has to be obtained for both the simulation and the measured sources. Then, the parameters of these calibrations are used in the Gaussian instrumental width function of [Abr64] to widen the simulation (see Sub. C.2.2 in the Appendixes).

Anytime we need to compare the simulations with the measured data, a recalibration has to be done, because simulation and data have different energy calibrations. This recalibration has to be done in a way that the statistical fluctuations of the data are conserved, so the non deterministic and Poisson-like distribution of counts of [Hel96] is used.

Finally, a simulated gamma response matrix is built using the simulated responses to individual monoenergetic γ rays of several energies (this is only valid for the electron capture analysis). This matrix contains the information related to the dependence of the response function on the detector. To include also the dependence on the level scheme that is being measured, the above mentioned matrix should be convoluted with the branching ratio matrix calculated in Sub. 2.2.1. In this way, the final global response to solve Eq. 2.4 is obtained.

At this point, we have all the ingredients we need to extract the feedings by solving the inverse problem: the response matrix R and the data d (to be discussed in the next section).

2.2.3. Extracting the feedings

The first study of different analysis methods for TAS data can be found in [Can00]. In this work, the EM (Expectation Maximization) Algorithm was found to be the best, and the details of the tested algorithms as well as their results were published in [Tai07]. The EM Algorithm is a general method for maximum likelihood estimation of parameters from incomplete data.

What we understand as "data" here, is the measured spectrum of the decay of interest free of contaminants. But in the TAS singles spectra, all the activity of the decay chain is present. As mentioned in Sub. 2.1.3, ancillary detectors can be

placed inside the TAS to separate the different components of the decay by tagging/gating (making coincidences between detectors). In this work, all the studied cases undergo electron capture decay, so the x-ray tagging was used for the isotopic separation (x rays are like a footprint of each isobar). For this, a coincidence was required between the x-ray detector (covering the K_α peaks which are usually the most intense) and the TAS detector, event by event. This EC tagging gives a TAS spectrum that is clean of isobaric contamination and has low background. In part II of this work, none of the studied cases suffered from a strong electron conversion that could be misleading when looking at the gated spectrum. In part III, an upper limit was estimated for this contamination, since the HR information was very limited in some of the cases.

Sometimes, it is possible that even with a narrow x-ray gate, few counts coming from the tails of the adjacent x-ray peaks produced by the other isobars end up in the final gated spectrum. In this case, one possible solution is to make the coincidence with gates in the x-ray peaks of the isobars to extract their decay spectra from the total TAS spectra and so determine the percentage in which they appear in the gate of interest. It is important to search for any other contaminations, backgrounds, contributions from β^+ decay, etc. that appear in every particular case. The pileup can be calculated using the algorithm of [Can99b]. The maximum counting rate that a TAS handles is usually limited in our experiments to maximum 10^4 Hz to reduce the impact of the pileup, but if the decay is exotic this counting rate is normally low, and in these cases the pileup is not an important distortion.

The EM Algorithm is implemented in two steps: first, the expectation of the likelihood for the current parameters is calculated, and secondly, the parameters that maximize the likelihood are found. The EC feedings are calculated using the iterative algorithm of Eq. 2.6:

$$f_j^{(s+1)} = \frac{1}{\sum_i R_{ij}} \sum_i \frac{R_{ij} f_j^{(s)} d_i}{\sum_k R_{ik} f_k^{(s)}} \tag{2.6}$$

where the feeding f^{s+1} at step $(s+1)$ is related to the feeding obtained in the previous step $f^{(s)}$, through the calculated response function R_{ij}, taking into account the measured data information d_i.

The outputs at this stage of the analysis are a file with the EC feedings and a file with the recalculated spectrum. The recalculated spectrum is obtained by the multiplication of the resulting f_i distribution by the R_{ij} matrix (adding the contaminants if any, the backgrounds and the pileup). The less the difference of this spectrum with the measured one, the more reliable the calculation is. From these EC feedings it is possible to calculate the total $I_{EC+\beta^+}$ feedings, that can then be used in Eq. 2.2 (noticing that $I_{EC+\beta^+} = I_\beta$) to obtain the experimental strength.

And here the analysis will come to its end. It is possible that the results don't fit well to the data, in this case the procedure has to be repeated changing different parameters and studying the dependence of these changes in the results.

— ❦ —

In this chapter the general aspects of the measurement technique and the data analysis used for the 6 studied nuclei presented in this work were described. A more detailed description of the analysis procedure in the form of steps is listed in Appendix A so that they can be referenced from the text when discussing the different analysis.

Part

II

Neutrino Physics

3 Motivation

Neutrinos have been the most elusive particles in the history of experimental particle physics. The history of neutrinos is one of the most interesting ones, and after almost one century there are still open questions about them. In 1930, Wolfgang Pauli proposed their existence to explain the conservation of energy, momentum, and angular momentum in beta decay. It was not until 1956, with the Reines-Cowen experiment, that the interaction of electron neutrinos was detected for the first time (Nobel Prize in 1995). Then, with the work of Leon M. Lederman, Melvin Schwartz and Jack Steinberger in 1962, the world knew of the existence of another type of neutrino, the one associated with the muon (which had already been discovered in 1936 by Carl D. Anderson, another Nobel Prize). Finally, after the discovery of the third lepton in 1975: the tau, it was expected that a third type of neutrino associated with it could exist. And indeed, the tau neutrino was first detected in 2001 by the DONUT collaboration [Kod01].

The Standard Model predicts massless neutrinos, however, it has been widely demonstrated that, although small, the neutrino mass is not zero. One of the consequences of this is the phenomenon of *neutrino oscillations*. This phenomenon was first proposed by Bruno Pontecorvo in 1957. According to the quantitative theory developed by him during the following 10 years, neutrinos oscillate between three available flavours (electron, muon and tau) as they propagate through space [Gri69], in analogy with kaon oscillations.

The hint of this effect came from the measurements of the flux of solar neutrinos (which were supposed to be mainly electron neutrinos), when the number of neutrinos measured was only 1/3 of the expected. The first observation of this neutrino deficit was made in 1968 and soon it was called "*The Solar Neutrino Problem* ", but it was not clear if the problem was in the Standard Solar Model or in a poor understanding of neutrino physics. The phenomenon proposed by Pontecorvo predicted the other 2/3 of neutrinos missing or not detected in the solar flux, which are those electron neutrinos that had already oscillated and transformed into one of the other two types. In 2001, the SNO (*Sudbury Neutrino Observatory*), and later kamLAND

in 2002, solved definitely the solar problem by bringing the first clear evidence that solar neutrinos oscillate [Ahm01].

Specifically, the oscillation occurs because the neutrino flavour eigenstates:

$$\nu_\alpha(\alpha = e, \tau, \mu)$$

mismatch the neutrino mass eigenstates:

$$\nu_k(k = 1, 2, 3)$$

as they are related by:

$$\nu_\alpha = \Sigma_k U_{\alpha k}(\theta_{12}, \theta_{23}, \theta_{13}; \delta)\nu_k \tag{3.1}$$

where $U_{\alpha k}$ is the *Pontecorvo-Maki-Nakagawa-Sakata matrix* or PMNS matrix (it is the analogue of the CKM matrix describing the mixing of quarks). As this matrix is different from the identity matrix, the flavour eigenstates are not the same as the mass eigenstates, thus producing the oscillations. The θs are the "mixing angles", where θ_{12} is important for the "solar component", θ_{23} for the "atmospheric component" and θ_{13} for the "reactor component".

The oscillations show that neutrinos have mass, but the absolute neutrino mass scale is still not known, since neutrino oscillations are only sensitive to the difference of the squares of their masses. Indeed, the probability of oscillation depends on these square differences. For example, the probability of an electron neutrino changing to a muon neutrino after traveling a distance L with energy E can be written as [Esp10]:

$$\begin{aligned} P(\nu_e \to \nu_\mu) \approx s_{23}^2 \sin^2 2\theta_{13} \sin^2\left(\frac{\Delta m_{13}^2 L}{4E}\right) + c_{23}^2 \sin^2 2\theta_{12} \sin^2\left(\frac{\Delta m_{12}^2 L}{4E}\right) \\ + \tilde{J} \cos\left[\left(\pm\delta - \frac{\Delta m_{13}^2 L}{4E}\right)\frac{\Delta m_{12}^2 L}{4E}\right] \sin\left(\frac{\Delta m_{13}^2 L}{4E}\right). \end{aligned} \tag{3.2}$$

where $s_{ij} = sin\theta_{ij}$, $c_{ij} = cos\theta_{ij}$, $\tilde{J} = c_{13} sin2\theta_{12} sin2\theta_{23} sin2\theta_{13}$, and the signs $\pm$ refer to neutrinos/antineutrinos. The expression has a similar structure for the other oscillations. The best estimates for the mass differences and the observed values of the mixing angles are listed in Table 3.1. From atmospheric and solar neutrino oscillation experiments, it is known that $|\Delta m_{12}^2| << |\Delta m_{13}^2| \sim |\Delta m_{23}^2|$, which leads to Eq. 3.2 after simplification of a more complex expression of $P(\nu_e \to \nu_\mu)$ (see [Esp10, p. 42]). This implies either $m_1 \leq m_2 << m_3$ or $m_3 << m_1 \leq m_2$. From the same experiments it is also known that two mixing angles of the PMNS matrix are large and the third is smaller (this is in sharp contrast to the CKM matrix in which

all three angles are small and hierarchically decreasing). Nothing is known about the charge-parity (CP) violating phase of the PMNS matrix δ. This phase factor is nonzero only if neutrino oscillation violates CP symmetry. This is expected [Cab78], but not yet observed experimentally (nothing prevents the phase factor from being zero, but it is unlikely). The value of θ_{13}, together with the signs of Δm_{13} and Δm_{23} are currently unknown.

Table 3.1: Latest global fit of the neutrino squared mass differences and the mixing angles for $\pm$ 1σ. Where there are two values, the upper one corresponds to normal neutrino mass hierarchy and the lower one to inverted hierarchy. Values taken from [Sch11].

Parameter	Value	Experiment
Δm^2_{21} $[10^{-5}$ eV$^2]$	$7.64^{+0.19}_{-0.18}$	SNO
Δm^2_{31} $[10^{-3}$ eV$^2]$	2.45 ± 0.09 $-(2.34^{+0.10}_{-0.09})$	SKamiokaNDE
$\sin^2(\theta_{12})^a$	0.316 ± 0.016	KamLAND
$\sin^2(\theta_{23})$	0.51 ± 0.06 0.52 ± 0.06	SKamiokaNDE
$\sin^2(\theta_{13})^a$	$0.017^{+0.007}_{-0.009}$ $0.020^{+0.008}_{-0.009}$	CHOOZ

[a] There is an update on these values that slightly modifies the actual ones [Fog11], $\sin^2(\theta_{12}) = 0.312$ and $\sin^2(\theta_{13}) = 0.025$

To find all the still unknown values (θ_{13}, δ, hierarchy of ν masses), more measurements are required. For example, it would be desirable to have an intense tunable neutrino source. There are several sources that have been used for neutrino studies, for example: the solar neutrinos coming from nuclear fusion reactions in the Sun, the atmospheric neutrinos, coming from decays after interactions of cosmic rays with atomic nuclei in the atmosphere, the beta decay of neutron rich fission fragments in nuclear reactors, supernova emissions, earth neutrinos, and particle accelerators. Although evidence of neutrino oscillations has been collected from many sources, over a wide range of neutrino energies and with many different detector technologies, particle accelerators offer the greatest control over neutrino beams.

Eq. 3.2 shows that the probability of observing an oscillation depends, among other quantities, on the distance between the point in which the neutrino is produced and the point in which it is detected (L), so, neutrinos should be detected after they had traveled a long distance for the oscillation to occur. In this way, appearance and

disappearance experiments can be done, where the appearance or disappearance of a flavour is detected. Also, $\Delta m^2 L/4E$ should take values so that the sin function is maximum. Below, examples of the most recent neutrino experiments and the sources they use are listed:

1. **First generation (already finished)**
   - SuperKamiokande, gave evidence for neutrino oscillation in 1998, but the results were not conclusive. Uses solar, atmospheric and accelerator neutrinos.
   - SNO, a ν_e disappearance/ν_μ, ν_τ appearance experiment, uses solar ν_e's and its results were the first to directly demonstrate conversions in solar neutrinos in 2001.
   - KamLAND, a $\bar{\nu_e}$ disappearance experiment, uses a reactor as source.
   - MINOS, a ν_μ disappearance experiment, uses the intense NuMI ν_μ beam created at Fermilab with a baseline of 735 km.
   - OPERA, a ν_τ appearance experiment in the Gran Sasso laboratory, uses a ν_μ beam produced at CERN, with a baseline of 730 km[1].
   - CHOOZ, uses a reactor as source of $\bar{\nu_e}$s.
2. **Second Generation (under construction)**
   - T2K, a ν_e appearance experiment, produces ν_μ's in a baseline of 295 km.
   - Nova, a ν_e app./ν_μ dissapp. experiment, with a baseline of 810 km.
   - Double CHOOZ, that uses ν_e from a reactor, will give a more precise limit for θ_{13} than CHOOZ.
   - Daya Bay, a ν_e disappearance experiment, uses a reactor as source.
3. **Third Generation (under study)**
   - *Super beams*, of about 4MW beam power, combined with gigantic detectors. T2HK, T2KK and the CERN-SPL are some examples.
   - *Neutrino factories*, which generate pions from protons, that then decay to muons and these produce the neutrinos. The muons are well collimated in a storage ring of straight sections.
   - *Beta beams*, are neutrino beams from beta decays, first suggested by P. Zucchelli to measure CP (Charge-Parity) violation in the lepton sector.
   - *EC (Electron Capture) Beams*, neutrino beams from electron capture decays.

In this part of the work we concentrate on the beta/EC beam concept, presenting the study of possible sources of neutrino beams for the case of EC beam facilities.

[1]Recent results from OPERA related to "superluminic neutrinos" have attracted a lot of attention.

3.1. Beta, EC and hybrid beam facilities

As mentioned previously, particle accelerators offer the greatest control over neutrino beams. In these accelerator facilities it is important that the source beam is well collimated and the beam line is straight (since neutrinos can travel a long distance without interacting with matter, once they are produced with a certain direction, they will keep that direction). The beam that will produce the neutrinos could be collected in a storage ring with straight sections, in a similar way as in neutrino factories. Moreover, Eq. 3.2 shows that, for an accelerator facility with a fixed baseline L, the detailed study of the energy dependence of the oscillations allows to disentangle if there is CP violation or not. For this, a neutrino beam with adjustable energy will be desirable. Finally, high intensities are needed to have enough statistics.

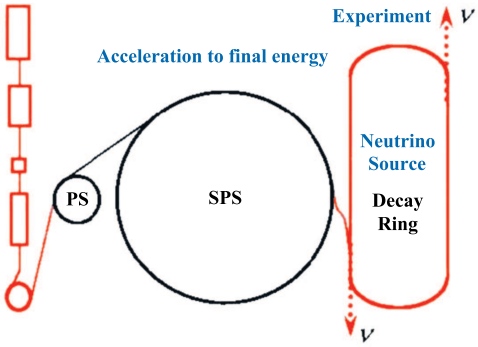

Figure 3.1: Example of a Beta Beam facility. This design was based on existing CERN synchrotrons PS and SPS, where the beta beam would achieve its maximum energy, before being injected into a storage ring (possible development). The area of this ring essentially corresponds to the SPS circumference constrained in a rectangular field of 600×3100 m^2, resulting in a straight section length of about 2500 m [Zuc02].

Regarding the third generation facilities mentioned in p. 22, super beams and neutrino factories were conceived for producing, collecting and storing beams to produce neutrinos with the desired properties. Nevertheless, this can also be achieved using the decay of a beta unstable nucleus which is even simpler. This lead P. Zucchelli [Zuc02] to propose in 2002 the *beta-beam concept* for the construction of a neutrino beam facility. His idea was to use beta-decaying nuclei to provide high-intensity neutrinos of a single flavour, free of intrinsic background contamination, and with well defined energy spectrum. He found that the neutrino flux in such a facility could be 128 times larger than in a "conventional" neutrino factory, and that it could allow stronger collimation because of the larger Lorentz boost[2]. In Fig. 3.1

[2]In beta decay the neutrinos are emitted isotropically in their reference frame. When the radioactive ions are accelerated to high energies and subsequently beta decay in the straight sections of the storage ring, the Lorentz boost provides a better focusing of these neutrinos in the forward direction.

a schematic view of a beta beam facility is shown.

The best candidates for the beta beam are nuclei that decay with a low Q value (so that the final possible energies of the neutrinos are reduced) and short half-life (for reasons related to the design of the ring). Although this is in contradiction with nature laws in most of the cases (low Q values imply more stable nuclei), he proposed two possible beams:

- ^6He, that produces electron antineutrinos in a β^- decay (with $t_{1/2} = 806.7(1)$ ms, $Q_{\beta^-} = 3507.8(11)$ keV, $I_{\beta^-} = 100$ % [Til02] and average energy $E_\nu = 1.937$ MeV):

$$^6_2He \rightarrow ^6_3Li + e^- + \bar{\nu}_e \tag{3.3}$$

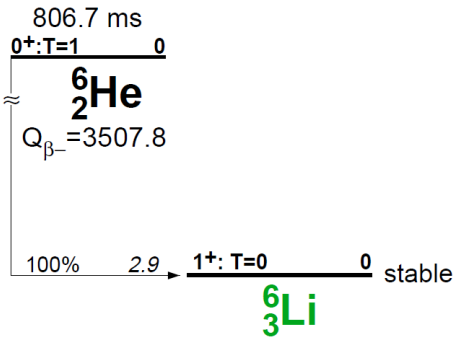

Figure 3.2: Decay of ^6He [Til02].

- ^{18}Ne, that produces electron neutrinos in β^+ decay (with $t_{1/2} = 1.672\ (8)$ s, $Q_{\beta^+} = 4445.7(47)$ keV, $I_{\beta^+} = 100$ % [Til95], and average energy $E_\nu = 1.86$ MeV):

$$^{18}_{10}Ne \rightarrow ^{18}_{9}F + e^+ + \nu_e \tag{3.4}$$

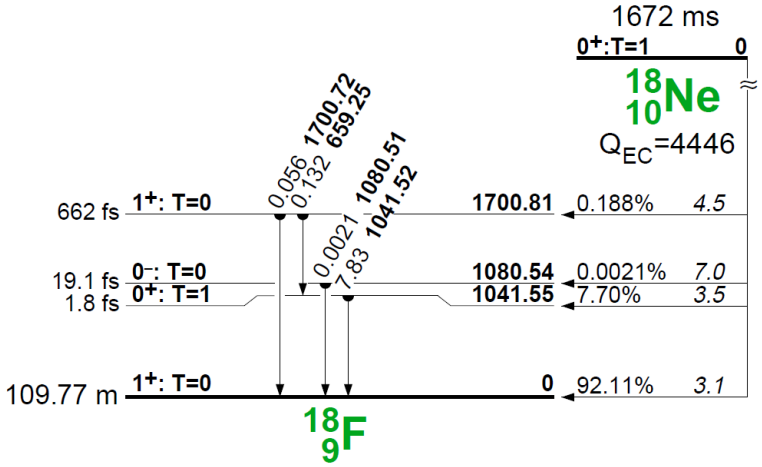

Figure 3.3: Decay of ^{18}Ne [Til95].

As the recoil energy of the daughter nucleus is negligible[3] the final available energy is shared between the $\nu_e(\bar{\nu_e})$ and the $e^+(e^-)$. This means that the energy of the $e^+(e^-)$ has to be measured and from it the $\nu_e(\bar{\nu_e})$ energy is reconstructed. The available energy is defined by $Q - E^*$ (the Q value minus the excitation energy E^* of the level populated in the daughter nuclei).

In comparison with the proposed two reactions, the *monochromatic neutrino beam* concept [Ber05] presents great advantages. Here the neutrino sources are nuclei that decay by means of the electron capture process:

$$ {}^{A}_{Z}X_N + e^- \rightarrow {}^{A}_{Z-1}Y^*_{N+1} + \nu_e \tag{3.5} $$

In this case, if the electron capture process proceeds to *mainly one* level of the daughter, (that is, the beta decay is dominated by a level with a high beta feeding probability I_β), the neutrino energy will be better defined than in the beta beam case, since in the final state all the available energy is taken by neutrino. This energy is again given by $Q - E^*$. In this way, a monochromatic neutrino beam can be produced, and then its energy can be tuned by changing the Lorentz boost. For a fixed baseline, this allows to probe the different energy regions of interest in Eq. 3.2.

In addition, it is possible to unify these two concepts in a *hybrid approach*: As EC and β^+ are competing processes, when the Q value is larger than $2m_ec^2$, the same nucleus can decay by EC or by β^+ with a certain probability. This probability changes with the energy of the level populated in the decay (higher lying levels have lower β^+ probability). In this way, neutrinos coming from EC and β^+ can be used simultaneously to exploit the information from the first and second oscillation maxima of Eq. 3.2 with a single beam, using the monochromatic beam at higher energies and the beta beam at lower energies. This hybrid option offers the major coverage in energy in the same measurement, as can be seen in Fig. 3.4.

3.2. Proton rich nuclei

Proton rich nuclei can be used to produce beta, EC or hybrid neutrino beams, as will be discussed below, but also, they are interesting from the point of view of nuclear structure. The development of techniques to produce these nuclei with higher intensities can be positively affected by the developments for a neutrino beam facility that uses these nuclei as neutrino sources. In this section the importance of the study of proton rich nuclei is discussed.

[3] $E_{rec} \sim p_e^2/2M_NA \sim (2000A)^{-1}$, where p_e is the electron momentum, M_N is the mass of the recoiling nucleus and A the number of nucleons.

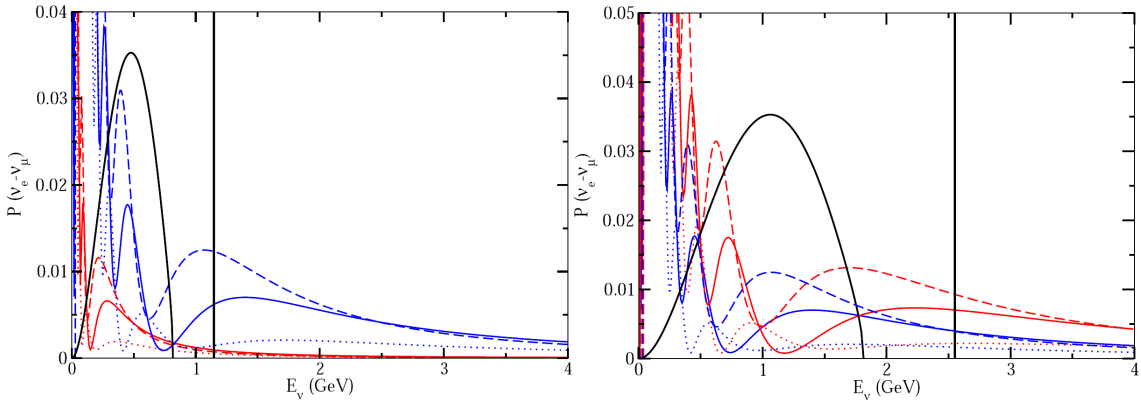

Figure 3.4: Different energy regions of $P(\nu_e \rightarrow \nu_\mu)$ covered by a hybrid facility, showing the β^+ continuum spectrum at low energies and the monochromatic EC spike at high energies. Blue lines: CERN-Canfranc (L = 650 km). Red lines: CERN-Frejus (L = 130 km) for the left panel and CERN-Boulby (L = 1050 km) for the right panel. Solid lines: $\delta = 0°$, dashed: $\delta = 90°$, dotted: δ = -90°, $\sin^2 2\theta_{13} = 0.01$. Taken from [Ber09].

Proton rich nuclei can be used for the study of the GT resonance, a spin-isospin oscillation mode predicted in 1962 by Ikeda, Fujii and Fujita and first observed in 1975. It has been measured by means of charge exchange reactions (using stable nuclei and mainly neutron-rich nuclei) and also with beta decay measurements (using unstable nuclei). Using both techniques, the problem of the "missing strength" was observed (Sub. 2.1.1). In the case of charge exchange reactions, 40 % of the strength was missing in the measurements. In beta decay experiments, for some cases, a possible explanation was the Pandemonium effect (Sub. 2.1.2), in other cases it was due to the fact that part of the B(GT) strength was not accessible in the decay. It is known that for most of the beta decay cases in the nuclear chart, this resonance lies outside the Q value window, so that it remains unobserved. However, there are three restricted regions in which this resonance is accessible: the nuclei with $N \sim Z$ up to A∼70-80, the nuclei around ^{100}Sn and proton rich rare earths above ^{146}Gd.

In the rare earths region, beta decay studies of even Z and $N = 82$ nuclei above the gadolinium are particularly attractive for the determination of the absolute GT strength. ^{146}Gd is magic in neutrons ($N = 82$) and quasi-magic in protons ($Z = 64$, that is, a magic shell closure at $Z = 50$ and the other 14 protons filling the orbitals $g_{7/2}$ and $d_{5/2}$ with a relatively large gap to the next orbital). In an Extreme Single Particle Model picture[4], the valence protons in the $h_{11/2}$ orbital and the free

[4]The Extreme Single Particle Model is a simple model to explain that the ground states of even-even nuclei all have $J^\pi = 0^+$. The simplest description of odd nuclei is to assign all of the ground-state nuclear properties to the last odd nucleon. This model is remarkably successful in predicting ground state spins and parities as the levels are filled according to the minimum energy and the Pauli principle.

neutron $h_{9/2}$ orbitals available, lead to a narrow resonance (in fact the narrowest GT resonance observed in heavy nuclei). This is the reason why the proton rich nuclei above ^{146}Gd have allowed spin-isospin transitions to giant GT resonances in the case of Z odd, and to the population of one single state in the even-even case. However, as Z increases, this resonance gets wider, mainly because of configuration mixing, among other reasons. As the study of this resonance in the decays of Tb, Dy, Ho, Er, and Tm has already been addressed ([Nac04a, Can00]) it would be interesting to make a systematic study increasing in number of protons, further than Yb, and see how the resonance behaves. The nuclei studied in this work as well as the cases studied in [Nac04a] and [Can00] are shown in Fig. 3.5.

3.3. Neutrino beam facilities from proton rich nuclei

In a neutrino beam facility, the nuclei used as neutrino sources have to fulfill certain constrains. Some of them had already been mentioned in the text, but below a complete list of features is provided:

- They should be radioactive nuclei that beta decay.
- They should have a good production rate, to reach the desired intensities.
- One state should be mainly populated in the daughter, so that the neutrino energy is well defined in the EC decay.
- Any other radioactivities, like α decay, proton emission, etc. should be small or zero.
- The half-lives should be within a reasonable interval, not too short to allow reasonable intensities in a storage ring, and in the case of the EC facility not too long since partially charged ions would have a short vacuum half-life.
- For the monochromatic beam facility, larger percentage of EC than β^+ decay. For the hybrid facility, a good percentage of both.

We have made a systematic study of possible even-even candidates for the neutrino beam facility in the Gd region with masses $A = 148$, 150, 152, 154 and 156 (The odd-odd and odd-even cases were not taken into account as their disintegration will be more fragmented into several levels). In these cases, it is expected that the beta decay of nuclei with even Z and $N > 82$ will proceed dominantly through an allowed GT transition to states of spin $J^\pi = 1^+$ in the odd-odd daughter. From this preliminary study, the best candidates seem to be ^{152}Yb, ^{150}Er and ^{156}Yb. The relevant information about them is shown in Table 3.2 and in Figs. 3.6, 3.7 and 3.8.

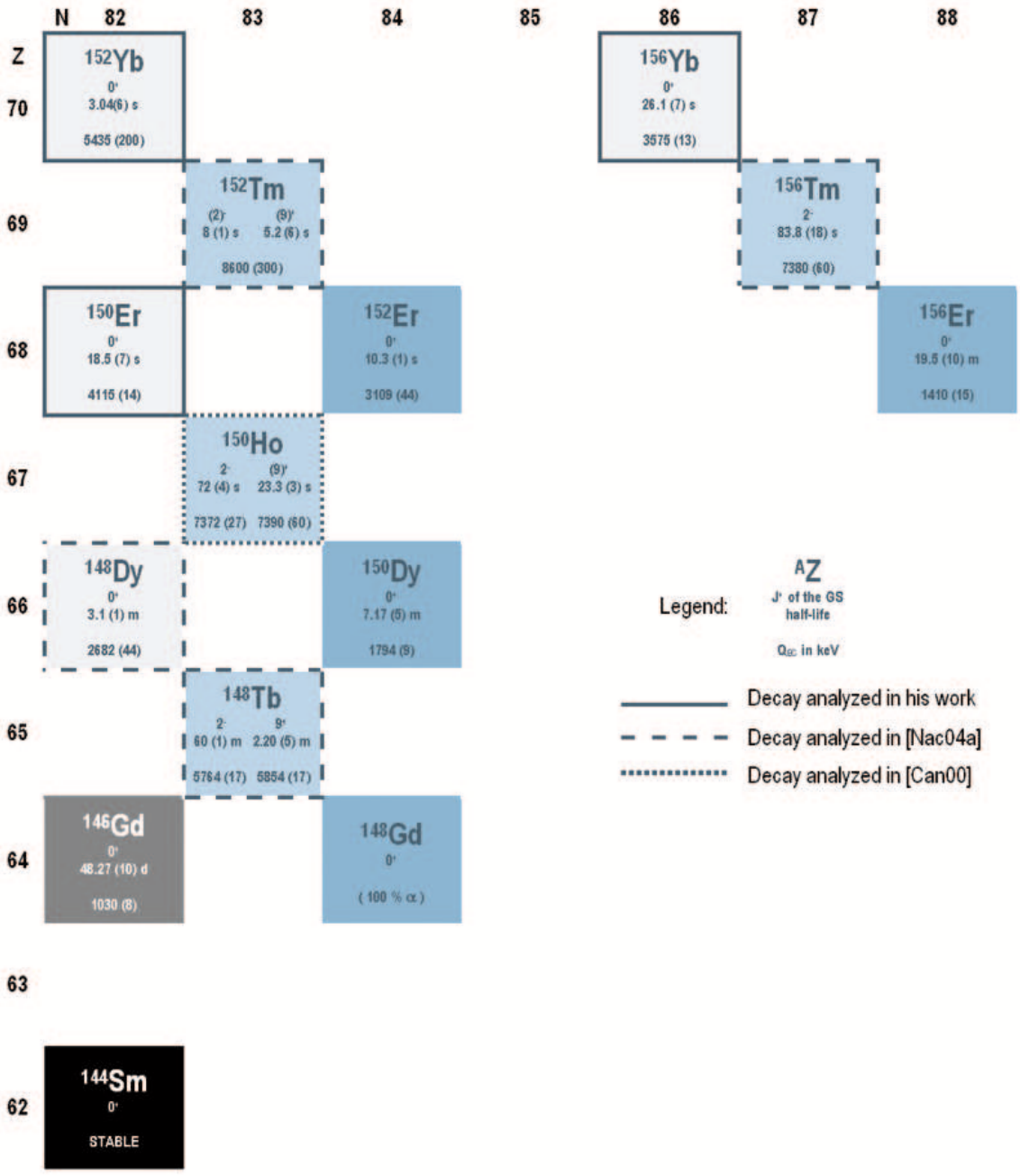

Figure 3.5: Nuclei above ^{146}Gd measured with the TAS technique relevant for the systematics discussion.

Table 3.2: Relevant data for the studied candidate nuclei as neutrino beam sources. The Q values were taken from [Aud03]. The (EC + β^+)/α is the ratio of beta decay to alpha decay. I_β is the total beta feeding to that level (sum of the I_{EC} and $I_{\beta+}$ components). The available energy is the total energy of the neutrino in the case of an EC decay, and in the case of a β^+ decay it is the energy shared by the neutrino and the positron. An energy of $\sim$ 4 MeV is well suited to the intermediate baselines of Europe and the USA with available or future technology [Ber09].

Parent Nucleus ($^A_Z X_N$)	$^{152}_{70}Yb_{82}$	$^{150}_{68}Er_{82}$	$^{156}_{70}Yb_{86}$
Daughter Nucleus ($^A_Z Y_N$)	$^{152}_{69}Tm_{83}$	$^{150}_{67}Ho_{83}$	$^{156}_{69}Tm_{87}$
Half-life [s]	3.04(*6*)	18.5(*7*)	26.1(*7*)
Q value [keV]	5470(*200*)	4115(*14*)	3575(*13*)
(EC + β^+)/α [%]	100/0	100/0	90.0(*20*)/10(*2*)
Strongest populated level E [keV]	482.4	476	115.2
I_β ($I_{EC+\beta^+}$) to level E [%]	87.2(*5*)	99.60(*23*)	85.2(*5*)
I_{EC} to level E [%]	29(*3*)	59.4(*6*) *	57.9(*12*) *
$I_{\beta+}$ to level E [%]	58(*3*)	40.2(*5*) *	27.3(*17*) *
Log*ft* to level E	3.52(*8*)	3.655(*18*) *	3.796(*25*) *
Available E (Q - E^*) [keV]	4987.6	3632	3461.8
Reference	[Art96]	[Der95]	[Rei03]

* These numbers were calculated using the LOGFT tool of the Nuclear Data Center web [LOGFT]. In the case of ^{150}Er the compilation values are I_{EC} = 0.0540(*6*) % and $I_{\beta+}$ = 99.55(*23*) % with a Log*ft* of 8.804(*17*). We consider that these numbers should be revised and appear wrongly in the compilation. In the case of ^{156}Yb the intensities are normalized to 90 % because of the α decay branch of 10 %.

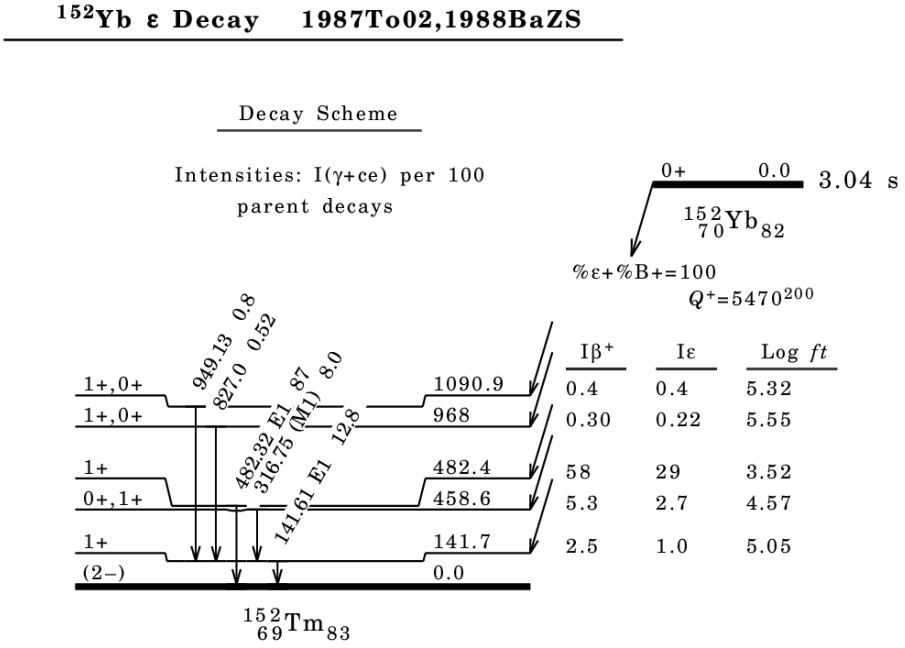

Figure 3.6: Levels populated in the decay of ^{152}Yb according to HR measurements. Level 482.4 keV is the strongest level populated in the decay. Taken from [Art96].

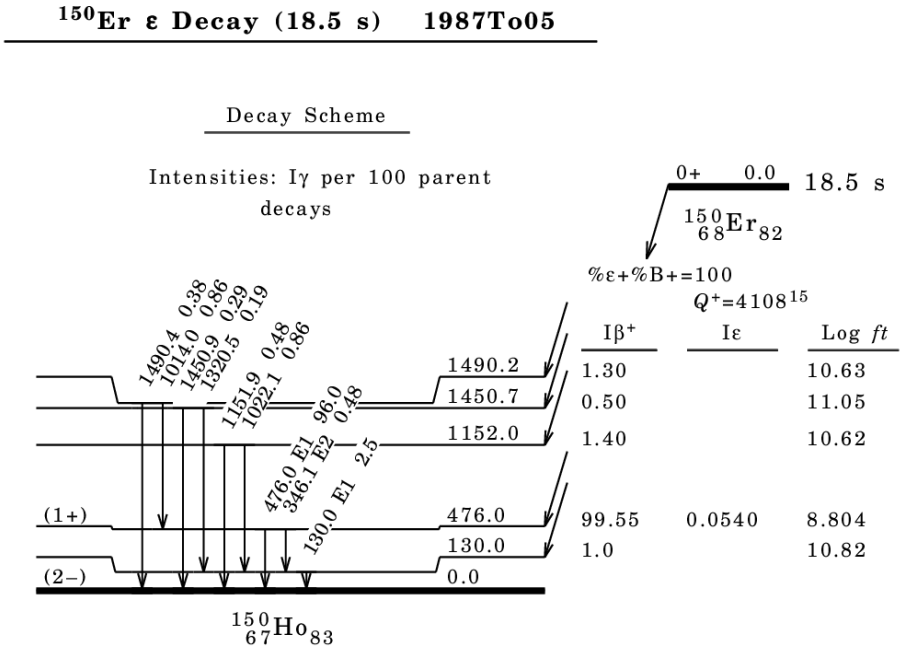

Figure 3.7: Levels populated in the decay of ^{150}Er according to HR measurements. Level 476 keV is the strongest level populated in the decay. Taken from [Der95].

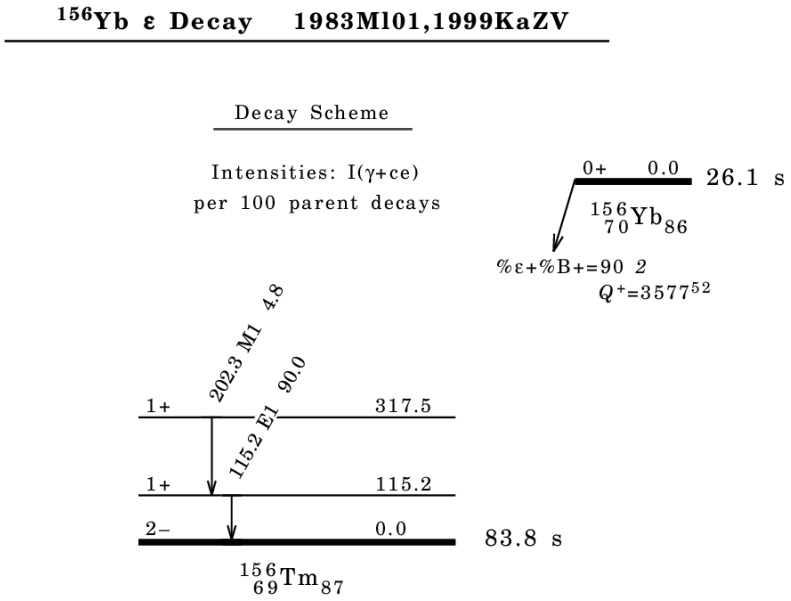

Figure 3.8: Levels populated in the decay of ^{156}Yb according to HR measurements. Level 115.2 keV is the strongest level populated in the decay. Taken from [Rei03].

Regarding the yields, it is not more difficult to produce these heavy nuclei than to produce lighter He or Ne. The present status of a facility like ISOLDE for these rare earths is compatible with the He and Ne production with the desired intensities, and new techniques are being developed.

The rare earths come out together from the ISOLDE ion source (no Z selection) because they are chemically similar, and nuclei closer to stability are produced in higher amounts, which leads to saturation of the system and contamination. But there is one possible solution for this: the use of laser ionization, like in the RILIS ion source, already working at ISOLDE, and tested with other nuclei with nice results (see Part III of this work). In Table 3.3, the intensities that can be produced nowadays at ISOLDE are shown. Looking at the yields there is no real difference in terms of production under the present ISOLDE conditions between the candidates of Zucchelli and the ones proposed in the present work.

Higher production yields can be expected in the future if these nuclei are going to be used in the new facility. Even if more exotic isotopes are needed, techniques to produce them are in hand. A future beta or EC beam facility will need higher intensities and will demand a MW proton driver anyway. For this application, detailed experimental results on the properties of the EC/β^+ transitions occurring in the presented nuclei are needed, together with realistic estimates of the production rates of these ions with the future MW proton driver, and its comparison with the production rate for light ions.

For these reasons, we propose the use of proton rich nuclei above ^{146}Gd for the production of neutrino beams in beta, EC or hybrid beam facilities.

Table 3.3: Comparison of production yields for light and heavy ions at ISOLDE. These yields are measured using a proton beam of 600 MeV and 6×10^{12} particles per second (1μA).

Nucleus	ISOLDE yield [atoms/μC]
^{6}He	1.6×10^{7}
^{18}Ne	3.5×10^{6}
^{152}Yb	No info. available
^{150}Er	7×10^{6}
^{156}Yb	3.2×10^{7}

If a neutrino beam facility is going to be designed relaying on beams produced from the three nuclei mentioned in the last section, the information about their beta feedings has to be trustworthy. But for the nuclei of interest only HR (high resolution) measurements are available. As this technique can suffer from the "Pandemonium effect" (Sub. 2.1.2), it would be desirable to have a determination of the feeding probabilities with a technique that is free of systematic errors related to this phenomenon, like the TAS technique (Sub. 2.1.3).

In the following chapters we present the results of the analysis of earlier TAS measurements performed at the GSI On-Line Mass Separator where these nuclei were produced. The measurements were not optimized for the nuclei presented here, but from the available data the decays of interest (^{152}Yb, ^{150}Er and ^{156}Yb) show sufficient statistics for a TAS analysis.

The main purpose of the study is to answer the question whether there is beta-feeding at higher excitation not detected in high resolution experiments which may modify the known feeding distributions of the beta decay of the nuclei of interest.

4 Experiments

4.1. GSI Facility

The GSI (*Gesellschaft für Schwerionenforschung*, for detailed information see [GSI]) is a German heavy ion research laboratory. The three measurements explained in this Part of the work took place at the On-Line Mass Separator, in the low-energy experimental hall of this facility (see Fig. 4.1). Not only the yield of the lanthanides studied (Er and Yb) but also the other rare earths yields were excellent at this separator.

The beam coming from the linear accelerator (UNILAC) hit a target and produced the reaction of interest, whose products entered into a Thermal Surface and FEBIAD Ionization Sources. Then, the separator selected the ion to be studied (with a mass resolving power of $\Delta M/M \approx 1/1500$). The beam energy E that maximized the cross section of the channel of interest was adjusted by placing degraders in front of the target that slightly modified E to the desired value. The purity of the radioactive sources was achieved by playing with the beam energy, the reaction channel, the mass separation, sources half-life discrimination, and in this particular case with coincidences between the TAS and the ancillary detectors. Installed at the end of the separator there was a TAS experimental setup (Sub. 2.1.3, Sec. 4.2) where the measurements took place.

Two different experiments are presented, one for the study of the ^{152}Yb decay (Sec. 4.3) and another for the decays of ^{150}Er and ^{156}Yb (Sec. 4.4). For full details of the experiments see [Nac04a] and [Can00].

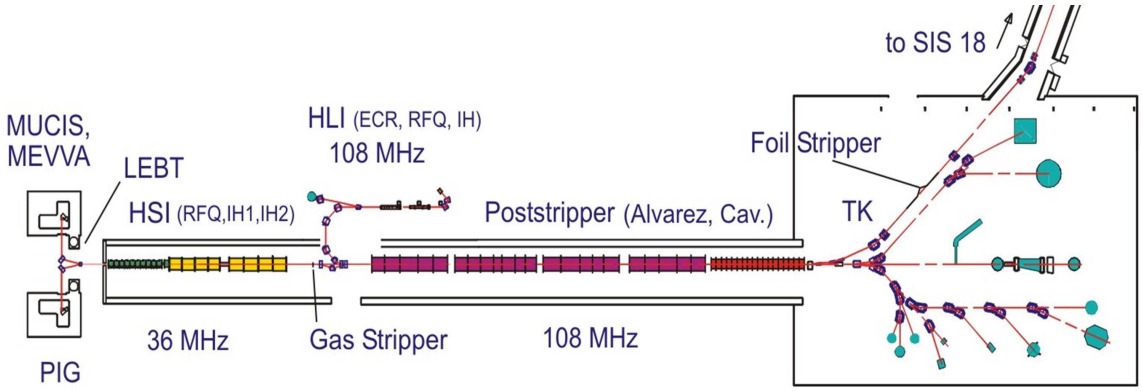

Figure 4.1: Layout of UNILAC and the low energy hall at the GSI facility.

4.2. TAS measuring station

The TAS measuring station installed at the GSI is shown in Fig. 4.2. It had a tape transport system that allowed: first, the collection of the ions coming out of the separator (they were implanted in the tape), and second, the transportation of those ions from the collection position to the center of the TAS for the measurement (by means of the movement of the tape). The collection time plus the measurement time defines one cycle of the tape movement. The duration of each cycle is changed according to the half-life of the species to be measured. In general the tape is moved after 2 or 3 half-lives of the decaying parent nucleus of interest.

The collection time was equal to the measurement time. While the tape was collecting ions, the previously collected sample was measured inside the TAS. Also, one cycle of background was measured every X cycles of data measurements, where X had a different value for the two experiments (see Secs. 4.3 and 4.4). During the cycle devoted to background measurements, the beam coming from the separator was deviated and implanted in another tape station placed in a monitoring setup. The goal of this periodic measurement was to control the production yields of the isotope of interest during the experiment.

The TAS at this station was made of a cylindrical NaI crystal of ϕ = h = 35.6 cm, with a concentric cylindrical well in the direction of the symmetry axis. This hole was filled by a NaI plug detector (4.7 $\times$ 15.0 cm) with a holder that allowed the placement of ancillary detectors and two rollers for the tape. Different ancillary detectors were used for each measurement so their details will be described in the corresponding sections.

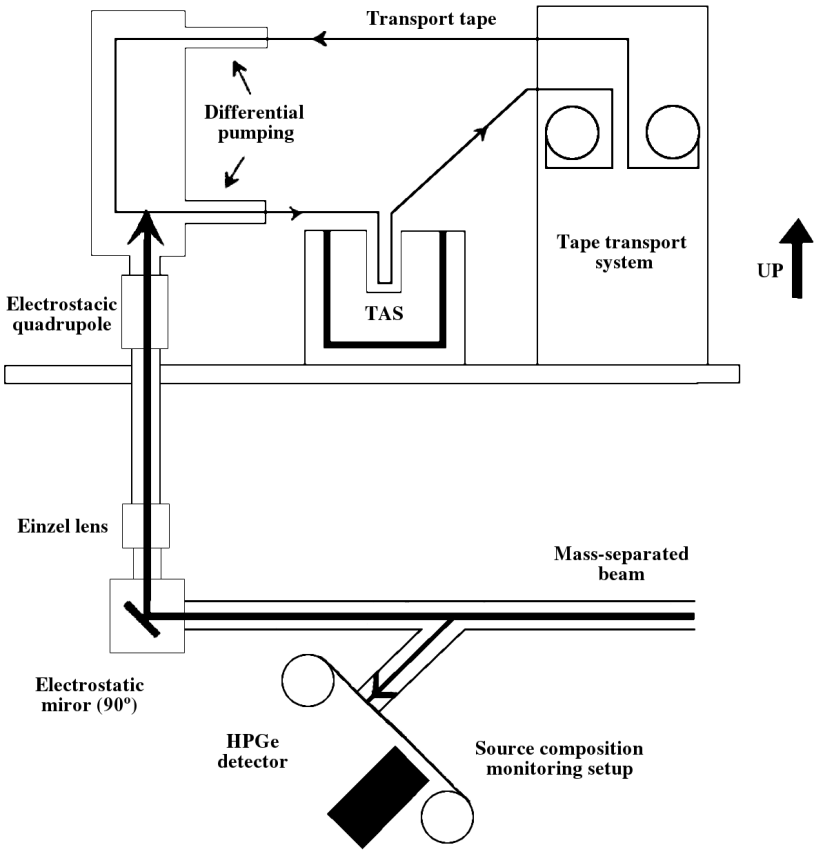

Figure 4.2: TAS Measuring Station installed at GSI showing also the monitoring setup (taken from [Kar97]). For general information about the TAS technique see Sub. 2.1.3.

4.3. Mass A = 152 measurement

This experiment took place in 2001 at the GSI facility and the aim was to study the decay of ^{152}Tm into ^{152}Er, so tape cycles were optimized for this decay. The results of this analysis are presented in [Nac04a]. However, in these measurements the decay data of ^{152}Yb to ^{152}Tm, which is of interest for the present work, was also collected, but never analyzed. The aim of this part of the work is to analyze this decay.

The ancillary detectors attached to the lower part of the plug detector for this measurement were: one germanium planar detector placed just after the plug, to measure x rays, and two silicon detectors, one above the tape and the other below, to measure the β particles. The bottom silicon detector was in reality a telescope, composed by a thinner detector and a thicker one. In this way, not only β particles but protons and alpha particles could be measured and discriminated. Also, to avoid (or at least minimize) the penetration of these charged particles into the TAS, a piece of absorber material made of beryllium was placed below the bottom silicon detector.

The measurement was divided in two parts:

1. **Low Spin Isomer Measurement:** To produce the low spin isomer of thullium ($J^\pi = 2^-$), by means of the fusion evaporation reaction ${}^{96}_{44}Ru_{52}({}^{58}_{28}Ni_{30}, 2p){}^{152}_{70}Yb_{82}$. This reaction produces ^{152}Yb that can only populate the low spin isomer of ^{152}Tm because of β-decay selection rules.

2. **High Spin Isomer Measurement:** To produce the high spin isomer of thullium ($J^\pi = 9^+$), with the reaction ${}^{102}_{46}Pd_{56}({}^{58}_{28}Ni_{30}, \alpha 3pn){}^{152}_{69}Tm_{83}$, that can also produce the $^{152}Tm_{2-}$ isomer.

The collection of $^{152}Tm_{2-}$ was optimized by adjusting the duration of the cycles of the tape movement to 16 s, taking into account the half-lives of the nuclei in the decay chain (as said in Sec. 4.2 the ideal cycle length is 2 or 3 half-lives of the parent):

$$^{152}Yb[t_{1/2} = 3.04(6)\text{ s}] \Rightarrow {}^{152}Tm_{2-}[t_{1/2} = 8(10)\text{ s}] \Rightarrow {}^{152}Er[t_{1/2} = 10.3(1)\text{ s}]$$

With this cycle, the ^{152}Yb was also reasonably well collected, given its half-life. As the half-lives in this decay chain are similar, at least 3 different decays are present in the total TAS spectra (half-lives taken from [Art96]).

A summary of the details of the experiment can be found in Table 4.1 and Fig. 4.3.

4.4. Mass A = 150,156 measurements

In this section we summarize the details of the experiment that took place in 1996 with the same TAS setup but different ancillary detectors. The results of this analysis are presented in [Can00], but, as in the case of Sec. 4.3 the interest here is in decay data that was not analyzed, that is, the decays of ^{150}Er into ^{150}Ho and ^{156}Yb into ^{156}Tm.

In this measurements the configuration of ancillary detectors placed in the holder of the plug detector was very similar to that of the measurements of Sec. 4.3, but there were two thin Si(Li) detectors instead of one thin detector and one telescope, and the absorber placed below the bottom silicon detector was a piece of polyethylene instead of beryllium.

In the case of mass A = 150, there were also two independent measurements for the production of the low and high spin of holmium, from which again we used only the low spin data set for the analysis.

1. **Low Spin Isomer Measurement:** To produce the low spin isomer of holmium ($J^{\pi} = 2^{-}$), by means of the fusion evaporation reaction ${}^{96}_{44}Ru_{52}({}^{58}_{28}Ni_{30}, 4p)^{150}_{68}Er_{82}$. This reaction produces ${}^{150}Er$ that can only populate the low spin isomer of ${}^{150}Ho$ because of β-decay selection rules.

2. **High Spin Isomer Measurement:** To produce the high spin isomer of holmium ($J^{\pi} = 9^{+}$), with the reaction ${}^{95}_{42}Mo_{53}({}^{58}_{28}Ni_{30}, 3p)^{150}_{67}Ho_{83}$, that can also produce the ${}^{150}Ho_{2-}$ isomer, through the β decay of the $2pn$ reaction channel.

The decay chain in this case is (half-lives taken from [Der95] and [Tot74]):

$$^{150}Er[t_{1/2} = 18.5(7)\text{ s}] \Rightarrow {}^{150}Ho_{2-}[t_{1/2} = 72(4)\text{ s}] \Rightarrow {}^{150}Dy[t_{1/2} = 7.17(2)\text{ min}]$$

For the production of mass 156 a fusion evaporation reaction that populated ${}^{156}Tm_{2-}$ directly was used (${}^{103}_{45}Rh_{58}({}^{58}_{28}Ni_{30}, 4pn)^{156}_{69}Tm_{87}$). In this case there is only one β-decaying state, which is the ground state. The duration of the tape cycles was fixed to a value of 120 s, taking into account the half-lives of the nuclei of the decay chain (half-lives taken from [Der95] and [Zol80]):

$$^{156}Yb[t_{1/2} = 26.1(7)\text{ s}] \Rightarrow {}^{156}Tm_{2-}[t_{1/2} = 83.8(18)\text{ s}] \Rightarrow {}^{156}Er[t_{1/2} = 19.5(10)\text{ min}]$$

A summary of the details of the experiment can be found in Table 4.1 and Fig. 4.4.

Table 4.1: Details of the measurements of masses 152, 150 and 156.

	A = 152	A = 150	A = 156
Ion source	Thermal and FEBIAD		
Intensity	∼30pnA		
Beam	^{58}Ni		
Reaction channel	$^{96}_{44}Ru_{52}(^{58}_{28}Ni_{30}, 2p)^{152}_{70}Yb_{82}$	$^{96}_{44}Ru_{52}(^{58}_{28}Ni_{30}, 4p)^{150}_{68}Er_{82}$	$^{103}_{45}Rh_{58}(^{58}_{28}Ni_{30}, 4pn)^{156}_{69}Tm_{87}$
E (initial) [MeV/u]	5.5	5.3	5.3
Degrader 1	Ta 3.25 mg/cm^2	^{93}Nb 0.85 mg/cm^2	-
Degrader 2	^{92}Mo 0.99 mg/cm^2, 97.37 %	-	-
Target	^{96}Ru 2.0 mg/cm^2, 96.53 %	^{96}Ru 1.8 mg/cm^2, 96.52 %	^{103}Rh 2.86 mg/cm^2
Cycle duration	16 s	120 s	
Cycle structure	1 cycle for bg[a], 8 cycles for data	1 cycle for bg, 4 cycles for data	
Ge detector	16×10 mm	16×10 mm	
Si detector	**Top:** 17.4×0.5 mm, **Bottom:** Telescope (*thin*: 17.4 mm×35 μm and *thick*: 27.4×0.55 mm)	Two of 22×1 mm	
Absorber	Beryllium 51×20 mm	Polyethylene, 51×21 mm	

[a] Here, bg stands for background.

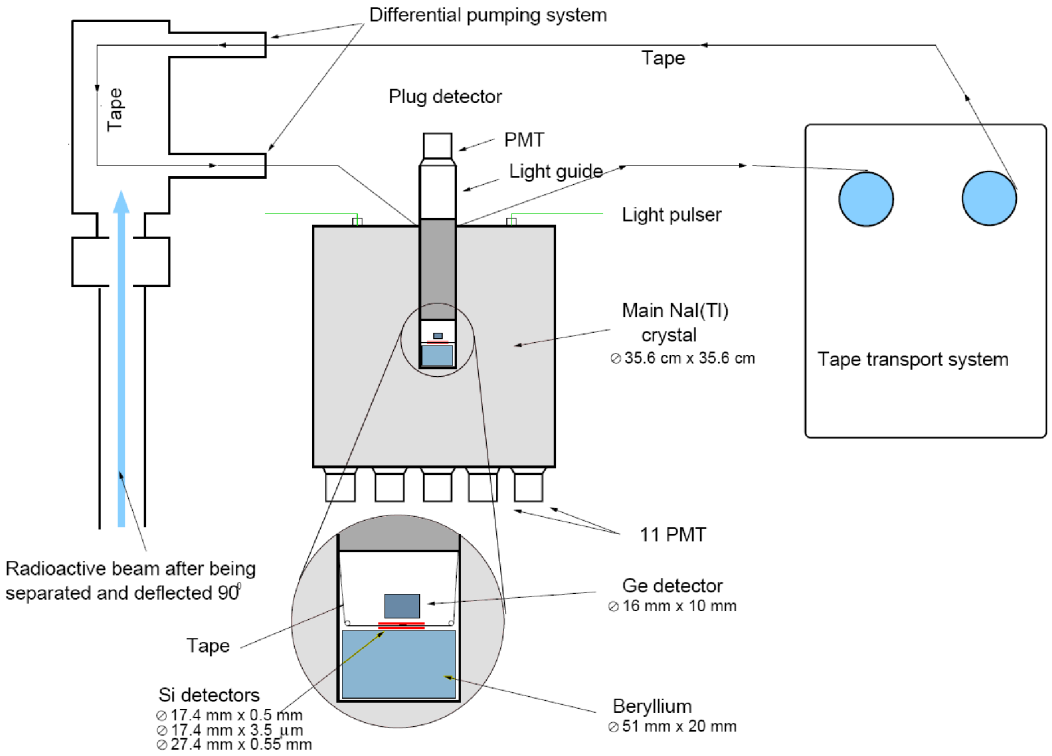

Figure 4.3: Setup and ancillary detectors used in mass A = 152 measurement.

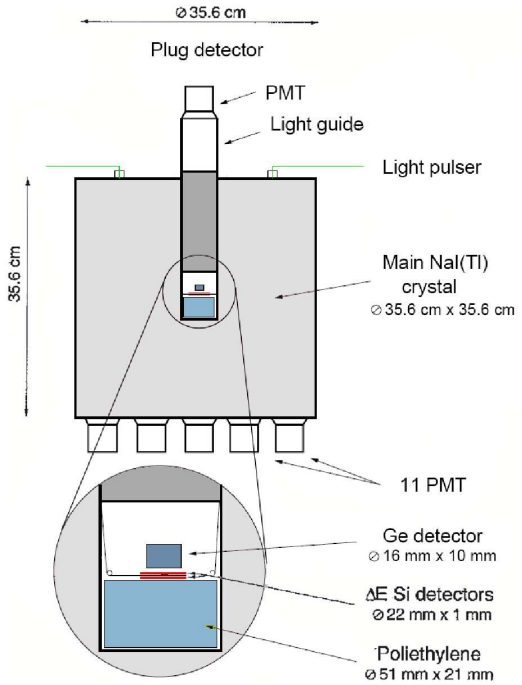

Figure 4.4: Setup and ancillary detectors used in mass A = 150,156 measurements.

5 Analysis and Results

The general procedure for the analysis of TAS data is listed in Appendix A and explained in Sec. 2.2. Part of the data presented in this chapter was already analyzed in [Can00] and [Nac04a], so the MC simulations and calibrations calculated then are still valid for these analyses and there is no need to calculate them again.

The data to be analyzed had to be obtained again from its original storage. When these experiments took place, the data were stored in magnetic tapes. After reading these tapes again with the appropriate device, the files were copied to a modern computer for the analysis. The listmode files stored in these tapes where written in the GOOSY format (GSI Online Offline SYstem [Goo91]) which is not used anymore. The conversion of these files to the more convenient ROOT format [ROOT] is explained in Appendix B "*Preparation of the data for Part II: Rediscovering* GOOSY".

5.1. Mass A = 152

In this section the details of the analysis for the EC decay of ^{152}Yb into $^{152}Tm_{2^-}$ (see Sec. 4.3) are presented.

Taking into account the discussion of [Nac04a, p. 84-85], we decided to use a Q value of 5435(200) keV, instead of the value of 5470(*200*) keV found in the literature [Aud03] (the following Q values discussion is schematically shown in Fig. 5.1). This decision was based in the fact that the Q values of the decay of the two ^{152}Tm isomers to ^{152}Er are 8730(*70*) keV [Aud03] for the decay of the low spin $^{152}Tm_{2^-}$ isomer and 8700(*200*) keV [Nac04a] for the decay of the high spin $^{152}Tm_{9^+}$ isomer. This means that the low spin isomer lies above the high spin isomer in energy, and thus the high spin isomer should be considered the ground state. Then, the mentioned Q value of 5470(200) keV for the decay of ^{152}Yb into ^{152}Tm should be the mass difference with respect to the high spin isomer, since the Q values are typically

calculated between ground states (unless stated otherwise). Taking the above into account, a Q value of 5435(200) keV was used for the decay of the $^{152}Tm_{2^-}$ isomer.

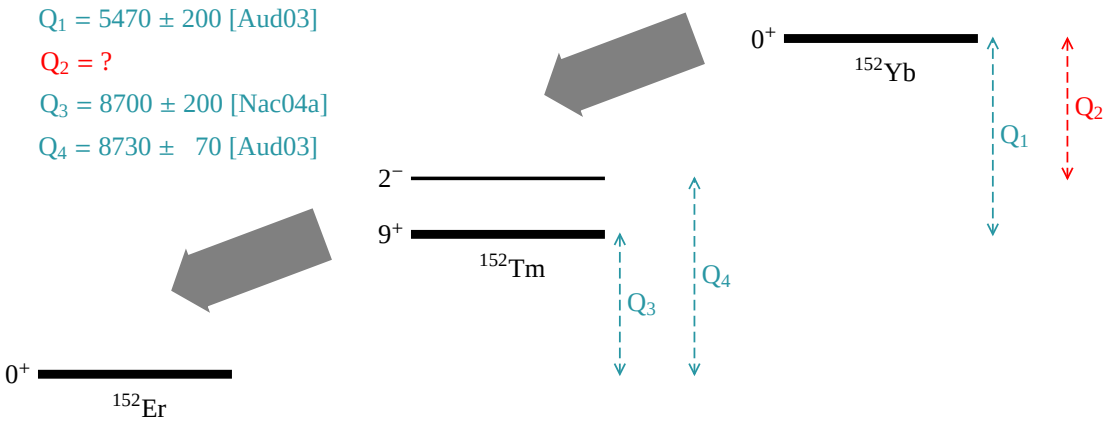

Figure 5.1: Schematic diagram of the Q values in the decay chain of ^{152}Yb.

After many trials with the different parameters of the analysis, the set that better reproduced the data was found and is presented here. For clarity, the steps of Appendix A are followed.

1. **Average branching ratios calculation:**

a) Known Levels: A file was prepared for the known levels of thulium, taken from the last compilation found in the databases [Art96]. In Table 5.1 the final known level scheme used for the analysis is shown.

Table 5.1: Known levels used in the analysis of the EC decay of ^{152}Yb (taken from [Art96]).

E level	J^π	E_γ	$I_\gamma{}^\star$	α_{total}
0.0	2^-	0.0	0.0	0.0
141.6	1^+	141.6	100.0	0.134
458.4	1^+	316.7	100.0	0.128
482.3	1^+	482.3	100.0	0.00631
968.6	0^+	827.0	100.0	0.0
1090.74	0^+	949.13	100.0	0.0

* The intensity of the γ rays is relative to the level. In this case, every level decays by only one γ ray, so the relative intensities should be 100% for all of them.

b) Level Density Parameters: No level density parameters were available from the literature [RIPL] so the procedure outlined in Appendix A was followed. To perform the fit that gives the parameters a and Δ, two excitation energies were

used: one at low excitation energy and another as close to the Q value as possible. From the calculations of [Gor01] and [Dem01], 6 levels are found up to an excitation energy of 500 keV, while 67100 levels are found up to 5000 keV. With these values, the fit gives a = 13.126 MeV^{-1} and Δ = -0.63225 MeV. Slightly changing these values does not seem to have an appreciable effect over the final analysis results.

c) Gamma Strength Function Parameters: According to [Mol95, p. 135], the deformation parameter for ^{152}Tm is β_2 = -0.052. The neutron energy separation is S_n = 9130 keV [Art96]. In Table 5.2 the values of the gamma strength function parameters obtained with these values are shown. The results of the analysis were stable when these values were changed 30% up and down.

Table 5.2: Giant resonance parameters for the E1, E2 and M1 gamma strength functions of ^{152}Tm (β_2 = -0.052, S_n = 9130 keV).

Type	E [MeV]	w [MeV]	Γ [mb]
E1	15.288	4.754	363.298
	14.507	4.301	401.550
M1	7.695	4.000	4.522
E2	11.825	4.286	4.373

d) Average branching ratios calculation: As said before, the chosen binning was 40 keV per channel. Regarding the range of the unknown part of the level scheme, the last known level lays at an energy of 1090.74 keV, which means that it is smaller than 28×40 = 1120 keV. Thus, the initial bin of the unknown part should be bin number 28. For the final bin of the range, since the Q value used for the analysis is 5435 keV, the corresponding final bin is 136. This means that the energy range to be used in the calculation of the branching ratios for the unknown part of the level scheme is from 1120 to 5440 keV. Using a), b), c) and d), the branching ratio matrix of the decay was obtained and it is shown in Fig. 5.2.

2. **Response simulation:**

In this part of the analysis, the gamma response simulations already prepared by [Nac04a] for this measurement were used. In Fig. 5.3 the response matrix of the detector (R_{ij}) obtained by the convolution of this monoenergetic gamma response simulations with the average branching ratios calculated in the previous step is shown.

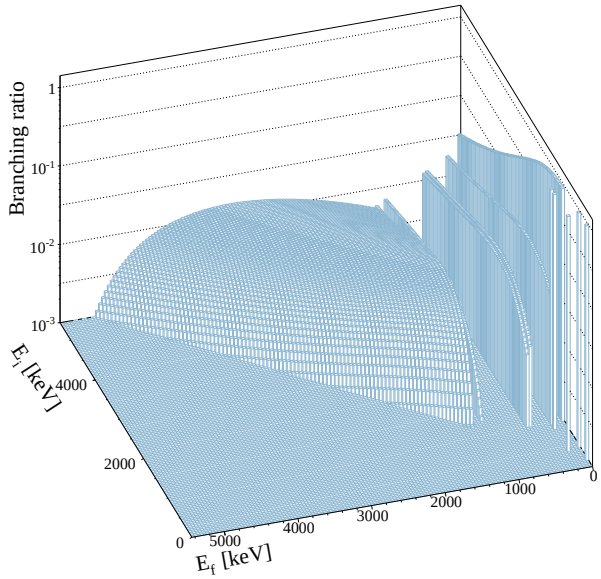

Figure 5.2: Average branching ratio matrix for the EC decay of ^{152}Yb. The E_i axis is the energy of the initial level of the gamma transition and the E_f axis is the energy of the final level. The Z axis is the branching ratio value for the transition from E_i to E_f represented by the (E_i, E_f) pair. Note that this branching ratio matrix is binned (ΔE = 40 keV) and normalized.

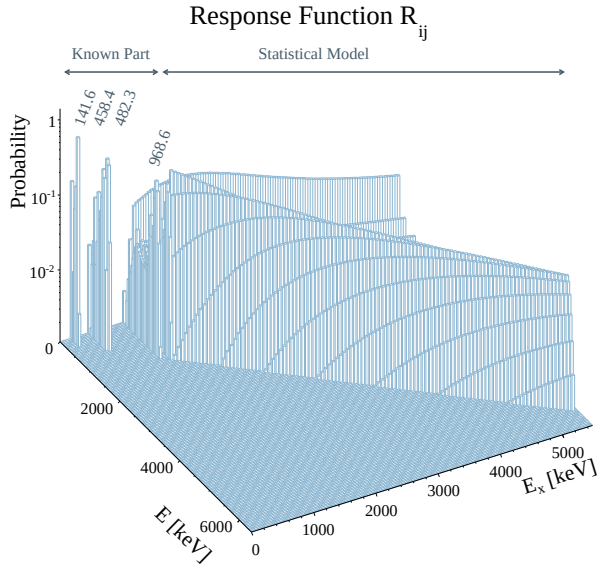

Figure 5.3: Gamma response matrix of the TAS detector for the EC decay of ^{152}Yb. The E axis represents the distribution of energy deposited in the detector by gamma cascades following the de-excitation of the levels. The E_x axis represents the excitation energies of the daughter nucleus, that is, the level energies. The Z axis is the normalized response (R_{ij}). Note that this matrix is normalized and binned (ΔE = 40 keV).

3. **Extracting the feedings:**

a) X-ray tagging: Since the interesting decay for this application is the EC decay of ^{152}Yb into ^{152}Tm, a spectrum with all the statistics of the germanium detector (747 929 counts) was prepared to set the x-ray gates. The most intense peaks in this spectrum are those of the K_α rays of Erbium, given that the experiment was optimized for the production of its parent ^{152}Tm.

In Fig. 5.4, the gates for the nucleus of interest and all the possible contaminants, together with their background gates are shown. The width of the gates was chosen according to a compromise between making a clean gate and having enough statistics. Sometimes this can be difficult, as the gates could be slightly contaminated by their neighbors. For the decay of interest, 2 gates can be used, one in the thulium $K_{\alpha1}$ x rays, that has the higher statistics (44 446 counts) but is also more contaminated with the tails of the surrounding peaks, and one in the K_β x rays (6080 counts). These two gates were added to make the final thulium gate.

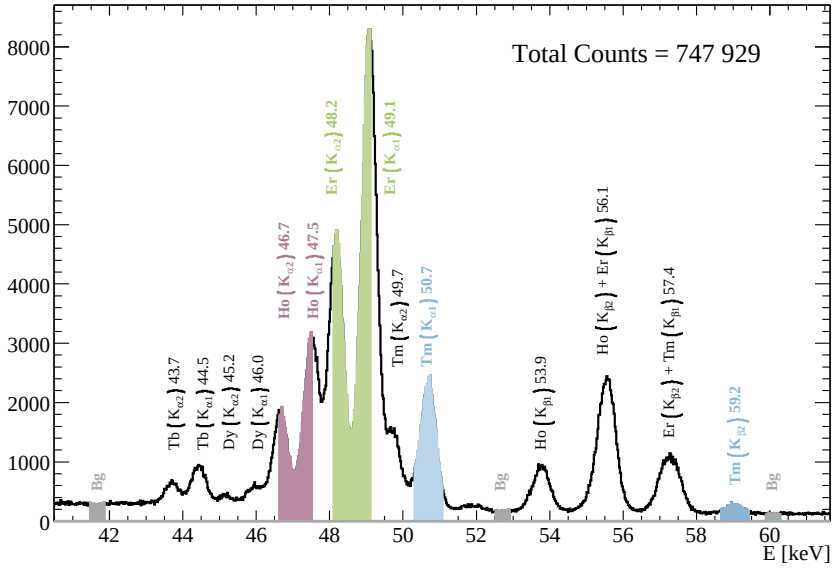

Figure 5.4: Germanium x-ray spectra showing the gates used for the analysis of the EC decay of ^{152}Yb. The background gates are also shown. The x-ray peaks of the isobars were very close to each other, so the background gates could not be taken next to every peak.

b) Contaminants, pileup, backgrounds: In Fig. 5.5 the gated spectra generated from the gates of Fig. 5.4 is presented. Their corresponding backgrounds are also shown. Changing the widths of these gates in a reasonable range it was found that even the thulium $K_{\alpha1}$ x-rays gate does not show contributions from the tails of the other isobars, or if they are present, they are negligible.

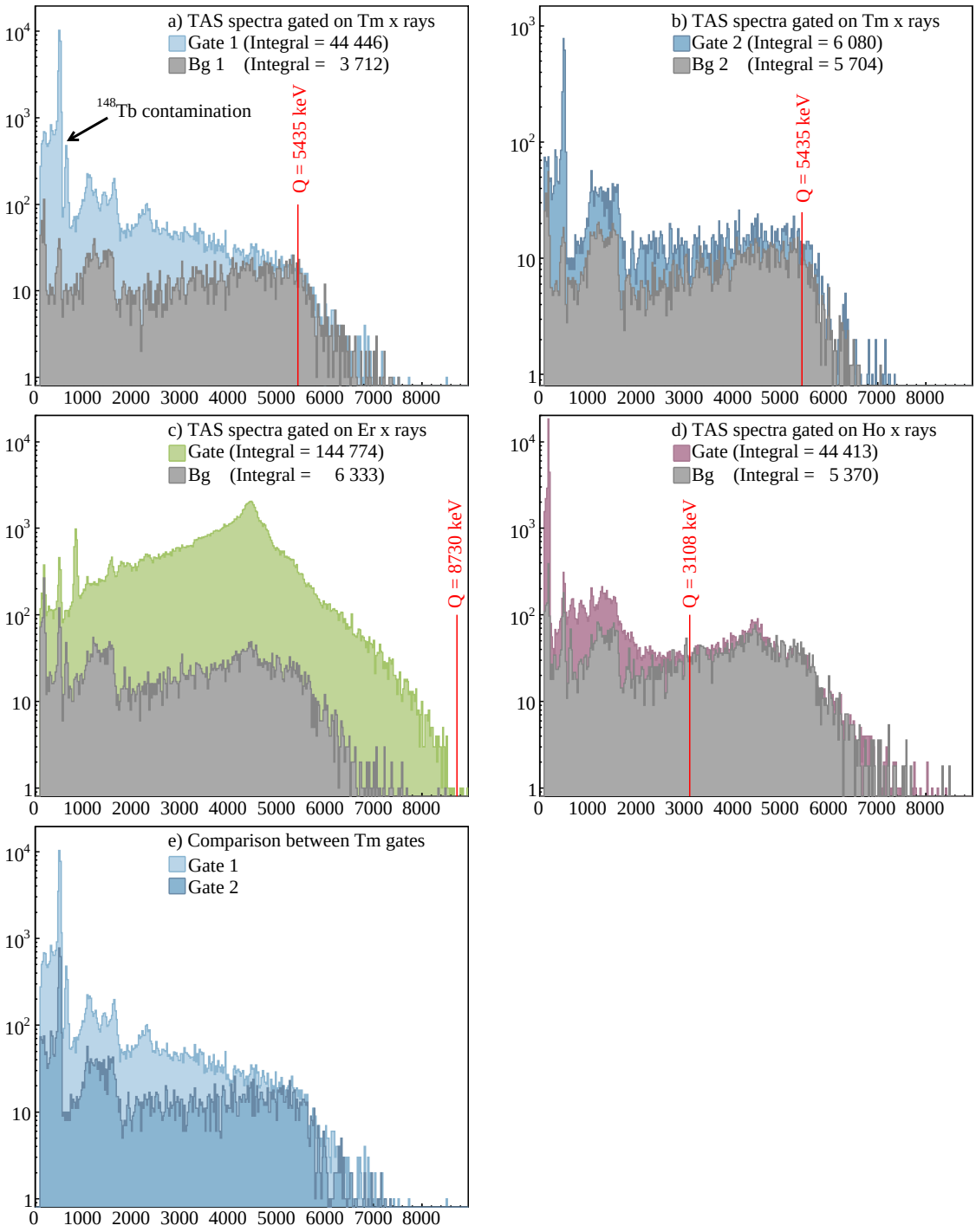

Figure 5.5: Gates of the isobars produced in the EC decay chain of ^{152}Yb: a) $K_{\alpha 1}$ thulium gate b) K_{β} thulium gate. c) K_{α} erbium gate d) K_{α} holmium gate e) Comparison of the two thulium gates (no background subtracted). The Q values are taken from [Aud03]

Having a closer look at the backgrounds, in the first gate of thulium there is a peak that can not be associated with any of the isobars of the EC decay chain. The presence of this peak is due to the fact that ^{152}Er α decays to ^{148}Dy (α branch: $90(4)\%$) that then EC decays to ^{148}Tb. In this EC decay, the most populated level of ^{148}Tb (with a beta feeding of $I_{EC} = 92.91\%$) is at 620 keV and it de-excites to the ground state by a γ ray of the same energy with $I_\gamma = 97\%$. As ^{148}Tb has a half-life of 1 hour, it is present during all the measurement. This peak can be seen when a coincidence is required between the TAS background cycles and any x ray, and also, the terbium signature can be seen in the x-ray spectra of the background cycle (Fig 5.6).

$$\underbrace{^{152}Er}_{(t_{1/2}=10.3s)} \xrightarrow[Q_\alpha=4934\ keV]{90\%\ \alpha} \underbrace{^{148}Dy}_{(t_{1/2}=3.1m)} \xrightarrow[Q_\alpha=2678\ keV]{100\%\ EC} \underbrace{^{148}Tb}_{(t_{1/2}=1h)} \left[1^+ \xrightarrow[E_\gamma = 620\ keV]{I_\gamma = 96.8\%} 2^-\right]$$

The last contamination contributing to the gate comes from the decay itself. After several iterations of the analysis producing results that did not reproduce the data, it was found that there was also a small contribution from the β^+ competing decay that slipped in the EC gate. The β^+ decay can contaminate the EC gate if any of the transitions de-exciting the levels populated in the decay is converted (see Sub. 2.2.1). The internal conversion may be responsible for some of the x rays arriving at the peak of interest for the gate. For this reason, a β^+ spectrum was calculated with the MC simulation of step 2 and used in the analysis as another contaminant. To this end, 10^6 β^+ decay events were launched to the level of interest. The ratio to the gate of interest of this β^+ contamination normalized by its corresponding factor, $(3.2 \cdot 10^{-3})$ was comparable to the conversion coefficient normalized by the fluorescence yield and the β^+ branch $(3.9 \cdot 10^{-3})$.

Finally, for the calculation of the pileup, a TAS spectrum with all the statistics of the measurement was prepared. Using the pulse of Fig. 5.7a), the pileup of Fig. 5.7b) was obtained.

All the contributions to the decay and their normalization factors are listed in Table 5.3.

Table 5.3: Normalization factors of all the contributions to the measured spectrum. The ID is a number to make it easy to refer to them through the text.

Contribution	ID	Norm. factor
X-ray gated background	1	0.6
TAS background in coincidence with any XR	2	1.43
Simulated β^+ decay contribution	3	160.78
Pileup	4	293.03

c) Algorithm application: The experimental spectra has 499 channels once recalibrated to the MC. For this case, the spectra has to be rebinned by a factor of 2 before applying the recalibration. The data, background and pileup used as inputs for the analysis program are shown in Fig. 5.8.

As said before, the bin of the Q value is 135, but since the analysis includes the contaminants, it was made from 120 keV (bin 3, approximately) to 5560 keV (bin 139, appox.). After 200 iterations the difference between χ^2 was less than $1/10^8$. In Fig. 5.9 the extracted feedings and the recalculated spectrum are presented. The relative differences between the recalculated spectrum and the data are calculated in the following way:

$$relat.\quad dev. = \frac{rec - data}{data}$$

The most conflictive zones are those were the statistics are low since there are more fluctuations, as can be seen in the plot of the lower left panel of Fig. 5.9 b).

d) Strength calculation: The calculation of the strength was made from 0 to 5200 keV, to prevent the logft value from having unphysical values. The $t_{1/2}$ and the Q value were taken from Table 3.2. In this step of the analysis the total $I_{EC+\beta^+}$ feedings were calculated from the I_{EC} feedings obtained in the previous step. The values of the EC and total feedings and the experimental strength can be found in Table 5.4. The TAS results for the levels at 458.4 keV and 482.3 keV are given together, since the TAS resolution does not allow to separate them.

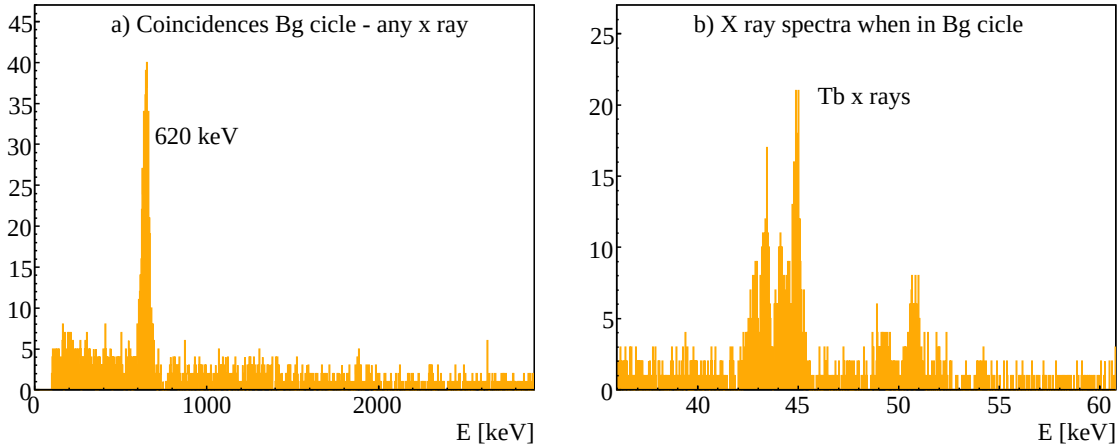

Figure 5.6: Alpha branch contamination in the ^{152}Tm gate: a) Coincidence between the TAS spectra measured during the background cycle and any x ray. The peak at 620 keV appears very clearly. b) X-ray spectra measured in the background cycle, showing the x rays of terbium.

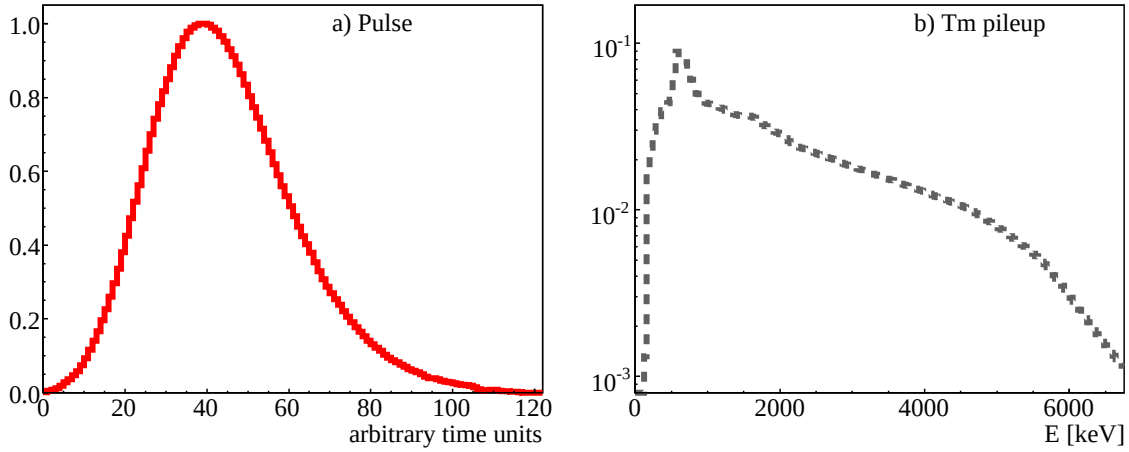

Figure 5.7: a) Pulse used for the calculation of the pileup. The pulse was measured with a digital oscilloscope, and then normalized (length 120 bins). The maximum is at bin 40 (this binning has nothing to do with the analysis binning of the gated spectra). b) Pileup present in the decay of ^{152}Yb into ^{152}Tm, calculated with pulse a).

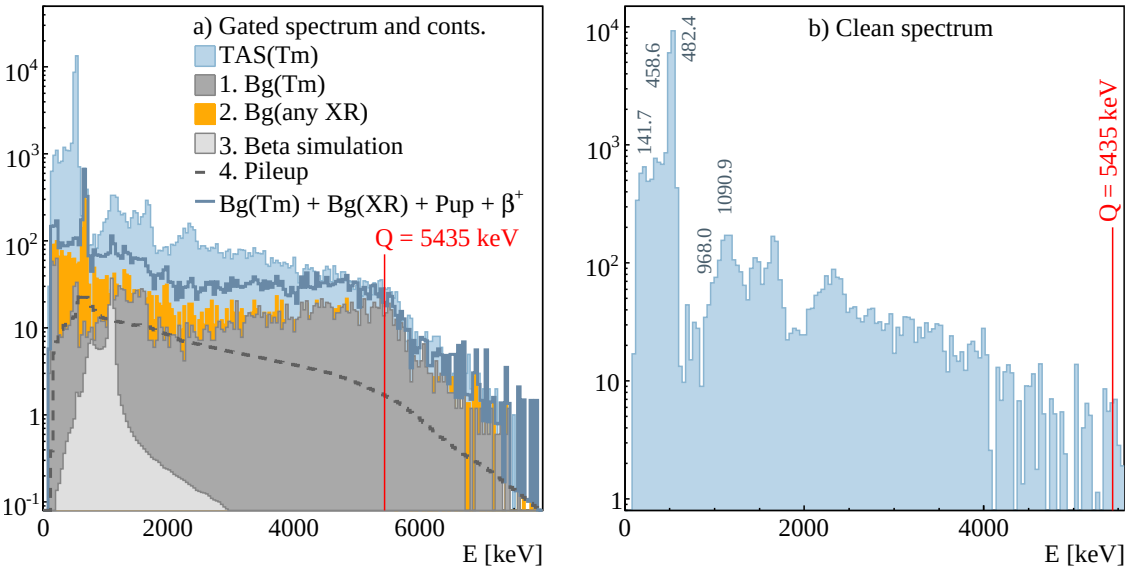

Figure 5.8: a) TAS gated spectra for the decay of ^{152}Yb into ^{152}Tm and contributions of Table 5.3 multiplied by their normalization factors. The sum of all the contributions is also shown. When this sum spectrum is subtracted to the thulium gate, the clean spectrum of *b*) is obtained. Spectrum *b*) was not used for the analysis and is only shown for completeness. All the spectra are binned and recalibrated to the MC.

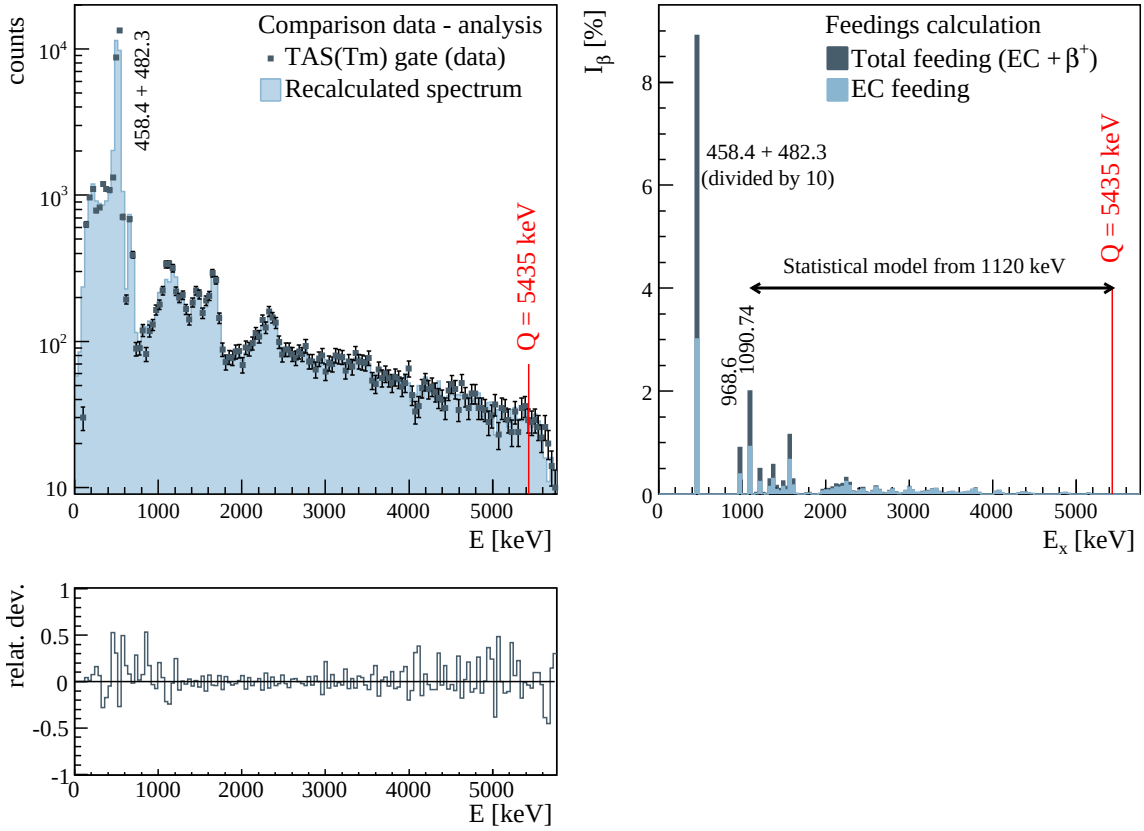

Figure 5.9: Final results of the analysis of the EC decay of ^{152}Yb: Upper left panel: Comparison between the recalculated spectrum and the measured one (Both spectra contain the contribution from contaminants). Lower left panel: Relative differences between data and recalculated spectrum. Upper right panel: Beta feedings (total and EC component)

Table 5.4: Deduced $I_{EC+\beta^+}$ values for the levels populated in the decay of ^{152}Yb. Columns labeled "TAS" stand for the Total Absorption Gamma Spectroscopy technique results, while HR refers to high-resolution results [Art96]. The TAS results for the 458.4 and 482.3 levels are given together, since the TAS resolution does not allow to separate them.

E_{lev}	J^π	I_{EC} [%]		$I_{EC+\beta^+}$ [%]		B(GT) $[g_A^2/4\pi]$	
[keV]		TAS	HR	TAS	HR	TAS	HR
141.6	1^+	-	1.0(3)	-	3.5(9)	-	0.04(2)
458.4	0^+,1^+	-	2.7(4)	-	8.0(6)	-	0.10(2)
482.3	1^+	30(3)	29(3)	89(2)	87.2(5)	1.2(3)	1.2(3)
968.6	1^+,0^+	0.4(2)	0.22(5)	0.9(5)	0.52(9)	0.020(4)	0.008(2)
1090.7	1^+,0^+	0.9(2)	0.4(1)	2.0(3)	0.8(3)	0.04(1)	0.012(4)
1120 - Q		5.7(2)	-	8.0(3)	-	1.74(2)	-
TOTAL		37.0(7)	33.3(3)	99.9(2)	100.0(1)	3.0(3)	1.3(3)

5.2. Mass A = 150

1. **Average branching ratios calculation:**

a) Known levels: For the known part of the level scheme, the information of Ref. [Der95] was used. After trying several combinations for the known levels, the best solution was to set the unknown part after the level at 1152 keV, that is, from 1160 keV on. The file used for the analysis is reproduced in Table 5.5, where the two known levels at 1450.7 and 1490.2 keV are not included.

Table 5.5: Known levels used in the analysis of the EC decay of ^{150}Er [Der95]. There are more known levels but the unknown part was fixed to start at an energy of 1160 keV. The description of the table is the same as for Table 5.1.

E level	J^π	E_γ	I_γ	α_{total}
0.0	2^-	0.0	0.0	0.0
130.0	1^+	130.0	100.0	0.158
476.2	1^+	346.1	0.5	0.0438
476.2	1^+	475.8	100.0	0.0595
1152.0	1^+	1022.1	100.0	0.0
1152.0	1^+	1151.9	56.0	0.0

b) Level Density Parameters: As a and Δ were not available in the literature, we made the fit with 3 levels up to 250 keV and 9450 levels up to 4 MeV ([Gor01], [Dem01]). The result of the fit was: a = 12.856 MeV^{-1}, Δ = -0.462 MeV.

c) Gamma Strength Function Parameters: The neutron separation energy for ^{150}Ho is 8.479 MeV [Der95] and the deformation parameter is $\beta_2 = -0.052$ [Mol95]. With these two values, the gamma strength parameters of Table 5.6 are obtained.

Table 5.6: Giant resonance parameters for the E1, E2 and M1 gamma strength functions of ^{150}Ho (β_2 = -0.052, S_n = 8479 keV).

Type	E [MeV]	w [MeV]	Γ [mb]
E1	15.335	4.782	355.371
	14.552	4.327	392.789
M1	7.729	4.0	3.122
E2	11.877	4.310	4.155

d) Average Branching Ratios Calculation: As mentioned in step 1 a), the unknown part was set from 1160 keV to 4120 keV. Using *a*), *b*), *c*) and *d*) the branching ratio matrix was generated.

2. **Response simulation:**

In Sec. 4.4 it was mentioned that the same TAS setup of the experiment of Sec. 4.3 was used, but with different ancillary detectors. This fact changes the response of the detector, so the Monte Carlo simulation used for this analysis is different from the one used for mass 152. In consequence, a different simulated monoenergetic response matrix was used for this analysis and the analysis of mass 156 (Sec. 5.3). This matrix is the same as the one used for the analysis of [Can00]. The convolution of this simulated gamma response with the average branching ratio matrix calculated in step 1 d) gives R_{ij}, which is shown in Fig. 5.10

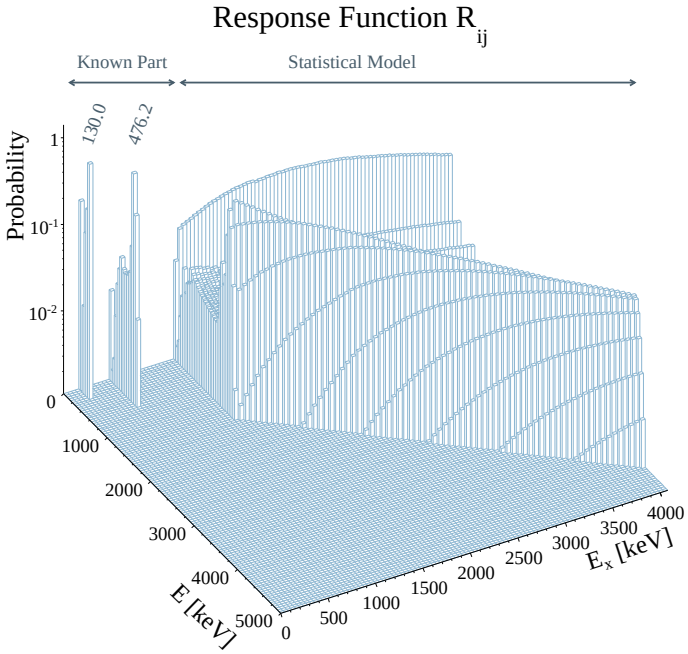

Figure 5.10: Response matrix of the detector (R_{ij}) for the EC decay of ^{150}Er. The description of the plot is analogue to that of Fig. 5.3.

3. **Extracting the feedings:**

a) X-ray tagging: In Fig. 5.11 the gates fixed for this mass are shown. Again, as this experiment was optimized for the production of Holmium, the x rays of its daughter (^{150}Dy) are the most intense. The two gates for the $K_{\alpha 1}$ (gate 1) and K_{β} (gate 2) x rays of holmium were added generating one spectrum for the holmium gate, in the same way as for mass 152.

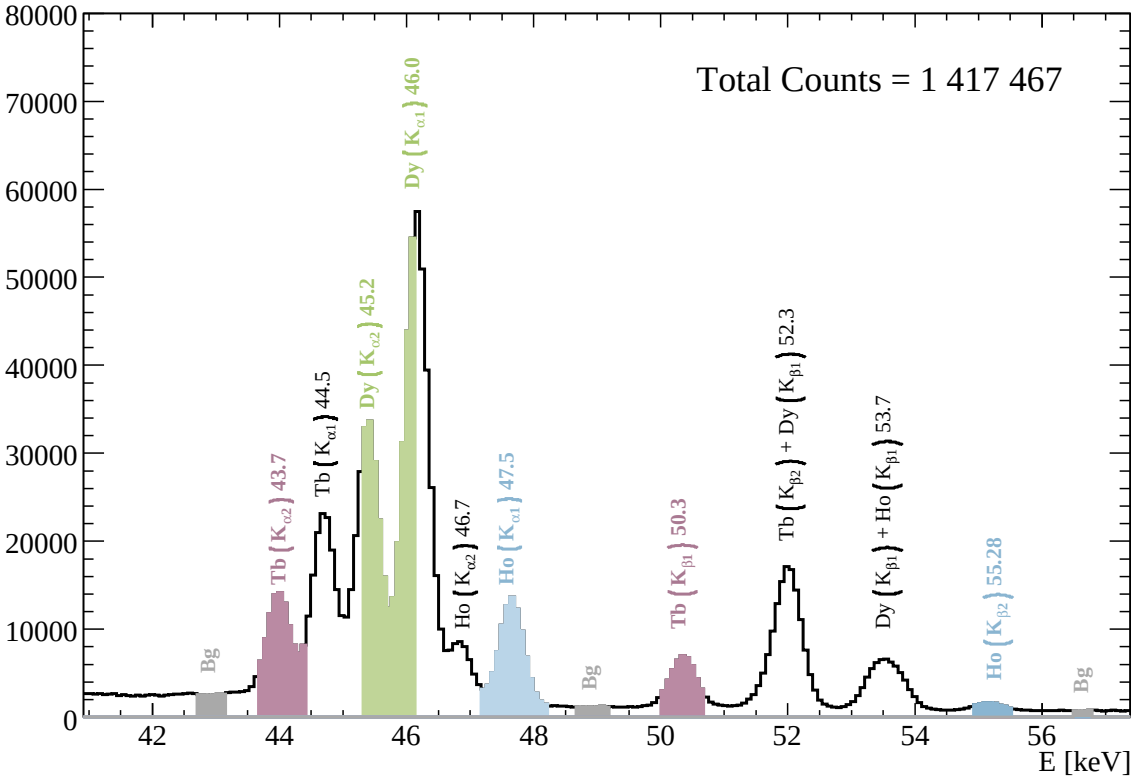

Figure 5.11: Same as Fig. 5.4 for mass 150.

b) Contaminants, backgrounds, pileup: In Fig. 5.12 the gates obtained from the coincidences between the spectrum of Fig. 5.11 and the TAS singles are shown with their respective backgrounds.

The contribution of the isobars in the x-ray gated TAS spectrum was considered negligible, as the windows in the x-ray peaks were chosen in a conservative way. This was checked by comparison with other gates.

No other background apart from the x-ray gated background spectrum was found. However, a small beta plus contamination appears as in the case of mass 152. Again a simulation of this component was made to be used as a contaminant.

The pileup was calculated with the pulse measured at GSI in the corresponding experiment which is shown in Fig. 5.13. Note that it is slightly different from the other pulse (Fig. 5.7). The normalization factors for all the contributions to the decay of interest appear in Table 5.7. The background used for the analysis is the sum of contributions 1 and 2.

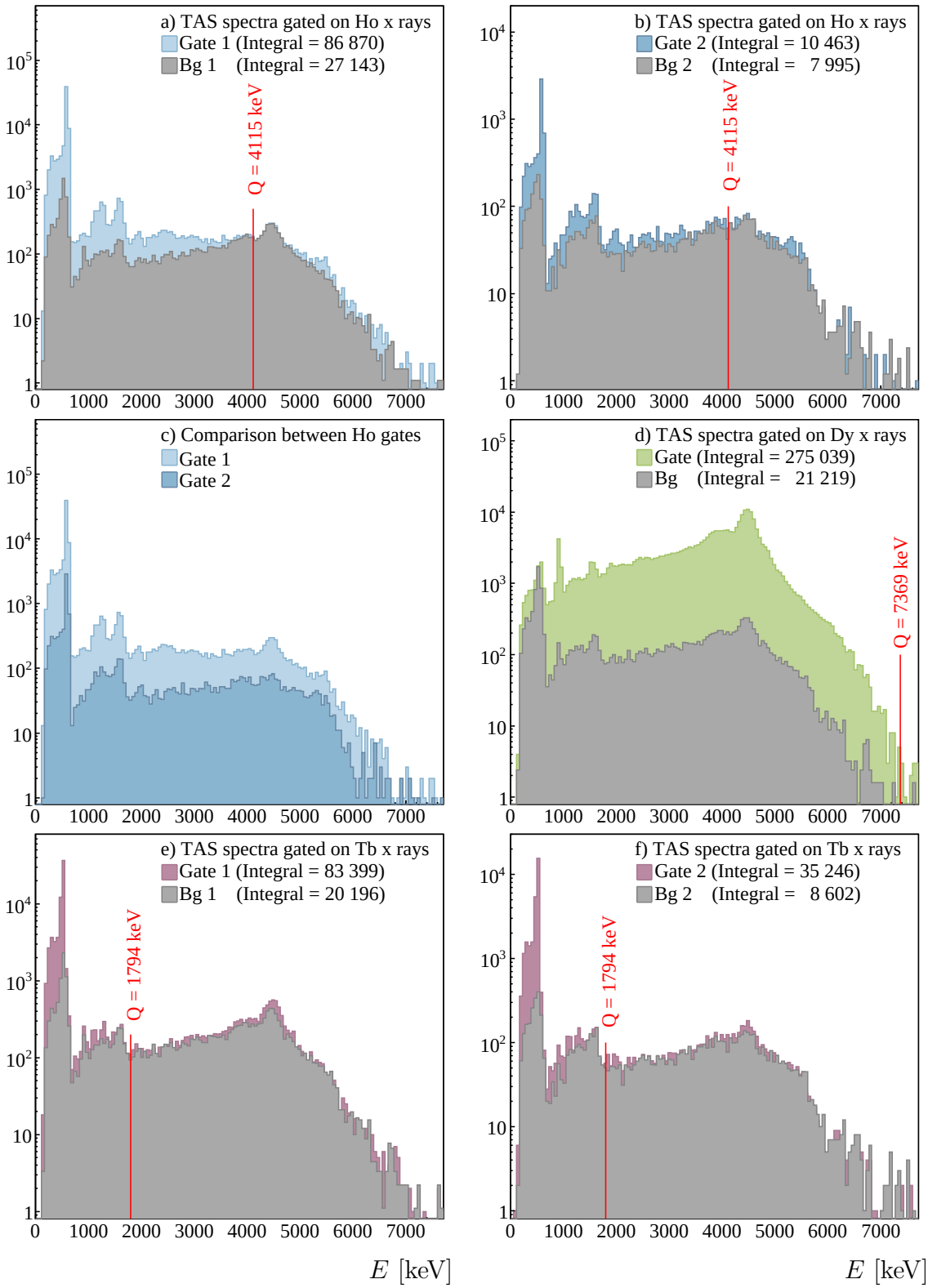

Figure 5.12: Gates of the isobars produced in the EC decay chain of ^{150}Er: a) $K_{\alpha 1}$ holmium gate. b) K_{β} holmium gate. c) Comparison between gates (no background subtracted). d) K_{α} dysprosium gate. e) K_{α} terbium 1 gate. f) K_{β} terbium 2 gate.

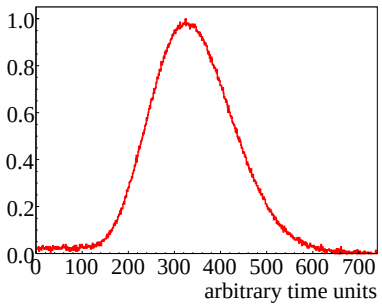

Figure 5.13: Pulse measured in this experiment (see Sec. 4.4), used for the calculation of the pileup of mass 150 and 156.

Table 5.7: Normalization factors of all the contributions to the decay. Contributions 1 and 2 were added to create one background file for the analysis.

Contribution	ID	Norm. factor
X-ray gated background	1	0.55
Simulated β^+ decay contribution	2	297.6
Pileup	3	625.22

c) Algorithm application: The measured spectra was recalibrated to the MC. There is no need to rebin as in the case of the analysis of mass 152. In Fig. 5.14 the input spectra used in the analysis program are shown. The analysis was performed in the range from 120 keV to 8000 keV. The results of the analysis are shown in Fig. 5.15.

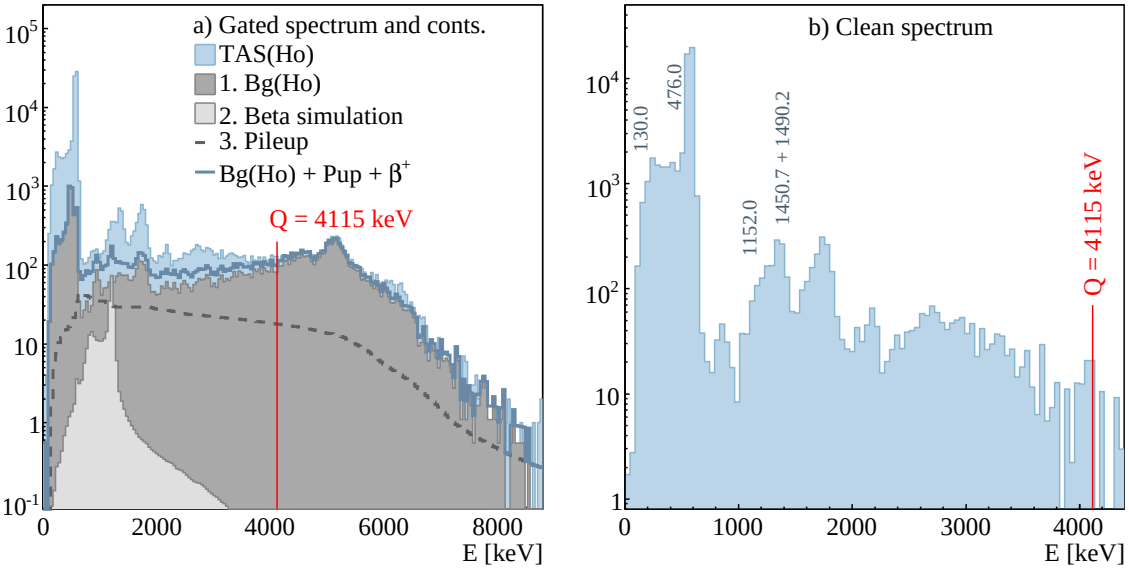

Figure 5.14: Same as Fig. 5.8 for mass 150.

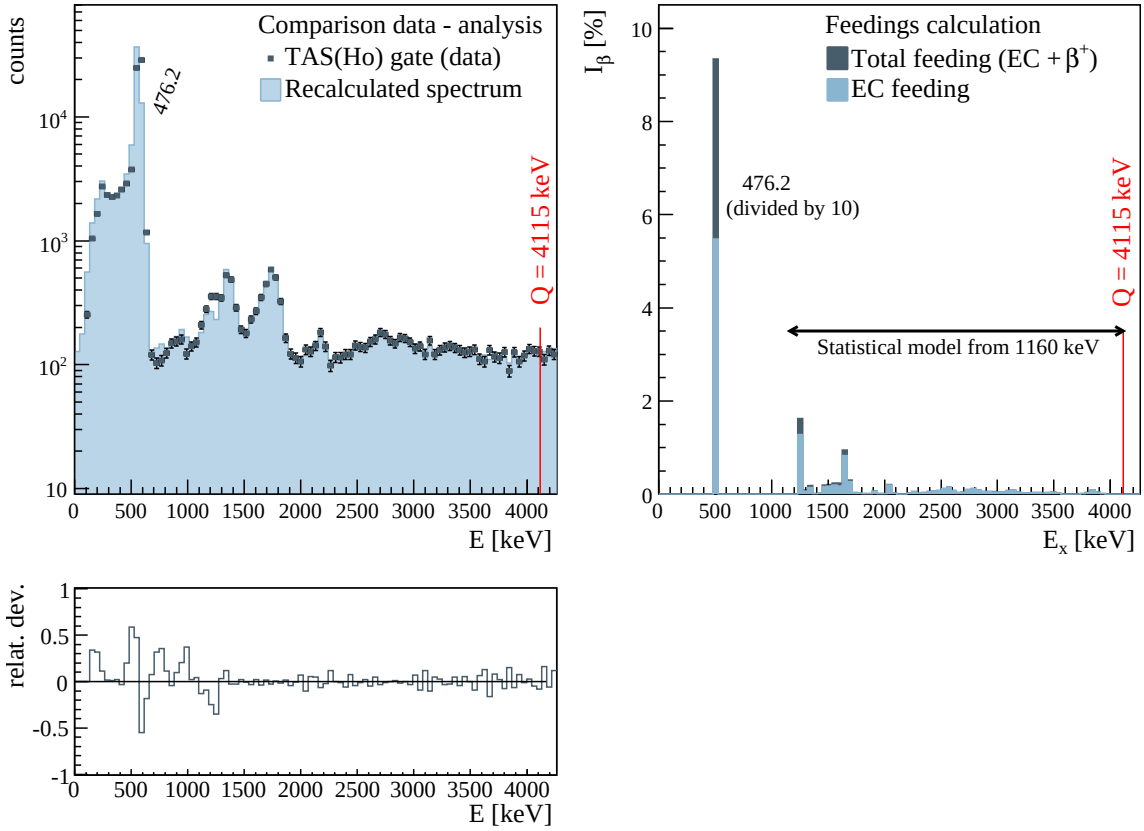

Figure 5.15: Final results of the analysis of the EC decay of ^{150}Er: The description of the panels is the same as for Fig. 5.9

d) Strength calculation: The strength for mass 150 was calculated from 0 keV to 4040 keV with the $t_{1/2}$ and Q_β value of Table 3.2. In Table 5.8 the results of the analysis are shown.

Table 5.8: Deduced $I_{EC+\beta^+}$ values for the levels populated in the decay of ^{150}Er. The HR I_{EC} values were deduced from the $I_{EC+\beta^+}$ column using the LOGFT tool [LOGFT] of the National Nuclear Data Center.

E_{lev}	J^π	I_{EC} [%]		$I_{EC+\beta^+}$ [%]		B(GT) $[g_A^2/4\pi]$	
[keV]		TAS	HR	TAS	HR	TAS	HR
130.0	1^+-3^+	-	0.5(1)	-	1.0 (4)	-	0.006(1)
476.2	1^+	55.2(6)	59.3(5)	94.2(7)	99.60(23)	0.78(3)	0.80(4)
1152.0		1.3(2)	1.1(2)	1.6(2)	1.40(23)	0.03(1)	0.024(4)
1450.8		0.2(5)	0.4(1)	0.2(5)	0.50(15)	0.0104(4)	0.010(3)
1490.3		0.8(5)	1.1(2)	0.9(6)	1.30(23)	0.0236(8)	0.028(4)
1160 - Q		3.5(6)	-	4.3(7)	-	0.21(2)	-
TOTAL		60.3(7)	62.6(6)	100(1)	103.8(6)	1.04(4)	0.87(4)

5.3. Mass A = 156

1. **Average branching ratios calculation:**

a) Known levels: This case is more difficult since less information is available from HR measurements. According to the most recent compilation, [Rei03], only two levels are known to be populated in ^{156}Tm, and they are listed in Table 5.9.

Table 5.9: Known levels used in the analysis of the EC decay of ^{156}Yb (taken from [Rei03]).

E level	J^π	E_γ	I_γ	α_{total}
0.0	2^-	0.0	0.0	0.0
115.2	1^+	115.2	100.0	0.231
317.5	1^+	202.3	100.0	0.434

b) Level Density Parameters: For ^{156}Tm, the calculations of [Gor01] and [Dem01] predict 1 level up to 250 keV and 10300 levels up to 3500 keV. With this values, the fit to find the level density parameters gives a = 18.285 MeV^{-1} and Δ = -0.222 MeV.

c) Gamma Strength Function Parameters: The neutron separation energy in ^{156}Tm is S_n = 8.243 MeV [Rei03], and its deformation parameter β_2 is -0.161 [Mol95]. With these values, the gamma strength function parameters of Table 5.10 are obtained.

Table 5.10: Giant resonance parameters for the E1, E2 and M1 gamma strength functions of ^{156}Tm (β_2 = -0.161, S_n = 8243 keV).

Type	E [MeV]	w [MeV]	Γ [mb]
E1	13.249	3.617	487.715
	15.500	4.881	361.382
M1	7.629	4.0	3.122
E2	11.723	4.238	4.309

d) Average branching ratios calculation: Since in this case only two levels are known, the range of the unknown part was fixed from 320 keV (bin 8, approx.) to the Q value 3575. With these values and using *a)*, *b)* and *c)*, the average branching ratio matrix was obtained.

2. **Response simulation:**

For this part of the analysis the same simulations calculated for the analysis of mass 150 can be used, since the geometric configuration is the same. When this simulation is convoluted with the branching ratios calculated in step 1 *d)* the detector response matrix shown in Fig. 5.16 was obtained for the analysis of mass 156.

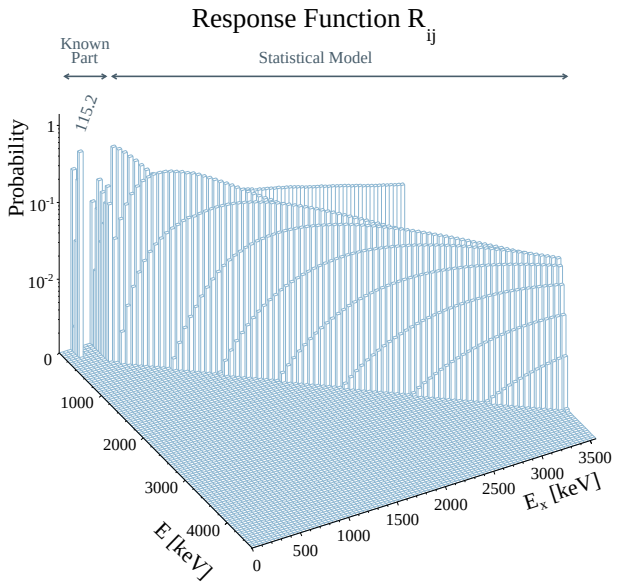

Figure 5.16: Response matrix of the EC decay of ^{156}Yb used in the analysis (same as Fig. 5.3).

3. **Extracting the feedings:**

a) X-ray tagging: The x-ray germanium spectrum for this measurement was very similar to that of mass 152. In Fig. 5.17 the gates chosen for this mass are shown (gate 1: $K_{\alpha 1}$ of Tm, gate 2: K_{β} of Tm).

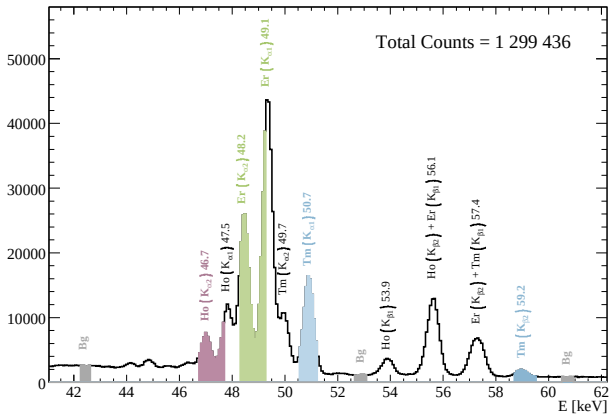

Figure 5.17: Germanium x-ray spectra showing the gates used for the analysis of the EC decay of ^{156}Yb. (same description given in Fig. 5.4 applies).

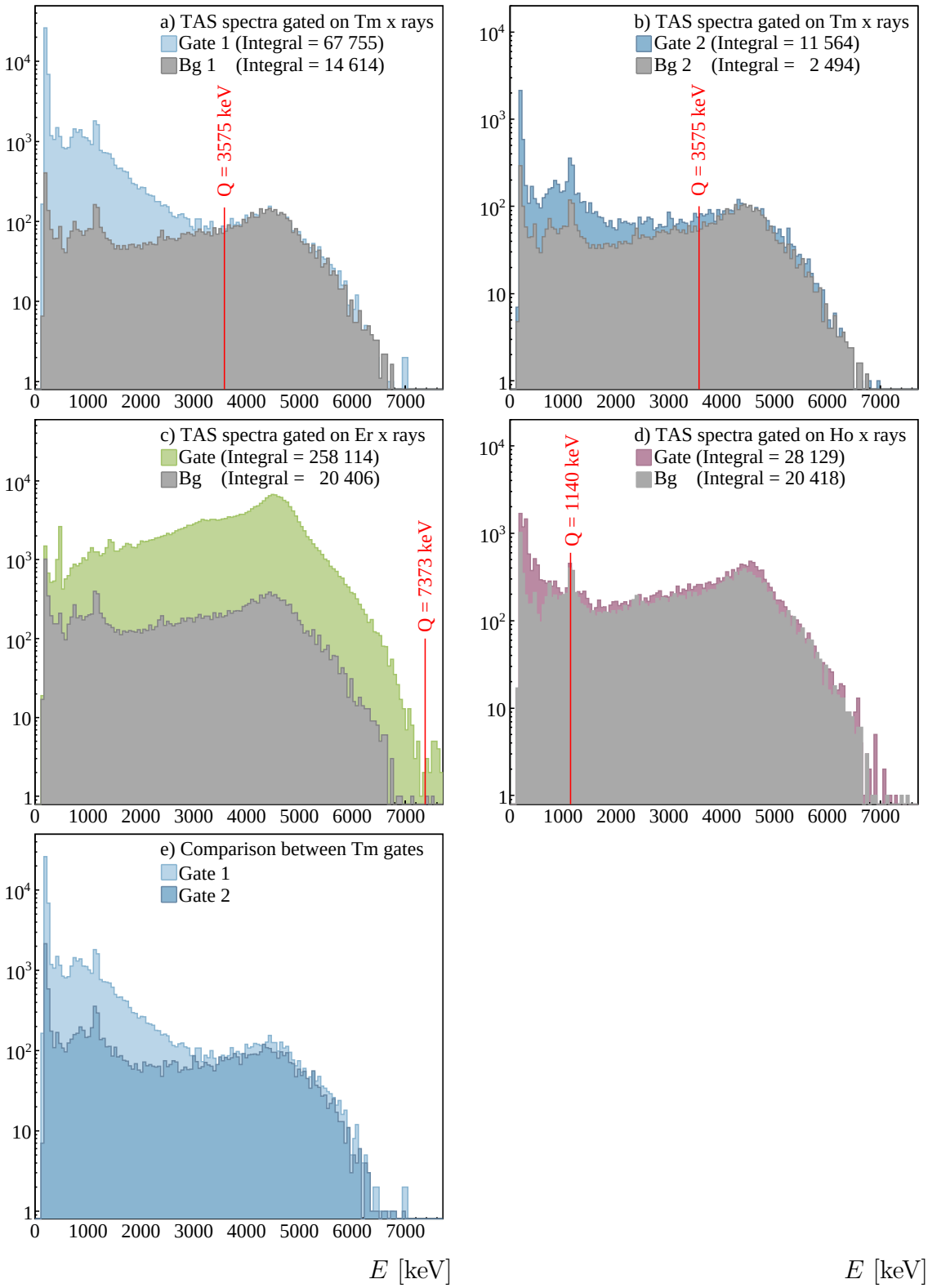

Figure 5.18: Gates of the isobars produced in the EC decay chain of ^{156}Yb. Same description of Fig. 5.5 applies.

b) Contaminants, backgrounds, pileup: In Fig. 5.18 the TAS gated spectra obtained from the gates of Fig. 5.17 are shown with their respective backgrounds. As in the other cases, the contribution of the isobars in the x-gated TAS spectrum was considered negligible. No other backgrounds, apart from the x-gated background spectrum and the beta plus contribution were found in the gate of interest. A simulation of the beta contamination was also made for this mass in the same way as explained for the other masses. The pileup was calculated with the same pulse used for mass 150. The normalization factors appear in Table 5.11. Again, contribution 1 and 2 were added to generate a background file.

Table 5.11: Normalization factors of all the contributions to the decay.

Contribution	ID	Norm. factor
X-ray gated background	1	0.45
Simulated β^+ decay contribution	2	3292.77
Pileup	3	50.0

c) Algorithm application: In Fig. 5.19 the input spectra for the analysis program are shown. The analysis was made from 120 keV (∼ bin 3) to 3760 keV (∼ bin 94). The results of the analysis are shown in Fig. 5.20.

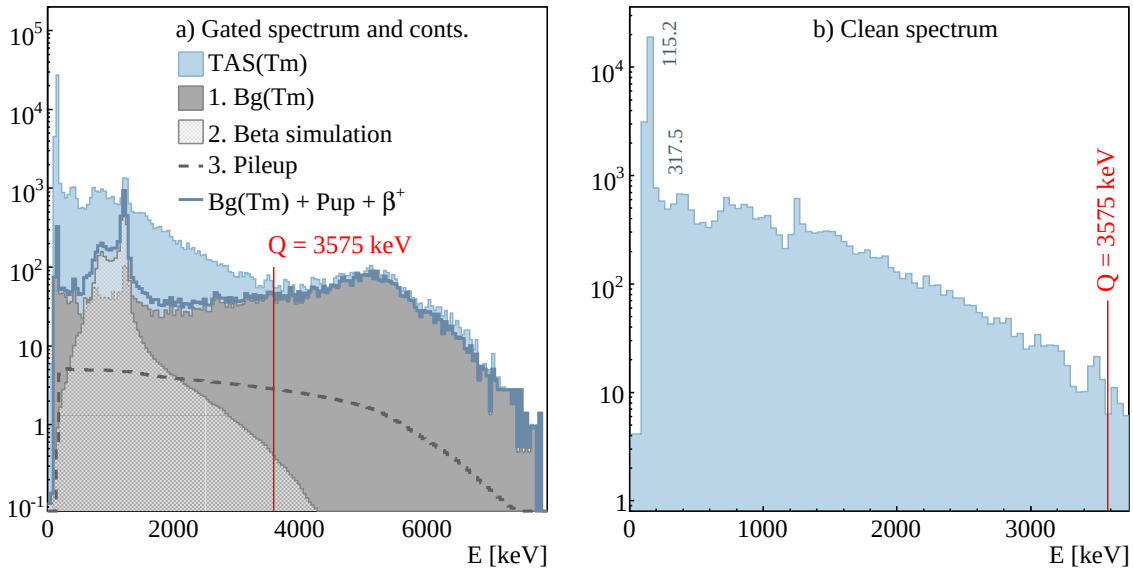

Figure 5.19: Same as Fig. 5.8 for mass 156.

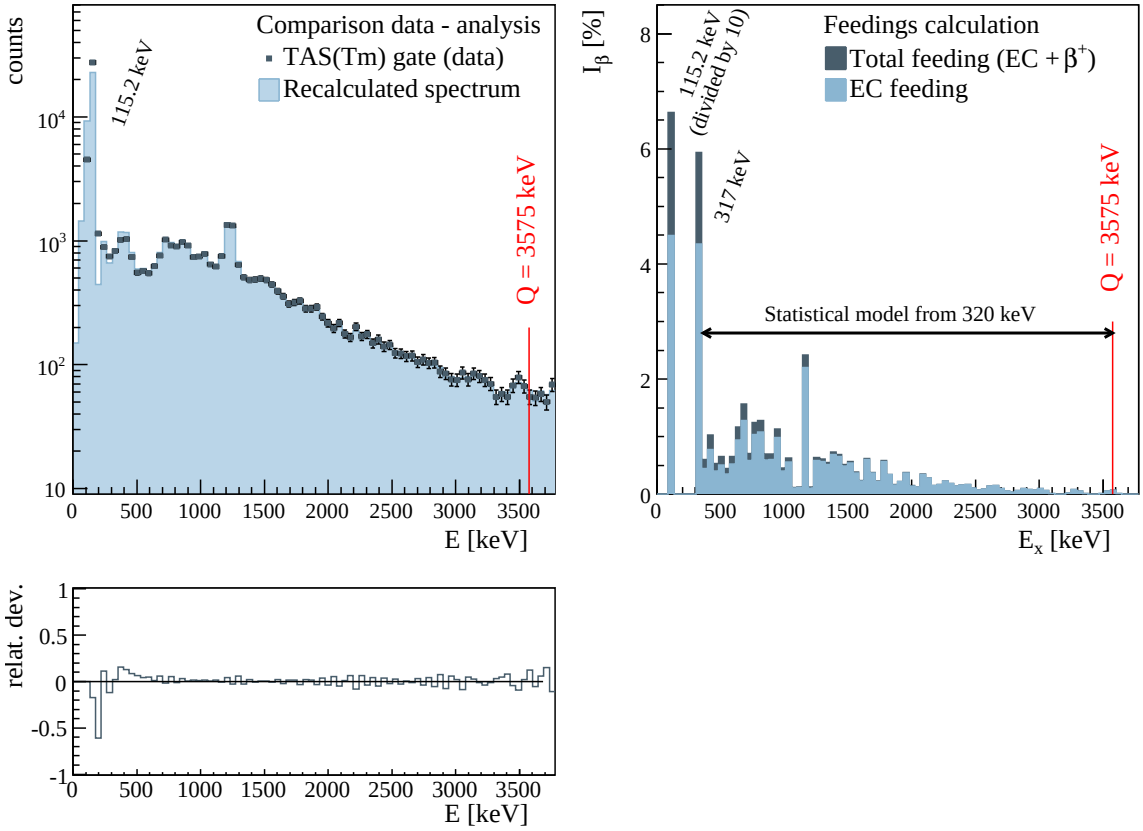

Figure 5.20: Final results of the analysis of the EC decay of ^{156}Yb. Same description of Fig. 5.9 applies.

d) Strength calculation: The strength for mass 156 was calculated from 0 keV to 3480 keV, with the $t_{1/2}$ and Q_β value of Table 3.2. In Table 5.12 the results of the analysis are shown. The total beta feedings are calculated from the EC feedings on a 100 % basis. Since this nucleus has an alpha branch of 90(2) % [Rei03], the results were normalized by this value to obtain the feedings per 100 parent decays, which is the important value for this application.

Table 5.12: Deduced $I_{EC+\beta^+}$ values for the levels populated in the decay of ^{156}Yb. The high-resolution results were taken from [Rei03] and the Q value from [Aud03].

E_{lev}	J^π	I_{EC} [%]		$I_{EC+\beta^+}$ [%]		B(GT) $[g_A^2/4\pi]$	
[keV]		TAS	HR	TAS	HR	TAS	HR
115.2	1^+	41(2)	58.0(13)	60(3)	85.2(5)	0.4(1)	0.6(2)
317.5	1^+	3.7(7)	3.5(4)	5(1)	4.8(5)	0.04(1)	0.04(2)
320 - Q		22(2)	-	25(3)	-	1.0(2)	-
TOTAL		67(3)	61.5(2)	90(4)	90(2)	1.4(2)	0.6(2)

6

Discussion and Conclusions

In this part of the work the study of the beta decay of ^{152}Yb, ^{150}Er and ^{156}Yb was addressed with the TAS technique. The goal of this study was to confirm the values of the feedings obtained with the high resolution technique with this alternative technique that does not suffer from the Pandemonium effect.

These nuclei are found in a region of the nuclear chart where the full strength of the decay can be accessible in the Q value window. Due to this, the results obtained with the TAS for the beta feeding values are very useful. In addition, these nuclei have their total beta feeding concentrated mainly in one level with spin-parity 1^+. The TAS results confirm these large feeding values to the levels of interest for ^{152}Yb and ^{150}Er, but in the case of ^{156}Yb a larger discrepancy was observed. In this case, also the high resolution data is incomplete, suggesting that this nucleus should be revisited using the HR technique.

Tables 5.4, 5.8 and 5.12 present a comparison of the results of the TAS and HR techniques. The numbers show a reduction of the TAS feedings at low energies in comparison with HR for the three nuclei. This is due to the fact that the TAS is able to see feeding at higher energies where the HR technique fails to detect it. The feeding to these levels is small in the cases studied (except for mass 156 where the discrepancy is larger). Given that the decay is "monopolized" by one level, the difference between the results of both techniques is relatively small.

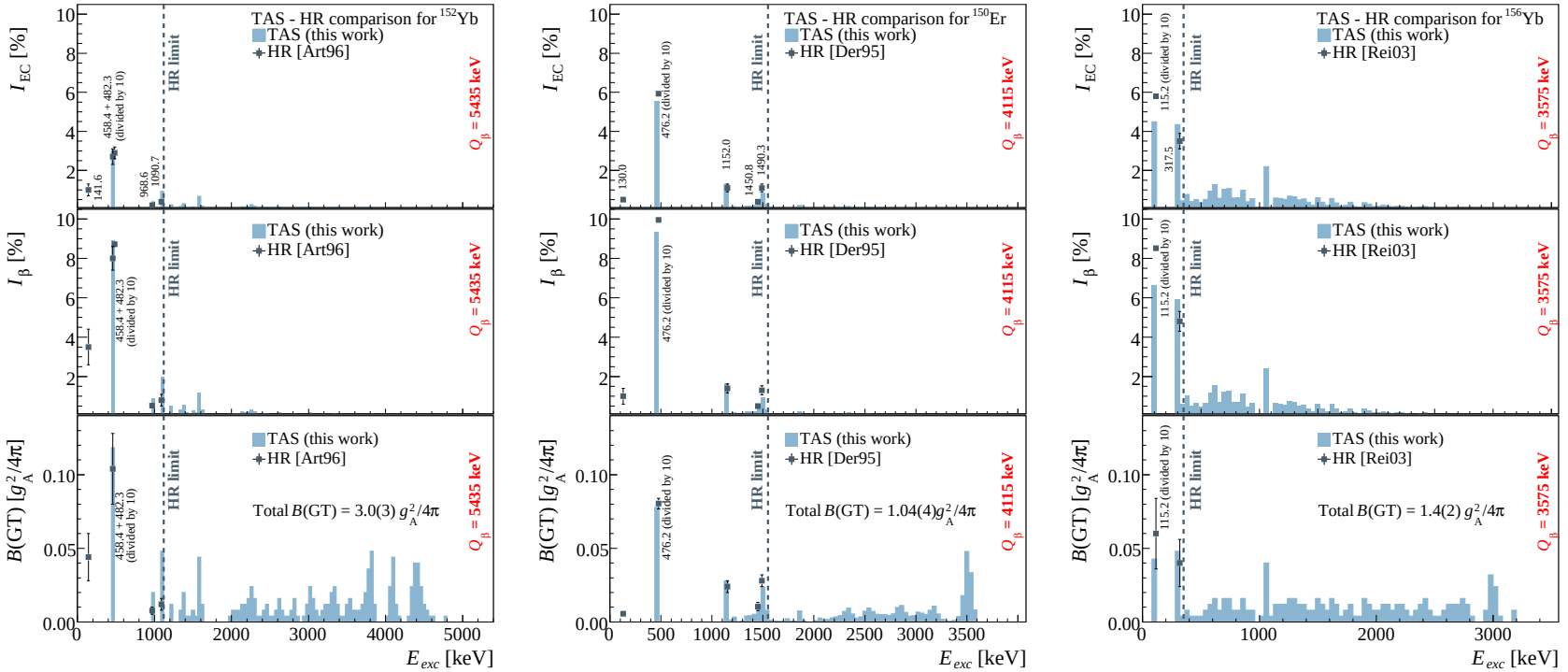

a) Mass 152. *b*) Mass 150. *c*) Mass 156.

Figure 6.1: Comparison of the results. Upper panels: Comparison between TAS and HR EC feedings. Middle panels: Comparison between TAS and HR total feedings. Lower panels: Comparison between TAS and HR strength. The dotted vertical lines show the limit between the intensity seen by the HR technique and the rest of the intensity seen with the TAS technique. The most intense level of each nucleus has its intensity divided by 10 to make the plot more readable. The bin size is 40 keV.

In Fig. 6.1 the EC feedings, total feedings as well as the strength distributions are shown in comparison with the HR results. As mentioned before (Chapter 3), for this application, the relevant information is how many times the most fed level is populated in the decay. In the case of mass 152, the level with the higher intensity lies at 482.3 keV and has a total feeding of 87.2(5) % according to HR data. In the TAS results, the feeding to this level could not be resolved and is mixed with the feeding to the level at 458.4 keV giving a total of 89(2) per 100 parent decays (this combined feeding corresponds to a logft of 3.5). This value has to be compared with the sum of the HR feedings to these two levels which gives a 95.2(8) per 100 parent decays. This represents a reduction of $\sim$ 6 % with respect to the tabulated values. In the case of mass 150, the total feeding to the level at 476.2 keV is 94.2(7) % according to the TAS results, which corresponds to a logft value of 3.7, and 99.6(23) % according to HR, that is, a reduction of $\sim$ 5 %. In the A=156 case the reduction is much larger, the feeding to the 1^+ level has changed from 85.2(5) % to 60(3) % and the corresponding logft value has changed from 3.8 to 4.0. The total B(GT) value is 3.0(3) $g_A^2/4\pi$ for mass 152, from which a 40 % goes to the levels at 458.4 and 482.3 keV. For masses 150 and 156, 75 % and $\sim$ 29 % of the whole beta strength goes to the most intensely fed levels. Also, no new levels are seen at low energies. These results are summarized in Table 6.1.

Table 6.1: Summary of the results of the I_β calculation from TAS data.

A	E_{level} [keV]	TAS	HR	$t_{1/2}$ [s]	Q_{EC} [keV]
152	458.4 + 482.3	89(2)	95.2(8)	3.04(6)	5435(200)
150	476.2	94.2(7)	99.6(23)	18.5(7)	4115(14)
156	115.2	60(3)	85.2(5)	26.1(7)	3575(13)

The values for the total B(GT) in the case of masses 152, 150 and 156 are 3.0(3), 1.04(4) and 1.4(2) $g_A^2/4\pi$ respectively. However, looking at the plots of Fig. 6.1, it is clear that some strength is missed above the HR limit. According to our results for mass 152, a 58 % of the total strength is distributed in the levels beyond 1120 keV that is not previously reported by the HR technique. In the case of mass 150 this percentage is not as relevant and reaches the $\sim$ 17 %. This percentage is calculated using the value of the strength from 1160 keV to the Q value subtracting the strength to the levels of 1450.8 and 1490.3 keV that were included in the unknown part of the analysis. A 71 % of the strength lies from 320 keV to the Q value in ^{156}Yb decay, making this nucleus the one that differs most from the information available in databases, which is not surprising because it is not well known. This summary is presented in Table 6.2.

Table 6.2: Summary of the results of the B(GT) calculation from TAS data.

Description	B(GT) $[g_A^2/4\pi]$		
	Mass 152	Mass 150	Mass 156
B(GT) to the most intense level	1.2(3)	0.78(3)	0.4(1)
Amount of missing strength in HR data	1.74(2)	0.21(2)	1.0(2)
Total B(GT) seen by the TAS	3.0(3)	1.04(4)	1.4(2)

As mentioned in the motivation (Sec. 3.3), proton rich nuclei above ^{146}Gd with even Z and $N > 82$ will beta-decay dominantly through an allowed GT transition to states of spin $J^\pi = 1^+$ in the odd-odd daughter. Recalling the results of [Nac04a, Alg04] for the decay of ^{148}Dy and with our results for the decays of ^{150}Er and ^{152}Yb, the systematics of the strength when increasing Z can be discussed for the even-even nuclei with $N = 82$ above ^{146}Gd, while the results for mass 156 are relevant for the $N > 82$ cases, that is, when neutrons are added (Fig. 3.5).

It was already discussed by Toth *et al.* [Tot82] that even-even nuclei ^{148,150,152}Dy, ^{150,152,154}Er and ^{156}Yb decay in a similar fashion: a concentrated electron capture plus positron decay to one single 1^+ level, which subsequently decays by an E1 gamma transition to a 2^- ground state. The existence of similar levels and similar decay patterns in nuclei with $N = 83, 85, 87$ raised questions concerning the nature of their configurations and made this region interesting from the point of view of nuclear structure. In Ref. [Tot82] it was proposed that, even though there is a subshell closure at $Z = 64$, a small prolate deformation may be needed to explain the nature of the 2^- ground state and the strong beta-decay transition. Later it was suggested in Ref. [Kle88] that the 2^- ground state configuration is of $(\pi d_{3/2}\nu f_{7/2})$ nature (Fig. 6.2 b)) and that in these nuclei the only possible GT decay is the $\pi h_{11/2} \rightarrow \nu h_{9/2}$ transition (Fig. 6.2 a)). This decay proceeds to $(\pi h_{11/2}\nu h_{9/2})1^+$ states in the odd-odd daughter nuclei, which appear at low excitation because of the strong two-body attraction of the 1^+ coupling (Fig. 6.3 a)).

Under the assumption that:

- no other GT-transitions are possible,
- there are no higher-lying 1^+ states with $(\pi h_{11/2}\nu h_{9/2})$ configuration and
- removal of GT strength through mixing at high energies in the daughter nuclei is unlikely,

the decays of these nuclei are expected to give the full GT strength associated with the decay of the even-even ground state [Kle88]. This fact can result in a better agreement between TAS and HR results for the strength of these nuclei, since the most of it is concentrated in the strongly populated level.

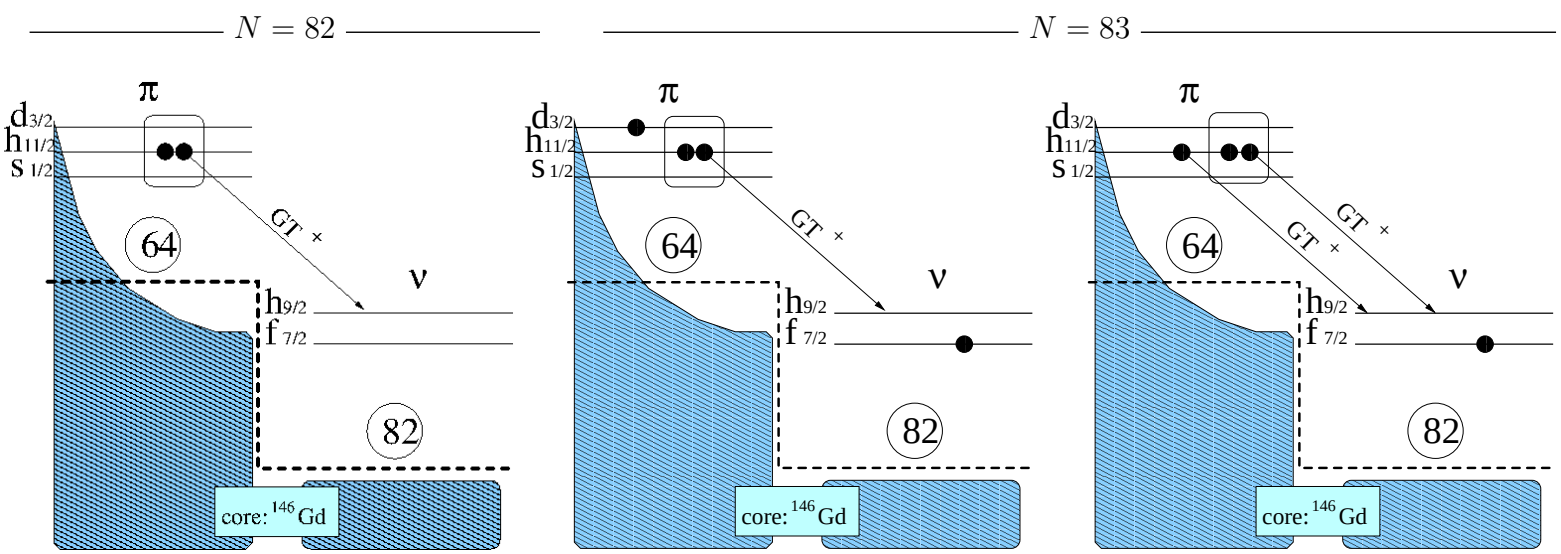

a) Ground state of even Z, $N = 82$ nuclei, $2n$ "valence" protons coupled to 0^+:

$$(\pi h_{11/2}^{2n})_{0^+}$$

b) Ground state of odd Z, $N = 83$ nuclei, with two possible configurations with low (2^-) and high (9^+) spin:

$$(\pi h_{11/2}^{2n})_{0^+}(\pi d_{3/2}\nu f_{7/2})_{2^-} \qquad (\pi h_{11/2}^{2n})_{0^+}(\pi h_{11/2}\nu f_{7/2})_{9^+}$$

Figure 6.2: Configuration of the ground state of the parent nuclei discussed in the text (according to the Extreme Single Particle model). The proton pair in the $h_{11/2}$ orbital represents a number n of proton pairs depending on the Z of the nucleus. They are enclosed in a box because in reality each pair will scatter between the three proton orbitals due to pairing correlations. Although 64 is not a magic number, the gap separation of ∼2.4 MeV between the $2d_{5/2}$ and $3s_{1/2}$ orbitals supports the idea of ^{146}Gd being a quasi-doubly magic nucleus (see for example, the discussion in [Nac04a] (chapter 11) regarding the ^{144}Sm smaller gap). Thus, in a very simple approximation, it is possible to treat the nuclei above ^{146}Gd as excitations of valence particles above the ^{146}Gd core. The possible GT transitions are also shown by arrows.

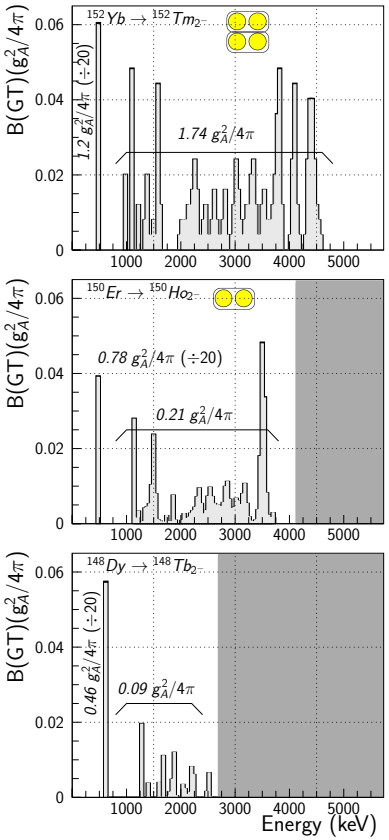

a) Decays of the even-even $Z > 64$, $N = 82$ nuclei. The breakup of the proton pair strongly populates a 1^+ low energy level in the odd-odd daughter that takes almost all of the strength of the decay. Mass 150 and 152: this work. Mass 148: [Alg04].

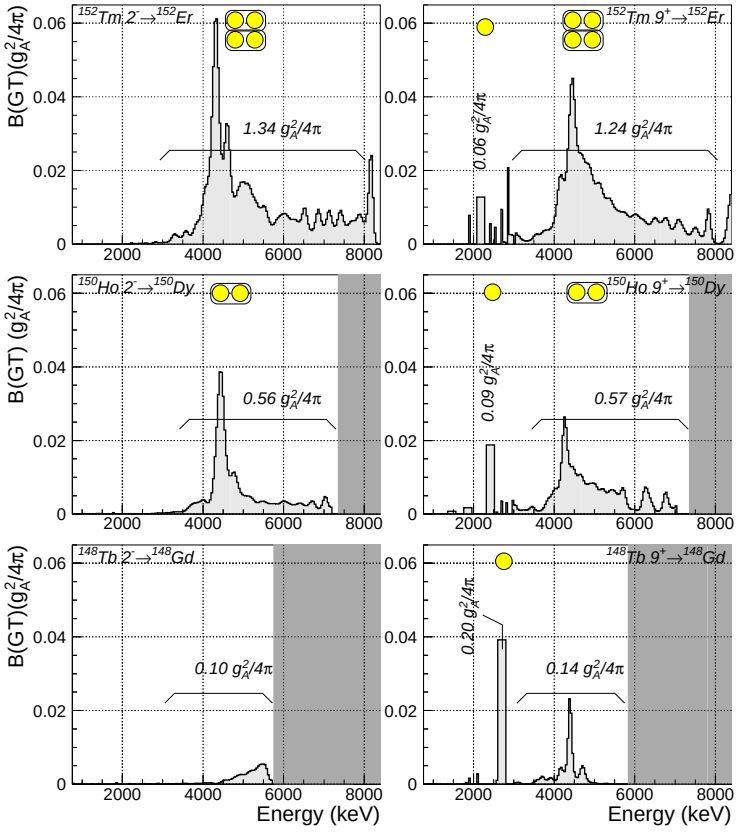

b) Decays of the odd-odd $Z > 64$, $N = 83$ nuclei. The breakup of the proton pair populates a high-energy narrow resonance but a small amount of the strength may be outside the Q_β window. Left: low spin. Right: high spin. Image taken from [Nac04a].

Figure 6.3: Systematics of the region above ^{146}Gd.

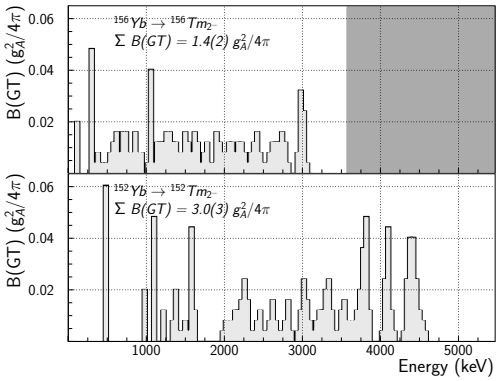

a) Decay of the even-even $Z = 64 + 6$, $N = 82$, $82 + 4$ nuclei (this work). The strength is ∼2.1 times lower when adding neutrons.

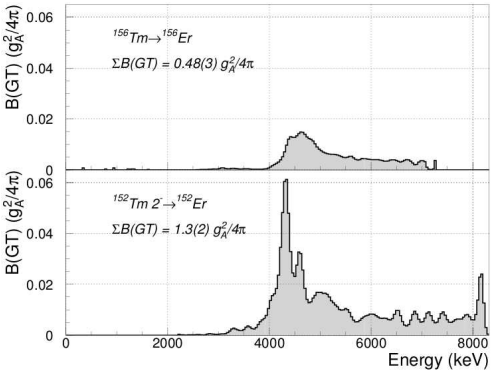

b) Decay of the odd-odd $Z = 64 + 5$, $N = 82 + 1$, $82 + 5$ nuclei [Nac04a]. The strength is ∼2.7 times lower when adding neutrons.

Figure 6.4: Variation of the strength in the decays with $Z = 69$,70 when adding neutrons.

For that reason these decays were considered very important in this context. The present TAS results for mass $A = 150$, 152 and 156 confirm this expectation, but now free of possible systematic uncertainty related to the Pandemonium effect. The results are complementary to the ones obtained for A = 148 [Alg04].

Recalling also the systematics covered in [Nac04a] and [Can00] for odd-odd nuclei with $N = 83$, we can put together all the TAS results for the region of interest. In these decays, most of the strength is concentrated not in a single level but in a resonance at 4-5 MeV. This resonance gets wider as Z increases because configuration mixing appears (among other effects), shifting the strength to ever-increasing energies and eventually decreasing the amount of accessible GT strength (Fig. 6.3 b)). However, for the odd-odd studied cases, still most of the strength is kept inside the Q value window and is accessible with the TAS technique, although for the present application, the optimal situation is offered by the even-even cases as discussed above. In the case of mass 156, the larger amount of valence protons and neutrons makes up a situation where some of the strength is lost (Fig. 6.4 b)). The values of the total strength for the nuclei in the region that were measured with the TAS technique are shown in Table 6.3. A tendency of increasing total strength with increasing proton occupation number can be seen. The theoretical value (from [Tow85]) is also given for a comparison.

Table 6.3: Summary of the TAS results for the strength in the ^{146}Gd region. The parent nuclei is specified for each case, as well as the energy up to which $B(\mathrm{GT})$ is integrated. The even-even nuclei with $N = 82$ can only populate the low spin isomer of the odd-odd daugther. The last column shows the theoretical value of the strength, calculated according to the work by Towner as: $B(\mathrm{GT}) = \mathrm{n}\frac{4l}{2l+1}$ where n is the number of protons in the $\mathrm{h}_{11/2}$ orbital of the ground state of the parent, and l=5 for an h orbital (extreme single particle model).

	TAS $B(\mathrm{GT})$ $[g_A^2/4\pi]$								$B(\mathrm{GT})$
n	$N = 82$		$N = 83$		$N = 86$		$N = 87$		$[g^2/4\pi]$
6	$\left(^{152}Yb\right)^{5.2\mathrm{MeV}}$	3.0 (3)[a]			$\left(^{156}Yb\right)^{3.76\mathrm{MeV}}$	1.4 (2)[a]			10.91[e]
5			$\left(^{152}Tm_{9^+}\right)^{8\mathrm{MeV}}$	1.3 (3)[b]					9.09[e]
4	$\left(^{150}Er\right)^{4.04\mathrm{MeV}}$	1.04(4)[a]	$\left(^{152}Tm_{2^-}\right)^{8\mathrm{MeV}}$	1.3 (2)[b]			$\left(^{156}Tm_{2^-}\right)^{7.2\mathrm{MeV}}$	0.48(3)[b]	7.27[e]
3			$\left(^{150}Ho_{9^+}\right)^{7.12\mathrm{MeV}}$	0.73(9)[c]					5.45[e]
2	$\left(^{148}Dy\right)^{2.6\mathrm{MeV}}$	0.55(1)[d]	$\left(^{150}Ho_{2^-}\right)^{7.28\mathrm{MeV}}$	0.58(4)[c]					3.64[e]
1			$\left(^{148}Tb_{9^+}\right)^{5.8\mathrm{MeV}}$	0.34(4)[b]					1.82[e]
0			$\left(^{148}Tb_{2^-}\right)^{5.7\mathrm{MeV}}$	0.10(1)[b]					

[a] This work. [b] [Nac04a]. [c] [Can00]. [d] [Alg04]. [e] [Tow85].

The newly deduced feedings allow us to determine the hindrance factors for favoured GT transitions based on the work of Towner [Tow85] for the dominantly populated 1^+ states. The corresponding hindrance factors without taking into account additional corrections ($h = B_{s.p.}(\mathrm{GT})/B_{exp}(\mathrm{GT})$) are, for the ^{148}Dy, ^{150}Er and ^{152}Yb cases, 7.9, 9.1 and 9.2. These values were obtained assuming a single particle occupancy of the $\pi h_{11/2}$ orbital of 2, 4, and 6 respectively. If all the correction factors considered in Ref. [Tow85] (pairing correlations, core-polarization and higher-order effects) are taken into account for the most favorable interaction, the calculated hindrance amounts to 4.8, 5.0, and 4.7 respectively, which shows that all the factors taken into account so far are not sufficient. This problem was also studied from another perspective in [Suh88], where it was shown that with an appropriate particle-particle interaction strength it was possible to reproduce the experimental strengths for these nuclei. Since our TAS results differ only slightly from the earlier high resolution results, the conclusions drawn in [Suh88] are still valid. A summary of the results for the strength in the beta decay Q window obtained by our group in the Gd region is given in Fig. 6.5.

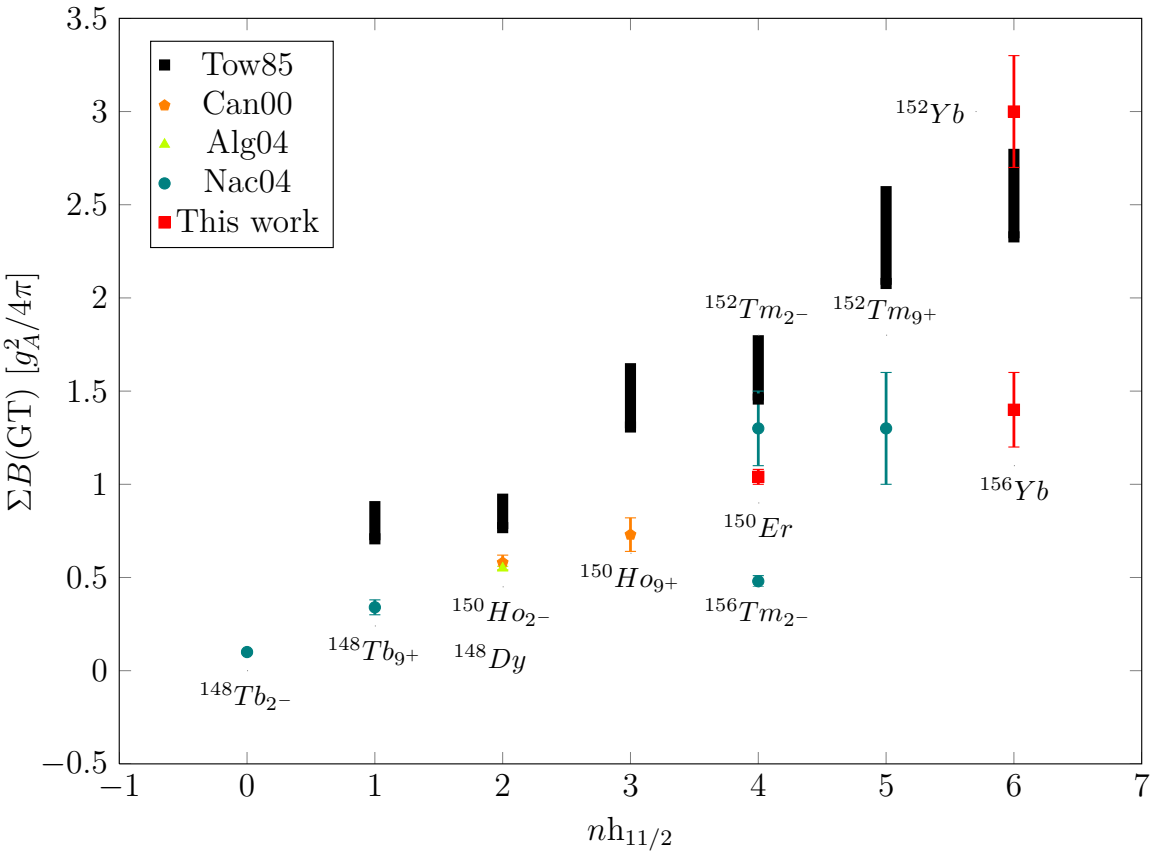

Figure 6.5: Evolution of the strength with the occupation number of the orbital $h_{11/2}$ in the ground state of the parent nucleus. The theoretical values of Table 6.3 are shown, multiplied by the corresponding hindrance factors calculated in [Tow85].

From the three masses studied, and taking into account the constrains of Sec. 3.3, ^{152}Yb seems to be the best suited candidate for a monochromatic neutrino beam facility. It has a reasonable beta-feeding intensity to the level at 482.3 keV, and its half-life is the smallest of all the cases, which is relevant for such a facility. In addition, it decays 100 % by EC/β^+ so it is free from intrinsic decay, like alpha contamination, for example. In addition, the percentage of β^+ intensity makes it suitable also for the hybrid type facility.

Part

III

Nuclear Deformation

7 Motivation

The shape of the nucleus is governed by the interplay of macroscopic properties and microscopic shell effects. In nature, few nuclei have a spherically shaped ground state. The magic numbers (associated with closed shells and sphericity) and their possible combinations are finite. If we move away from the closed shells where the majority of spherical shapes are found, the possibility of finding nuclei with deformed or even coexisting shapes increases. Moreover, new magic numbers and deformed shapes may appear in exotic nuclei, if they minimize the energy of the system. Until this "stable" situation is reached, it is possible that multiple shapes coexist in the same nucleus. The first experimental observation of shape coexistence came in 1956 by Morinaga *et al.*, who reported shape coexistence in ^{16}O [Mor56].

In this part of the work, the interest is around the closed shell at $Z = 82$. The lead isotopes stay spherical in their ground state at the neutron mid-shell ($N \sim 104$) and beyond. In the case of neutron-deficient lead isotopes, the ground state was found to be spherical down to ^{182}Pb. However, these lead isotopes exhibit a shape coexistence of the spherical ground states with prolate or oblate excited configurations. They even can exhibit a triple shape coexistence (spherical, prolate and oblate) at neutron mid-shell, that is, around ^{186}Pb. Shape coexistence is closely related to the apparition of "intruder states". In even-even lead nuclei, the first excited state is in general around 1 MeV and has spin parity 2^+. However, when going to more neutron-deficient lead, intruder states appear below 1 MeV in the form of low-lying oblate and prolate states with 0^+ spin-parity. The weakening of the magicity of the $Z = 82$ shell manifests itself through the appearance of these low-lying 0^+ states.

The first search for shape changes in lead nuclei was made in 1984, when neutron-deficient lead isotopes from mass 198 to 192 where measured [Van84] from the beta decay of bismuth isotopes. Apart from the 0^+_1 spherical ground state, they found a low lying 0^+_2 deformed excited state in these nuclei. Rotational bands on top of these levels have also been observed and helped to identify 0^+_2 and 0^+_3 states as associated with prolate and oblate deformations. In even-even neutron-deficient lead nuclei down to ^{190}Pb, those low lying states have been associated with weakly deformed

oblate shapes, and from ^{188}Pb down with oblate and prolate shapes. The first experimental evidence for prolate states in ^{188}Pb and ^{186}Pb came from Heese *et al.* in the nineties [Hee93] and in 2000 Andreyev *et al.* were able to identify oblate and prolate states in ^{186}Pb at low energy [And00]. Indeed, the topic of shape coexistence in the Pb region has a very extensive literature. The 0_i^+ energy systematics for the lead isotopes studied in this work are shown in Table 7.1 and Fig. 7.1.

Table 7.1: Energies of the intruder 0^+ states in the lead isotopes studied in this work, with their associated deformation.

Nucleus	State	Deformation	Energy [keV]	Reference
^{192}Pb	0_1^+	Spherical	0	[Bag98]
	0_2^+	Oblate	768.84(*23*)	
^{190}Pb	0_1^+	Spherical	0	[Sin03]
	0_2^+	Oblate	658(*4*)	
^{188}Pb	0_1^+	Spherical	0	[Sin02]
	0_2^+	Oblate	591(*2*)	
	0_3^+	Prolate	725(*2*)	
^{186}Pb	0_1^+	Spherical	0	[Bag03]
	0_2^+	Oblate	536(*21*)	
	0_3^+	Prolate	655(*21*)	

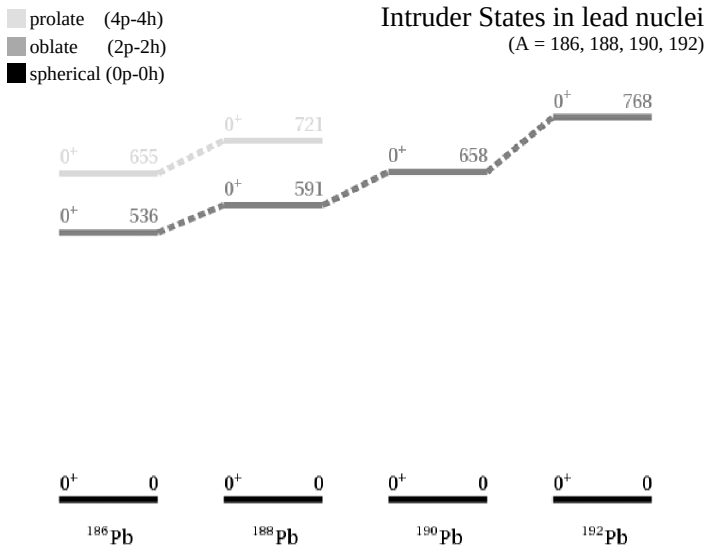

Figure 7.1: Energies of the intruder states in even-even lead isotopes. Same description of Table 7.1 applies.

From the theoretical side, calculations have long suggested the co-existence of different shapes in these nuclei. The first calculation for lead nuclei taking into account this feature was made in 1977, where the equilibrium shapes of low-lying states in light even-mass Pt, Pb and Po isotopes were determined by minimizing an effective deformation energy [May77]. From a general perspective, the most common theoretical methods for the study of the co-existence of low-lying excited 0^+ states can be grouped in two: a shell model approach or a mean field approach (although they are not the only alternatives).

In the shell model approach, the excited 0^+ states are interpreted as two quasiparticle and four quasiparticle configurations, that is, 2 particle - 2 hole (2p-2h) and 4 particle - 4 hole (4p-4h) configurations [Hey91]. The appearance of the coexistence of shapes can be explained as follows:

1. In the proton side, the energy gap of the proton shell at $Z = 82$ is 3.9 MeV, which is large enough to explain the existence of a spherical ground state.

2. However, this energy is small enough for proton-pair excitations to appear across the gap, that produce valence protons and holes. The valence protons are promoted to the first free orbital, $1h_{9/2}$. This is what is called a "2p-2h configuration" and introduces an extra pairing correlation.

3. In the neutron side, between the closed shells at $N = 82$ and $N = 126$ there is a large number of possible valence nucleons. Then, a quadrupole interaction appears between valence protons and valence neutrons, that is, between the nucleons outside the inert core.

The interplay of these effects, and mainly the third one (the neutron-proton interaction) produce the low lying intruder states with deformed shape as we approach the mid-shell $N = 104$.

The energies of the intruder states can be calculated in terms of these interactions, as shown in Eq. 7.1 for the case of a 2p-2h excitation [Hey91]:

$$E_{intr}(2p-2h) \sim 2(\epsilon_p - \epsilon_h) + \Delta E_M(2p-2h) - \Delta E_{pair} + \Delta E_Q(2p-2h) \qquad (7.1)$$

where $2(\epsilon_p - \epsilon_h)$ is the unperturbed energy needed to form the excitation (3.9 $\times$ 2 = 7.8 MeV), $\Delta E_M(2p-2h)$ is the monopole energy shift that takes into account the change in single particle energies when the number of nucleons changes (in this case, the number of neutrons), ΔE_{pair} takes into account the extra pairing correlation energy among the 0^+ coupled particle-hole pair, and $\Delta E_Q(2p-2h)$ is the quadrupole proton neutron interaction. A similar expression can be found for the energy of the 4p-4h configuration.

On the other hand, in the mean field approach, the appearance of several 0^+ intruder low-lying states means coexistence of collective nuclear shapes [Dug03], [Egi04]. The very name "shape coexistence phenomenon" comes from the mean field description. In a mean field calculation, a many-body problem is solved by replacing the n-body problem by one-body problem plus an average or effective interaction. The problem is solved to find the potential energy surface. In this picture, the closed proton shell forces a spherical ground state which is associated with the minimum of this potential energy surface, while the valence neutrons favour a deformed configuration represented by the different local minima that could appear along this surface.

Examples of such approaches are model calculations based on phenomenological mean field models that predict the existence of several competing minima in the deformation surface [Naz93]. Self-consistent mean field calculations [Nic02], [Smi03] and calculations including correlations beyond the mean field [Egi04] confirm these results.

Apart from the shell model and mean field approaches, this problem has also been studied in the framework of the *Interacting Boson Model* (IBM), which is an algebraic model (see [Fra04] for example). Another purely phenomenological approach, the shape mixing approach [Woo92], has also been used to interpret the experimental findings. In this model, the observed states are the result of the interaction between several multiparticle-multihole configurations, that is, the superposition of spherical, oblate and prolate shapes whose relative weights are determined by a fit to experimental data.

7.1. A new signature of deformation

From the experimental point of view, there are some well established signatures that can give information about nuclear deformation:

- the quadrupole moment, which describes the effective shape of the nuclear charge distribution. If the nucleus is not spherically symmetric, it will have a quadrupole moment, otherwise it will be zero. Apart from providing information about deformation, the measurement of the quadrupole moments can also be used to test nuclear models in general.
- the change in the mean square radius $\delta < r^2 >$, that can be measured in scattering experiments. Also related are isotope shifts studies like the measurements using laser spectroscopy that compared with the droplet model predictions can give information about the evolution of the nuclear radii with the number of nucleons.
- nuclear spectroscopy, like γ-ray and conversion electron spectroscopy. With γ-ray spectroscopy, rotational band structures build on low-lying 0^+ states,

which are a fingerprint of deformation, can be accessed. Regarding conversion electrons, the $E0$ transition (electric monopole transition) is particularly important in decays from 0^+ initial states to 0^+ final states, which cannot occur by any other direct process and provide information about shape mixing. Comparison of $E2$ and $E0$ rates can also reveal information about the internal structure of the excited 0_i^+ state.

The production of exotic nuclei for the measurement of these signatures becomes more and more difficult as we go to more and more exotic nuclei, so there is a need for alternative ways of study. Theoretical calculations predicted a new possible signature of deformation: the GT strength distribution of the daughter nucleus measured in beta decay, can be sensitive to the deformation of the β decaying nucleus. This method was first developed for deformed nuclei around $Z = 50$ [Fri95], and was successfully applied in [Nac04b] to demonstrate that the ground state of ^{76}Sr was prolate with a deformation parameter of $\beta_2 \sim 0.4$, and that ^{74}Kr ground state has a mixed character [Poi04a, Poi04b]. Sarriguren *et al.* [Sar05] performed calculations for nuclei around $Z = 82$. These calculations show different strength patterns (that is, different distribution of the strengths) depending on the assumed deformation of the parent nucleus. These calculations were fine tuned in [Mor06]. The latter calculations are used in this work for the comparison with the experimental data and could provide an alternative method to study the ground state deformation of these nuclei.

7.1.1. Brief description of the theoretical formalism

The formalism of [Mor06] uses the quasiparticle-random-phase approximation (QRPA), with an axially deformed Hartree-Fock (HF) mean field generated by Skyrme forces (SLy4), and pairing is treated in the BCS framework. The equilibrium deformation is obtained self-consistently as the shape that minimizes the energy. The potential energy curves obtained with this formalism exhibit oblate, spherical and prolate minima at very close energies which are identified as the ground state and low lying intruder states. These energies are sensitive to the Skyrme force and the type of pairing, as shown in Fig. 2 of Ref [Sar05].

The HF+BCS+QRPA approach is applied to the calculation of the Gamow-Teller strength (Eq. 2.1), assuming that parent and daughter nucleus have the same deformation. In this way, the profile of the B(GT) can be an indication of the deformation of the parent nucleus. Hence, the relevant measurement will be the β-decay feeding distribution from lead to thallium. The deduced GT strength distribution in thallium will be used to determine the deformation of the ground state of lead. Contrary to the relative energies of the minima appearing in the potential energy curves, the B(GT) does not seem to change significantly when different forces or pairing strengths are used, as shown in Fig. 4 of Ref [Sar05].

In Fig. 7.2 the resulting strengths calculated for every deformation are shown, where it can be appreciated that the GT strength distributions of the $^{184-194}Pb$ isotopes show clearly different patterns depending on the assumed deformation of the parent state. This feature can be used to infer the shape of the decaying nucleus.

This approach reproduces global properties along the whole nuclear chart and has a great predictive power because it is based on an universal interaction widely tested for many years. This is why it is expected that the global decay properties, as the general behaviour of the B(GT) contained in the Q_β window and the half-lives, can be well reproduced. However, the approach can have difficulties in reproducing local spectroscopic details, so we can not expect from the present approach a perfect description of all experimental data.

Although the lead nuclei are known to be spherical in their ground state, the use of this complementary method will be a test to confirm its viability in this region, with the idea to extend it to other possible cases of interest, like for example Pt, Po, Hg, etc. which are not necessarily spherical in their ground state. With the availability of a trustworthy technique to measure the B(GT) strength along the whole Q_β window (see Sub. 2.1.3), the possibility is open for further tests of nuclear models in the region around $Z = 82$ [Pro07].

In Table 7.2 a summary of the relevant quantities of the lead isotopes studied in this work is shown.

Table 7.2: Relevant nuclear data for the neutron deficient Pb nuclei of this work. The Q_β is the mass differences between the parent and daughter nuclei when a β decay occurs, respectively. The S_n and S_p are the neutron and proton separation energies in the daughter. The ISOLDE yields are taken from [Kos03], and the Q_β values from [Aud03].

Parent Nucleus ($^A_Z X_N$)	$^{192}_{82}Pb_{110}$	$^{190}_{82}Pb_{108}$	$^{188}_{82}Pb_{106}$
Daughter Nucleus ($^A_Z Y_N$)	$^{192}_{81}Tl_{111}$	$^{190}_{81}Tl_{109}$	$^{188}_{81}Tl_{107}$
Half-life	3.5(*1*) min	71(*1*) s	25.1(*1*) s
Q_β [keV]	3320(*30*)	3920(*50*)	4530(*30*)
(EC + β^+)/(α + (EC + β^+))	99.9941(*7*) %	99.60(*4*) %	90.7(*9*) %
S_n [keV]	7800(*300*)	7976(*550*)	8304(*459*)
S_p [keV]	2560(*20*)	2017(*513*)	1574(*327*)
ISOLDE yield [ions/μC]	$4.0{\cdot}10^7$	$2.3{\cdot}10^7$	$1.7{\cdot}10^6$
Reference	[Bag98]	[Sin03]	[Sin02]

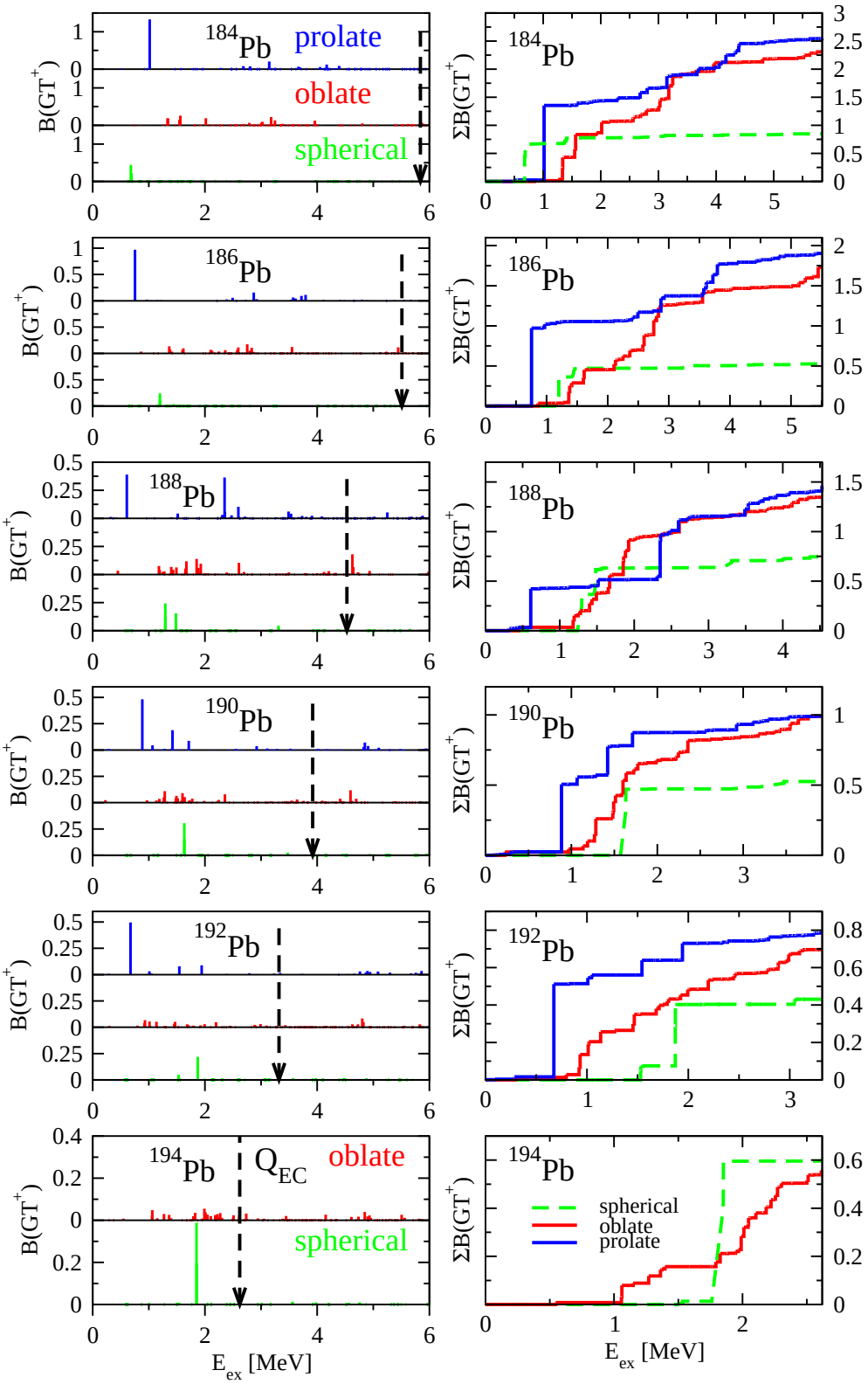

Figure 7.2: Strength (left panel) and accumulated strength (right panel) calculated with the formalism described in [Mor06]. The accumulated strength was obtained by adding the strength observed up to that energy. Taken from [Mor06].

8 Experiment

8.1. ISOLDE facility

The choice of the facility to perform an experiment can be critical in terms of experimental success. In the case of the measurements of the beta decay of the three lead nuclei presented in this part of the work, it was clear that ISOLDE [ISO] was the optimal one.

ISOLDE is the *Isotope Separator OnLine DEvice* installed at CERN (Fig. 8.1). It is a world-leading laboratory for production and studies of radioactive nuclei. It is supplied with proton beams at energies of 600 keV or 1.4 GeV from the PSB (*PS-Booster*)[1]. The protons can impinge in several types of targets to produce a wide variety of radioactive species. These targets are coupled to ion sources to allow the ionization and extraction of the radioactive beams that can then be directed to one of the two different separator systems: GPS (*General Purpose Separator*) or HRS (*High Resolution Separator*), to perform separation in mass. Finally the selected isotope is transported to the different experimental lines.

ISOLDE was the best suited for this application because in this facility it is possible nowadays to use a laser ion source (RILIS [RIL]) to select the lead, that otherwise will be "mashed" by the overwhelming surface ionization of thallium. The lead beta-daughter, thallium, can be surface ionized easily without the need of the laser. This allow us to make two measurements:

- with LASER ON, to produce the nuclei of interest (lead), that can only populate the low spin isomer of thallium through beta decay, and
- with LASER OFF, to produce both the low and high spin isomers of thallium and to study possible contaminants in the measurements.

[1]The PSB gives one pulse of $\sim 3 \cdot 10^{13}$ protons (maximum) every 1.2 s. Each of these proton pulses lasts for 2.4 μs. A PSB supercycle contained 14 pulses during our measurement, so the total duration of one supercycle was 16.8 s. But the number of pulses can be changed during the measurements, as it was the case in the measurements presented here.

In this way, RILIS is used for selection in Z and the GPS for separation in mass.

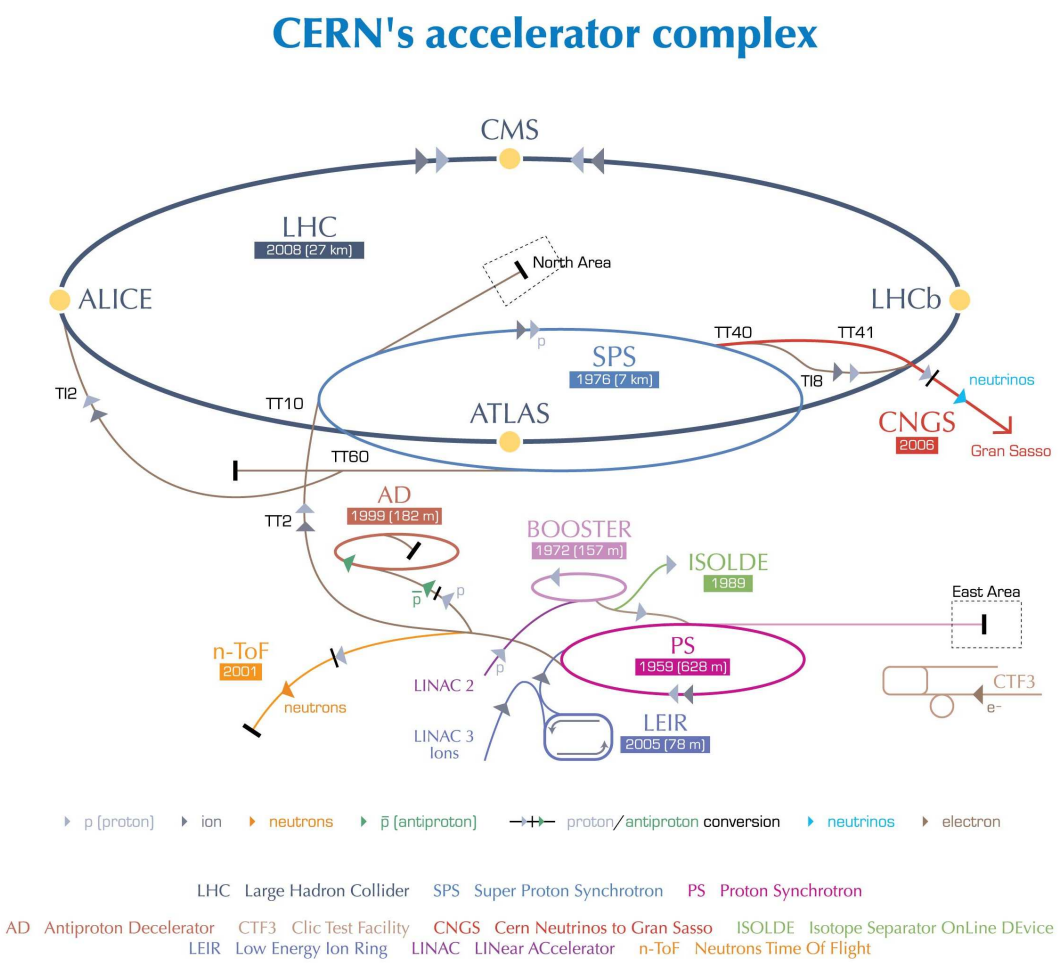

Figure 8.1: CERN accelerator complex, showing ISOLDE in green.

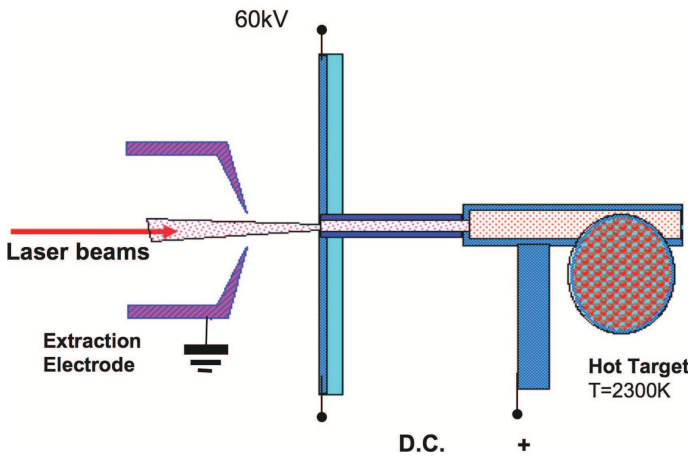

Figure 8.2: Schematic view of the RILIS laser ionization source installed at ISOLDE.

8.2. *Lucrecia* measuring station

This measuring station, installed at the end of one of the ISOLDE beamlines, consists of a TAS (Sub. 2.1.3), and a tape station. In this experiment, the DACQ (*Data ACQuisition system*) developed by our group was used [Agr11].

A similar procedure to the one described in Sub. 4.2 regarding the tape system and the cycles duration was followed in these measurements. The main difference was related to the background measurements, that were made at the end of each mass measurement and after each calibration source measurement by simply stopping the beam. In this station, the beam pipe, and not a plug detector, is used to hold the tape. The beam was also implanted in the tape outside of the TAS, that was then transported to the center of the detector for the measurement, but in this station it is also possible to implant the beam directly in the center of the TAS, by changing the position of the rollers. The latter procedure allows the measurement of more exotic nuclei with very short half-lives.

Lucrecia[2] is the TAS at this station. It is made of one piece of NaI(Tl) material cylindrically shaped with $\phi = h = 38$ cm (the largest ever built to our knowledge). It has a cylindrical hole of 7.5 cm diameter that goes through perpendicularly to its symmetry axis. (See Fig. 8.3). The purpose of this hole is to allow the beam pipe to reach the measurement position so that the tape can be positioned in the center of the detector. It also allows the placement of ancillary detectors in the opposite side to measure other types of radiation emitted by the activity implanted in the tape (x rays, e^-/e^+, etc). However, the presence of this hole makes this detector less efficient as compared to the GSI TAS (*Lucrecia*'s total efficiency is around 90 % from 300 to 3000 keV). *Lucrecia*'s light is collected by 8 photomultipliers. During the measurements *Lucrecia* is kept measuring at a total counting rate not larger than 10 kHz to avoid second and higher order pileup contributions.

Surrounding the TAS there is a shielding box 19.2 cm thick made of four layers: polyethylene, lead, copper and aluminium. The purpose of it is to absorb most of the external radiation (neutrons, cosmic rays, and the room background).

The DACQ was controlled by a software that allowed a rough online analysis. It was based on ROOT libraries and saved the data in listmode files but also in ROOT tree structures [Agr11].

The ancillary detector was the same for all the measurements. It consisted on a germanium detector, *Tirant Lo Blanc*, formed by a planar germanium detector and

[2]Named after Lucrecia Borgia (Lucrècia Borja in catalán), daughter of Rodrigo Borgia, the powerful Renaissance Valencian who later became Pope Alexander VI, and the italian Vannozza dei Cattanei. Very little is known of Lucrecia, and the extent of her complicity in the political machinations of her father and brothers is unclear.

a coaxial germanium detector. They were used with different gains (energy range: planar: $\sim$ 700 keV; coaxial: $\sim$ 2 MeV). The planar detector was the closest to the tape, and was used for the measurement of the x rays emitted in the EC decay. The coaxial detector was used for the measurement of the individual gammas emitted in the de-excitation cascades (see Table 8.1 for details).

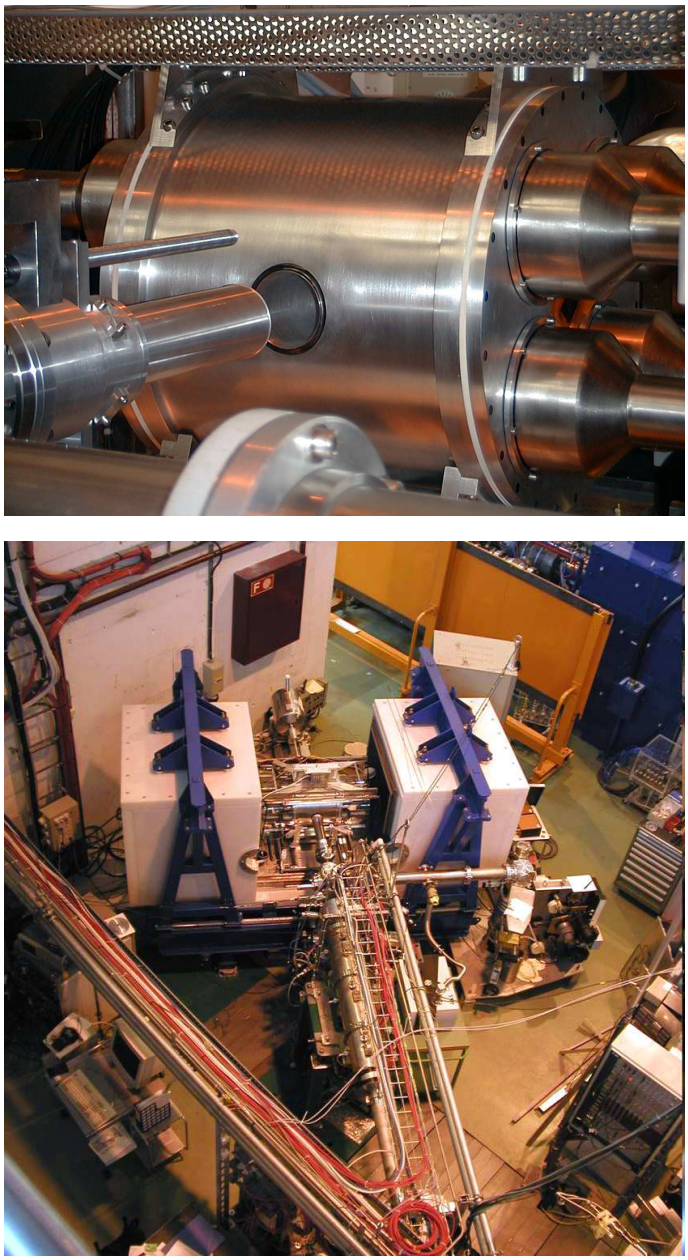

Figure 8.3: *Lucrecia* measuring station. Top: Picture of *Lucrecia*, showing the perpendicular hole and the telescopic beam pipe. Bottom: Picture of the whole station, where the shielding can be seen in white.

8.3. The measurement

A summary of the details of the experiment can be found in Table 8.1. An alignment and tuning of the detector was performed before the measurements took place, achieving a TAS energy resolution of 7.9 % (at the cesium peak) for the measurements. The same was done for the germanium detectors, resulting in resolutions of 0.5 keV at 600 keV for the planar and 2.8 keV at 1332.5 keV for the coaxial.

For mass 192, a cycle of 4 min for the laser ON measurement and 10 min for the laser OFF was used, taking into account the half-lives of the nuclei in the decay chain (taken from [Bag98]):

$$^{192}Pb[t_{1/2} = 3.5(1)\text{ min}] \Rightarrow {}^{192}Tl[t_{1/2} = 9.6(4)\text{ min}] \Rightarrow {}^{192}Hg[t_{1/2} = 4.85(20)\text{ h}]$$

In the case of mass 190, the cycles were 2 and 3 m for the laser ON and OFF respectively (half-lives taken from [Sin03]):

$$^{190}Pb[t_{1/2} = 71(1)\text{ s}] \Rightarrow {}^{190}Tl[t_{1/2} = 2.6(3)\text{ min}] \Rightarrow {}^{190}Hg[t_{1/2} = 20.0(5)\text{ min}]$$

Finally, for mass 188, the cycle was 45 s for both measurements [Sin02]:

$$^{188}Pb[t_{1/2} = 25.1(1)\text{ s}] \Rightarrow {}^{188}Tl[t_{1/2} = 71(2)\text{ s}] \Rightarrow {}^{188}Hg[t_{1/2} = 3.25(5)\text{ min}]$$

Conventional sources where used for energy, width and efficiency calibration of the detectors (^{22}Na, ^{24}Na, ^{60}Co, ^{133}Ba, ^{137}Cs, ^{152}Eu, ^{228}Th and ^{241}Am). The relevant information of the sources used in the analysis is presented in Table C.11. Two ^{22}Na sources were measured, but for the analysis the less intense was used. The ^{152}Eu and ^{251}Am sources were used for the calibration of the germanium detectors.

For the calibration measurements, the source was positioned in the center of the TAS. To this end, the source was attached to the end cap of the beampipe from inside. During these measurements the shield was closed to avoid undesired backgrounds.

A beam of ^{24}Na was produced using 25 proton pulses of $5 \cdot 10^{12}$ protons for the ^{24}Na source measurement. After this measurement the tape was moved to remove the sodium activity ($t_{1/2} = 14.9$ h), but in some of the later measurements hints of ^{24}Na were seen, so it is possible that some sodium was implanted in the collimators or in the beam pipe[3]. Nevertheless, this does not affect the lead gates because for the analysis an x rays - TAS coincidence spectrum is used.

[3] In an ideal case, a stable Na-centered beam is used, but in this case the settings for the Pb beam were re-scaled to the sodium mass.

A first look at the x rays for mass 192, for example, shows that, in comparison with the cases of Part II of this work, these cases are cleaner, as can be seen by comparing Fig. 9.5 with Fig. 5.11 for example.

Table 8.1: Details of the measurements. L_{ON} = Laser ON, L_{OFF} = Laser OFF.

	A = 192	A = 190	A = 188
Beam	p		
E (initial)	1.4 GeV		
Proton pulses	4 with $5.3 \cdot 10^{12}$ p	5 with $5.6 \cdot 10^{12}$ p	16 with $5 \cdot 10^{12}$ p
Target	$^{238}UC_x$/graphite, 50/10 g/cm^2, 2050 °C		
Ion source	RILIS		
Ionizer	Ta		
Ion. Pot. (eV)	7.42		
Transmission	79 % from GPS.FC490 to RC3.FC90, $\sim$ 95 % from RC3.FC90 to the Faraday cup.		
Yield [atoms/μC]	L_{ON}: $4 \cdot 10^7$ L_{OFF}: $1.5 \cdot 10^6$	L_{ON}: $1.3 \cdot 10^7$ L_{OFF}: $1.9 \cdot 10^6$	L_{ON}: $2.5 \cdot 10^6$ L_{OFF}: $1.2 \cdot 10^6$
Cycle duration	L_{ON}: 4 min L_{OFF}: 10 min	L_{ON}: 2 min L_{OFF}: 3 min	$L_{ON} = L_{OFF}$: 45 s
Ge Planar	l×ϕ = 10×50 mm		
Ge Coaxial	l×ϕ = 50×50 mm		
TAS	l×ϕ = 380×380 mm		

9 Analysis and Results

The procedure followed for the preparation of the data can be consulted in Appendix C. Due to technical problems during the measurements, some extra difficulties appeared when doing the sort of the data. Sec. C.1 shows how this was solved. See Appendix A for a detailed description of the analysis steps that are followed in the next sections. As mentioned before in this work, Sec. 2.2 describes the analysis procedure in a more general way.

9.1. Mass A = 192

1. **Average branching ratios calculation:**

a) Known Levels: Fig. 9.1 shows the known level scheme populated in the beta decay of ^{192}Pb into ^{192}Tl(taken from the HR technique, see Subs. 2.1.2 and 2.1.3). When this level scheme was used in the analysis, the recalculated spectrum (obtained in step 3 *c*) of the analysis, p. 97) did not reproduce the measured spectrum. To solve this, several modifications to the known level scheme were tested and will be presented in detail in step 3 of this analysis. These changes affect the resulting branching ratio matrix, and in consequence, the response matrix.

b) Level Density Parameters: According to [Gor01] and [Dem01], there are 12 levels in ^{192}Tl up to an excitation of 500 keV, and 10500 up to 3250 keV. With these values, the fit gives a value of 13.886 MeV^{-1} for the parameter a, and -0.6 MeV for the parameter Δ.

c) Gamma Strength Function Parameters: The quadrupole deformation for ^{192}Tl is β_2 = -0.061 and the neutron separation energy 7.8 MeV [Bag98]. Using these values the parameters of Table 9.1 were obtained.

d) Average branching ratios calculation: Depending on the known level scheme used (cases presented in step 3), the start of the unknown part was taken from a different excitation energy, and up to 3400 keV (approx. bin 85, the Q value bin).

With the above parameters, a branching ratio matrix was generated for every case.

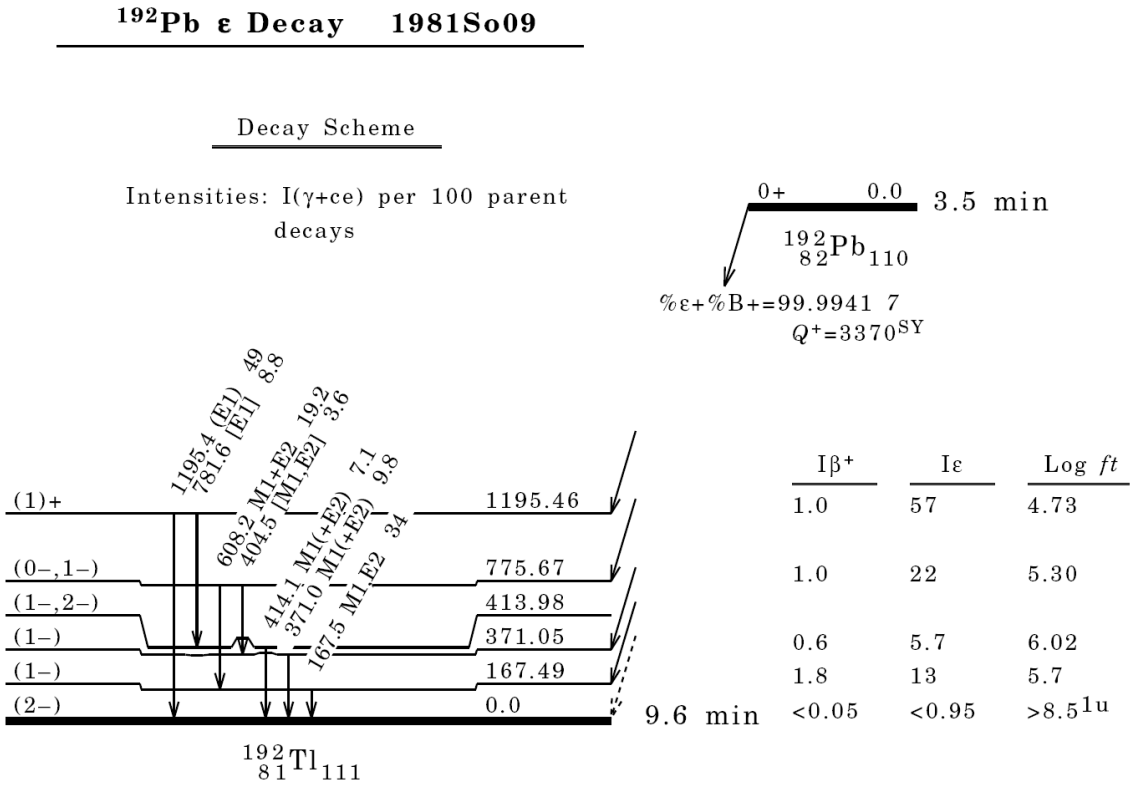

Figure 9.1: Known level scheme of ^{192}Tl showing the levels populated in the beta decay of ^{192}Pb. The diagram shows the total intensities (gamma + conversion electrons) for every transition, as well as the β^+ and electron capture (ϵ) components of the beta feeding to every level. There is no beta information for the level at 413.98 keV, since the intensities feeding and leaving the level give a negative balance. This will be discussed in step 3 *c*) of the analysis. Taken from [Bag98].

Table 9.1: Giant resonance parameters for the E1, E2 and M1 gamma strength functions of ^{192}Tl (using β_2 = -0.061, S_n = 7800 keV).

Type	E [MeV]	w [MeV]	Γ [mb]
E1	14.571	4.338	494.876
	13.701	3.856	556.647
M1	7.119	4.0	2.595
E2	10.939	3.806	5.373

2. **Response simulation:**

a) MC code: For the simulation of *Lucrecia*, the same MC code used in Ref. [Nac04a] for the analysis of ^{76}Sr was used, since in this simulation the geometry of *Lucrecia* was accurately introduced. However, the code was slightly modified to update the distance between the germanium detector and the center of the TAS detector, since it was moved 3 mm forward due to the removal of the beta detector. In Fig. 9.2 the final geometry used in the simulation is shown. Also, the physics and the light production function of the simulation package were checked. The simulated spectra were generated at 2 keV per channel.

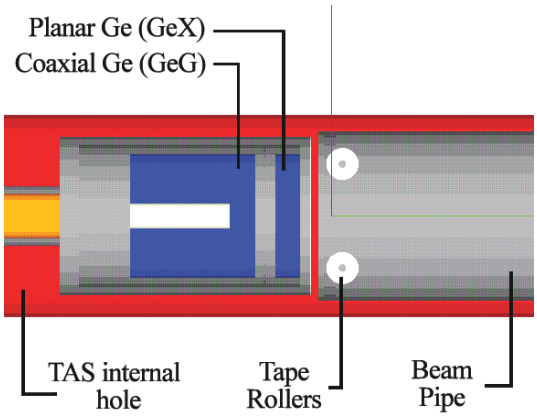

Figure 9.2: Detail of the geometry of the cylindrical hole inside *Lucrecia* implemented in the MC, showing the germanium detector and the beam pipe.

b) MC calibration: As presented in Appendix C.2.1 and C.2.2, the following calibrations in energy and width were found for the TAS detector:

- TAS detector calibration:

$$E(x) = \begin{cases} -10 + 1.8x + 4 \cdot 10^{-4}x^2 & \text{if} \quad x < 356 \\ -42 + 2.067x & \text{if} \quad x > 356 \end{cases} \tag{9.1}$$

$$\sigma^2(E) = 0.45E + 20 \cdot 10^{-5}E^2 \tag{9.2}$$

- Simulation calibration:

$$E(x) = \begin{cases} -15 + 2x + 4 \cdot 10^{-5}x^2 & \text{if} \quad x < 649 \\ -33 + 2x & \text{if} \quad x > 649 \end{cases} \tag{9.3}$$

$$\sigma^2(E) = 0.25E + 9 \cdot 10^{-6}E^2 \tag{9.4}$$

- From 9.2 and 9.4 we obtain the empirical instrumental resolution distribution function used for the correction of the width of the MC peaks:

$$\boxed{\sigma^2_{instrum.}(E) = 0.25E + 17 \cdot 10{-}5E^2} \tag{9.5}$$

c) MC test: To test the reliability of the Monte Carlo, a simulation of the sources measured in the experiment was done. By comparing the measurements and the simulations it is possible to tune the simulations and calibrations until the experimental spectra is reproduced. The simulated sources were ^{22}Na, ^{24}Na, ^{60}Co, and ^{137}Cs, although more sources were measured (see Table C.11). A comparison between the simulations and the measured sources is shown in Fig. 9.3.

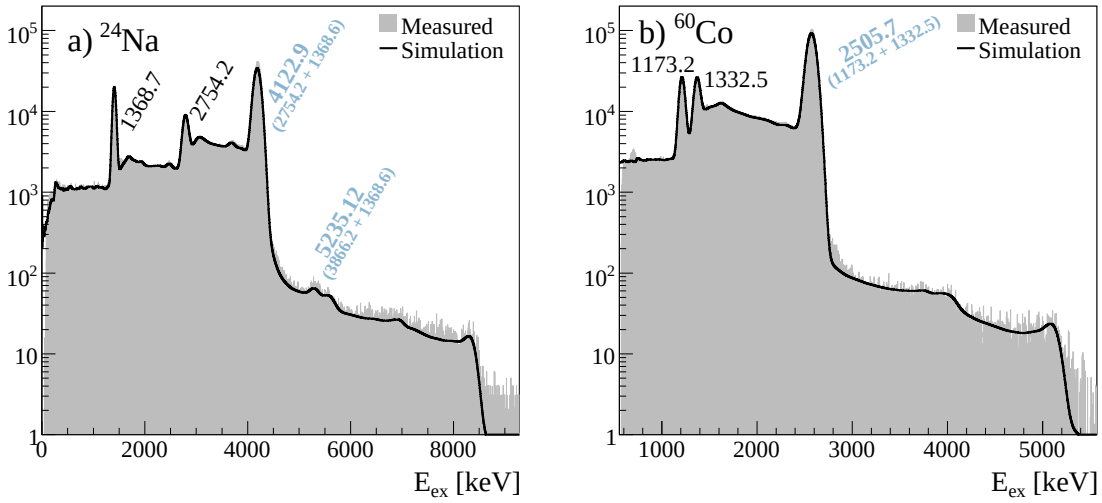

Figure 9.3: Comparison between measured and simulated sources, the former with background subtracted, the latter with pileup added: a) ^{24}Na, b) ^{60}Co . The complete level schemes can be found in Sec. C.4.

d) Build response: Once the quality of the simulation is verified, the next step is to build the gamma response. To this end, a simulation was done in which monoenergetic gammas were launched from the center of the detector at energies ranging from $\Delta E = 40$ keV (the bin size) to a value high enough to include all the Q values of the nuclei to be analyzed in this chapter (a maximum of 8000 keV was chosen), in steps of 40 keV. Some of the TAS spectra produced in this simulation are shown in Fig. 9.4 where the energy deposited by a gamma of certain energy can be seen.

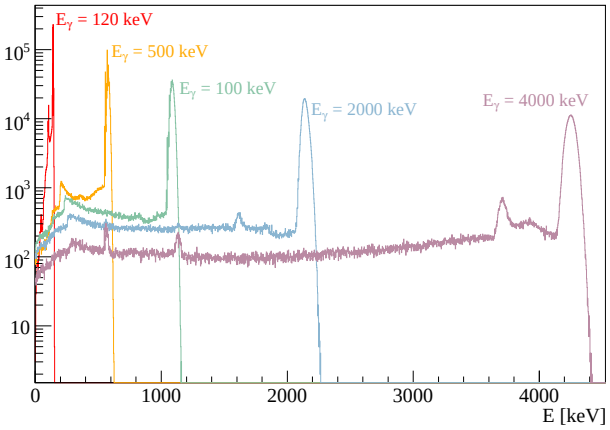

Figure 9.4: *Lucrecia*'s gamma response for monoenergetic gammas of different energies.

e) Create matrix: The response matrix of the detector to EC decay, obtained by the convolution of the different average branching ratio matrices produced for the different level schemes and the simulated monoenergetic response generated in the previous step, was calculated for each test of step 3.

3. **Extracting the feedings:**

a) X-ray tagging: The measuring time for mass 192 was 5 hours and 10 minutes approximately. The full x-ray spectrum obtained with all the statistics of the planar germanium detector for this mass has 18 557 710 counts. The gates placed in this spectra for the extraction of the different components of the decay are shown in Fig. 9.5.

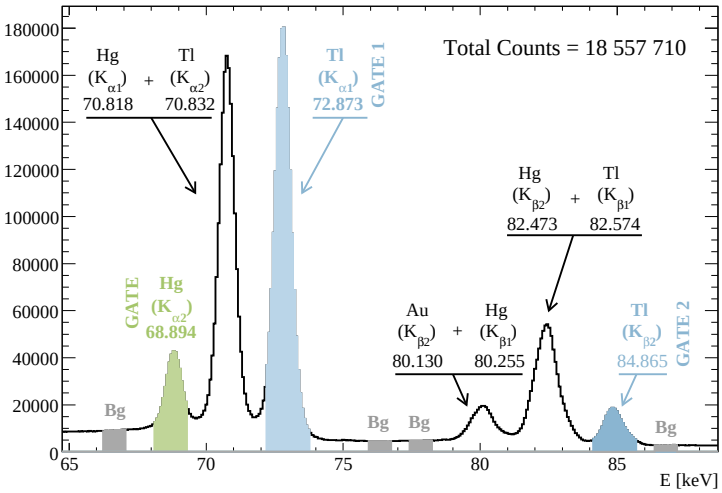

Figure 9.5: X-ray spectra produced in the EC decay of ^{192}Pb showing the gates used for the analysis. The background gates are also shown. The purity of the beam arriving at the TAS is demonstrated by the fact that only the peaks of Tm and Hg can be seen (the tape's time-cycle structure also contributes to purify the beam).

b) Contaminants, backgrounds, pileup: As mentioned in 8.3, the use of RILIS in combination with the GPS separator provided a clean measurement. The rest of the cleaning was achieved by adjusting the tape's cycles duration, as explained in Sec. 8.2, and setting the gates in the x rays. This is appreciated in Fig. 9.5 were only the x rays up to Hg are seen. The x-ray gated TAS spectra generated from the gates of Fig. 9.5 and the related backgrounds are presented in Fig. 9.6.

In the gates of interest (Fig. 9.6 a) and b)), no contamination coming from Hg was found or it is negligible (< 1 %). This is easy to understand, as the x-ray peak used for the gating is at the right-most side of the x-ray spectrum, and can only be affected by Comptons of higher energy γ rays and x rays. This is not the case for the gates of the daughters, that can be contaminated with thallium, as can be seen in Fig. 9.6 c) and for the backgrounds, which show the most intense peak of thallium.

As in the case of Part II of this work, the percentage of beta plus contamination expected to be present in the x-ray gated spectra was negligible, in agreement with [Bag98] (that supposes a β^+ component of $\sim$1–2% for all the levels as seen in Fig. 9.1 and taking into account the internal conversion coefficient of the known transitions). However, a rough estimation was made from the coaxial germanium spectrum gated in the x rays of thallium (Fig. 9.11), comparing the area under the 511 peak and the area under the most intense gamma of the decay (1195 keV). The ratio of these two areas after efficiency correction is of the order of 15 %. But the 511 peak that has the contribution of all the levels of the decay, while the the single peak represents only a percentage of the total decay intensity, which is 48 % per 100 parent decays (that is, the EC intensity of the gamma per 100 parent decays). This very rough estimation gives a 3.6 % of possible beta plus contamination which should be taken as an upper limit, since only a part of this percentage is really due to the decay (the gates are not background subtracted).

No additional contaminations were found, as can be seen from Fig. 9.8, that shows a background measurement made for the measurement of the ^{192}Pb decay. The spectrum of the TAS and GeG detectors gated on the x rays of thallium are also shown. This spectrum confirms that there is no background contamination in the gated spectrum. For the pileup calculation, the pulse of Fig. 9.7 was used. This pulse was also used for the pileup calculations of the other lead isotopes that will be discussed in the following sections.

The analyzed spectrum is the sum of the two gates of Fig 9.6 a) and b). The background spectrum was generated in the same way. The normalization factors for the contributions to the decay spectrum are presented in Table 9.2. The only contributions found in this spectrum were the background gate and the pileup (Fig. 9.9). However, there are some unidentified peaks in the TAS and in the germanium detectors whose possible origin will be discussed in step 3 *c*).

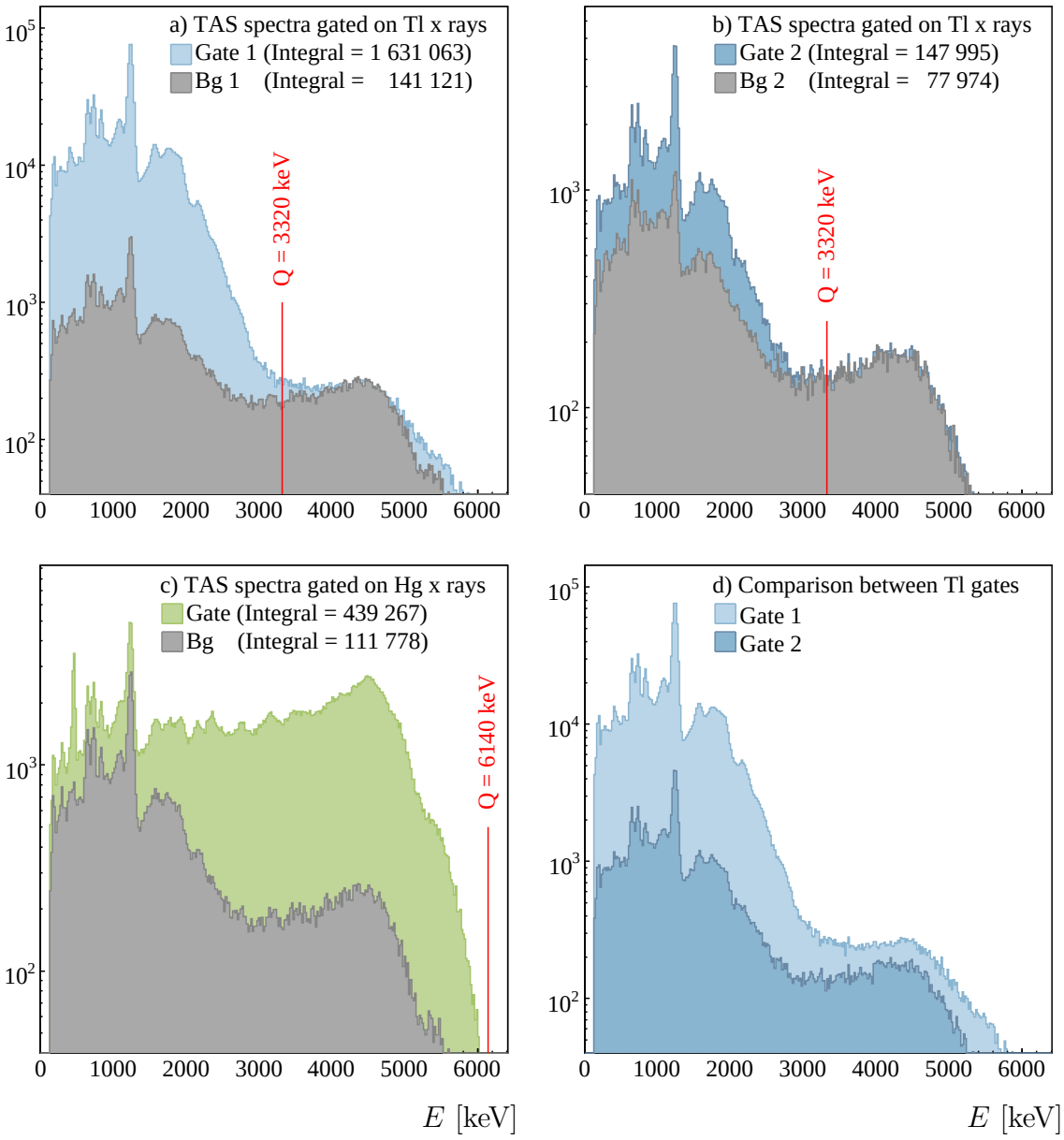

Figure 9.6: X-ray gated TAS spectra of the isobars produced in the EC decay chain of ^{192}Pb (the X axis is the energy in units of keV): a) K_α thallium gate b) K_β thallium gate. c) Mercury gate d) Comparison between K_α and K_β thallium gates. The K_β gate is supposed to be cleaner than the K_α one. The fact that these two gates are so similar is an indication that the K_α gate is also clean.

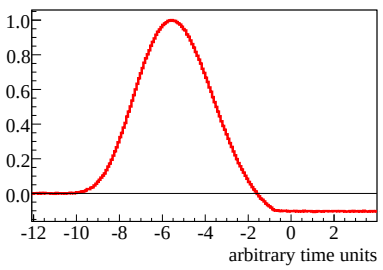

Figure 9.7: Pulse measured in this experiment (see Sec. 8.3), used for the calculation of the pileup of all the masses. The pulse is normalized and has 110 bins. The maximum is at bin 61.

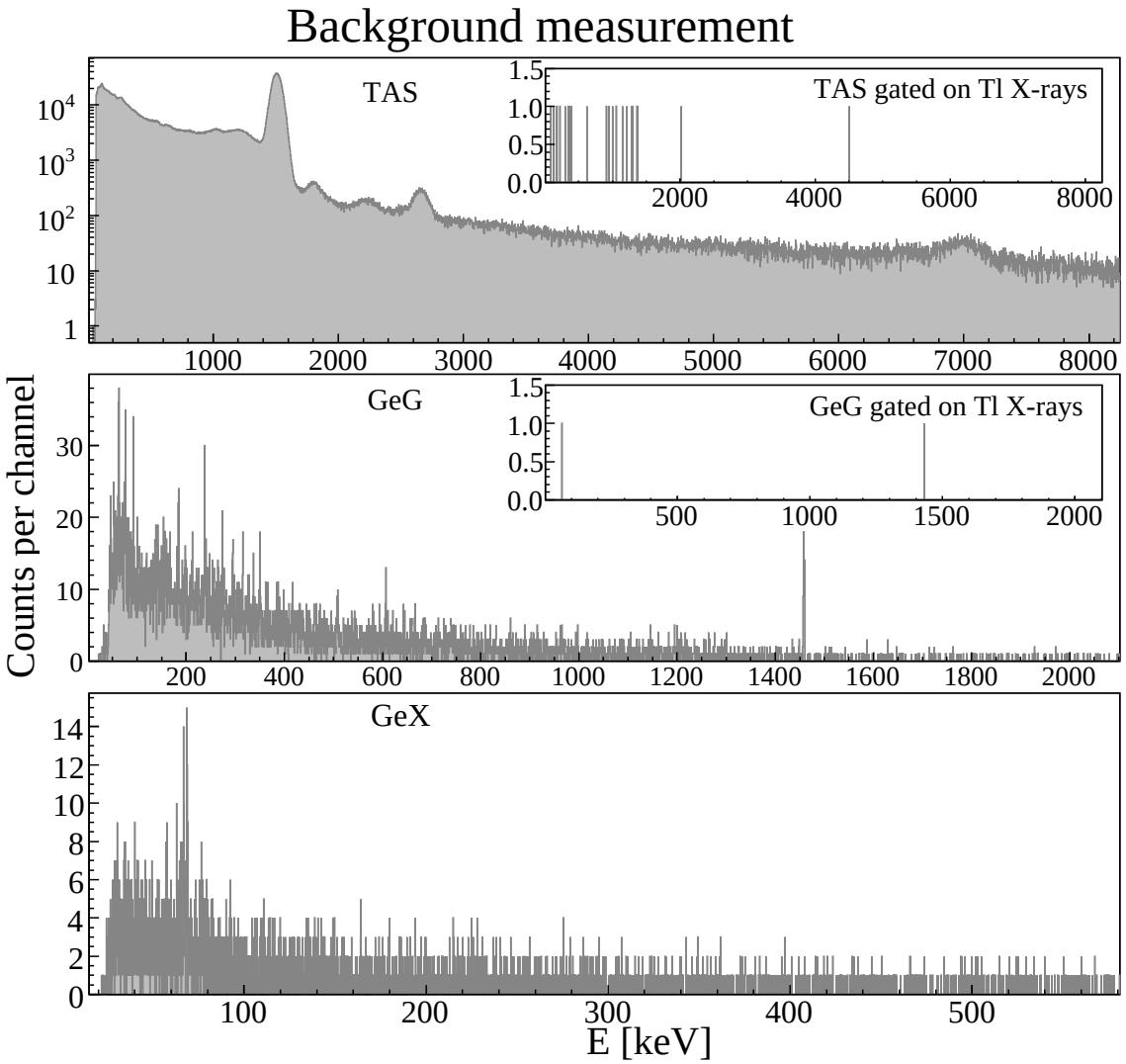

Figure 9.8: TAS, GeG (coaxial germanium detector) and GeX (planar germanium detector) single spectra from a background measurement for mass 192. The gates of the TAS and the GeG detector in coincidence with the thallium x rays are also shown in the small panels of the upper-right corner. These plots show that the gated spectra are clean of unidentified contaminations.

Table 9.2: Normalization factors of the contributions to the decay of ^{192}Pb.

Contribution	ID	Norm. factor
X-ray gated background	1	0.94
Pileup	2	10027

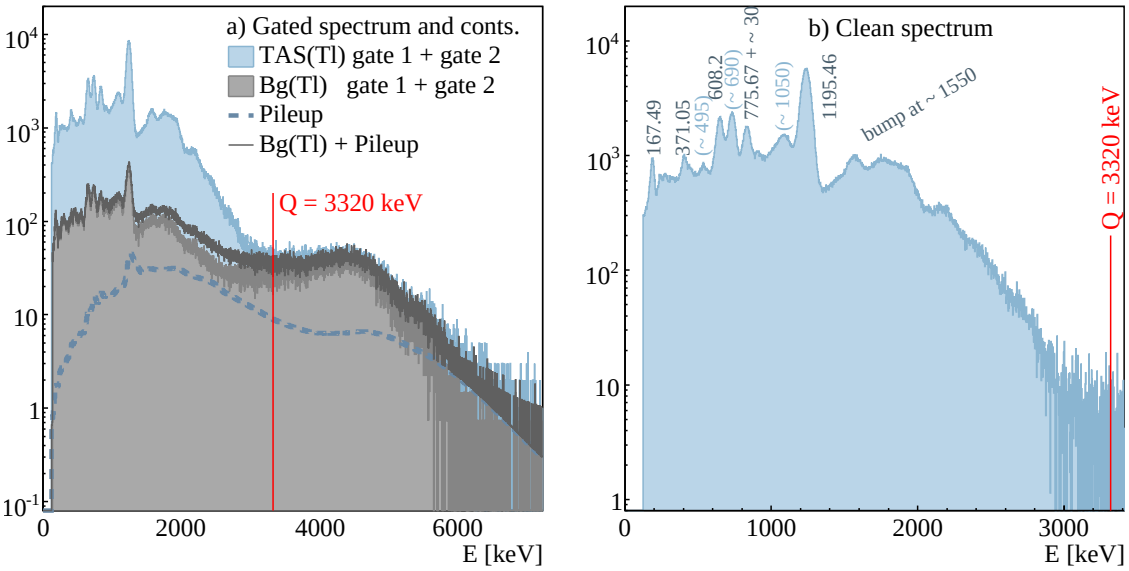

Figure 9.9: Contaminants of the thallium x-ray gated spectrum: a) TAS spectrum gated on Tl x rays with its contaminants. The background and pileup are already multiplied by their normalization factors. b) TAS gate after subtracting the sum of the contaminants. This spectrum is shown only for information, the spectrum used for the analysis is the spectrum with contaminants. Some of the most intense peaks are labeled; those between parenthesis are not reported by the literature.

c) Algorithm application: The measured spectrum was recalibrated to the Monte Carlo calibration using Eqs. 9.1 and 9.3, and was then rebinned by a factor of 20. The first analysis was made from 120 keV to 4440 keV. The recalculated spectra, shown in Fig. 9.10 did not reproduce the measured spectra. For this reason, several tests were made changing the known levels file of step 1 *a*) (reasonable changes in the J^{π} of the levels had no influence in the results.).

To understand the peaks that are not reproduced by this analysis, the information of the individual gammas is needed. To this end, a spectrum of the GeG detector spectrum in coincidence with the thallium x rays was prepared with all the statistics of the mass 192 measurement and it is shown in Fig. 9.11. All the peaks reported in Ref. [Bag98] are seen here. Also, there are some unidentified peaks that we tried to understand by doing several analysis. In Fig. 9.12 the full x-ray spectrum is shown, again with all the statistics of mass 192 measurement. In Table 9.3 a summary of this information is shown. In the "Type" column the multiplicity of the peak is presented, where "Single" means that the TAS peak was produced by a single γ ray (an escape γ ray or a cascade of only one γ ray), "Double" means that the peak is produced by a cascade of two γ rays, and so on.

Table 9.3: The first column shows the approximate energies of the peaks seen in the measured TAS spectrum in coincidence with the ^{192}Tl x rays. The second column refers to the multiplicity of the cascade de-exciting the level (see Sub. 2.2.2). GeG(Tl) stands for the coaxial germanium detector spectrum gated in thallium x rays and GeX is the planar detector spectrum. These two columns show the gammas related to the levels seen in the TAS. All the energies are given in keV.

TAS(Tl)	Type	Comments[a]	GeG(Tl)	GeX
167.5	Single	HR	167.5	167.5
371.0	Single	HR	371.0	371.0
414.0	Single	HR, Not seen	414.1	414.1
∼495	?	Not understood	511 ?	511? 494.2[b]?
608.2	Escape[c]	HR	608.2	608.2
∼690	Single?	Not seen	689.6?	
775.7	Double	HR	608.2, 404.5	404.5
∼1045	?	Not understood	group, $E \sim 1030$	Out of range
1195.5	Single, Double	HR	1195.4, 781.6	Out of range

[a] HR refers to the levels proposed by high-resolution measurements [Bag98].
[b] This gamma was not reported in [Bag98], but appears in the GeX spectrum.
[c] It is not really a level, but a γ ray that escaped from a cascade.

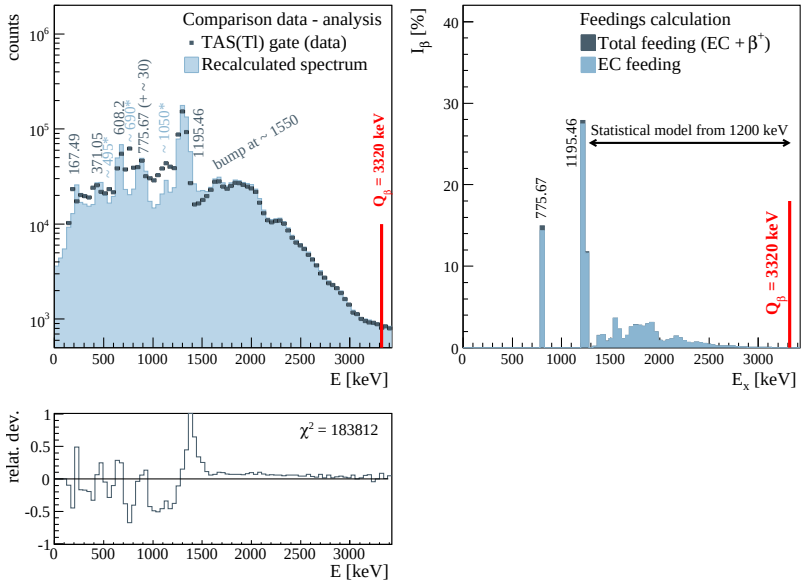

Figure 9.10: Results of the analysis when the known level scheme of Fig. 9.1 is used. The upper-left panel is the ^{192}Pb EC decay TAS spectrum (dots) compared with the recalculated spectrum. Clearly, there is a poorer reproduction of the data compared to the cases of part II, as can be seen at the lower-left panel, where the relative deviation between the two is shown. Finally, the feedings spectrum calculated from the data and the response matrix is presented in the upper-right panel. More details in the text.

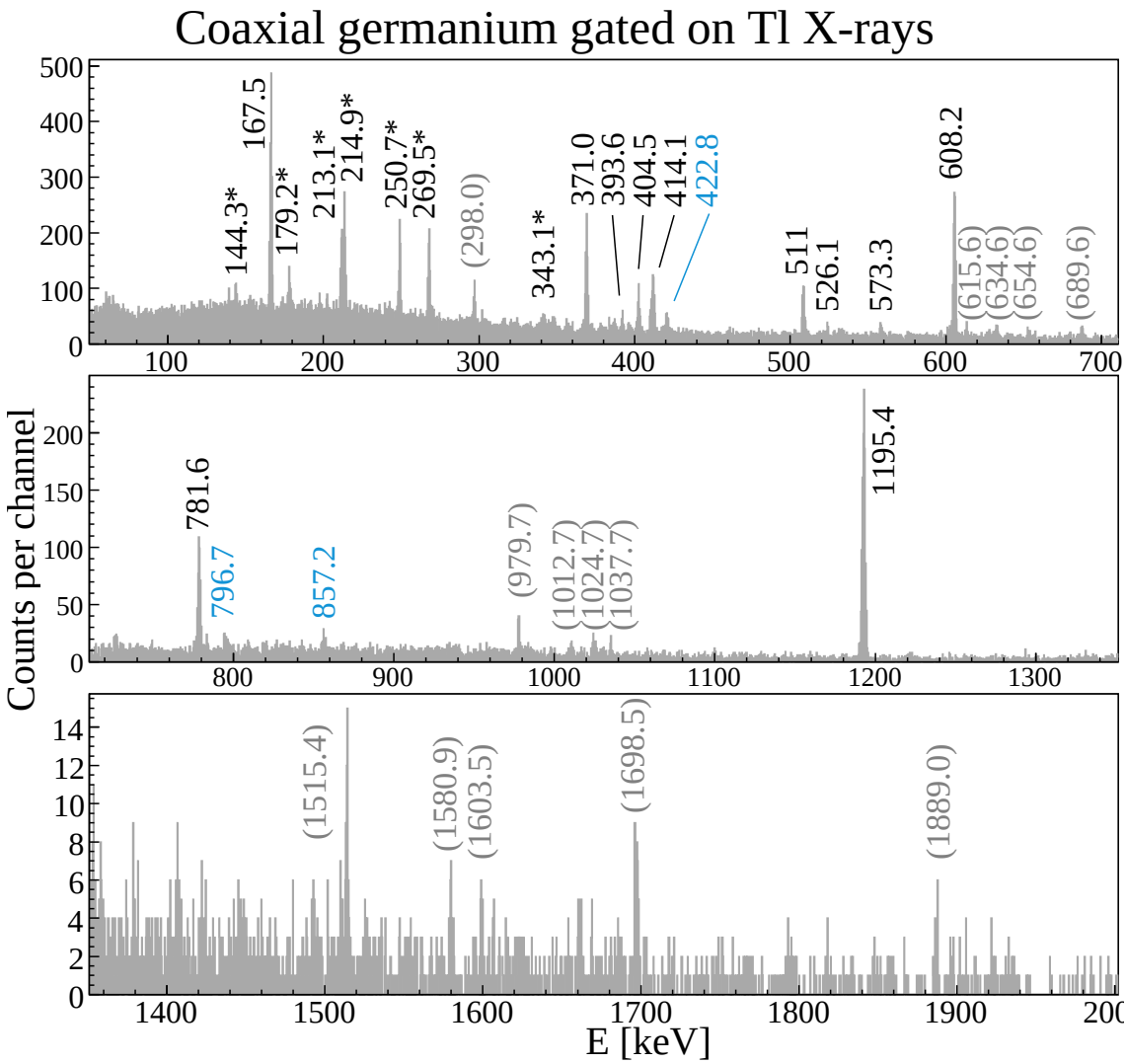

Figure 9.11: GeG detector spectrum in coincidence with the Tl x rays (no background subtracted). The peaks marked with "*" are those gammas reported in [Bag98] but not placed in the level scheme. The peaks marked in parentheses are unidentified or not reported gammas. Those in blue are comming from the decay of ^{192}Tl into ^{192}Hg, whose most intense peak (422.79 keV) appears in this spectrum with a low intensity, confirming that the contamination of the Tl gate with the Hg isobar is negligible. Finally, a gamma of ∼298 keV appears in both GeG and GeX detectors, not only for mass 192, but also for mass 190 (Fig. 9.23). The origin of this γ ray is presently unknown.

Looking at Table 9.3 and Fig. 9.10, some comments must be made:

- The first not explained peaks appear at low energy (after the peak of the level at 167.49 keV) and have low intensity. This zone is not well reproduced by the analysis. However, some peaks at this range of energies were found in the

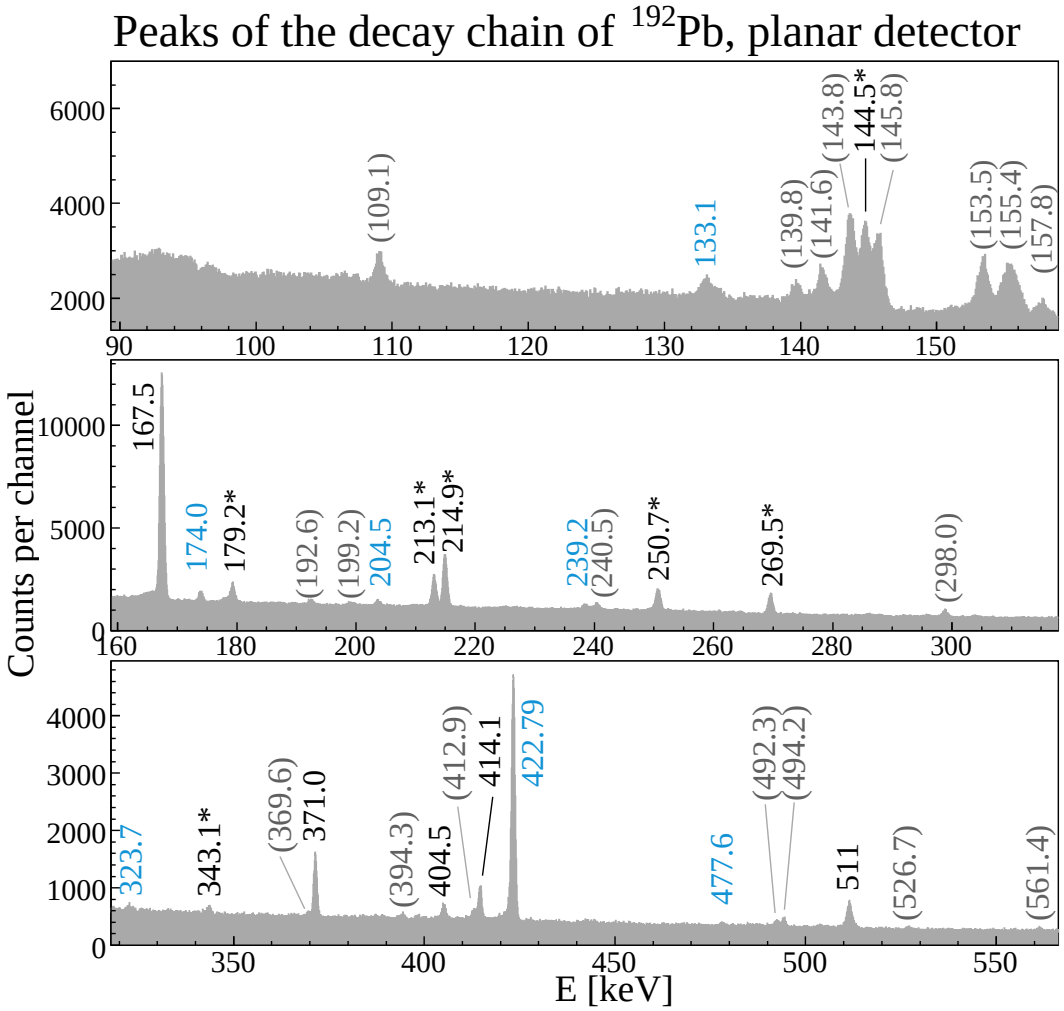

Figure 9.12: GeX detector singles spectrum. The same description of Fig. 9.11 applies, but here the most intense peak of Hg is more intense than in Fig. 9.11, because all the low energy γ rays of the decay chain are shown, since it is not possible to make coincidences of the detector with itself.

germanium detectors. These peaks correspond mainly to the gammas reported by [Bag98] and not placed in the level scheme. On one hand, taking into account their energies, an analogy with the β-decay level scheme of ^{190}Tl can be made. On the other hand, the gamma intensities of these not-placed gammas is high enough that coincidences between them should have been observed, but this is not reported in the cited reference, so no levels could be proposed by the addition of these gamma's energies. Based on these two facts, one possibility could be that these gammas come from low energy levels with the same energy than the gammas' energy. Some tests were made including these gammas as levels, (see Fig. 9.13, test 4) but as the observations are not conclusive no levels are proposed here. This question should be clarified by a HR measurement with higher sensitivity.

- In Ref. [Bag98], a level is proposed at 413.98 keV based in coincidences and analogies with heavier thallium isotopes. This gamma is part of a two-gammas' cascade that follows the de-excitation of the most intensely fed level at 1195.46 keV (1195.46 → 413.98 + 781.6). The authors are not sure about the order of these gammas, since "*their intensities are equal within the experimental uncertainties*". However, they choose the gamma with the lower intensity as the one that connects the ground state, making the beta feeding to the level negative (see Fig. 9.1). In our TAS spectra a level at 413.98 keV is not observed, or its beta intensity is too low. Additionally, there is a non-explained peak around 865 keV, with very low intensity but visible, that could explain a level at 781.6 keV with a multiplicity ~ 3[1]. In both cases the information is not enough to draw a conclusion. When a test was made inverting the order of these gammas (Fig. 9.13, test 3), the reproduction of the spectrum of Fig. 9.10 was not really improved.

- Two of the peaks of Fig. 9.10 not reproduced by the analysis are at energies of ∼495 and ∼1045 keV. The possibility that they could come from a beta plus contamination (511 and 1022 (+30) keV) was discarded, since the beta plus contamination in the gate was not enough to explain the intensity of the peaks, as explained in step 3 *b*) of the analysis. Another possibility for the peak at ∼495 is to be a level, based on a gamma of 494.2 keV found in the GeX detector. But this evidence again is not enough as the GeX detector can not be gated with itself so it shows the gammas of all the decay chain (maybe it is a gamma comming from other isotopes of the decay chain). It must be noticed at this point that in [Bag98, Table III] the authors present two coincidences (they were not placed in the level scheme) that could explain the $\sim$ 495 keV peak. One is 167.5 + 323.7 = 491.2 keV an the other is 167.5 + 343.1 = 510.6 keV. Two analysis including these possibilities were made but did not reproduce the peak at that energy. The test including a level at that energy is shown in Fig. 9.13 (test 2). With respect to the other peak, a group of very low intensity peaks can be seen around 1030 keV in the GeG detector. If they de-excite to the ground state by a single gamma this could partially explain the presence of the ∼1045 peak.

- The peak at 608.2 keV should not be understood as a level but as an escape peak. It is the third most intense gamma emitted in the decay and the most intense gamma de-exciting the level at 775.67 keV, which at the same time is the second most strongly fed level. The analysis is able to reproduce it without the inclusion of any additional level at that energy.

- The last peak not reproduced by the analysis is at ∼690 keV. Several combinations of the gammas that can be seen in the GeX and GeG detectors were tested (see Fig. 9.13, test 1), but the analysis only reproduced the peak when

[1]It is worth to remember here that *Lucrecia* is a NaI scintillator, so the sum peaks will be displaced according with the multiplicity of the cascade, as explained in Sub. 2.2.2.

a level at 689.6 keV was added, de-excitating to the ground state by a γ ray of 689.6 that is found in the GeG(Tl) spectrum. But then again the poor intensity of this γ ray is not enough to explain the intensity of the peak in the TAS.

Regarding the unknown part, two cases were considered in these tests for the start of the application of the statistical model: after the last level at 1195.46 (from 1200 keV on) and after the level at 775.67 keV (from 800 keV on). This means that we assume that, from those energies on, there is a continuum where the model calculates the levels and the transitions. In the last case (statistical model from 800 keV on), the peak at ∼1045 is not anymore a problem, since the statistical model will reproduce it.

The first test following the raw analysis of Fig. 9.10 was made aiming to reproduce the TAS peak at ∼690, the most intense not-reproduced peak of our data. Then we tried to reproduce the peak at ∼495. A test removing the 414 keV level was also done. Finally, the low energy peaks were added. The electron conversion coefficients were calculated with the HSICC tool of the Brookhaven Laboratory web for a M1 multipolarity. An analysis was made in which the statistical model was used for the whole spectra. Of course, this was the case that better reproduced the data, but the feedings calculated in this way are not fully trustworthy, since then the analysis can place feeding in every bin of the low energy part of the level scheme where there may not be. This case was only used for reference. Its χ^2 is the lowest of all the tests, as can be expected ($\chi^2 = 2228$).

From all these tests, a selection of the most credible tests based on the available data are presented in Fig. 9.13 with their respective χ^2. In these illustrations, the best results are achieved when placing the start of the unknown part after the level at 775.67 keV, and adding a level at 689 keV and another at 494 keV. The inversion of the gammas of 414.1 and 781.6 keV does not seem to have an effect, since the χ^2 of this test and the raw analysis are of the same order, so the results here are not conclusive. From these tries, the one chosen is 2.b), and it is shown in Fig. 9.14, in comparison with the reference analysis (statistical model used in the whole Q value window) and the raw analysis (with the original HR level scheme).

From these analysis we conclude that it is not possible to fully explain all the peaks that appear at the TAS with the present knowledge, and the lack of information from HR detectors does not allow to reconstruct the level scheme from this measurement. For example, the proposed levels at 689 keV and 494 keV could be a group of levels. Until a better level scheme is provided by HR measurements and the coincidences technique, a TAS analysis cannot be better done, so we propose this nucleus to be re-measured with coincidences.

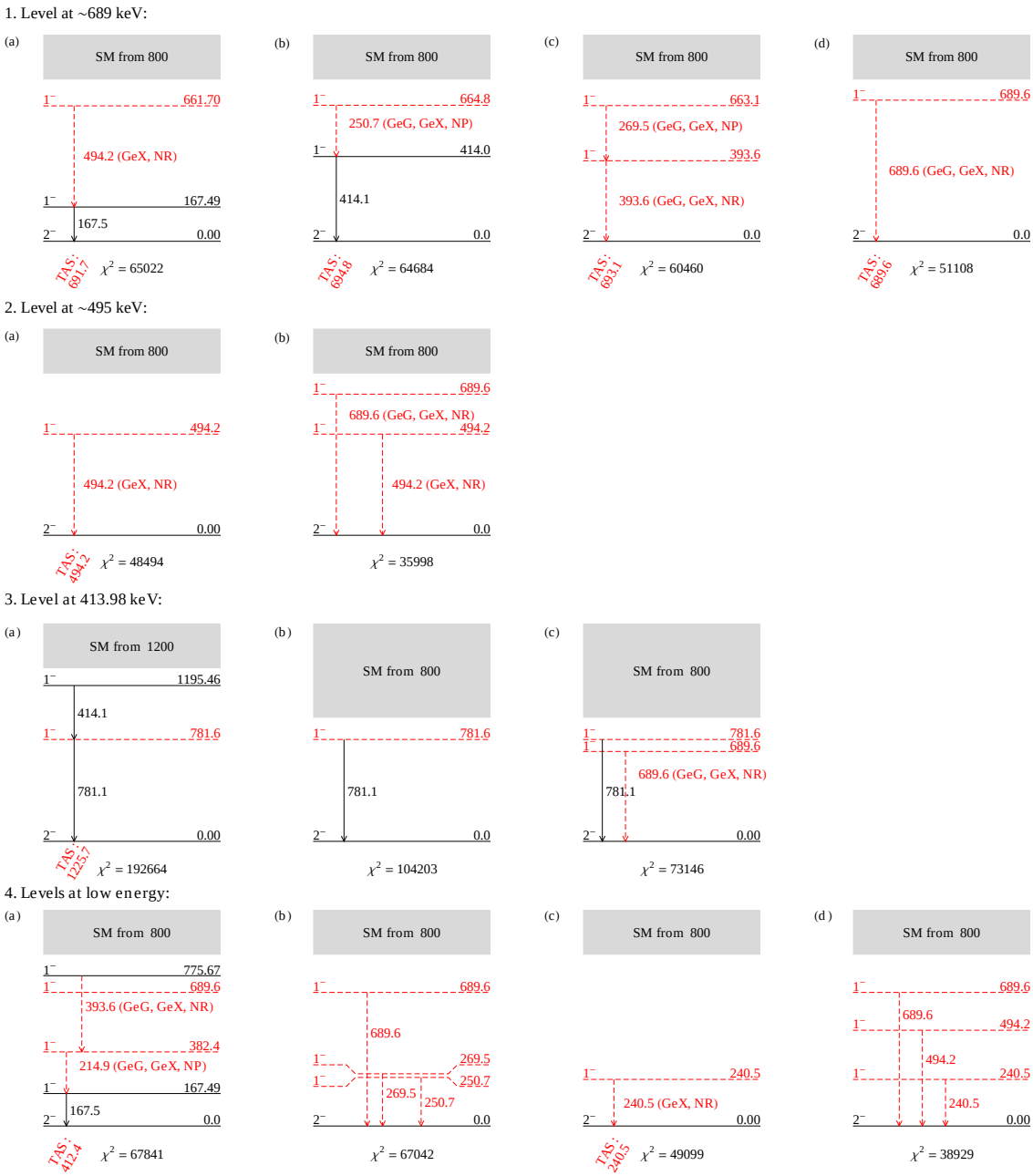

Figure 9.13: A selection of the best tries for the known level scheme are shown. The added levels and gammas appear with dashed lines. For clarity, only these levels and their transitions are shown. The levels at an energy above the start of the unknown part should be removed from the levels file. The different tries of every test are ordered by χ^2.

Legend:

SM = Statistical Model,

GeX = planar Ge detector,

GeG = coaxial Ge detector (in coincidence with Tl x rays),

NP = Not Placed (gammas reported in [Bag98] but not placed in the level scheme),

NR = Not Reported (gammas not reported in [Bag98] but seen in our measurement),

TAS: E = the position of the peak generated by that possibility in the TAS detector.

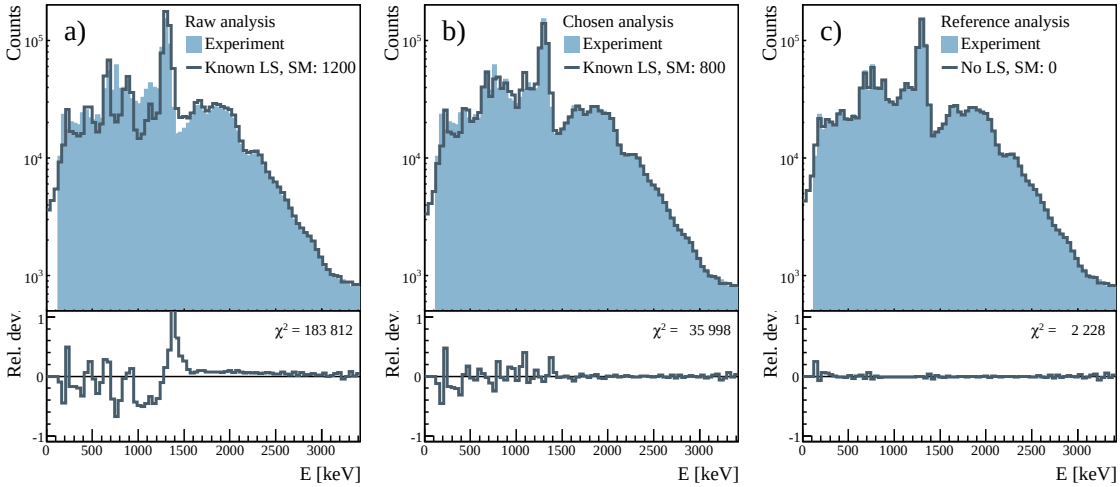

Figure 9.14: Comparison between: b) the analysis made with the chosen level scheme and: a) the raw analysis c) the reference analysis.

d) Strength calculation: Using the feedings obtained from the analysis of the previous step and the Q value and half-life of Table 7.2, the strength was calculated from 0 to 3210 keV. The results of this calculation are summarized in Table 9.4 and in Fig. 9.15. Also, the accumulated strength or $\Sigma B(\mathrm{GT})$ was calculated at each energy by adding the strength observed up to that energy. It is compared with the accumulated strength of the reference analysis in Fig. 9.16. In the next chapter, the discussion and conclusions of these results are presented.

Table 9.4: Deduced $I_{EC+\beta^+}$ values (I_β values) for the levels populated in the decay of ^{192}Pb for the selected analysis. The totals for the TAS data include the sum from the last level shown in the table up to the Q value. The HR data were taken from [Bag98] and the Q value from [Aud03].

E_{lev}	J^π	I_{EC} [%]		$I_{EC+\beta^+}$ [%]		$B(\mathrm{GT})$ [$g_A^2/4\pi$]	
[keV]		TAS	HR	TAS	HR	TAS	HR
167.49	(1^-)	∼0	13(9)	∼0	15(10)		0.008(4)
371.05	(1^-)	0.1(3)	5.7(14)	0.1(4)	6.3(15)	0.00008(20)	0.004(1)
413.98	(1^-)	0.003(25)	-	0.003(28)	-	∼0	-
[a]494.20	(1^-)	1.6(2)	-	1.8(2)	-	0.0012(2)	-
[a]689.60	(1^-)	3.1(22)	-	3.3(2.4)	-	0.003(2)	-
775.67	(1^-)	9.0(49)	22(3)	9.4(5.2)	23(3)	0.008(5)	0.020(4)
1195.46		30(15)	57(7)	31(16)	58(7)	0.04(2)	0.07(1)
TOTAL		98(18)	98(9)	100(18)	102(1)	0.24(3)	0.10(1)

[a] These levels were added to the known levels scheme to reproduce the experimental spectrum.

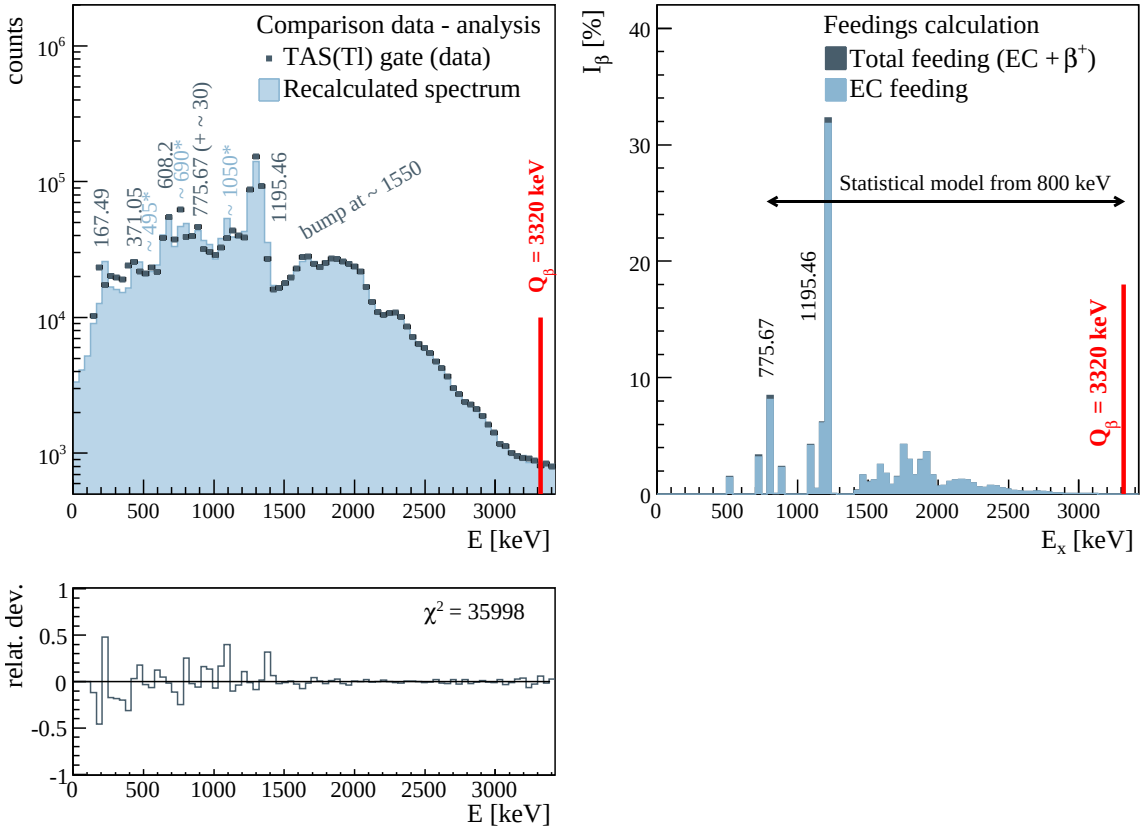

Figure 9.15: Results of the ^{192}Pb EC decay TAS analysis when using the original HR level scheme with the addition of the two levels of test 2 b) of Fig. 9.13. The explanation of the panels here is the same as in Fig. 9.10.

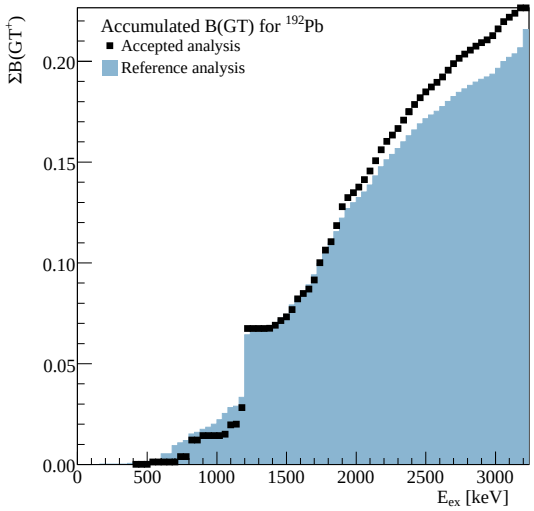

Figure 9.16: Comparison of the accumulated strength $\Sigma B(\mathrm{GT})$ for the selected analysis (Fig. 9.14-b)) and the reference analysis (Fig. 9.14-c)).

9.2. Mass A = 190

In this section the analysis of the beta decay of ^{190}Pb into ^{190}Tl is presented. As usual, the steps described in Appendix A are followed.

1. **Average branching ratios calculation:**

a) Known Levels: For mass 190, the known level scheme provided by the HR technique [Sin03] is better known than for mass 192 (Fig. 9.17), and it is also the best known of all the lead isotopes studied in this work. However, as in the previous case, this level scheme had to be slightly modified, as will be explained in step 3 *c*) of the analysis.

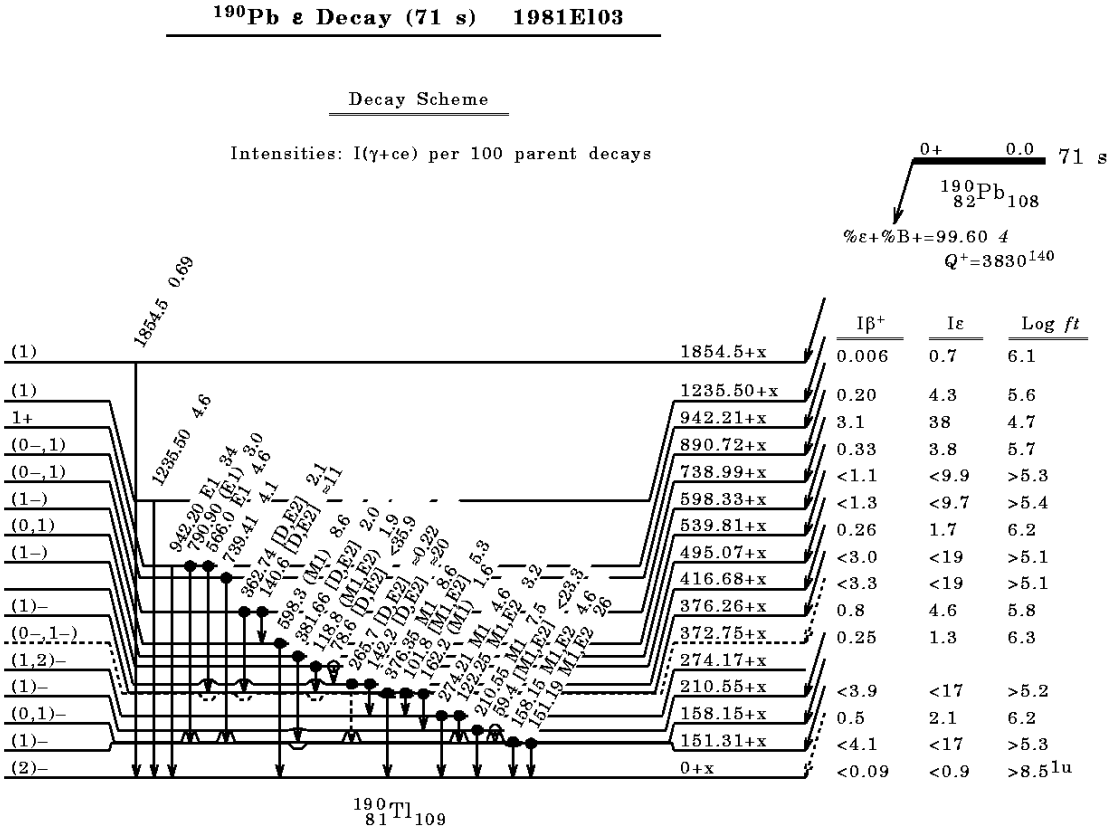

Figure 9.17: Known level scheme of ^{190}Tl showing the levels that are populated in beta decay. The explanation for the diagram is analogous to that of Fig. 9.1. Taken from [Sin03].

b) Level Density Parameters: There are 8 levels in ^{190}Tl up to an excitation of 500 keV, and 26900 up to 3750 keV according to theoretical calculations [Gor01, Dem01]. With these values, the resulting level density parameters are a = 13.821 MeV^{-1} and Δ = -0.594 MeV.

c) Gamma Strength Function Parameters: In the case of ^{190}Tl the quadrupole deformation is β_2 = -0.061 as in the case of ^{192}Tl, and the neutron separation energy 7976 keV. These values give the gamma strength function parameters of Table 9.5.

Table 9.5: Giant resonance parameters for the E1, E2 and M1 gamma strength functions of ^{190}Tl (β_2 = -0.061, S_n = 7976 keV).

Type	E [MeV]	w [MeV]	Γ [mb]
E1	14.607	4.358	488.808
	13.734	3.874	549.822
M1	7.144	4.0	2.857
E2	10.978	3.830	5.396

d) Average branching ratios calculation: As in the case of mass 192, several cases were analyzed, so the starting energy of the unknown part was different for each one. However, in most of the tests, it was taken from an energy of 760 keV, that is, after the level at 738.99 keV, and up to the Q_β value (see step 3 *c* of the analysis for a justification). Using *a*), *b*), *c*) and *d*) the branching ratio matrix was obtained for every possible level scheme.

2. **Response simulation:**

The same simulation of the individual gamma responses used for mass 192 was used for this and for the rest of the Pb isotopes. The convolution of the results of this simulation with the average branching ratio matrix calculated in the previous step gives the response of the detector for every analyzed case, as made for the analysis of ^{192}Pb.

3. **Extracting the feedings:**

a) X-ray tagging: The x-ray spectrum obtained with all the statistics of the planar germanium detector for mass 190 was very similar to that of mass 192 and has 16 217 325 counts (Fig. 9.18). Comparing this spectrum with the one for mass 192 (Fig. 9.5) a peak in the gold x rays position can be seen, together with a decrease of the thallium component. When moving to a more neutron-deficient lead isotope, the peaks of the thallium component start to go down in intensity, and the peaks of the Hg component start to go up. This is due to the shortening of the half-life of the lead isotope as its mass decreases, and to a reduction of its yield as the the purity of the beam decreases with the decrease of the mass number. In the x-ray spectrum for mass 190, the windows were taken in a similar way as in the decay of

^{192}Pb to extract the different gates of the components of the decay, and they are shown in Fig. 9.18.

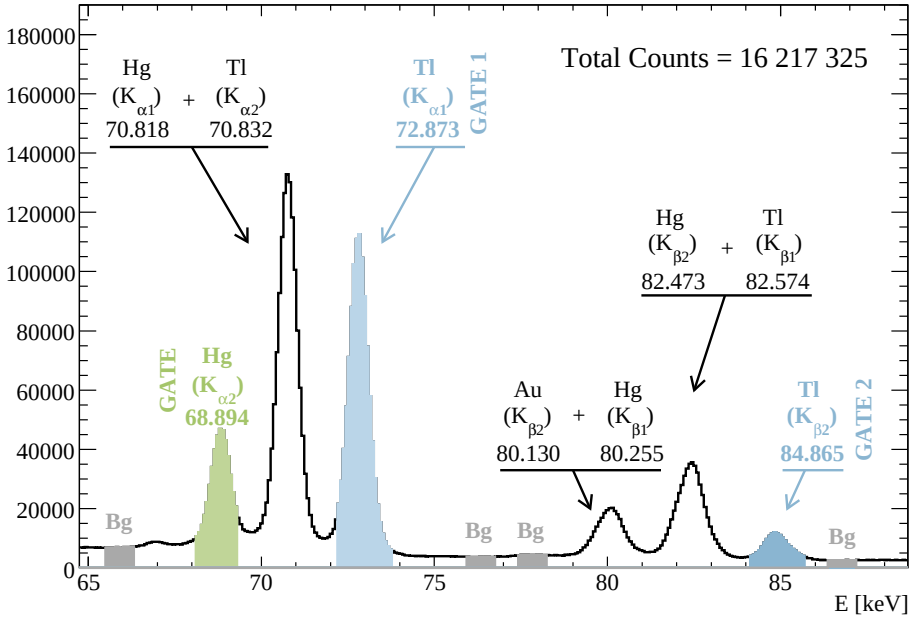

Figure 9.18: X-ray spectra produced in the EC decay of ^{190}Pb showing the gates used for the analysis. The description for this figure is similar to Fig. 9.5. If both figures are compared, a decrease of the thallium component and the appearance of a small peak at the gold x rays position can be seen.

b) Contaminants, backgrounds, pileup: The spectra obtained from the gates of Fig. 9.18 are shown in Fig. 9.19. No gate was produced for gold as the statistics are negligible. The part of the Hg gate that could contribute in a more visible way to the Tl gate is the bump of levels at the end of the spectrum that goes from $\sim$ 2000 keV up to the Q_β value. But after subtracting the corresponding background from the thallium gate, no bump appears in that region of the spectrum. Instead, this spectrum goes down, until it reaches the zero approximately around the Q_β value of the lead decay (3920 keV). From this the conclusion is that the contamination of the thallium gate with the mercury gate is negligible, thanks to the conservative gates that were defined in the spectrum of Fig. 9.18 and to the reasons exposed in the previous section for mass 192.

The β^+ component for the most intense level in ^{190}Tl is 3.1(*8*) % [Sin03], and it is around 3 % or less for the rest of levels, so the contamination by this means can be considered small. A similar calculation to the one made for mass 192 gives a contamination of 2.3 % as an upper level. In addition, the background measurement made for thallium does not show any other unknown sources of background, as can be seen from the thallium gated spectra of TAS and GeG detectors (upper-right panels of Fig. 9.20). Finally, the pileup was calculated using the same pulse as for

mass 192 (Fig. 9.7). The contributions to the decay gate are presented in Table 9.6 and Fig. 9.21. The two gates of thallium were added to make a unique gate. The same procedure was applied to the background gates.

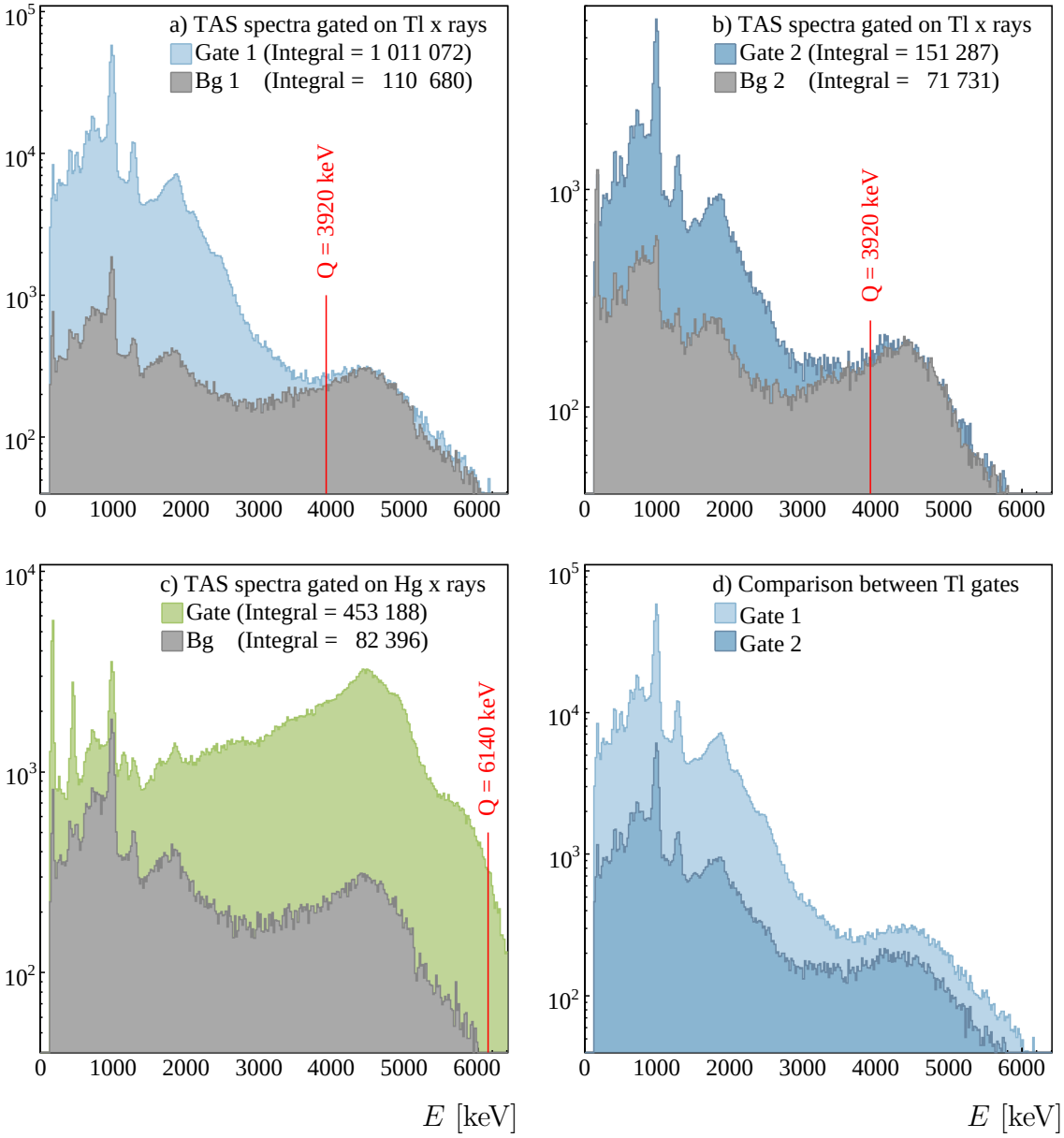

Figure 9.19: Similar to Fig. 9.6, X-ray gated TAS spectra of the isobars produced in the EC decay chain of ^{190}Pb: a) K_α thallium gate b) K_β thallium gate. c) K_α mercury gate d) Comparison between K_α and K_β thallium gates.

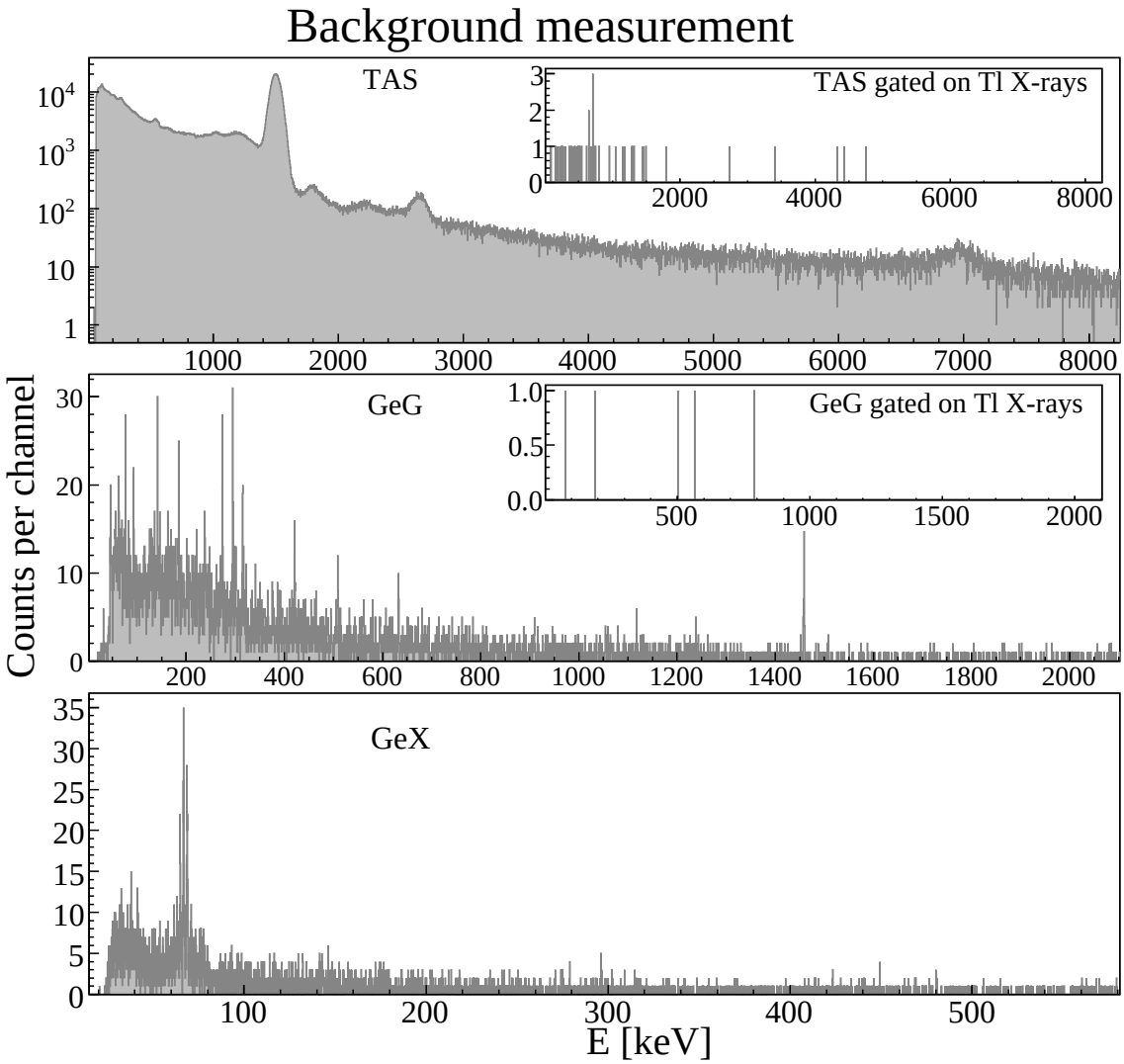

Figure 9.20: Same as Fig. 9.8 but for mass 190. No unknown background contributions are found.

Table 9.6: Normalization factors of the contributions to the ^{190}Pb decay.

Contribution	ID	Norm. factor
X-ray gated background	1	0.732
Pileup	2	8985

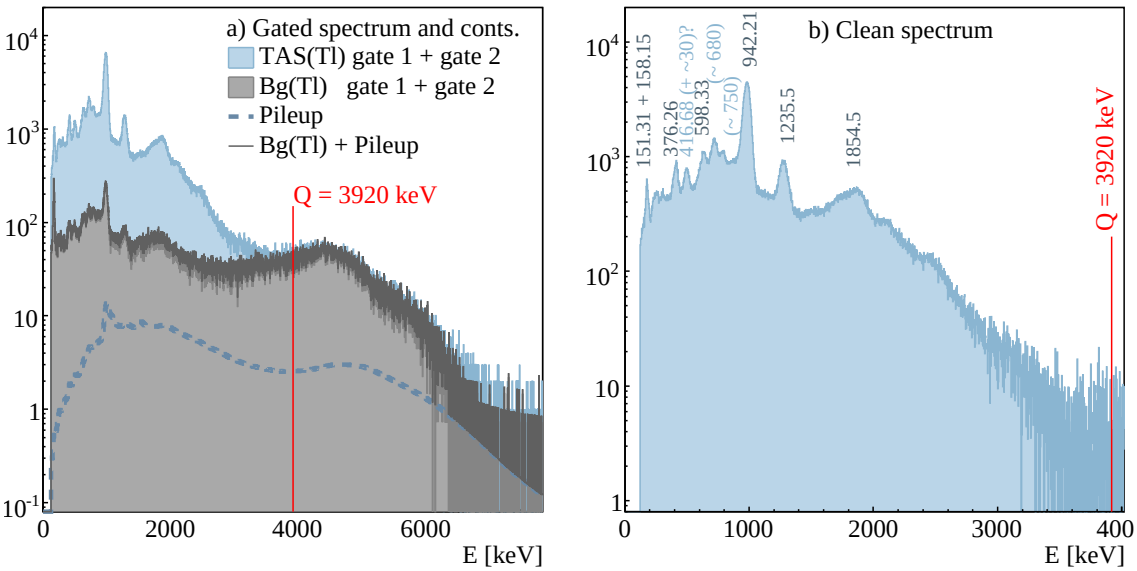

Figure 9.21: Same as Fig. 9.9 but for mass 190.

c) Algorithm application: After the thallium gate and its contributions (Table 9.6) were recalibrated and rebinned, an analysis was made from 120 keV to 5080 keV. Using the known level scheme of Fig. 9.17 without modifications, the results of Fig. 9.22 were obtained. In this Fig. it is seen that from the most intense level (942.21 keV) up to the Q_β value, the recalculated spectra fails to reproduce the measured spectra. This suggests that there are more levels in that energy region apart from the levels at 1235.5 and 1854.5 keV seen by the HR technique, so the start of the unknown part should be put at energies below 1800 keV. Then, below the most intense level, there are again two main peaks that are not reproduced, as in the case of mass 192. These peaks are at similar but lower energies than the two unexplained peaks appearing in the decay of ^{192}Pb. In mass 192 decay, they appeared at energies of $\sim$ 690 and 495 keV, while here they appear at energies of $\sim$ 680 and $\sim$ 450 keV. However, the rest of the low energy part of the spectrum is better reproduced than in the previous case, thanks to the fact that the level scheme is relatively better known.

In Table 9.7 the peaks appearing in the thallium x-ray gated TAS spectrum are presented. This spectrum, compared with the recalculated spectrum, and the feedings calculated from the analysis, are shown in Fig. 9.22.

Table 9.7: Same as Table 9.3 but for mass 190.

TAS(Tl)	Type	Comments	GeG(Tl)	GeX
151.31	Single	HR	151.31	151.31
158.15	Single	HR	158.15	158.15
210.55	Single, double	HR	210.55	210.55
274.17	Single, double	HR	122.25, 274.17	122.25, 274.17
372.75	Double, triple	HR	162.2	162.2
376.26	Single - triple	HR	101.8, 376.35	101.8, 376.35
416.68	Double, triple	HR	142.2	142.2, 265.7
495.07	Double - Qple	HR	-	118.8
539.81	Double	HR	381.66	381.66
598.33	Single	HR	598.33	598.33
$\sim$ 680	?	Not seen	193.16[a]? 343.0[b]? 676.8?	193.16[a]?
738.99	Double - Qple	HR	140.6, 362.74	140.6, 362.74
890.72	Double	HR	739.41	Out of range
942.21	Single - Qple	HR	566.0, 790.9, 942.21	566.0
1235.5	Single	HR	1235.5	Out of range
1854.5	Single	HR	1854.5	Out of range

[a] This gamma was reported in [Sin03] but not placed in the level scheme.
[b] This gamma was not reported in [Sin03], but was reported in [Bag98] as a contamination, and appears in the GeG(Tl) spectrum with similar intensity as in the GeG(Tl) spectrum of mass 192, however, it does not appear in the GeX spectrum.

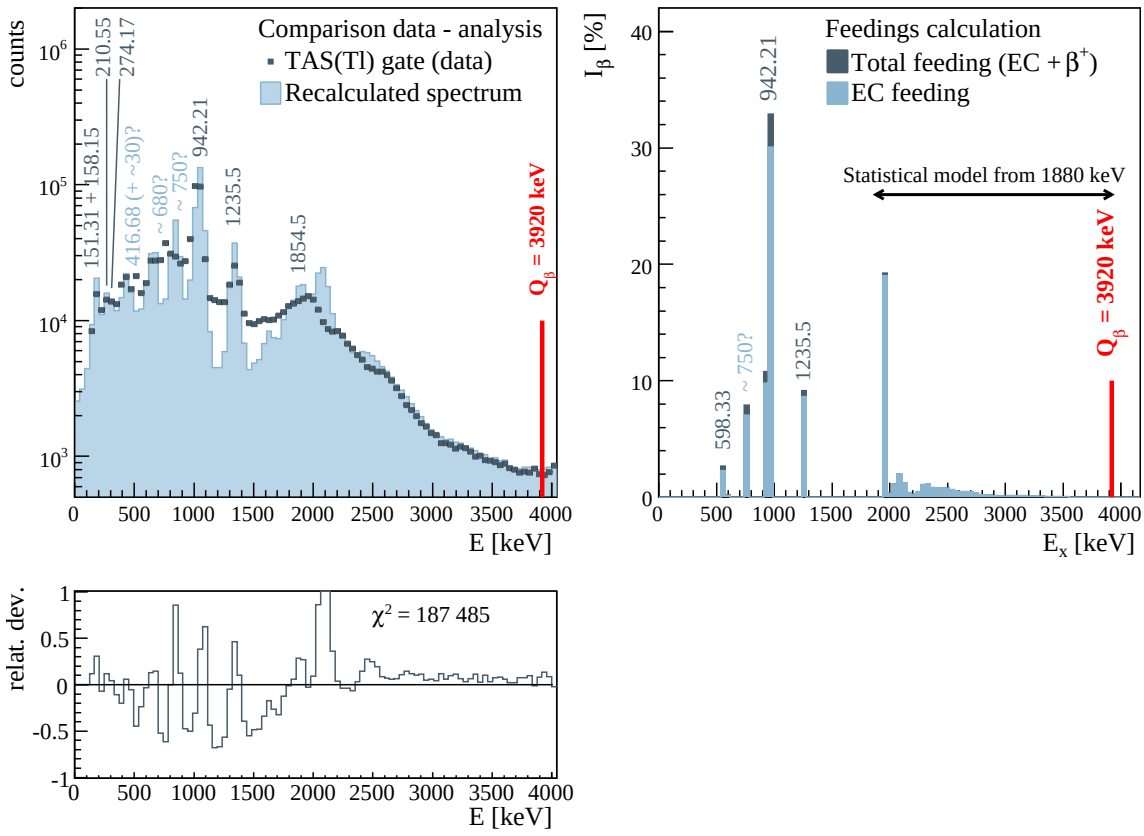

Figure 9.22: Results of the analysis when using the known level scheme of Fig. 9.17. Same description as in Fig. 9.10 applies.

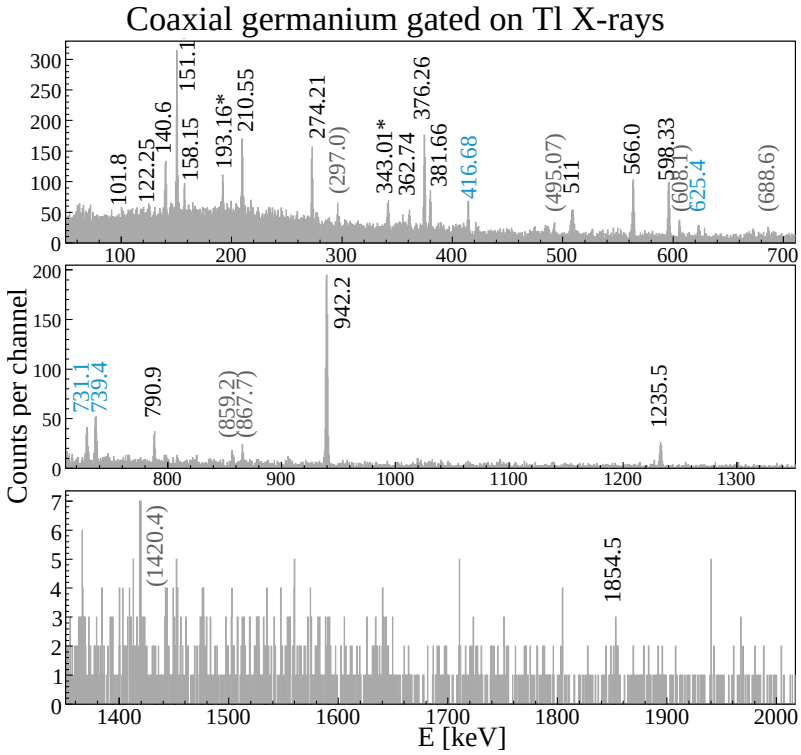

Figure 9.23: Same as Fig. 9.11 for mass 190. The labels in blue are for gammas emitted in the decay of ^{190}Tl into ^{190}Hg.

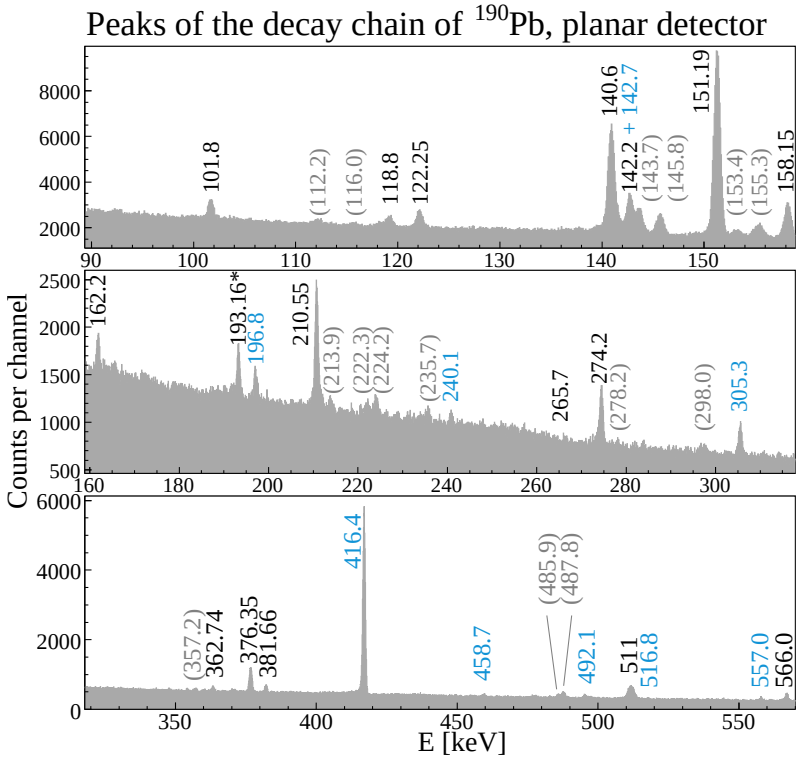

Figure 9.24: GeX detector, the same description of Fig. 9.12 applies.

Some comments must be made regarding Fig. 9.22 (and with the help of Figs. 9.23 and 9.24):

- The single levels at 151.31 and 158.15 are clearly seen in the TAS spectra although not resolved (first peak).

- The levels at 210.55 and 274.17 can be single or double. In the double case, the level at 210.55 keV decays by a two-gammas' cascade of 59.4 and 151.19 keV (Fig. 9.17). The gamma at 59.4 was reported by [Sin03] but its placement is uncertain. In our measurements this gamma is not seen neither in the planar nor in the coaxial germanium detectors. The level at 274.17 decays in the double case by a gamma of 122,25 keV that also goes to the level at 151.19 and has a very low intensity compared to the single case (Figs. 9.17, 9.23).

- Around 370 keV there is a peak in the TAS spectrum. This peak is mainly attributed to the level at 376.26 keV. If the level at 372 keV can only be double or triple (meaning that it will appear displaced around 30 or 60 keV respectively in the TAS spectrum), it will be in the right tail of the 376.26 peak. As it decays to the level at 210.55 keV by a gamma of 162.2 keV that has very low intensity (Fig. 9.23), this level is hardly noticed in the spectra. On the contrary, the level at 376.26 decays mainly by a single gamma whose intensity is relatively high. In the double and triple cases it decays to the level at 274.17 by a gamma of 101.8 keV whose intensity is low. Taking the above into account, the peak at 370 should be interpreted as mainly due to the intense direct gamma transition to the ground state of the level at 376.26 keV (and the escape peak of cascades that include that gamma), whose right tail could be formed by the contributions of the double and triple cascades of the same level and the level at 372.75 keV.

- The level at 416.68 can be double or triple, so it could explain the peak seen around 453 (416.68 + ∼30 = ∼446.68 keV). This level de-excites to the level at 151.31 by a gamma of 265.7 keV or to the level at 274.17 keV by a gamma of 142.2 keV. According to [Sin03], the intensity of the gamma of 142.2 keV is larger than the intensity of the gamma of 265.7 keV. In addition, the intensities of this gamma and the gamma of 140.6 (de-exciting the level at 738.99 keV) are given together since their measurement is not able to resolve the two peaks. Looking at Fig. 2 of [Sin03] it looks like the gamma at 142.2 keV has a higher intensity. However, looking at Fig. 9.23, our measurements show the opposite: the gamma at 140.6 keV seems to be more intense than the gamma at 142.2 keV. In Fig. 9.24, that shows all the gamma activity of the decay, the peak at 142.2 keV appears more clearly, but its intensity is again lower than for 140.6. In addition, with the information provided by the HR technique, the analysis is not able to reproduce this peak. We can not find an explanation for this, nor an additional gamma or combination of gammas that may allow us to put a level at that energy.

- The next level at 495.07 keV can be double, triple or quadruple according to HR. It de-excites to the level at 376.26 by a gamma of 118.8 keV or to the level at 416.68 by a gamma of 78.6. None of these γ rays could be seen in the GeG(Tl) spectrum. However, the 118.8 keV gamma appears in the non-gated GeX spectrum (see Table 9.7), with a low intensity, as reported in [Sin03]. The gamma of 78.6 keV is not placed in the level scheme provided by [Sin03], or its placement is uncertain. In our measurements it is not seen in any of the germanium detectors. Finally, the feeding to this level is less than 22 % according to [Sin03]. This reference gives similar values for other levels in the level scheme (151.31, 210.55, etc). These upper limit values are too high to add up to a total of 100 % when the feedings of all the levels are added, so if these values could be better determined it is possible that their values are lower. In this case the feeding of the level at 495.07 could be lower. Since this level can decay in three different ways, our conclusion is that it contributes to the left tail of the next peak, (the one corresponding to the level at 598.33 keV, which is a single peak). However, the gamma of 495 keV seen in Fig. 9.23 may suggest a direct transition from this level to the ground state in addition to the mentioned transitions that de-excite the level. The same happens to the level at 539.81 which is a double peak with low feeding that will also be at the left tail of the peak at 598.33 keV.

- An analogous peak to that seen in the measured TAS spectra of mass 192 appears here around 678 keV. Also, an analogous gamma appears in the GeG gated on thallium x rays at an energy of 676.8 keV, although the intensity of this gamma is not enough to explain the intensity of the TAS peak. γ rays appear at 487.8 and 495.07 keV in the GeG detector that may suggest a de-excitation to the levels at 158.15 and 151.31 keV respectively, creating a possible double level around 646 keV. However the intensities of these gammas are low and no coincidences with the gammas of 151.31 and 158.15 have been reported by [Sin03]. Another possibility could be a de-excitation to the level at 416.68 keV by means of a γ ray of 193.16 keV that was reported but not placed in the level scheme in [Sin03], creating a level (appearing as a triple peak in the TAS spectrum) that could lie around 610 keV. However, although the intensity of this gamma could be enough to explain the intensity of the TAS peak, no coincidence with the cascade of the 416 level was observed in [Sin03]. Yet another gamma of 343.0 keV not observed in [Sin03] but appearing in our GeG(Tl) could de-excite a triple level that would lie around 620 keV to the level at 274.17 keV. These possible de-excitation schemes were studied and are shown in Fig. 9.25.

- With respect to the level at 738.99 keV, it can be a double, triple or quadruple peak. This fact and the intensities of the gammas of 140.6 and 362.74 keV that de-excite the level as well as the beta intensity that feds the level are compatible with the peak that appears around 750 keV in the measured TAS spectra. The level at 890.72 keV is a double level with relatively low beta

feeding, so it contributes to the left tail of the peak of the level at 942.1 keV.

- The case of the 943.21 keV level is clear, as it is the most populated level. It is dominated by the single de-excitation although it can also be a double, triple or quadruple peak depending on the cascades that de-excite it.
- The levels at 1235.5 and 1854.5 keV are reported as single by [Sin03]. However, although there is a clear peak at 1235.5 keV, the comparison with the recalculated spectrum shows that maybe there are more levels with low beta feeding around that peak. The same applies for the level at 1854.5, which appears in reality as a bump. In this region we enter the high level density "regime" so more levels can exist that have not been reported by the HR technique.

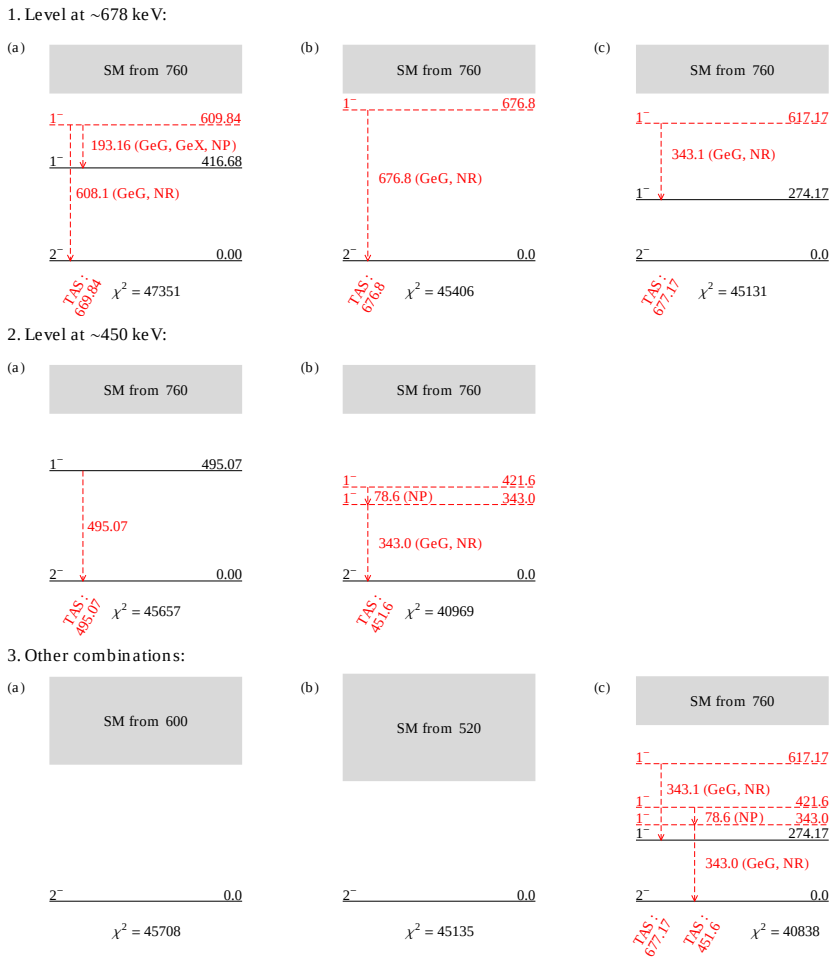

Figure 9.25: Same as Fig. 9.13 for mass 190. Known levels taken from [Sin03].

Summarizing, the TAS spectrum for mass 190 is understood in general, however the unknown peaks were not totally reproduced by any of the analysis tried. The analysis results are quite stable when adding the levels and gammas of Fig. 9.25

and when changing the Q value, the normalization factors, and the possibilities of spin change, apart from other tests, giving a resulting recalculated spectra that was very similar in all the cases. As in the case of mass 192, an analysis was made in which the whole Q_β value window was treated as the unknown part, to be used as a reference of the best results the analysis can give.

From all the tests, the results of the analysis with the level scheme of Fig. 9.17 and the unknown part taken from 520 keV were selected as the reliable results (χ^2 = 45135). On one hand, choosing the start of the unknown part at a lower energy could create results for the feedings that are less realistic because the analysis could create nonexistent levels at low energy (for example, when it tries to reproduce a peak that is an escape but not a level so it should not receive direct feeding). On the other hand, choosing a higher energy will also be unrealistic since the HR technique is not able to see all the levels over certain energy (which can be relevant for odd-odd daughter nuclei) and the analysis using the HR information at these energies could result in a recalculated spectrum with "holes" as in Fig. 9.26 a). No realistic combination of gammas was found to reproduce the two unexplained peaks, and the possibilities of Fig. 9.25 include gammas that are not seen in our data (although reported by [Sin03]). In Fig. 9.26, the chosen analysis is shown in comparison with the first analysis (using all HR information) and the reference analysis. In Fig. 9.27, the results of the chosen analysis are shown.

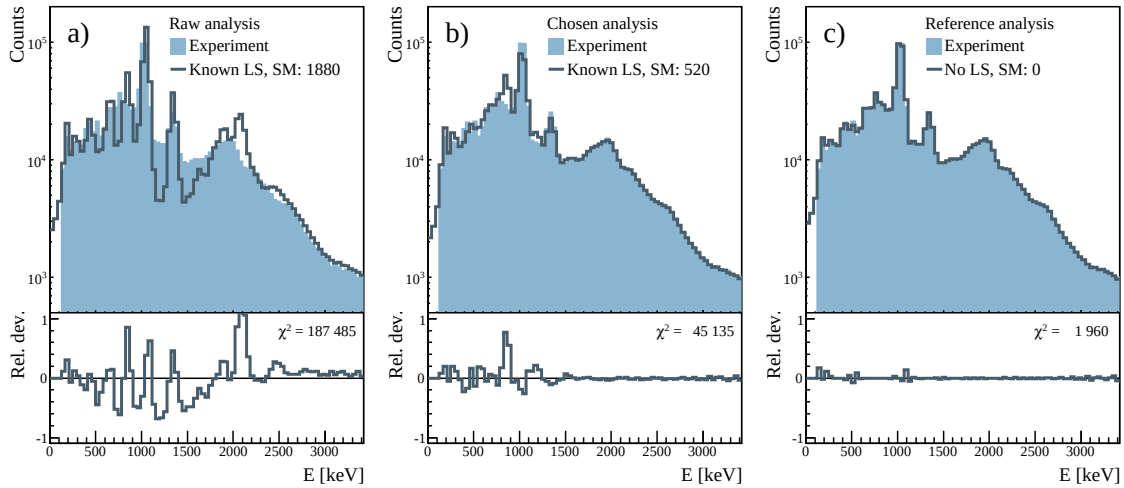

Figure 9.26: Comparison between: b) the analysis chosen from all the tests and: a) the raw analysis c) the reference analysis.

d) Strength calculation: Using the feedings file calculated in the previous step of the analysis, the GT strength was calculated from 0 to 3660 keV using the $t_{1/2}$ and Q_β value of Table 7.2. The results are presented in Table 9.8 in comparison with the HR data. In Fig. 9.27, the results are plotted. The B(GT) for the HR levels whose $I_{\beta+}$ is given as an upper limit was calculated by subtracting the sum

of the I_{β^+} with a fixed value to the total I_{β^+} and dividing the result by the number of levels with an unfixed value of I_{β^+}. Also, the accumulated strength or $\Sigma B(\mathrm{GT})$ was calculated at each energy by adding the strength observed up to that energy. It is compared with the accumulated strength of the reference analysis in Fig. 9.28.

Table 9.8: Same as Table 9.4. The HR data were taken from [Sin03] and the Q value from [Aud03].

E_{lev}	J^π	I_{EC} [%]		$I_{EC+\beta^+}$ [%]		$B(\mathrm{GT})$ [$g_A^2/4\pi$]	
[keV]		TAS	HR	TAS	HR	TAS	HR
[a]151.31	$(1)^-$	~ 0	< 17	~ 0	< 21	~ 0	0.012(*4*)
[a]158.15	$(0,1)^-$		2.1(*12*)		2.6(*15*)		
210.55	$(1)^-$	~ 0	< 19	~ 0	< 21	~ 0	0.008(*2*)
274.17	$(1,2)^-$	~ 0	?	~ 0	?	~ 0	?
[a]372.75	$(0^-, 1^-)$	~ 0	1.3(*5*)	~ 0	1.6(*6*)	~ 0	0.007(*2*)
[a]376.26	$(1)^-$		4.6(*16*)		5.4(*19*)		
416.68	-	~ 0	< 19	~ 0	< 22	~ 0	0.009(*3*)
495.07	(1^-)	~ 0	< 19	~ 0	< 22	~ 0	0.010(*3*)
539.81	(0,1)	0.7(*4*)	1.7(*4*)	0.8(*5*)	2.0(*4*)	0.0011(*8*)	0.0023(*6*)
598.33	(1^-)	4.0(*3*)	< 9.7	4.6(*5*)	< 11	0.007(*1*)	0.010(*3*)
738.99	$(0^-, 1)$	~ 0	< 9.9	~ 0	< 11	~ 0	0.011(*3*)
890.72	$(0^-, 1)$	25.5(*8*)	3.8(*6*)	28(*1*)	4.1(*6*)	0.051(*7*)	0.007(*1*)
942.21	1^+	15.2(*2*)	38(*5*)	16.4(*5*)	41(*5*)	0.031(*4*)	0.07(*1*)
1235.5	1	7.6(*3*)	4.3(*6*)	8.0(*5*)	1.6(*6*)	0.019(*3*)	0.009(*2*)
1854.5	1	2.08(*9*)	0.7(*2*)	2.1(*1*)	0.7(*2*)	0.010(*2*)	0.0028(*9*)
TOTAL		94(*2*)	$\sim$ 99.6(*4*)	100(*2*)	$\sim$ 100.0(*4*)	0.42(*7*)	0.16(*1*)

[a] These levels are not resolved by the TAS.

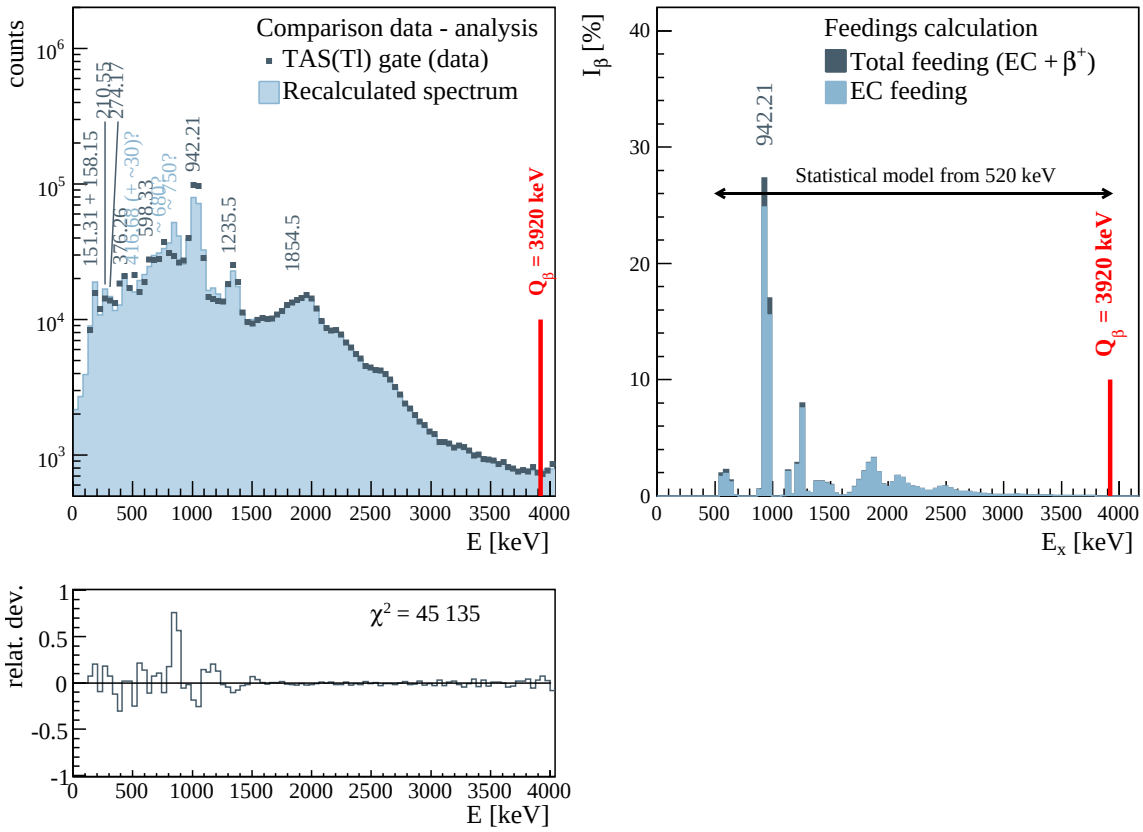

Figure 9.27: Same as 9.15 for mass 190.

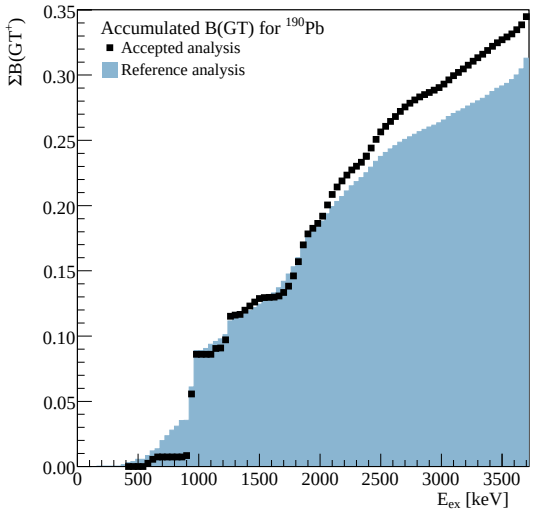

Figure 9.28: Comparison of the accumulated strength $\Sigma B(\mathrm{GT})$ for the selected analysis (Fig. 9.26-b)) and the reference analysis (Fig. 9.26-c)).

9.3. Mass A = 188

In this section, the analysis of the beta decay of ^{188}Pb is presented. To this end, the steps of Appendix A are followed.

1. **Average branching ratios calculation:**

a) Known Levels: The case of mass 188 is hard to analyze, as the HR measurements report only two levels linked to two single transitions to the ground state (Fig. 9.29). According to [Sin02] "Their total intensities per 100 (EC + β^+) decays, indicated in the figure, were determined by assuming no other γ-transitions proceeding to the ground state and a direct (EC + β^+) feeding of $< 1\%$ to the ground state (based on a logft value of > 8.5 for a unique first-forbidden transition)". As can be expected, the results of the analysis using this level scheme do not reproduce the measured spectrum, and looking at the TAS spectra, more levels seem to exist between the two reported levels. The relatively large Q_β value (see Table 7.2) and the odd-odd character of this nucleus supports the existence of more levels. In addition, the high apparent feeding associated to the lower level by the HR technique is in contradiction with the systematics of the levels populated in beta decay of neutron deficient lead isotopes (Fig. 9.40). This is a case were the TAS technique can be useful to back the idea of the existence of more levels and give better values for the feedings.

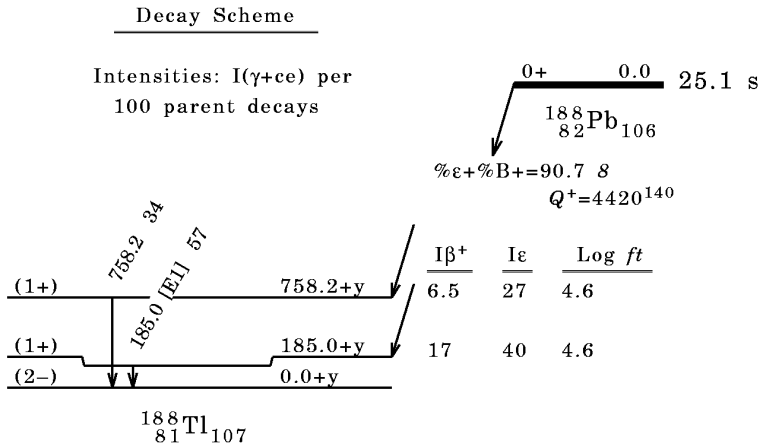

Figure 9.29: Same as Fig. 9.1 for mass 188. The theoretical calculations of [Gor01] and [Dem01] for example, predict ~ 60 levels up to an energy of 1 MeV with spins up to $J = 17$ ($n_{J=0} = 3.17$, $n_{J=1} = 2.73$, $n_{J=2} = 9.95$, $n_{J=3} = 8.9$, $n_{J=4} = 14.9$, etc.), and our measurements suggest that there could be more levels in that region, so this level scheme can be considered incomplete. The Q_β value of Table 7.2 was used for the analysis instead of the one in the Fig. Taken from [Sin02].

b) Level Density Parameters: According to [Gor01] and [Dem01], there are 13 levels in ^{188}Tl up to an excitation of 500 keV, and 150000 up to 4500 keV. With these values, the level density parameters are a = 19.573 MeV^{-1} and Δ = -0.51 MeV.

c) Gamma Strength Function Parameters: For this case the value of β_2 = -0.061 was used again for the quadrupole deformation [Mol95]. The neutron separation energy is 8.304 MeV according to [Sin02]. With these values the parameters of Table 9.9 are found.

Table 9.9: Same as Table 9.1 for mass 188 (using β_2 = -0.061, S_n = 8304 keV).

Type	E [MeV]	w [MeV]	Γ [mb]
E1	14.642	4.378	482.680
	13.768	3.892	542.929
M1	7.169	4.0	3.448
E2	11.017	3.854	5.419

d) Average branching ratios calculation: As there seems to be missing levels in the known spectra, several tests were made based on reasonable assumptions for the levels that could be populated in beta decay between 184.6 and 758.2 keV. One example is to take the beginning of the unknown part from 760 keV, since the last level is at an energy of 758.2 keV, and up to 4560 keV. With the above parameters, a branching ratio matrix was generated for every analyzed case.

2. **Response simulation:**

The response matrix was calculated in the same way as in the previous masses. As mentioned in Sec. 9.2, the same gamma response simulation was used for all the masses of this part of the work (details in Sec. 9.1). This gamma response was convoluted with the average branching ratios matrix obtained in the previous step of the analysis to obtain the final response matrix.

3. **Extracting the feedings:**

a) X-ray tagging: In the case of mass 188, the measuring time was 7 hours and 22 minutes approximately. After this time, the full x-ray spectrum accumulated 20 090 084 counts. In Fig. 9.30 this spectra is shown with the placement of the gates. Again, by comparison with Figs. 9.5 and 9.18, more peaks appear to the left, due to the decays to gold and to the other granddaughters, and conservative gates have to be chosen.

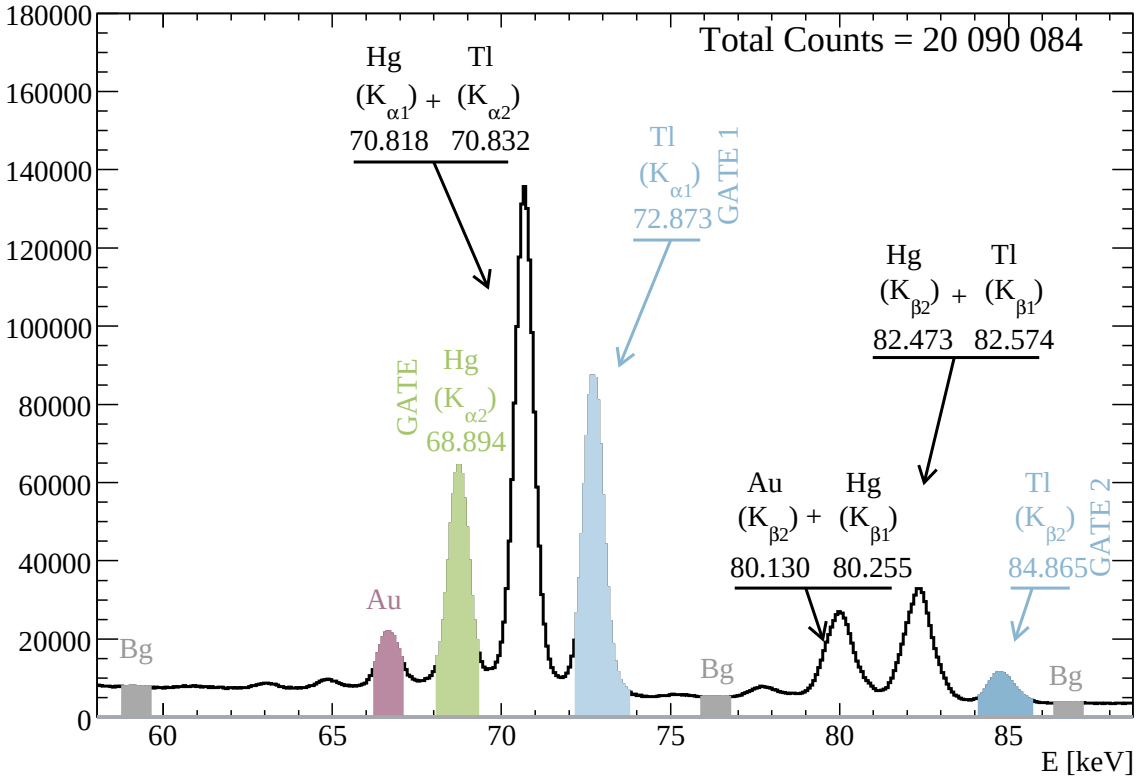

Figure 9.30: Same as Fig. 9.5 for mass 188. In this case, the x rays of gold and other isobars start to appear more clearly than in the previous cases.

However, the intensities of the x rays of the gold granddaughters are negligible. A gate for gold was generated in the case of this mass.

b) Contaminants, backgrounds, pileup: Fig. 9.31 shows the gated spectra produced with the gates of Fig. 9.30. In the gates of interest (Fig. 9.31 a) and b)), no contamination coming from Hg or Au was found or it is negligible. Also, the respective background gates show mainly the shape and structure of the thallium contribution, as in the previous lead masses studied.

This measurement was taken just after the production of the ^{24}Na beam for calibration purposes. Some ^{24}Na remained in the last collimator and due to this, the characteristic peaks of this source appear in the background spectra of the three detectors of the setup. However, the thallium x-ray gated spectra is clean and in the case of the planar germanium the energies of the ^{24}Na peaks are out of range, so the spectra that are relevant for the analysis are clean.

In this case the beta plus contamination present in the x-ray gated spectra could not be considered negligible a priori. [Sin02] reports an $I_{\beta^+} = 6.5(11)$ for the level at 758.2 keV and $I_{\beta^+} = 17(2)$ for the level at 184.6 keV. However, the β^+ contamination could be smaller if there are more levels that receive feeding and it

depends on the internal conversion coefficient of the transitions (seen and not seen previously). A rough estimation as in the other masses gives an upper limit for the β^+ contamination of ~ 3.4 %.

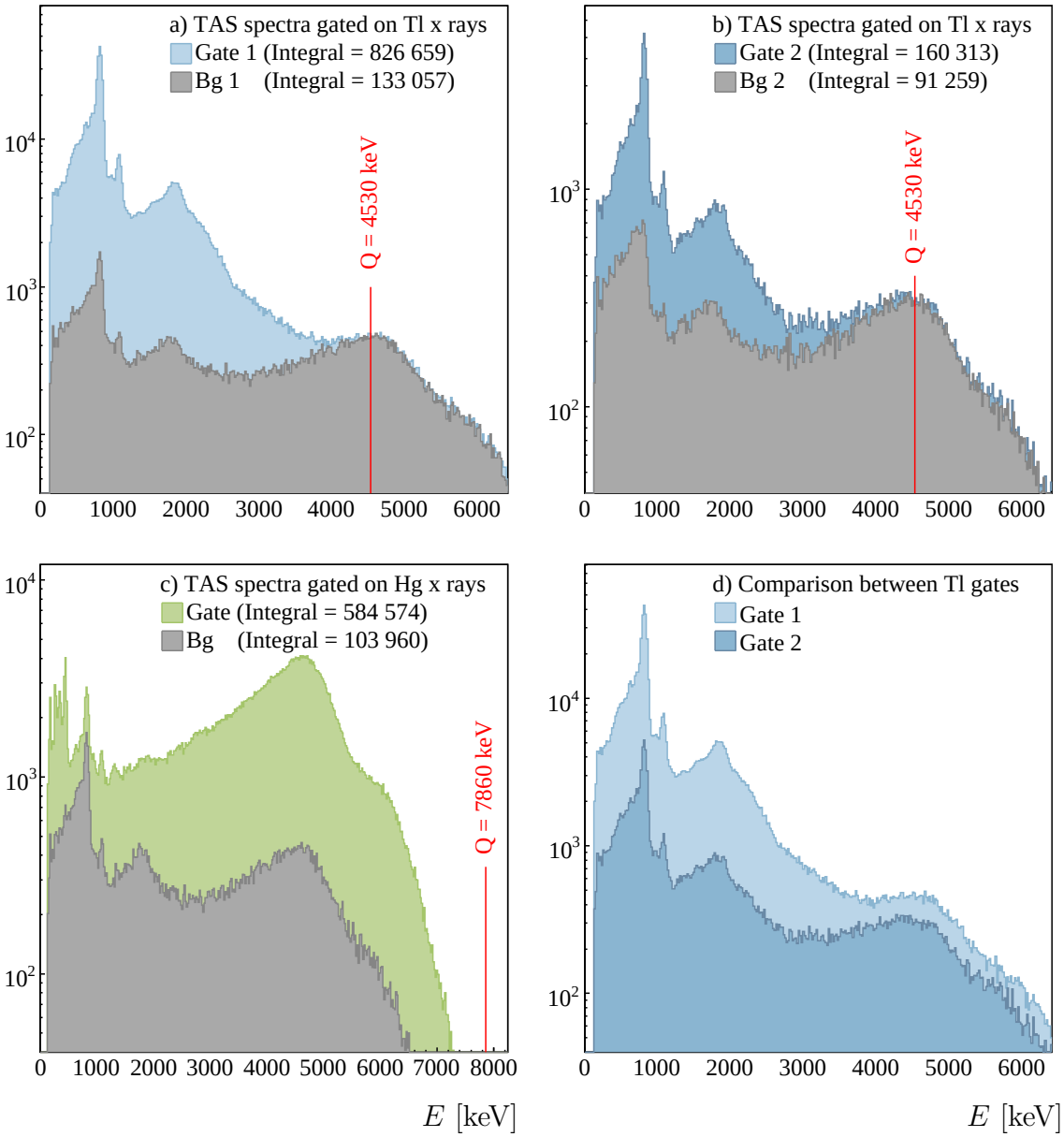

Figure 9.31: X-ray gated TAS spectra of the isobars produced in the EC decay chain of ^{188}Pb: a) K_α thallium gate b) K_β thallium gate. c) Mercury gate d) Comparison between K_α and K_β thallium gates. The gold gate is not shown here because of the low statistics.

The normalization factors for the contributions to the decay spectrum are presented in Table 9.10. These contributions are presented in Fig. 9.32 together with the thallium gate, made by adding the two thallium gates of Fig 9.31 a) and b). The background gate is also the sum of its two gates.

Table 9.10: Normalization factors of the contributions to the ^{188}Pb decay

Contribution	ID	Norm. factor
X-ray gated background	1	0.783
Pileup	2	7502

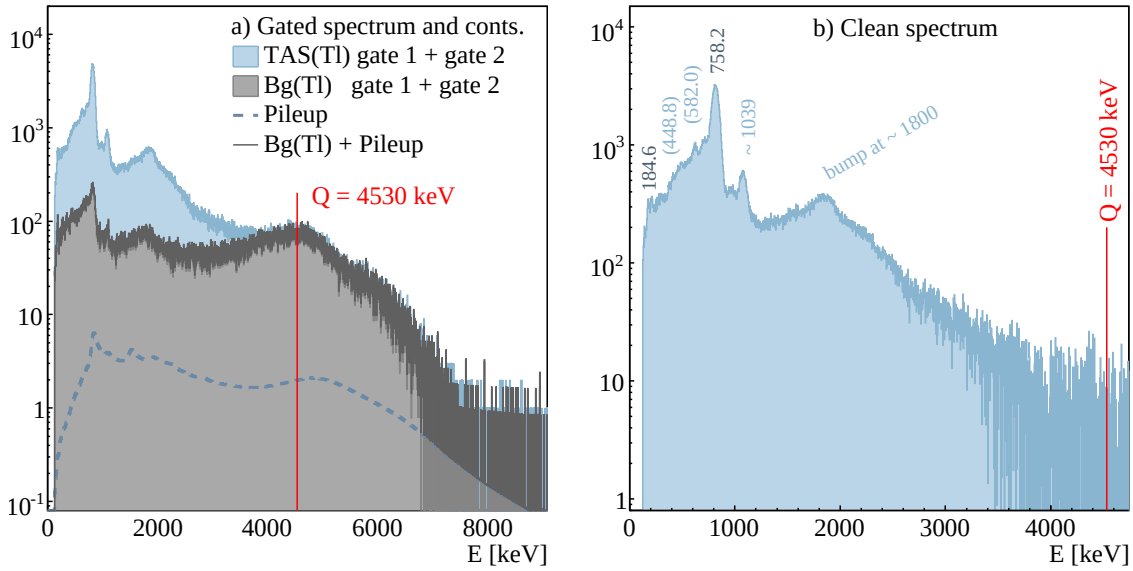

Figure 9.32: Same as Fig. 9.9 but for mass 188.

c) Algorithm application: The recalculated spectrum resulting from the raw analysis (that is, the analysis that uses all the known HR levels) does not reproduce the measured spectrum, as shown in Fig. 9.33, that suggests the existence of more levels that receive beta feeding between 184.6 and 758.2 keV, although the latter seems to be the level that receives most of the feeding, in analogy with the previous two masses, and in contradiction with literature. In [Sin02], the measurements at Oak Ridge were not able to see any levels between 184.6 and 758.2 keV, due to the poor efficiency of the separator ion source for lead plus the detector set-up used. In our measurement, more γ rays associated to this decay can be seen by looking at the coaxial germanium spectrum when it is in coincidence with the thallium x rays (Fig. 9.34). A future measurement of gamma-gamma coincidences could throw light on the thallium beta-populated missing levels and their associated transitions. In Fig. 9.35 the GeX spectra is shown with all the statistics for mass 188 (the x-rays zone is not shown). In Table 9.11 a summary of the information from Figs. 9.33 to 9.35 is shown.

A selection of the different analysis tests are presented in Fig. 9.36. The simpler supposition is to take all the levels seen in the TAS spectrum as single levels and try to find gammas in the gated germanium spectrum with similar energies. For

most of the peaks appearing in the TAS spectrum, a γ ray with similar energy was found (Table 9.11). The lower energy peak ($\sim$ 149 keV) appears in the gated TAS spectrum with very low intensity and so does its correspondent γ ray in the GeG(Tl) spectrum. The peak at $\sim$ 663 keV has also a low intensity in the TAS spectrum. Adding these levels to the known part of the level scheme gives better results, but there is still the possibility that some of these levels are also complex (double or triple, etc.) and also there can exist more levels, since there are still parts of the TAS spectrum that are not well reproduced (where the recalculated spectra has "holes").

Table 9.11: Same as Table 9.3 but for mass 188.

TAS(Tl)	Type	Comments	GeG(Tl)[a]	GeX[a]
$\sim$ 149	?	Not seen	148.4 ?	148.4 ?
184.6	Single	HR	184.6	184.6
$\sim$ 336	?	Not seen	338.8 ?	339.2 ?
$\sim$ 453	?	Not seen	448.9 ?	-
$\sim$ 583	?	Not seen	582.0 ?	582.0 ?
$\sim$ 663	?	Not seen	655.6 ?	Out of range
758.2	Single	HR	758.2	Out of range
$\sim$ 1039	?	Not seen	-	Out of range

[a] The gammas with "?" were not reported in [Sin02], but appear in the Ge spectra.

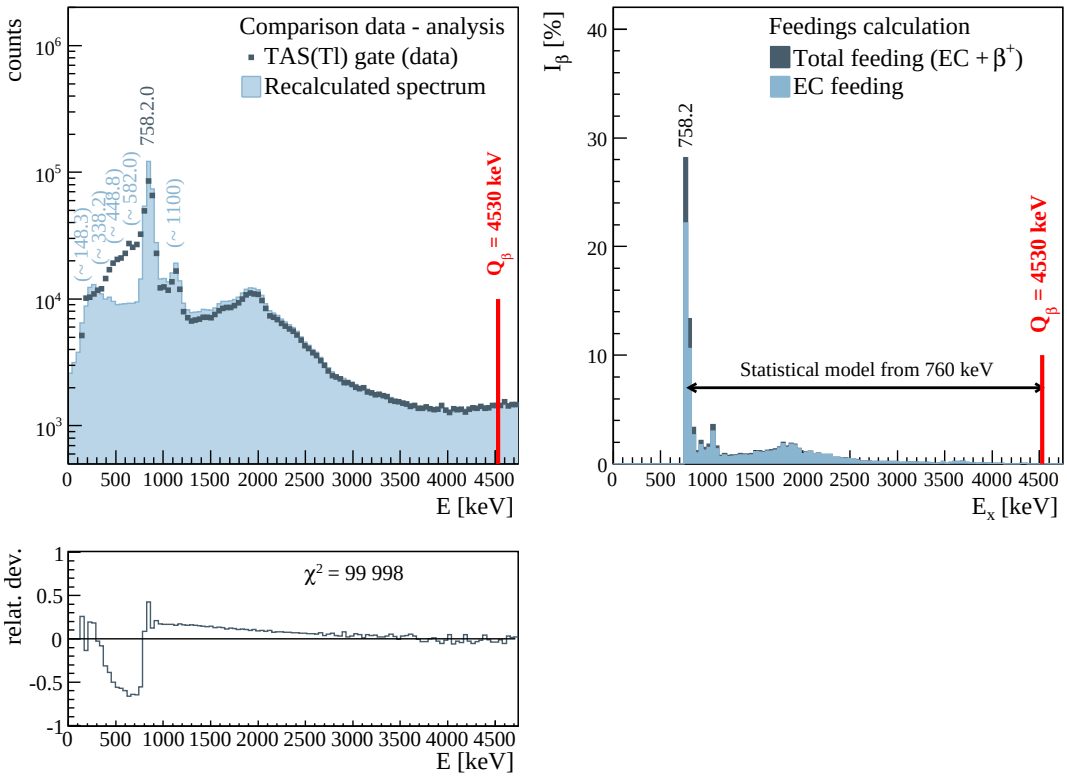

Figure 9.33: Same as Fig. 9.10 for mass 188.

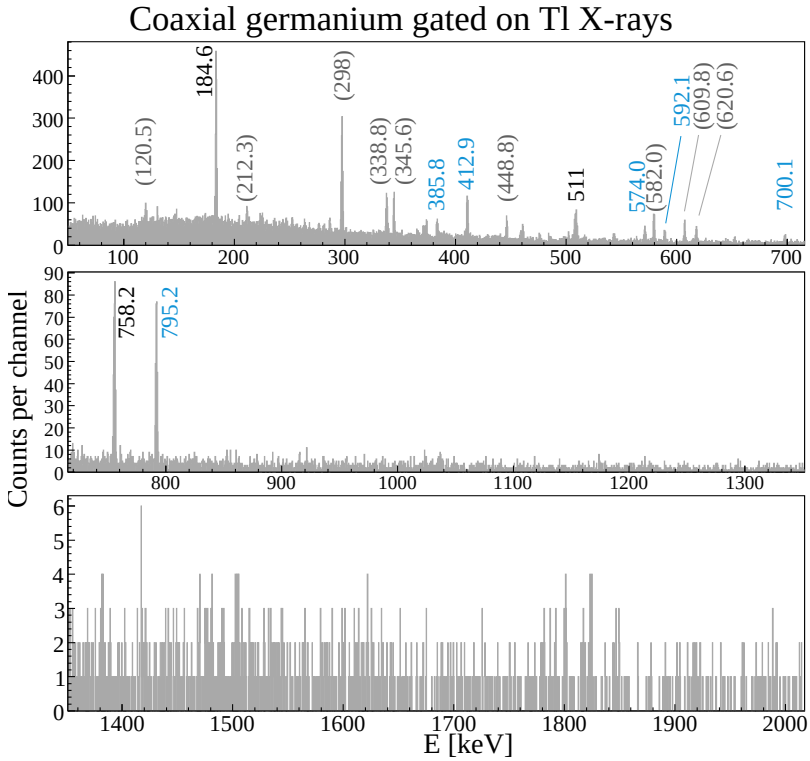

Figure 9.34: Same as Fig. 9.11 for mass 188.

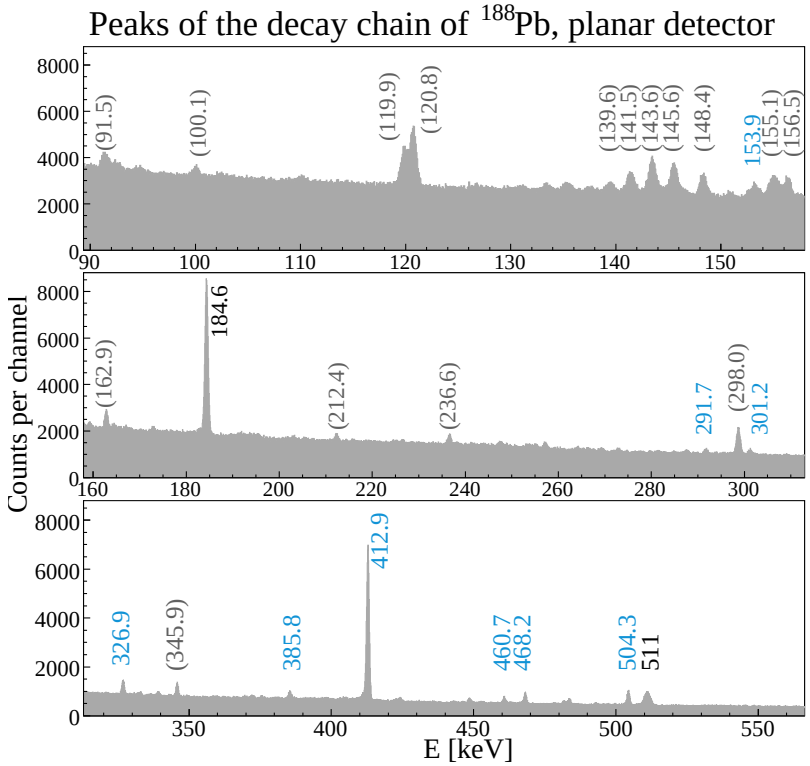

Figure 9.35: Same as Fig. 9.12 for mass 188.

No conclusions can be drawn from the available data until more information is provided from dedicated high-resolution measurements. For this reason, the analysis where the unknown part is taken from 200 keV up to the Q value was chosen as the working analysis. In Fig. 9.37, a comparison between the raw analysis, the analysis with the supposed levels that gives the best results, and the reference analysis (no known level scheme) is shown.

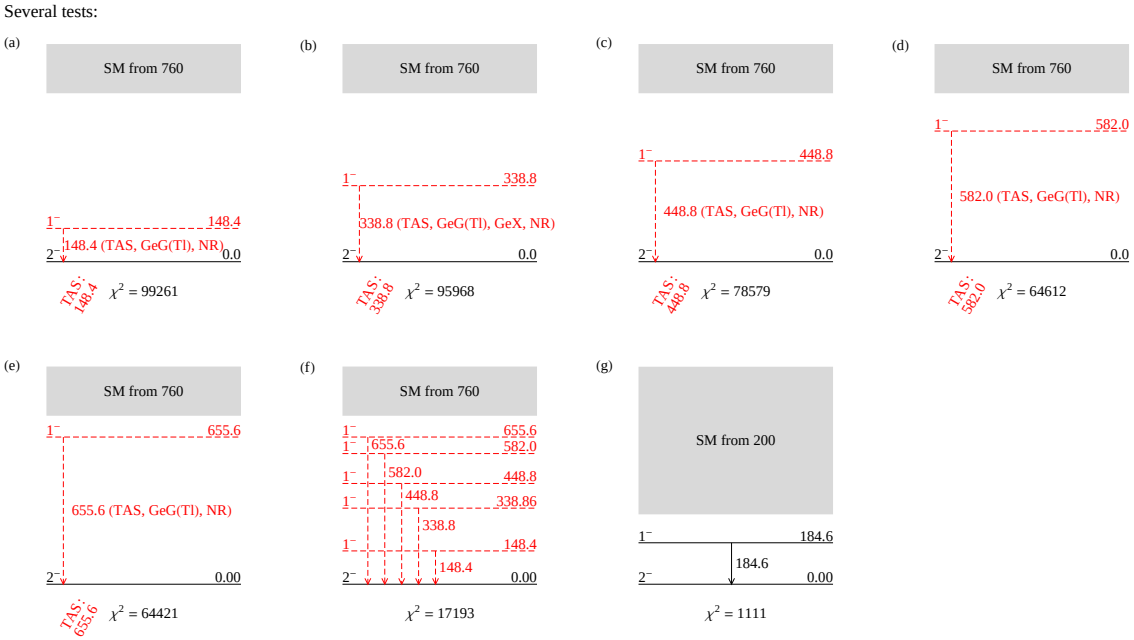

Figure 9.36: Same as Fig. 9.13 for mass 188.

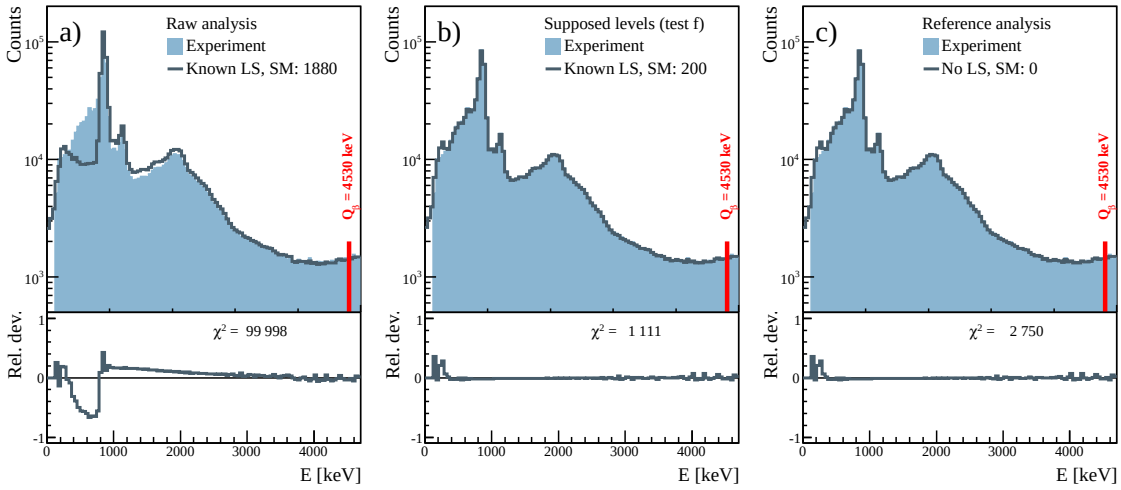

Figure 9.37: Comparison between: *a*) the raw analysis *b*) the analysis made with the levels of Fig. 9.36-g) *c*) the reference analysis.

d) Strength calculation: Using the feedings obtained from the analysis of the previous step and the Q value and half-life of Table 7.2, the strength was calculated from 0 to 4100 keV. The results of this calculation are summarized in Table 9.12 and in Fig. 9.38. The results are normalized to the β^+/EC component of the decay. In the next chapter, the discussion and conclusions of these results are presented. The differences between the values for the HR technique and the TAS technique are a clear example of why this nuclei should be revisited by the HR technique. Finally, the comparison of accumulated strengths is shown in Fig. 9.39.

Table 9.12: Same as Table 9.4 for mass 188. For absolute intensity per 100 decays, multiply by 0.907(*8*).

E_{lev}	J^π	I_{EC} [%]		$I_{EC+\beta^+}$ [%]		B(GT) [$g_A^2/4\pi$]	
[keV]		TAS	HR	TAS	HR	TAS	HR
184.6	(1^+)	~ 0	44(*5*)	~ 0	63(*6*)	~ 0	0.11(*1*)
758.2	(1^+)	14(*5*)	30(*3*)	17(*7*)	37(*4*)	0.04(*2*)	0.10(*1*)
TOTAL		83(*9*)	74(6)	100(*12*)	100(7)	0.52(*4*)	0.21(*1*)

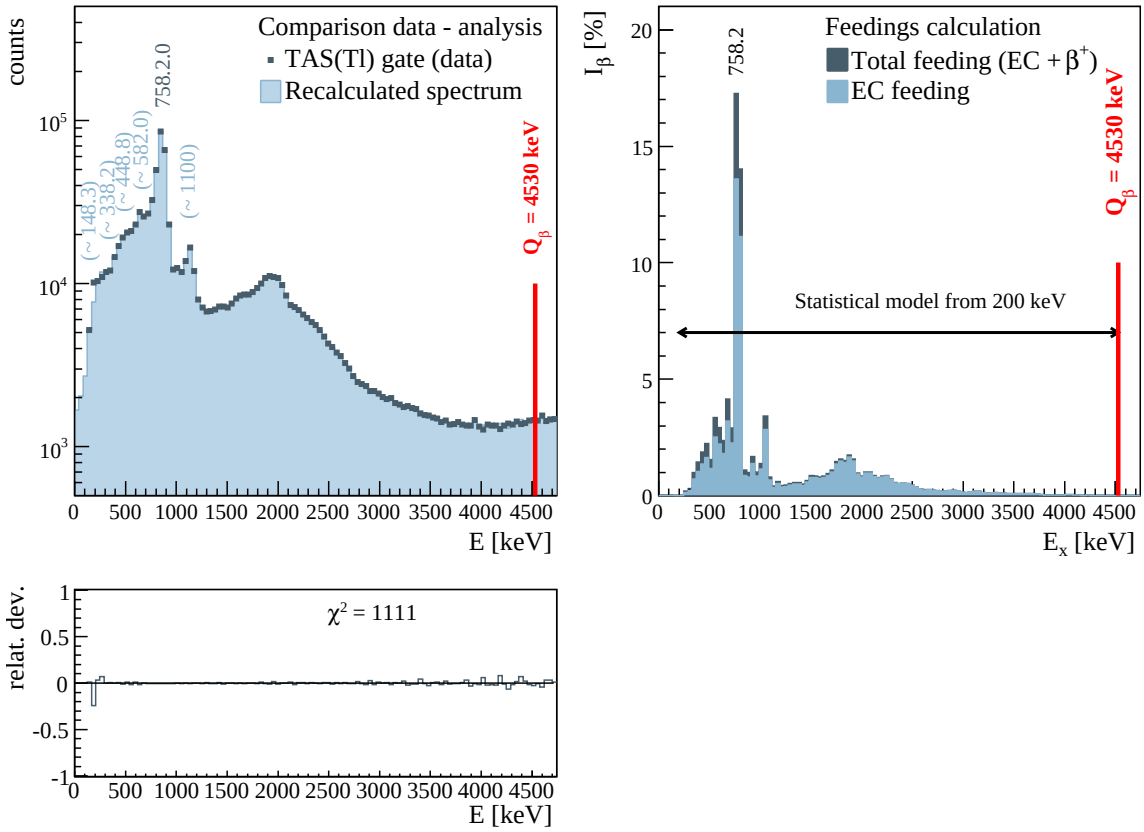

Figure 9.38: Same as Fig. 9.15 for mass 188.

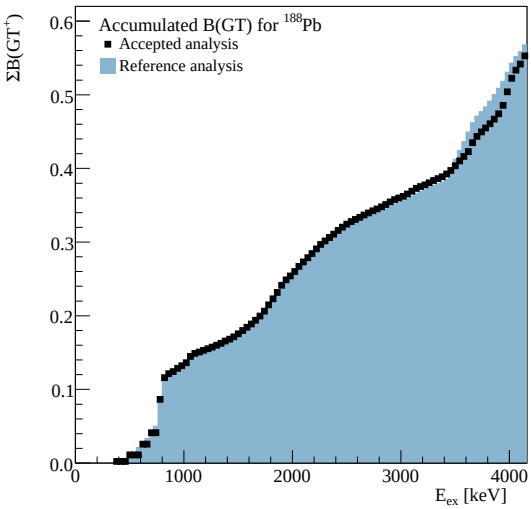

Figure 9.39: Comparison of the accumulated strength $\Sigma B(\mathrm{GT})$ for the selected analysis (Fig. 9.37-b)) and the reference analysis (Fig. 9.37-c)).

In Fig. 9.40 a systematic of the evolution of the levels for the studied nuclei is presented. Mass 186 was not analyzed because the statistics are very low and there is no HR data available for the beta decay of ^{186}Pb into ^{186}Tl. We measured approximately one hour of the decay of ^{186}Pb to see the feasibility of a future experiment.

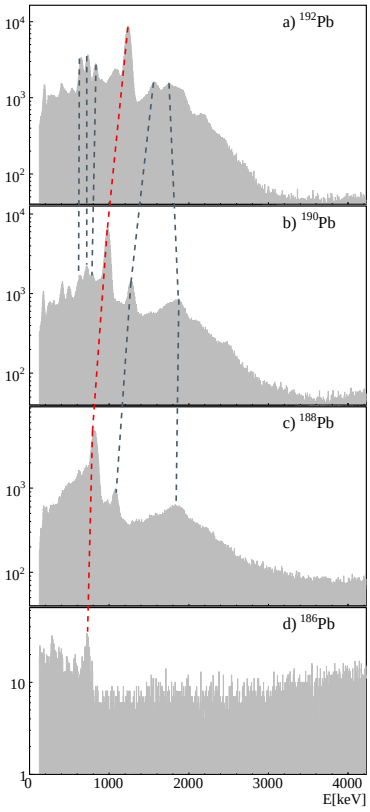

Figure 9.40: Systematics of the lead nuclei studied in this work. No background substracted.

10

Discussion and Conclusions

In this chapter, a discussion of the results of Part III of this work is presented. To this end, a comparison of the experimental strength distribution with the self consistent deformed HF-BCS-QRPA calculations introduced in the motivation (Chap. 7) and described in [Mor06] is presented. The theoretical results have been scaled for a better comparison with the data by a standard quenching factor $(g_A/g_V)_{eff} = 0.77(g_A/g_V)$, that is, a global factor of $0.77^2 \sim 0.6$.

First, the results of Table 9.4 are presented in Fig. 10.1. Our results show a possible overestimation of the feedings at low energy by the HR technique. This overestimation is due to all the HR-undetected feeding that was incorrectly assigned to the low energy levels reported in the literature. As mentioned in Sec. 9.1, the level scheme of ^{192}Tl populated in β-decay seems to be incomplete and should be revisited with the HR technique, not only due to this but also to make a better TAS analysis in the future. The same can be said for masses 190 and 188; in the case of mass 190, the level scheme is better known, however, still there is an overestimation of the feedings, as shown in Fig. 10.2 *a*), where the results of Table 9.8 are plotted. All the Pb decay cases suffered from the Pandemonium effect.

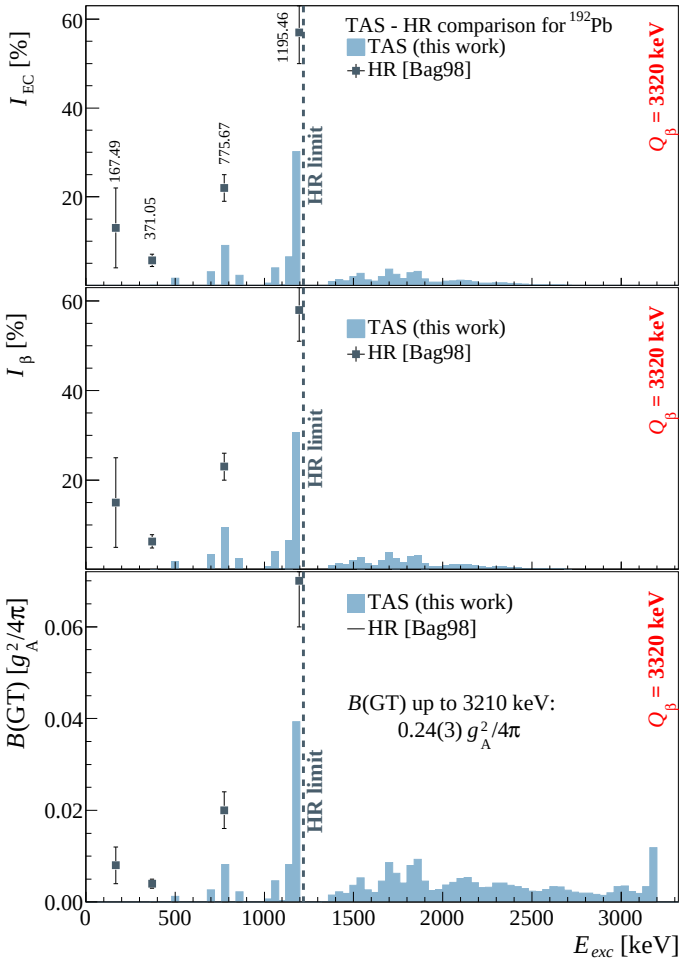

Figure 10.1: Comparison between TAS results and HR data for mass 192.
∗ Upper panel: EC component of the feedings.
∗ Middle panel: total β-feedings obtained from the EC component.
∗ Lower panel: Gamow-Teller strength obtained from I_β using Eq. 2.2.
The dashed line marks the last level seen by the HR measurements in β-decay. The continuous line shows the position of the Q_β value. The portion of the strength that is missed by the HR technique can be seen from the HR limit up to the Q_β value. The value of the total B(GT) obtained for the TAS is also given.

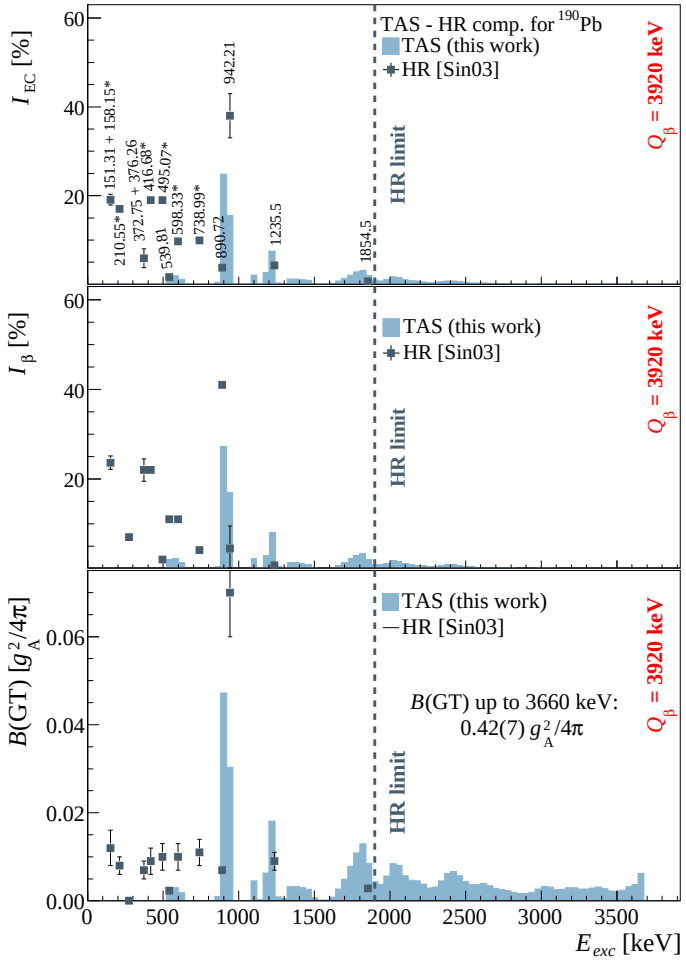

a) Same as Fig. 10.1 for ^{190}Pb.

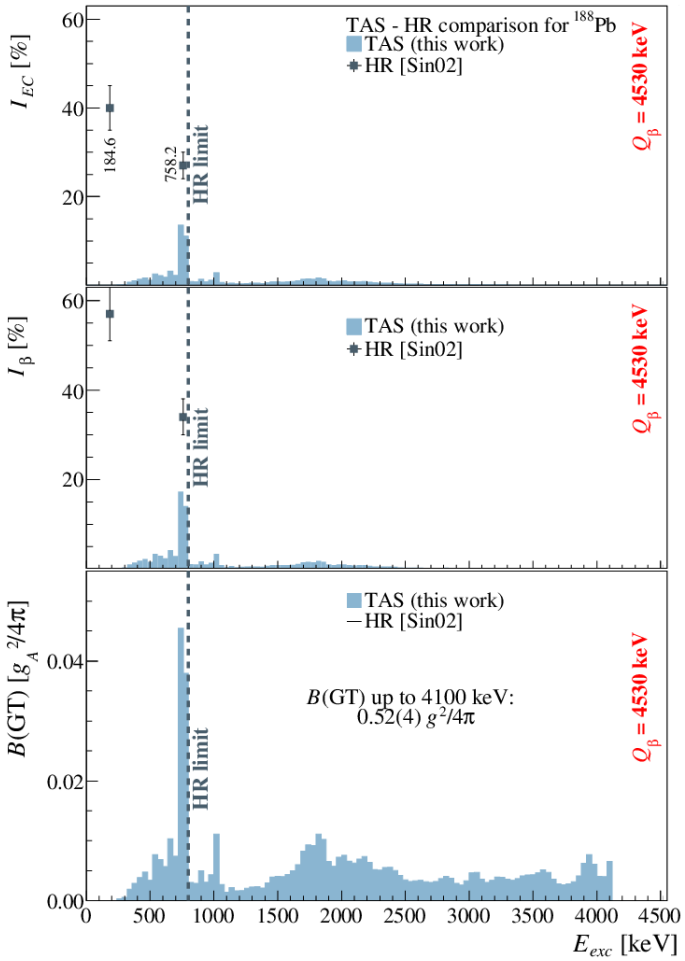

b) Same as Fig. 10.1 for ^{188}Pb.

Figure 10.2: Comparison between TAS results and HR data for ^{190}Pb and ^{188}Pb. In the case of mass 190, labels with asterisk indicate the upper limit given by [Sin03] to the assigned feeding. In the case of mass 188, the values for absolute intensity per 100 decays are a factor of 0.907 times lower.

In Fig. 10.3 a comparison between the theoretical calculations of Ref. [Mor06] and the data is presented for the ^{192}Pb decay case. A rebinning was made for a better comparison, with a bin size of 320 keV per channel.

In general terms, looking at Figs. 10.1 and 10.2, the experimental strength distributions of the three decays are dominated by a peak at low energy (around 1 MeV) surrounded by a smaller distribution, in the corresponding thallium daughter. The calculations produce fragmentation of the strength only in the deformed cases Fig. 10.3 does not show clearly that ^{192}Pb is spherical. The same happens for masses 190 and 188.

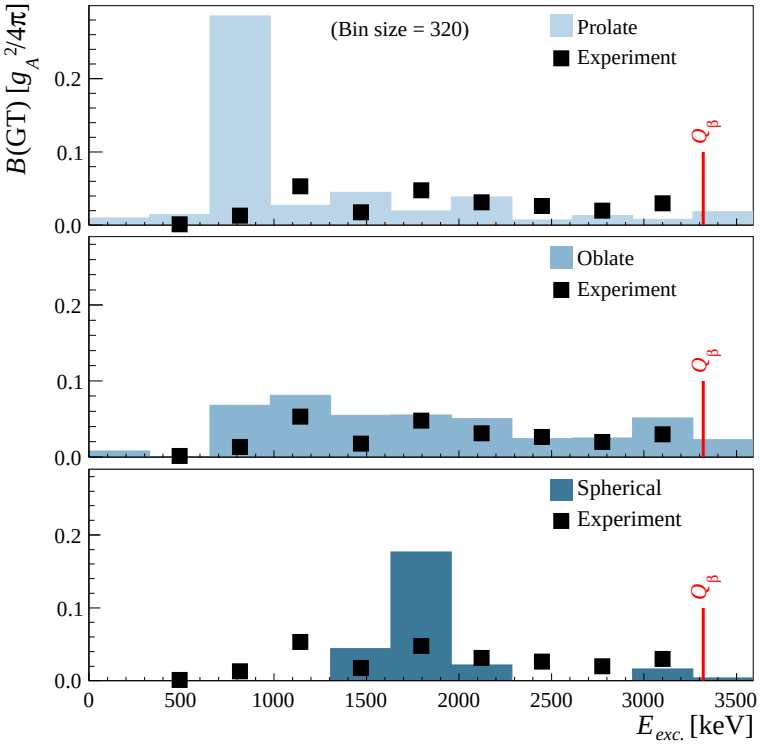

Figure 10.3: Comparison between TAS results and the calculations of Ref. [Mor06] for ^{192}Pb case. They are presented in the same scale and using a binning of 320 keV for a better comparison. The quenching factor used was 0.6.

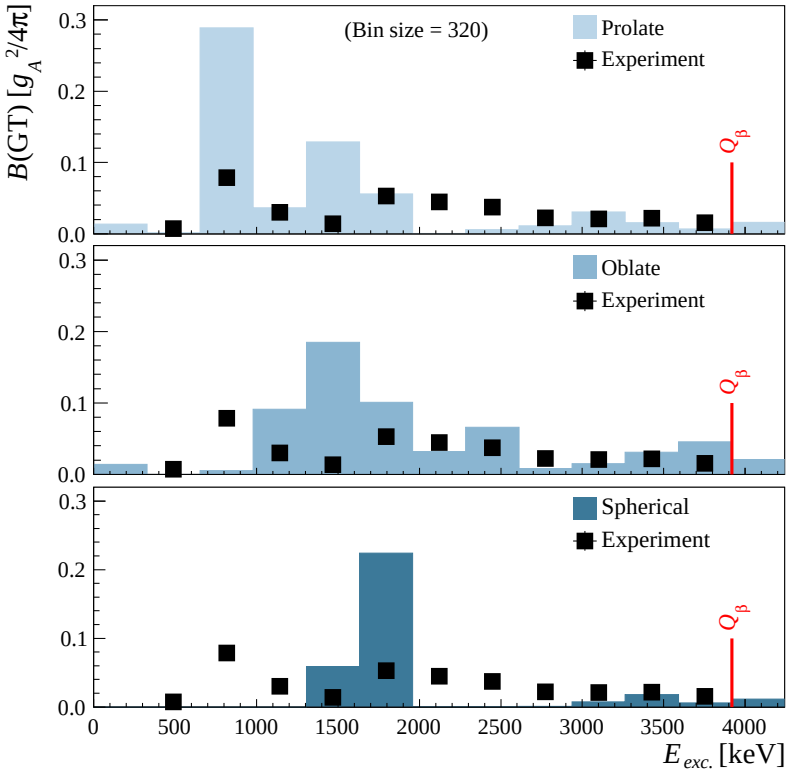

Figure 10.4: Same as Fig. 10.3 but for ^{190}Pb .

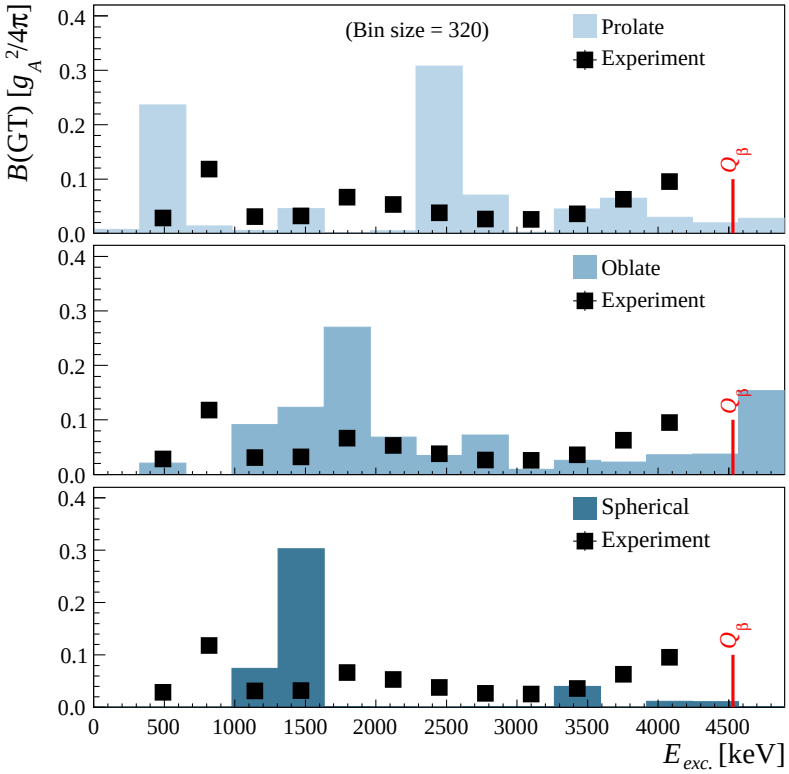

Figure 10.5: Same as Fig. 10.3 but for ^{188}Pb .

A comparison was also made between the theoretical accumulated strength and our results. The $\Sigma B(\mathrm{GT})$ at each energy was obtained by adding the strength observed up to that energy. The results are shown in Fig. 10.6 compared with theory, where a jump can be seen in the profiles every time there is a level that is strongly populated in the decay. In Table 10.1, the energy of the strongest populated level and its strength is presented, for both experiment and theory for the spherical case. A clear energy difference of approximately 0.7 MeV can be observed between theory and experiment. When going to more exotic lead (less neutrons) the measurements indicate that the level where most of the strength is concentrated moves to lower energies, as seen in the previous chapter in Fig. 9.40. The opposite happens with the total strength, it increases as we go to more exotic lead (see Table 10.2). This tendency is relatively well reproduced by the calculations.

Table 10.1: Energy and strength of the most strongly populated levels of the nuclei studied in this work. The experimental values of the energy levels are taken form the relevant Nuclear Data Sheets [Bag98, Sin03, Sin02] and the values of the strength are taken from the results of this work.

Nucleus	Energy (keV)		$B(\mathrm{GT})$ $(g_A^2/4\pi)$	
	Exp. (HR)	Theo.	Exp. (TAS)	Theo.*
^{192}Pb	1195.46(*18*)	1900	0.07(*1*)	0.20
^{190}Pb	942.21(*9*)	1600	0.031(*4*)	0.30
^{188}Pb	758.2(*5*)	1300–1500	0.04(*2*)	0.40

* Values are given for the spherical case.

Table 10.2: Comparison between the results of this work and the calculations of [Mor06] for the total Gamow-Teller strength lying inside the Q_{EC} window.

Nucleus	Total $B(\mathrm{GT})$ (g_A^2/g_V)			
	Exp.	Theory*		
		Spherical	Prolate	Oblate
^{192}Pb	0.24(*3*)	0.26	0.47	0.42
^{190}Pb	0.42(*7*)	0.32	0.59	0.59
^{188}Pb	0.52(*4*)	0.45	0.88	0.81

* Quenching factor: $h = 0.6$.

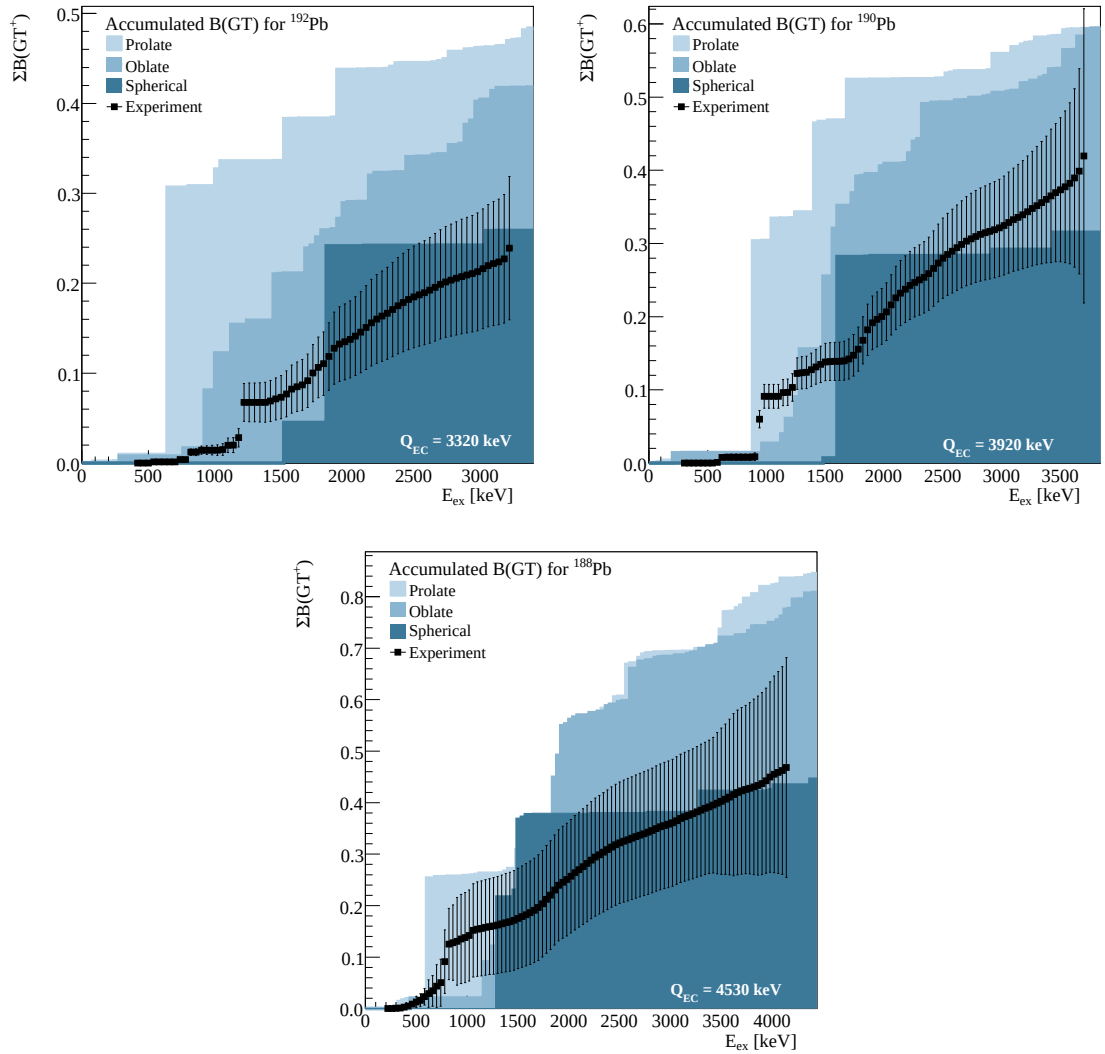

Figure 10.6: Accumulated strength, comparison between data and theory. The results for the calculations assuming the three shapes can be seen for masses 192, 190 and 188. A hindrance factor of 0.6 was used. The errors are larger for mass 188 because the errors in Q_β and $t_{1/2}$ are also larger. In addition, the strength for this mass was multiplied by $0.907(8)$ to show the strength per 100 parent decays, since this nucleus has an α branch.

The comparison with the theory is not as "spectacular" as in the cases measured previously in the mass $A = 80$ region (see [Nac04a], [Nac04b]), but a preference for spherical shapes can be inferred from these figures. Since in general the spherical ground state can be mixed with the contribution of the other shapes, one could also compare with the sum of the three theoretical shapes weighted by some percentage. In [Fos03], a calculation of these percentages is made in the framework of the Interacting Boson Model (IBM). The results of these calculations can be found in Table 10.3. Using these numbers the plots of Fig. 10.7 are obtained, where the theoretical curve is obtained by the linear combination $p_{0p-0h}S_s + p_{2p-2h}S_o + p_{4p-4h}S_p$, where

p are the percentages of mixing of the different shapes and S_s, S_o, S_p are the theoretical strengths for the three shapes. The same vertical scale as in Fig. 10.6 was used. This can be considered a first order approximation.

Table 10.3: Mixing of the ground state in the lead nuclei studied in this work, according to IBM calculations presented in [Fos03].

Nucleus	p_{0p-0h}	p_{2p-2h}	p_{4p-4h}
^{192}Pb	98 %	2 %	0 %
^{190}Pb	96 %	4 %	0 %
^{188}Pb	93 %	7 %	1 %

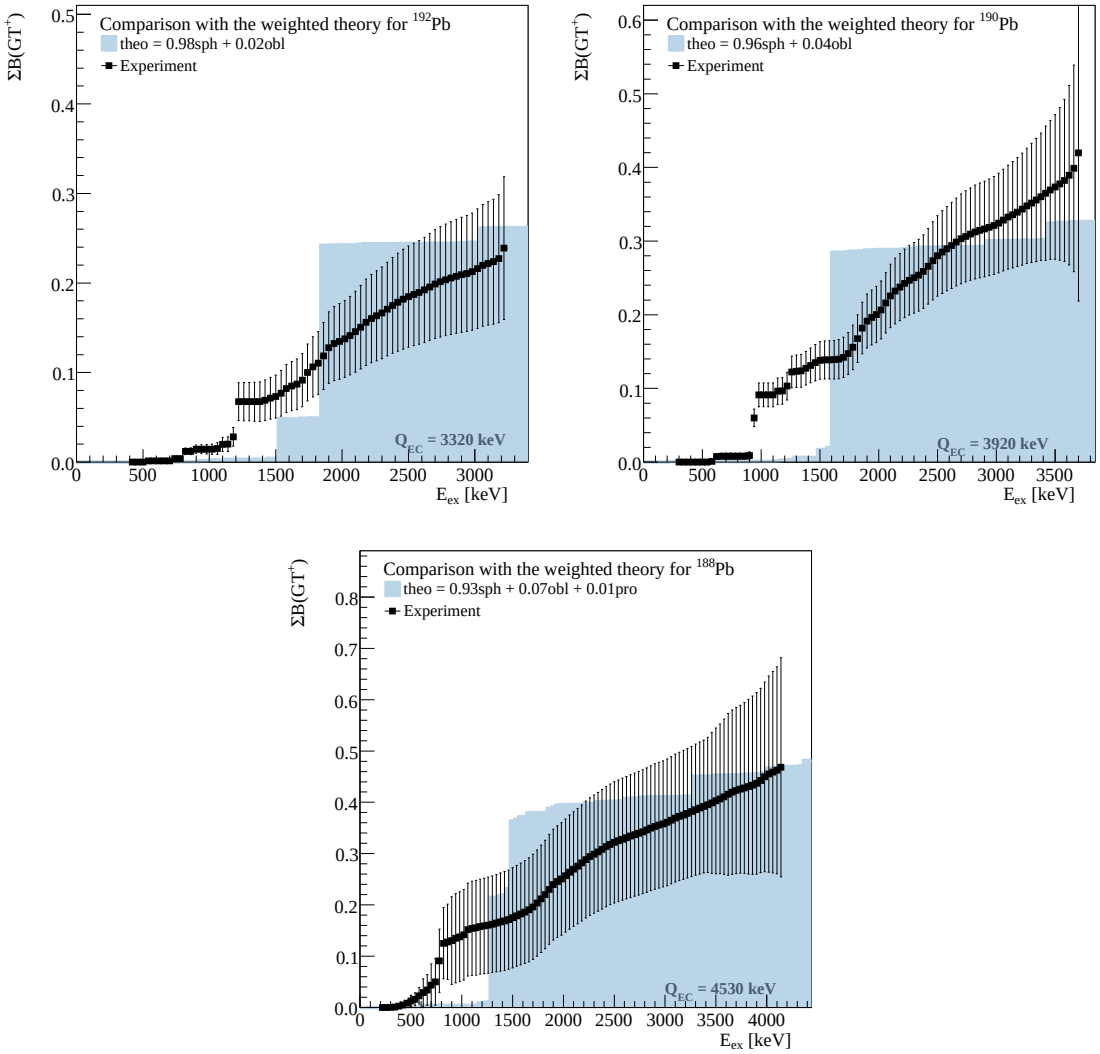

Figure 10.7: Accumulated strength, comparison with the weighted theory. The quenching factor used is 0.6.

Even with this approximation the theoretical shapes do not fit so well with the experimental results compared with the $A = 80$ results, but the agreement is reasonable. The existence of a level with high feeding is reproduced but its position is shifted to higher energies in the theoretical calculations.

Another possibility to present the results could be to widen the theoretical strength with some value that makes it more similar to the experimental width and then accumulate this widened theoretical strength to compare it with the experimental results. The widening is justified because of the effect of residual interactions not taken into account in the present theoretical approach. This manipulation will give an accumulated theoretical strength curve with a smoother profile related to effects not taken into account in the calculations. The widening was made with the same program used to widen the Monte Carlo peaks to the experimental width, but using a constant widening. After several tests with constant widening factors ranging from 100 keV to 1 MeV, a factor of 300 keV was used for the comparison. A higher value gives too much smoothening and is unrealistic (Fig. 10.8). The results are presented in Fig. 10.9.

From this comparison it is found that the total strength in the Q_{EC} window is well reproduced by the calculations (see also Table 10.2). In general terms, effective interactions adjusted to global properties of spherical closed shell nuclei may not describe exactly the structure of nuclei far from stability and the detailed spectroscopy (as, for example, the precise position of the strongest fed level). The quantitative description of coexisting shapes is beyond the presently used mean field approach, and one should consider that the results are in reasonable agreement because of the expected low degree of mixing.

Fig. 10.10 shows the systematics of the neutron-deficient even-mass thallium levels populated in beta decay for the cases where HR data are available (see [ENSDF]). Some of the levels proposed in this work are also shown in dotted lines. The strongly populated levels are marked with thicker lines. It is not easy to see a systematic trend in odd-odd- nuclei with the available information, as the large amount of levels can make this a very difficult task.

Finally, Fig. 10.11 show the systematics of the nuclear mean square radii ($\delta \langle r^2 \rangle$) for nuclei in the region around $Z = 82$, according to optical isotope shifts measurements [DeW07]. The charge radii determined in atomic spectroscopy give detailed information on the ground state wave function. It is clear from this figure that the ground state of lead is spherical through a wide range of values of N, while for mercury and platinum it deviates from the spherical droplet model prediction. After this work it is worth to continue exploring experimentally the beta decay of nuclei in this region, that are predicted to be deformed in their ground state [Mor06], where the calculations are supposed to work better (for example Pt, Hg, etc.).

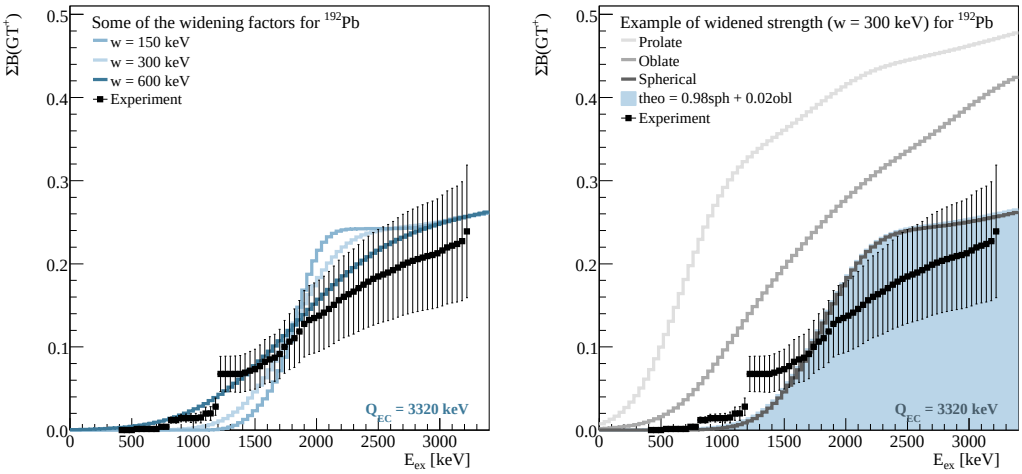

Figure 10.8: Widening of the theoretical calculations for mass 192. Left panel: theoretical strength for the spherical shape with some of the widening factors used in the tests. Right panel: the three shapes for the choosen factor.

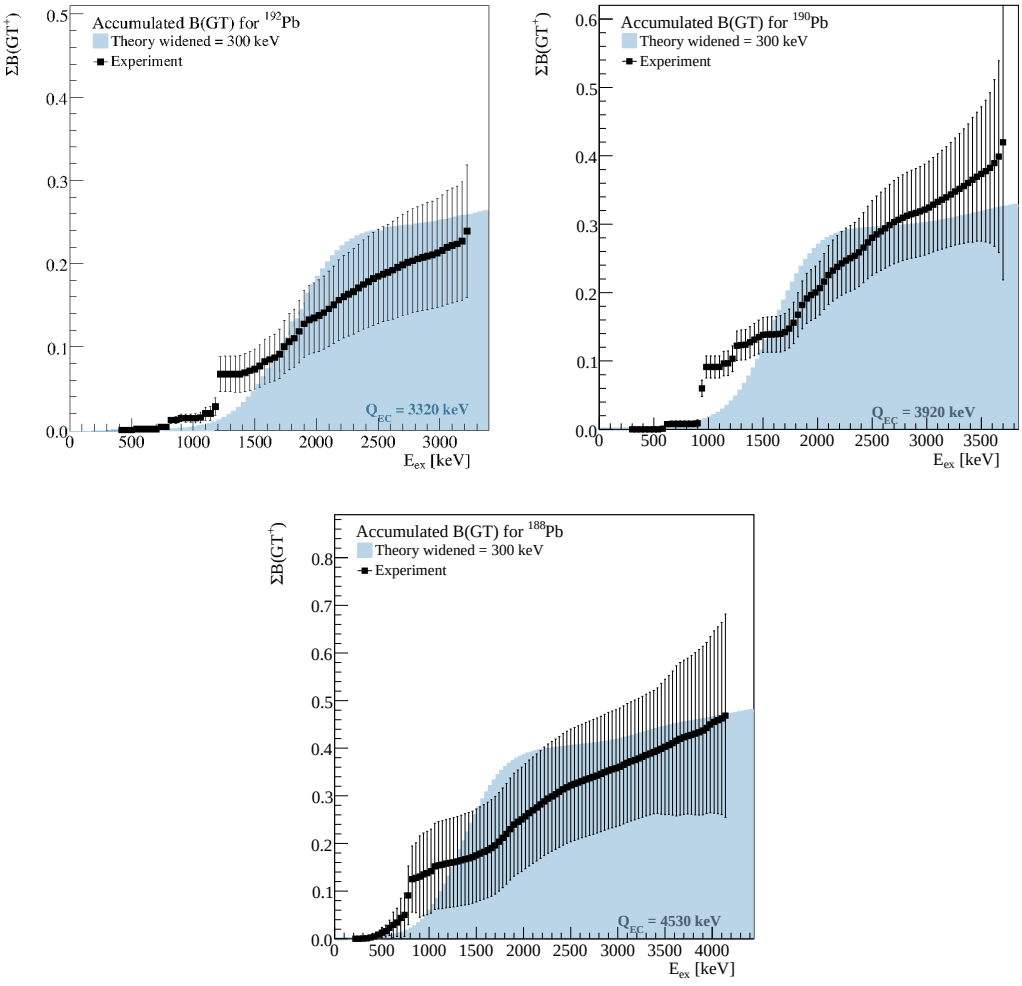

Figure 10.9: Same as Fig. 10.7 but using a widened theoretical strength.

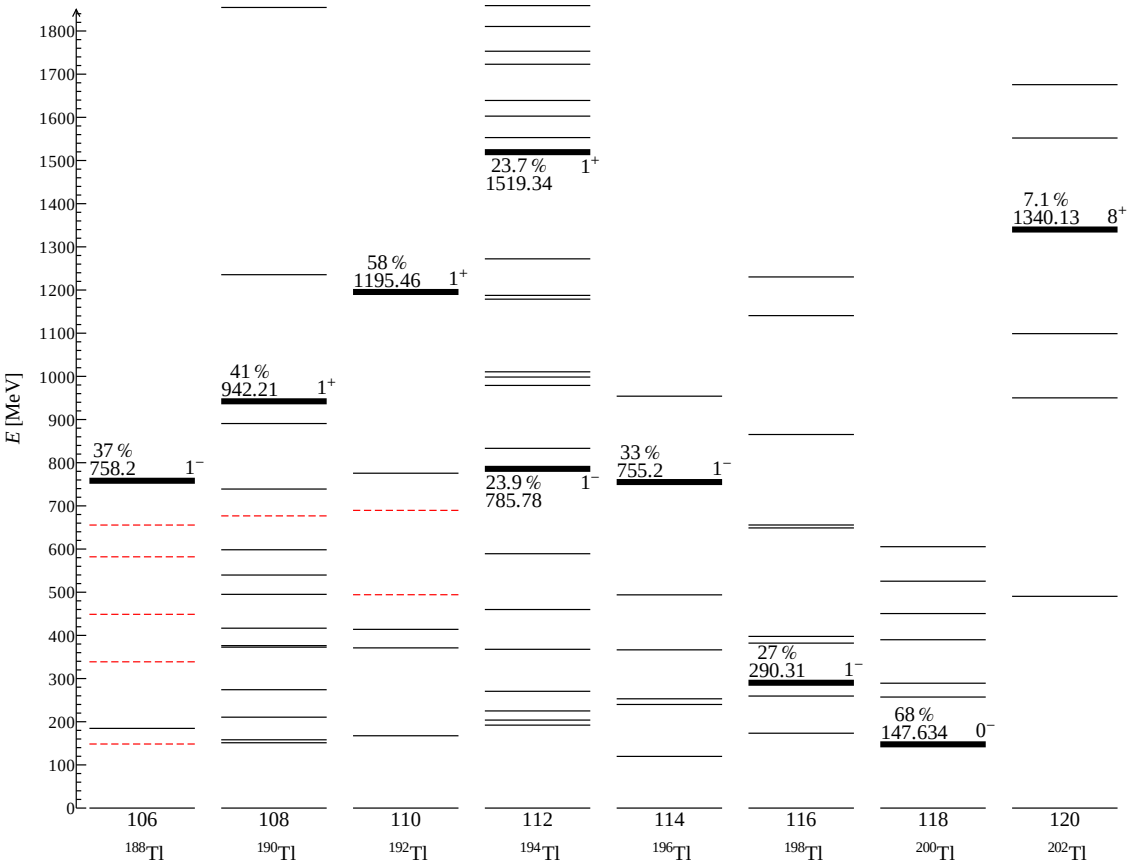

Figure 10.10: Systematics of the neutron-deficient even-mass thallium levels populated in beta decay for the cases where HR data are available (see [ENSDF]). The dashed lines represent the levels of Figs. 9.13, 9.25 and 9.36 selected for the analysis. The aim of this figure is to show the evolution of the strongest populated levels (in thick black lines) through the different nuclei. Their I_β, E and J^π are also shown.

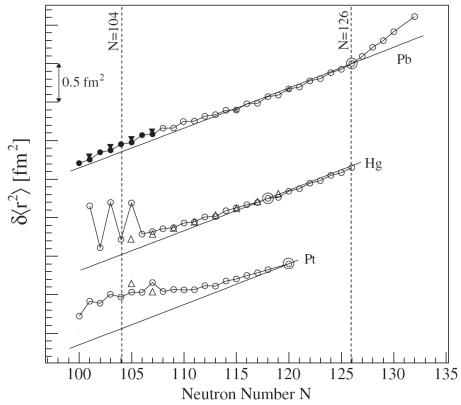

Figure 10.11: Mean square charge radii for lead, mercury and platinum. The data are compared to the droplet model predictions assuming zero deformation ($\beta = 0$). Taken from [DeW07].

Part

IV

General Conclusions

In this work, measurements using the Total Absorption Spectroscopy (TAS) technique were presented, and the analysis of the beta decay of six nuclei for two different applications was discussed. The aim of the work was to obtain the feedings to the levels of interest populated in the decay. In the application to neutrino physics, ^{152}Yb, ^{150}Er and ^{156}Yb TAS measurements are discussed, since they can be candidates for the production of neutrino beams in EC and beta beam facilities (Part II). The accurate determination of the feedings has a practical interest here, since it is related to the energy distribution of the neutrinos produced. This application is also important for nuclear structure, since it confirms the feeding to states in nuclei where the full GT strength is expected to lie within the Q value window. In the second application, ^{192}Pb, ^{190}Pb and ^{188}Pb TAS measurements were presented (Part III). In this case, the aim was to deduce the shape of the parent nuclei from the profile of the experimental beta strength in the daughter nuclei in comparison with theoretical calculations.

In the introduction of this work, the use of this highly efficient technique is justified for beta strength measurements, where high-resolution (HR) measurements can suffer from the "Pandemonium effect" (Sub. 2.1.2). The measurements of this work contribute to a better knowledge of the feeding distributions of the decays studied. As a result of our work, further measurements of ^{156}Yb and ^{188}Pb using germanium detectors are suggested, since the level schemes of these decays are poorly known.

The general way to perform a TAS analysis was explained for the study of an electron capture decay (Sec. 2.2, Appendix A). The analysis is reduced to solving the "inverse problem" given by Eq. 2.4 (Sub. 2.2.3), which is reproduced here:

$$\mathbf{d} = \mathbf{R}\mathbf{f} \qquad or \qquad d_i = \sum_{i=1,\, j=0}^{i_{max},\, j_{max}} R_{ij} f_j$$

This description was divided in three parts: first, the branching ratios are calculated, where the HR information is used and completed up to the Q value with calculations using the statistical model (Sub. 2.2.1), then the response of the detector to individual gammas is calculated by means of a Monte Carlo simulation that is later convoluted with the branching ratios to create the response $\mathbf{R}$ of the detector (Sub. 2.2.2), and finally the feedings $\mathbf{f}$ are extracted from the response $\mathbf{R}$ and the data $\mathbf{d}$ applying the EM algorithm to Eq 2.4. With the feeding distributions $\mathbf{f}$ or $I_\beta(E)$ ($\mathbf{f}$ per level E or bin energy ΔE), the experimental strength S_β can be obtained (Eq. 2.2).

$$S_\beta(E) = \frac{I_\beta(E)}{f(Q_\beta - E)t_{1/2}}$$

In both applications, the data were taken with a TAS detector that had ancillary detectors in the measuring position to tag the different components of the decays. A tape transport system was also used in both cases to collect the species of interest and place them in the center of the TAS detector. The collection and measurement times were fixed according to the half-life of the parent nucleus.

Since the EC component of the six decays under study is obtained by x-ray tagging, the EC spectrum obtained in this way is almost free of contamination. However, the possibility of contamination was also taken into account. The pileup distortion was calculated and the possible β^+ contamination was estimated for every studied case. Finally, their corresponding normalization factors were calculated to know in which amount the contaminations and distortions are present in the different EC spectra.

Neutrino Physics Application

The main goal of this part of the work was to find appropriate candidates from the nuclear structure point of view for the construction of an EC based monochromatic neutrino beam facility (Chapter 3). If such a facility is constructed, the accurate value of the β^+/EC branching ratio to the particular levels as well as the feeding, is very important. Of all the nuclei considered, ^{152}Yb seems to be the best candidate considering its half-life and the relatively large EC component to one level. In fact, it has a smaller EC component feeding to the level of interest than the other two candidates, but its half-life is probably better suited for the application.

With our measurements we have confirmed a large feeding to one level in the studied cases with an alternative technique, which does not suffer from the Pandemonium effect. The results can be found in Table 6.1 which is reproduced here:

Table 10.4: Summary of the results of the I_β calculation from TAS data.

A	E_{level} [keV]	TAS	HR
152	458.4 + 482.3	89(2)	95.2(8)
150	476.2	94.2(7)	99.6(23)
156	317.5	60(3)	85.2(5)

Moreover, the nuclei considered here have production rates at a nuclear facility such as ISOLDE [ISO] similar to those proposed in [Zuc02], but obviously, in order

to use them effectively for a possible future monoenergetic neutrino facility, more specific developments for the production of the selected isotopes are required. In any case, for an application like this one, the TAS technique is the most appropriate one to confirm the values of the feeding distributions.

Another issue is that the combination of beta-beam and electron capture neutrino experiments also has an added value [Ber09] due to the neutrino energy gap between the two decaying channels. This would allow a search for CP violation at a single Lorentz boost since the two channels would have different energies, and there would be no need to construct the neutrino-antineutrino asymmetry from different neutrino beams. This is an additional reason in favor of ^{152}Yb.

These results, and in particular the measurements of the beta decay of ^{150}Er and ^{152}Yb have also an impact in nuclear structure studies, as discussed in Chapter 6, since their decay is relevant from the point of view of the quenching of the GT strength in beta decay studies.

Nuclear Deformation Application

For the first time, the TAS technique was used in the $Z = 82$ region to validate the spherical shape of the ground state of neutron-deficient even-even lead nuclei. The reproduction of the experimental strength by the theoretical calculations of [Mor06] is not as spectacular as in the $A \sim 70$ region [Nac04b]. However, the results can be considered reasonably good taking into account that the present HF+BCS+QRPA approach (Sub. 7.1.1) is a calculation suitable to describe bulk properties of nuclei in the whole nuclear chart and not specilaly suited to spherical nuclei. Because of this universality, a detailed local description of spectroscopic properties for every nucleus or region can be considered beyond the scope of this approach. Hence, one could expect to account successfully for the general behavior of the GT strength distributions, such as total strength and GT resonances, as well as for the global decay properties, such as the GT strength contained in the Q_{EC} window and the half-lives, but not for the detailed spectroscopy (precise position of the states). One can also use the model to identify the underlying quasiparticle structure involved in the GT transitions, but a detailed quantitative description is unrealistic. In general, looking at the comparison between data and theory (Chapter 10) the global trends are well reproduced.

In the spherical case, the low-lying strength is practically collected in a single peak, which corresponds to the transition connecting the almost fully occupied $\pi h_{11/2}$ shell with the partially unoccupied $\nu h_{9/2}$ shell. The relative position of the two shells determines the GT excitation energy which is not so well reproduced. The effect of deformation is to allow for multiple transitions and thus fragmenting the strength. The theoretical results presented here have been scaled by a standard

quenching factor of 0.6.

These calculations (QRPA + HF + BCS) are expected to be better suited for deformed nuclei and even so they work relatively well to predict a spherical shape for the studied lead nuclei. For this reason, it is justified to extend these calculations to deformed nuclei of interest around the lead region that can be studied using the TAS technique. Calculations have already been performed for mercury and polonium isotopes [Mor06]. These studies, in combination with possible future experiments [Pro12], can provide a deeper understanding of shape effects in the lead region.

— ❦ —

The neutrino beam facility candidates were studied because they were considered interesting due to their nuclear properties, as discussed in Sec. 3.3. Further technology improvements may allow to produce these nuclei with better yields and in a cleaner way. Despite this fact, the same improvements could demonstrate in subsequent studies that there are better candidates for such a facility. In that case, since the feedings are an important issue for this application, it would be desirable to measure them with the TAS technique also.

In the case of the nuclear deformation study in the lead region, the results of the comparison between experiment and theory could be improved if calculations beyond mean field [Egi04] are used. Developments in this direction are foreseen in the next future [RRpc]. Also, the HR measurements for the masses studied in this part of the work should be improved. In that direction, a HR measurement for mass 188 has been approved [Add10] that could additionally allow the study of the beta delayed particle emission in this nucleus.

Part

V

Resumen en español

En este trabajo se presentaron medidas realizadas con la técnica de espectroscopía de absorción total o TAS (*Total Absorption Spectroscopy*), y se discutó el análisis de la desintegración beta de seis núcleos diferentes, relevante para dos aplicaciones. El objetivo de este trabajo era obtener la intensidad beta a los niveles de interés poblados en la desintegración. En la aplicación a la física de neutrinos, se presentaron las medidas de los núcleos ^{152}Yb, ^{150}Er y ^{156}Yb realizadas con la técnica TAS, ya que estos núcleos podrían ser utilizados en la producción de haces de neutrinos en instalaciones de haces beta y/o instalaciones de haces de captura electrónica (Parte II). La determinación precisa de las intensidades beta tiene aquí un interés práctico, ya que está relacionada con la distribución de energía de los neutrinos producidos. Esta aplicación también es importante para la estructura nuclear, ya que confirma la probabilidad beta a estados en núcleos en los cuales se espera que la fuerza de Gamow-Teller (GT) se encuentre dentro de la ventana de energía disponible Q. En la segunda aplicación, se presentaron las medidas realizadas con la técnica TAS de los núcleos ^{192}Pb, ^{190}Pb y ^{188}Pb (Parte III). En este caso, la forma del núcleo padre se dedujo a partir del perfil de la fuerza beta experimental en el núcleo hijo comparándola con el resultado de cálculos teóricos.

En la introducción de este trabajo, se justifica el uso de esta técnica altamente eficiente para medidas de la fuerza beta, ya que las medidas de alta resolución (HR o *high-resolution*) pueden sufrir del llamado "efecto Pandemonio" (Sub. 2.1.2). Los experimentos de este trabajo contribuyen a un mejor conocimiento de las distribuciones de intensidad beta de las desintegraciones estudiadas. Como resultado de este trabajo, se sugieren futuras medidas de ^{156}Yb and ^{188}Pb, ya que el conocimiento de estas desintegraciones es bastante pobre.

La forma general de realizar un análisis de los datos obtenidos con la técnica TAS se explicó para el caso de la desintegración por captura electrónica (Sec. 2.2, Apéndice A). El análisis se reduce a resolver el "problema inverso" dado por la ecuación 2.4 (Sub. 2.2.3), que se reproduce a continuación:

$$\mathbf{d} = \mathbf{R}\mathbf{f} \qquad or \qquad d_i = \sum_{i=1,\, j=0}^{i_{max},\, j_{max}} R_{ij} f_j$$

Esta descripción se dividió en tres partes: primero, se calculan las razones de ramificación gamma de la desintegración, donde se usa la información de HR, la cual se completa hasta el valor Q usando el modelo estadístico (Sub. 2.2.1). A continuación se calcula la respuesta del detector a los gammas individuales por

medio de una simulación Monte Carlo y se hace la convolución de esta respuesta con la matriz de ramificaciones para crear la matriz de respuesta **R** del detector (Sub. 2.2.2). Finalmente las intensidades beta **f** se determinan a partir de la respuesta **R** y los datos **d** aplicando el algoritmo de maximización de la expectación o algoritmo EM (*Expectation Maximisation*) a la ecuación 2.4. Usando las distribuciones de intensidad beta **f** o I_β (**f** por nivel de energía E o nivel de energía ΔE), se obtiene la fuerza beta experimental (Ec. 2.2):

$$S_\beta(E) = \frac{I_\beta(E)}{f(Q_\beta - E)t_{1/2}}$$

En ambas aplicaciones se tomaron los datos con un detector TAS que permitía situar detectores secundarios en su interior, para así etiquetar o poder diferenciar las diferentes componentes de la desintegración. También se usó un sistema de transporte de cinta en ambos casos, para acumular las especies de interés y situarlas en el centro del detector TAS. Los tiempos de colección y de medida se fijaron de acuerdo con la vida media del núcleo padre para optimizar las mismas.

Dado que la componente EC de las seis desintegraciones estudiadas se obtiene utilizando las coincidencias con los rayos x característicos, el espectro EC que se obtiene está casi libre de contaminación. Sin embargo, todas las posibilidades de contaminación fueron contempladas. La distorsión debida al apilamiento de pulsos también se calculó, se estimó la contaminación β^+ para cada caso estudiado, y los factores de normalización de ambas contribuciones se calcularon para saber en qué proporción se hallaban presentes en los diferentes espectros EC.

Aplicación a física de neutrinos

El principal objetivo de esta parte del trabajo era encontrar candidatos apropiados desde el punto de vista de la estructura nuclear para la construcción de una instalación de haces de neutrinos monocromáticos basada en el proceso EC (Cap. 3). Además, si se va a construir una instalación semejante, es muy importante saber el valor preciso de la razón β^+/EC así como la probabilidad de transición a los niveles de interés. De todos los núcleos considerados, el ^{152}Yb parece el mejor candidato considerando su vida media y su relativamente larga componente EC a un solo nivel. De hecho tiene una menor intensidad EC al nivel de interés comparado con los otros dos candidatos, pero su vida media es probablemente la más adecuada para esta aplicación.

Con nuestras medidas hemos confirmado la existencia de gran intensidad beta a un solo nivel en los casos estudiados, con una técnica alternativa que no sufre del efecto Pandemonio. Los resultados se pueden ver en la tabla 6.1 que se reproduce a continuación:

Table 10.5: Resumen de los resultados del cálculo de la I_β a partir de los datos del TAS.

A	E_{nivel} [keV]	TAS	HR
152	458.4 + 482.3	89(2)	95.2(8)
150	476.2	94.2(7)	99.6(23)
156	317.5	60(3)	85.2(5)

Los núcleos considerados tienen unas tasas de producción en instalaciones como ISOLDE [ISO] que son similares a las propuestas en [Zuc02], pero obviamente, para usarlas efectivamente en una posible instalación de neutrinos monoenergéticos, serán necesarios desarrollos específicos en relación con la producción de los isótopos seleccionados. En cualquier caso, para una aplicación como ésta, la técnica TAS es la que debe usarse para confirmar los valores de las distribuciones de intensidad beta.

Otro tema relacionado es el hecho de que la combinación de haces beta y EC para la creación de haces de neutrinos tiene un interés añadido [Ber09] debido a la diferencia de energía de los neutrinos entre los dos canales de desintegración. Esto permitiría la búsqueda de violación de carga-paridad (CP o *Charge Parity*) en un solo *boost* de Lorentz ya que los dos canales tendrían diferentes energías, lo cual eliminaría la necesidad de reconstruir la asimetría neutrino-antineutrino a partir de diferentes haces de neutrinos. Este es otro argumento a favor del ^{152}Yb.

Estos resultados y en particular las medidas de las desintegraciones beta del ^{150}Er y ^{152}Yb son también relevantes para la estructura nuclear. Como se discutió en el Cap. 6, estas desintegraciones son importantes en el estudio del *quenching* de las transiciones GT en desintegraciones beta.

Aplicación a deformaciones nucleares

Se ha usado por primera vez la técnica TAS en la región $Z = 82$ para validar la forma esférica del estado fundamental de los núcleos de plomo par-par deficientes en neutrones. Los cálculos teóricos de [Mor06] no reproducen la fuerza beta experimental de una manera tan espectacular como en la región $A \sim 70$ [Nac04b]. Sin embargo, los resultados se pueden considerar razonablemente buenos teniendo en cuenta que el presente modelo QRPA + HF + BCS (Sub. 7.1.1) es un cálculo adecuado para describir la mayor parte de las propiedades de los núcleos en toda la carta nuclear. Debido a esta universalidad, está más allá del alcance de este modelo el conseguir una descripción detallada y local de las propiedades espectroscópicas para cada núcleo o región. Teniendo esto en cuenta, se puede esperar una interpretación adecuada del comportamiento general de las distribuciones de fuerza GT, así como de las propiedades globales de la desintegración como la concentración GT contenida en la ventana de Q_{EC} y las vidas medias, pero no se debe esperar una

descripción detallada de la espectroscopía. También se puede usar el modelo para identificar la estructura de quasipartícula subyacente involucrada en las transiciones GT, pero esperar una descripción cuantitativa detallada es poco realista. En general, mirando la comparación entre datos y teoría (Cap. 10) se puede considerar que las tendencias globales están bien reproducidas por el modelo.

En el caso esférico, la fuerza beta a bajas energias se concentra practicamente en un solo pico, correspondiente a la transición que conecta la capa $\pi h_{11/2}$ casi totalmente ocupada con la capa $\nu h_{9/2}$ parcialmente desocupada. La posición relativa de las dos capas determina la energía de excitación GT que no se reproduce tan bien con el modelo. El efecto de la deformación es permitir múltiples transiciones, fragmentando así la fuerza beta. Los resultados teóricos se han escalado por un factor de *quenching* estándar de 0.6.

Aunque se espera que estos cálculos sean más adecuados para núcleos deformados, han funcionado relativamente bien para predecir la forma esférica de los núcleos de plomo. Por esta razón está justificado extender estos cálculos a otros núcleos deformados de interés en esta región que pueden ser estudiados usando la técnica TAS. Se han hecho ya cálculos para algunos isótopos del mercurio y el polonio por ejemplo [Mor06]. Estos estudios podrían aportar una comprensión más profunda de los efectos de forma en la región del plomo, si se combina con posibles nuevos experimentos en esta región [Pro12].

— ❦ —

Los núcleos candidatos para la instalación de haces de neutrinos fueron estudiados porque se consideraron de interés debido a sus propiedades nucleares, como se discutió en la Sec. 3.3. Futuros desarrollos tecnológicos en esta línea podrían permitir la producción de estos núcleos con mayores intensidades y de una forma más limpia. Aún así, las mismas mejoras podrían demostrar, en estudios subsecuentes, que hay mejores candidatos para dicha instalación. En ese caso, dado que las intensidades beta son un asunto importante para esta aplicación, sería necesario medirlas también con la técnica TAS.

En el caso del estudio de la deformación nuclear en la región del plomo, los resultados de la comparación entre experimento y teoría se podrían mejorar si se usaran cálculos *beyond mean field* [Egi04]. Trabajo en esta dirección está previsto en un futuro próximo [RRpc]. Además, las medidas de HR para las masas estudiadas en esta parte del trabajo deberían mejorarse. En ese sentido, ya han sido aprobadas unas medidas de HR de la masa 188 [Add10] las cuales podrían permitir adicionalmente el estudio de la emisión de partículas retardadas en la desintegración beta de este núcleo.

Part

VI

Appendixes

A

Summary: general steps of the analysis

The analysis of the TAS data is a complex task, but not impossible. In this appendix the general steps to be followed in the analysis of the TAS data are presented. These extend the summary described in Sec. 2.2 and are valid only for the study of an EC decay:

1. **Average branching ratios calculation:**

   a) Known Levels: Prepare a file for the known part of the level scheme of the daughter nucleus with information taken from literature (for example, the Nuclear Data Sheets [NDS], or in the last evaluation of [ENSDF]) in the following format: energy of the level, spin, parity, energy of all the γ rays de-exciting the level (one line for each γ), their relative intensity (related to the level: 100 for the most intense γ ray, the corresponding percentage for the rest) and the electron conversion coefficient α_T (See Tables 5.1, 5.5 and 5.9, for example). It is possible that this information has to be slightly modified to achieve a better reproduction of the data.

   b) Level Density Parameters: Use the program FITBSLEVDEN.F to make the fit that gives the values of a and Δ of the Back-Shifted Fermi Gas Model [Dil73] (in case they are not available in the literature, for example in [RIPL]). This program requires as input the number of excitation energies that are going to be used to make the fit, with the number of levels expected up to those energies (this information can be taken from [Gor01] and [Dem01]), and an error. The mass of inertia I_{eff} was fixed to a value of $0{,}5I_{rig}$ (See [Dil73, Table 1]) for all the cases studied in this work.

   c) Gamma Strength Function Parameters: Find the neutron separation energy and the quadrupole deformation parameter (β_2 deformation, see

table of [Mol95] for example) and run GRPARAM.F to find the parameters (E, w, Γ) for the E1, M1 and E2 γ-ray strength functions. This program implements the parameterization of [Kop90].

d) Average branching ratios calculation: Fix the binning (normally 40 keV, which is a value compatible with the TAS resolution) and the range of the unknown part. This range starts approximately 1 bin after the last bin of the known part, and goes up to the energy of the Q value, although this definition can be changed if necessary. Finally, use AVEBRAN.F to generate the branching ratios using the statistical model and the information from a), b), c) and this step, as well as considering only GT transitions to the states in the daughter nucleus ($\Delta J = 1$, $\Delta\pi$ no). One of the outputs of this program is the branching ratio matrix and the other is a file that allows to fix the feeding to selected levels if necessary.

2. **Response simulation:**

a) MC code: Write a Monte Carlo simulation that accurately reproduces the geometry and the physics of the measurement.

b) MC calibration: Launch monoenergetic gammas at some energies in a range of interest for an energy calibration. Make the convenient calibrations in energy and width for the MC and for the sources data (See Appendix C, Subs. C.2.1 and C.2.2 for details), and find the coefficients of Eq. C.7. This coefficients and the energy calibration of the MC are used in the program EXPWID.F that implements the empirical instrumental resolution distribution of [Abr64]. Use this program any time the response has to be widened.

c) MC test: Simulate the measured sources, recalibrate the measured sources to the simulated ones by using RECALPOIS.F (rebin in case it applies) and compare. If there are differences between the simulation and the measured sources, repeat 2*a*, 2*b* and this step until the simulation reproduces the data (see Sec. 9.1 for details).

d) Build response: To build the response for the case of EC decay, simulate monoenergetic gammas with energies from the bin size up to the Q value, increasing in steps of the bin size chosen. Then run CREARESP.F using this files and the final calibrations of 2*b* as inputs, to build the simulated monoenergetic response. The resulting matrix is binned, normalized and widened.

e) Create matrix: Finally, make the convolution of this monoenergetic response and the branching ratio matrix obtained in step 1 with RESPMAT.F to produce the EC response matrix. The inputs of this program are: the Q value and binning, the binned average branching ratios calculated in 1 and the simulated response matrix. The result of this convolution is written in a file containing the binned energy channels (spectrum channels), the level energy bin (fed levels) and the response.

3. **Extracting the feedings:**

a) X-ray tagging: Extract the gate of the decay of interest from the total TAS spectra by making coincidences with the relevant peaks of the x-ray spectrum. Find the background by putting gates in both sides of the x-ray peak used for the gate of the decay (as close to the peaks as possible), taking the same number of channels that in the gate of interest.

b) Contaminants, backgrounds, pileup: Repeat 3*a* for each of the isobars of the decay chain. Then, search for any other contamination, background, etc. Calculate the pileup of the x-ray gated TAS spectrum of the nucleus of interest with PILEUP.F. This program follows the procedure of [Can99b] and uses also the singles TAS spectrum and a measured pulse of the TAS amplified signal that must be normalized. Finally, determine in which percentage all of these spectra appear in the gate by finding the respective normalization factors. This step has to be made carefully since it can introduce systematic errors. In an imaginary case where there are 3 nuclei in the decay chain whose unknown clean TAS spectra are given by h_x, h_y and h_z, while the contaminated TAS spectra in coincidence with their x rays are given by h_1, h_2 and h_3, the problem can be expressed as follows:

$$\left.\begin{aligned} h_1 &= h_x + ah_2 + bh_3 \\ h_2 &= h_x + ch_1 + dh_3 \\ h_3 &= h_x + eh_1 + fh_2 \end{aligned}\right|$$

where a, b, c, d, e and f are the normalization factors that give the amount in which the other decays are present in the spectrum of interest. This problem has no analytic nor unique solution, and still the pileup, backgrounds and other contaminants (for example β^+ contamination of the EC gate) have to be included, but a first rough approach of their values can be obtained by comparing gate and contaminant and scaling to the ratio of the integrals of peaks appearing in both spectra (for the pileup, the integral is taken from the Q value to the end of the gate). Then, the "fine tunning" of the normalization factor is done visually.

c) Algorithm application: Recalibrate the spectra to the MC calibration with RECALPOIS.F (rebin in case it applies). The spectra have to be compressed so that they have the same calibration in energy than the simulated response function. Run BAYES.F to find the feedings, and the recalculated spectrum. If this spectrum does not reproduce the experimental data, change the parameters of the different steps of 1, 3*a* and 3*b*, until the difference is minimum. The inputs of the program are the spectrum to be analyzed (d_i), the response matrix calculated in step 2 (R_{ij}), the total number of data bins, the bin of the Q value, the range of data to analyze, and the number of iterations, with a maximum value of χ^2 and minimum variation $\Delta\chi^2$.

d) Strength calculation: Use STRENGTH.F to calculate the strength and the total $I_{EC+\beta^+}$ feedings (the S_β and I_β of Eq. 2.2) using the EC feedings calculated in 3*c* and the theoretical values of the EC/β^+ ratio [Nuc71]. For this, the Q value and half-life with their errors are needed. Note that it is better to do the calculation of the strength until some energy before the Q value, since there are large oscillations in the feeding because of the low statistics (the feeding to these last levels is very small, so the error when eliminating them is negligible). This is achieved by specifying the energy range of the calculation. The output of STRENGTH.F is a file containing the energy, the normalized EC component, the normalized total beta feeding with its error (calculated from the EC component with the help of the log*ft* tables), and the beta strength with its error. These errors are calculated by propagation of the statistical uncertainties, but they are not enough to account for the total error. To calculate the errors the deviation between different results when doing several tests has to be also taken into account.

The analysis of the decays presented in this work are an example of the application of these steps. The slight differences from this procedure for specific cases, if any, are listed in the appropriate sections.

B

Preparation of the data for Part II: Rediscovering GOOSY

In Chapter 5 the analysis of the two GSI experiments was presented. The data of these measurements was written in listmode (`lmd`) files in a format that is not used anymore, the GOOSY (GSI Online Offline SYstem [Goo91]) format. This fact made necessary a study of the structure of the events written with this system in order to be able to extract the data.

The `lmd` files of these two experiments where read from magnetic *Digital Linear Tapes* (DLT) by means of the appropriate device and copied to a modern computer. We tried to analyze the files with an old routine (GO4) used for a similar experiment that was written for the GOOSY format. However, this routine gave errors because the data structure was slightly different from the one expected by the program. After several unsuccessful tries of adapting it, we decided that it was better to make a routine from scratch that allowed a better control of every aspect of the sorting.

The aim was to convert the `lmd` files to ROOT files [ROOT]. ROOT is an interactive data analysis system written in C++ that replaces PAW ("*Physics Analysis Workstation*" written in Fortran). From the ROOT files it is easy to make the analysis, which in this case means: to accumulate the spectra of interest in histograms, to save it in ASCII files for later manipulation, to make coincidences event by event, etc. ROOT saves the data in a structure of trees, branches and leafs. A tree is optimized to reduce disk space and enhance access speed, and can hold all kind of data, keeping the correlation of the information. For detailed information and manuals, see [ROOT].

To achieve this conversion, the first task was to disentangle the events structure of the `lmd` files. By dumping the files in octal mode[1] the structures of [Goo91, p.

[1] This was the only way to read byte by byte. This was important, since some of the parameters had a size of just 1 byte

17] were identified visually, that is, the "buffer header blocks". The buffer header block has a size of 16384 bytes and is written at the beginning of every file, and the events and subevents have a structure of type 10, subtype 1 (see Fig. B.1). The events and subevents come after the header block. The dump of the files for each experiment, with the identification of the parameters, can be seen in Fig. B.2. The writing order of the parameters was swapped. Also, the parameters of size > 1 byte were swapped. Thus, the only way to recognize and later reconstruct the values of the parameters was by looking at the files in octal mode.

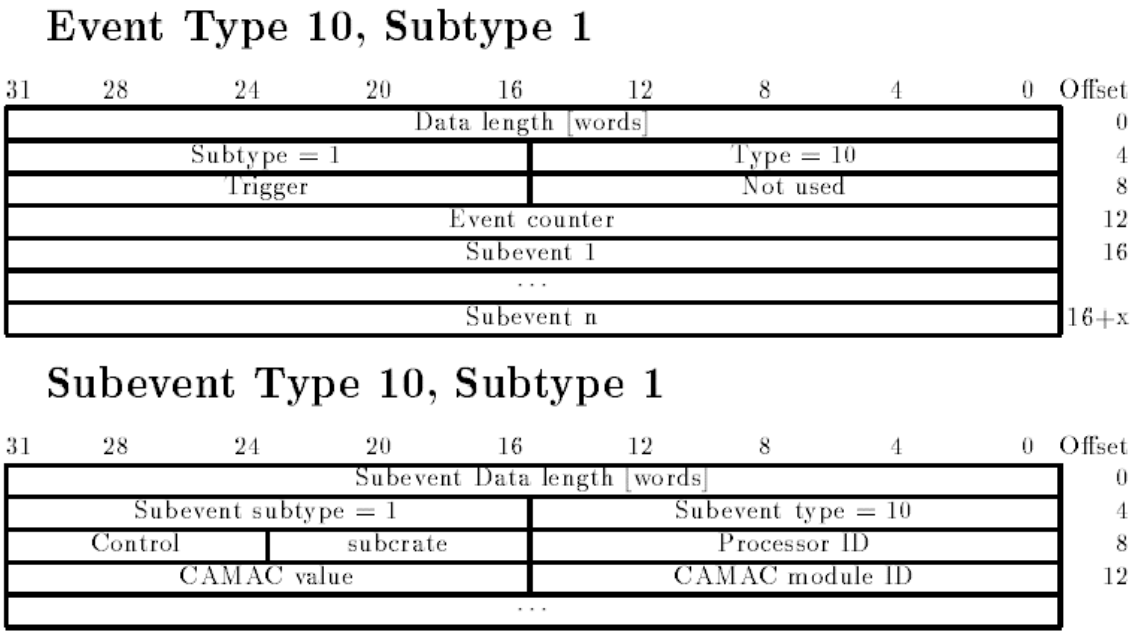

Figure B.1: GOOSY structure of an event and subevent of type 10, subtype 1. To be read from right to left and from top to bottom. The numbers in the upper part are the size of the parameters in bits and the numbers in the right are the number of bytes, where 1 byte = 8 bits. Depending of which of the two experiments is considered ([Can00] or [Nac04a]), the ID of the CAMAC is written or not, and this will change the data structure, as explained in the text. Taken from [Goo91, p. 28]

The experiment of 1996 was written in Zero Suppression mode (See Table B.1), that is, only the CAMAC modules (ADC, TDC, etc.) that gave a signal were written along with their ID, while in the 2000 experiment this was not the case, and all the values of the CAMAC modules were written, even if they had no signal. In the latter case, the parameters were written always in the same order so the ID was not written. As a consequence, the length of the events was fixed or variable depending on the case, thus making the two experiments to have a different data structure and a different number of signals. It is important to take this into account for a correct reading of the data stored in the files.

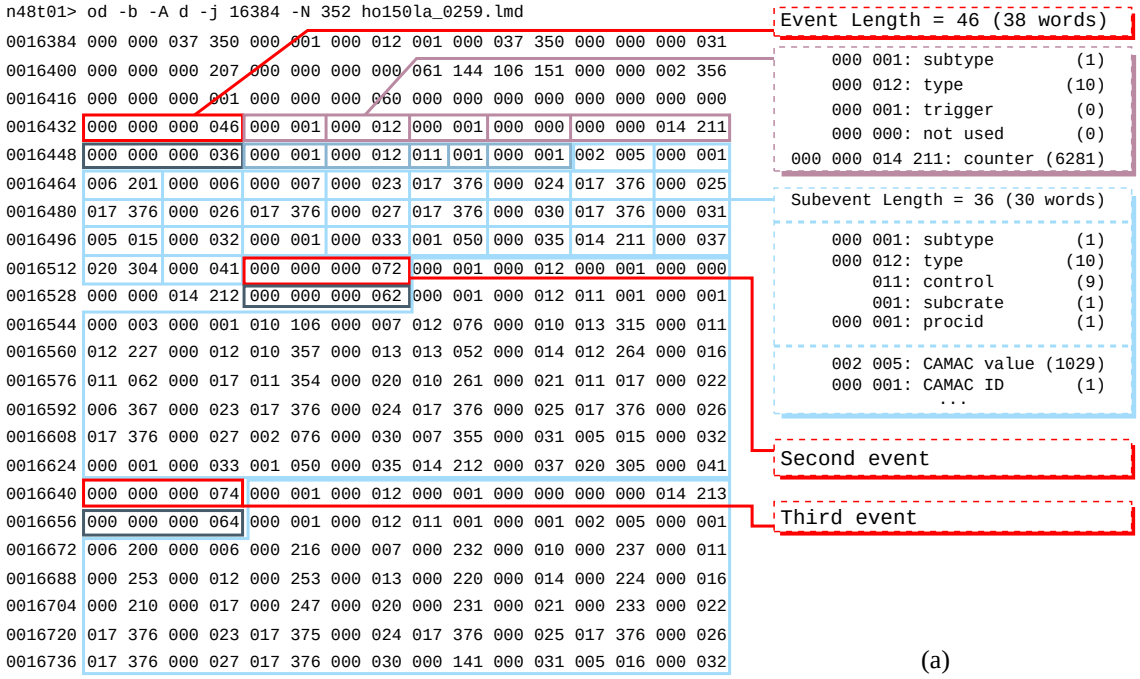

Figure B.2: Dump of two `lmd` files showing the identification of the parameters according to the scheme of Fig. B.1. The dump was made in octal mode for the reasons listed in the text. The numbers of the first column to the left are the number of bytes read. In these examples, the 16384 bytes header was jumped. a) First 352 bytes of an `lmd` file from tape N48T01 of experiment of 1996. b) Same for tape N59T02 of experiment of 2000.

Table B.1: Details of the data files.

	1996 experiment	2000 experiment
Event length	Variable.	Fixed (42 bytes per event).
Subevent writing	*Zero Suppression mode*: The ID and the value of the CAMAC module are written, but only if the module gave a signal.	ID of the CAMAC module is not written but all the module values are written, always in the same order.
♯ of parameters	34	24
♯ of signals	18 energies (12 from PMTs), 5 time signals, 5 scalers (1 not used) and TDC signal.	9 energies, 8 time signals, 5 scalers, 1 pattern byte.

Two programs where written to read this data structures and convert them to ROOT files [ROOT] that could be easily analyzable. The number of wrong events was of the order of 0.6 %. In Figs. B.3 and B.4 the structure of the ROOT trees is shown. The event and subevent parameters can be identified with those of Fig. B.1, that is: dlen (data length), type, subtype, dummy (not used) trigger, counter (event counter), sdlen (subevent data length), procid (processor ID), subcrate, control, and the CAMAC values or signals. As said before, the latter ones can change depending on the experiment that is considered, but in both experiments the important leafs for the analysis are E_GeG/T_GeG for the coaxial germanium detector, E_GeX/T_GeX for the planar germanium detector with a different gain to see the x-ray peaks, and E_TAS/T_TAS for the TAS detector, where E refers to energy signal and T refers to time signal.

A ROOT file was created from each `lmd` file. These ROOT files can then be summed to have all the statistics of one measurement. From example, a spectrum of the germanium detector can be obtained, where the peaks generated by the x rays of the daughter nucleus whose decay we want to extract are localized, and the channels of the relevant gates (placed on these peaks and its background) are defined. Event by event, the ROOT files are read and a coincidence is searched between the TAS (E_TAS) and the x-ray germanium gates (E_GeX). Everytime there is a coincidence, the corresponding energy channel of an x-ray gated TAS spectrum is incremented. If the coincidence is made with the background gates, the information is accumulated in another spectrum (a background-gated TAS spectrum). In this way, a TAS spectra of the nucleus of interest is extracted from the total TAS spectra with its background.

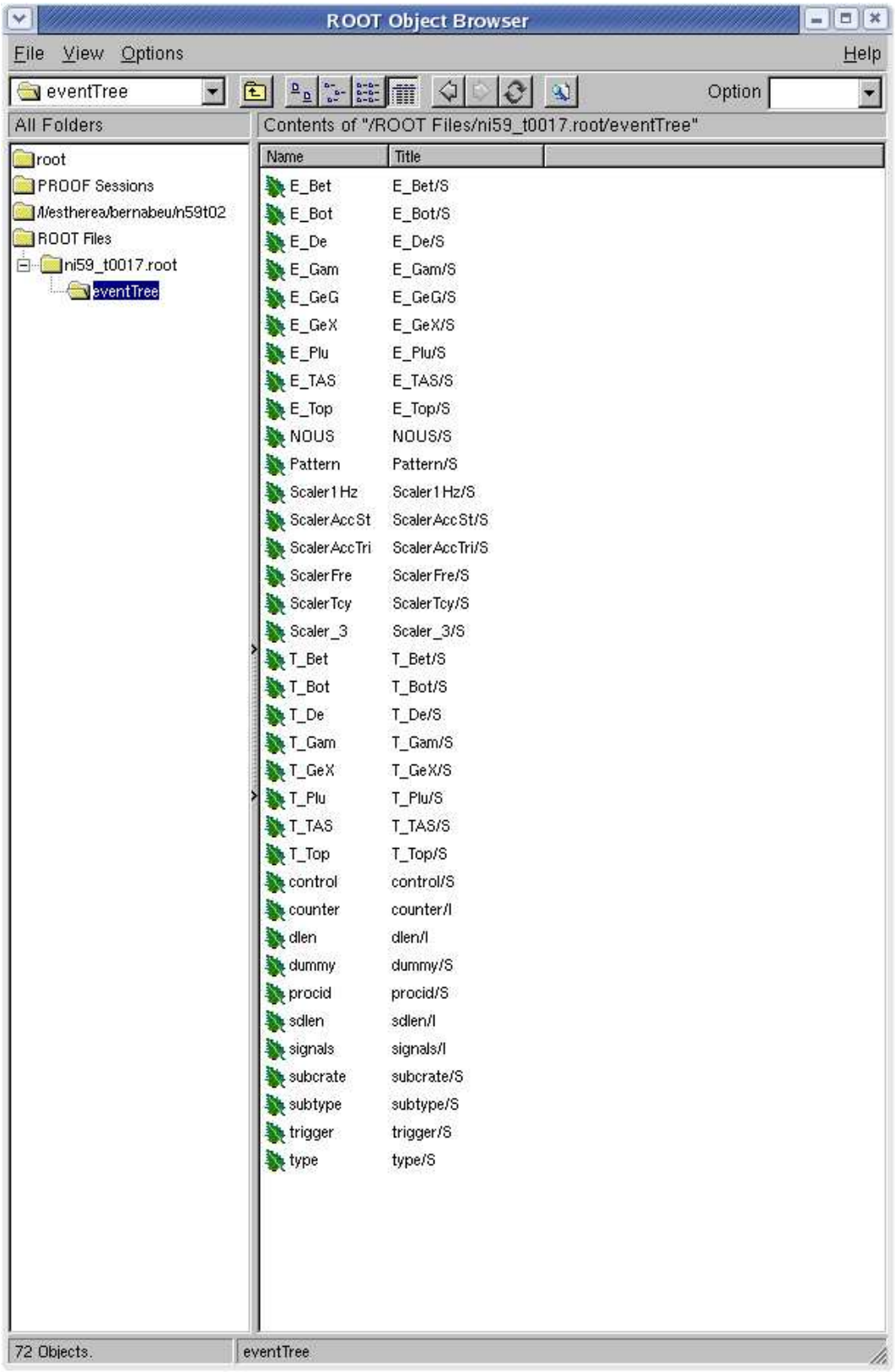

Figure B.3: Data structure of the ROOT files generated from the `lmd` files for the experiment of 2000. For more information about the experiment details, see Sec. 4.3.

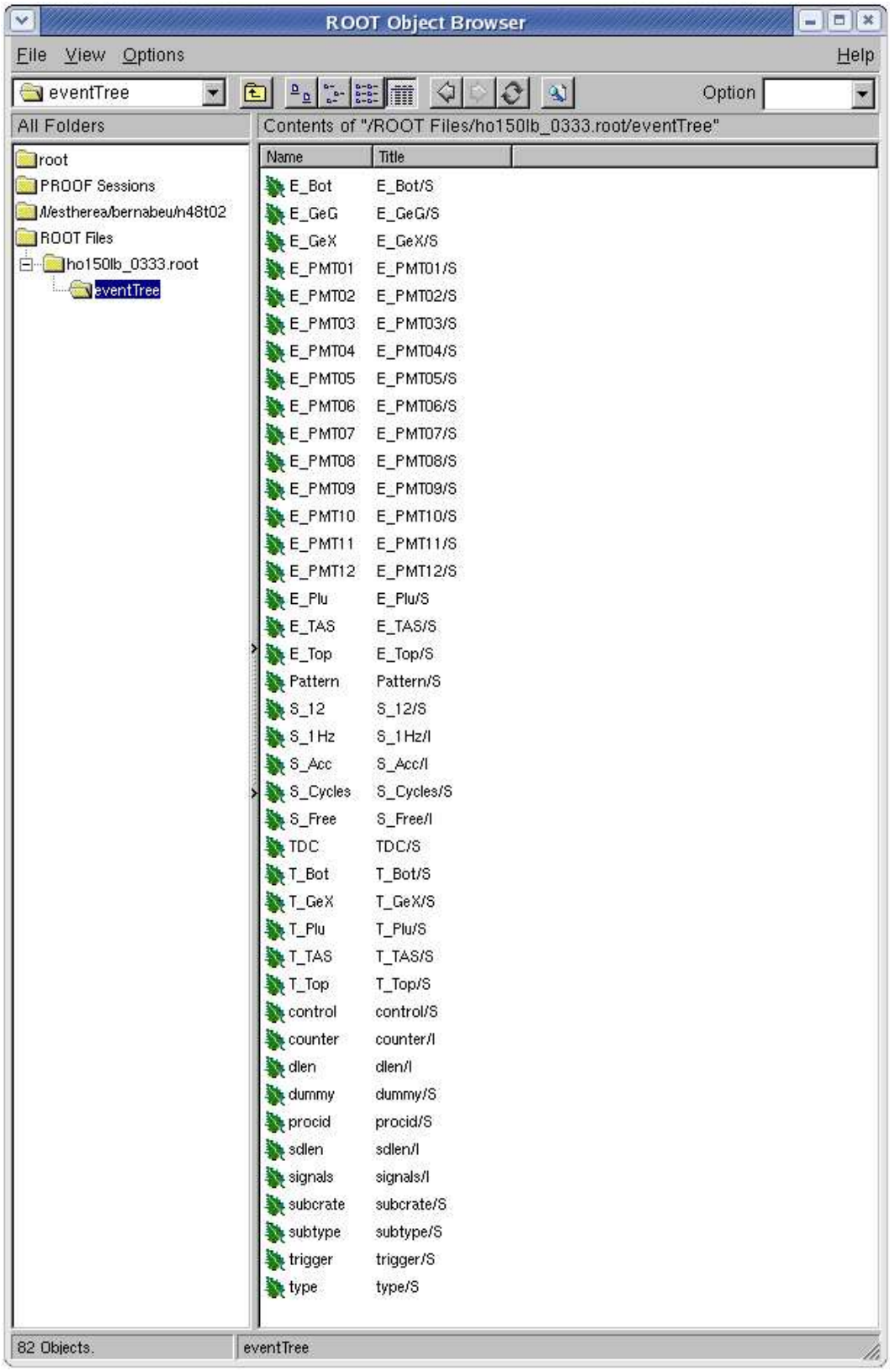

Figure B.4: Data structure of the ROOT files generated from the `lmd` files for the experiment of 1996. For more information about the experiment details, see Sec. 4.4.

C

Preparation of the data for Part III: Alignment, calibrations and efficiencies

In this appendix, the alignment of the spectra of the lead decays (Sec. C.1), the calibrations (Sec. C.2) and the efficiencies (Sec. C.3) are covered. For more information about the analysis see Chap. 9.

The data was read from the ROOT Trees generated by the DACQ program [Agr11] during the measurements. These Trees have the structure presented in Fig. C.1. Two different ADCs (*Analog to Digital Converters*) were used, which had different range. For the analysis, the data from the ADCs of 8 k channels was used (taken from the leafs whose name begins with "G"), because they are more linear. There was a signal for the energy and a signal for the time from every detector of the experimental setup (that is, coaxial germanium, planar germanium and TAS).

A program was written to read the ROOT files and make the gates, etc. The generated spectra was saved in ASCII files as explained in Appendix B. The ASCII files have two columns where the first column is the channel number of the spectrum and the second column is the content of the bin. In this way they are easy to plot and manipulate. The important leafs for the analysis are G_Coax/T_Coax, G_Planar/T_Planar and G_TAS_Hard/T_TAS_Hard[1] of Fig. C.1.

To avoid underflows and overflows, only energies in the range $2 <$ channel < 8190 were selected, and the same applies to the time leafs, where time signals in the range $3 <$ channel < 4000 were selected. To label an event as good, both a time signal and an energy signal in the good range were required. For example, an x-ray gated TAS spectra would require a good E/T signal from both the planar detector and the TAS detector.

[1]The sum of the signals of the PMs can be done via software or via hardware. G_TAS_Hard is the sum via hardware.

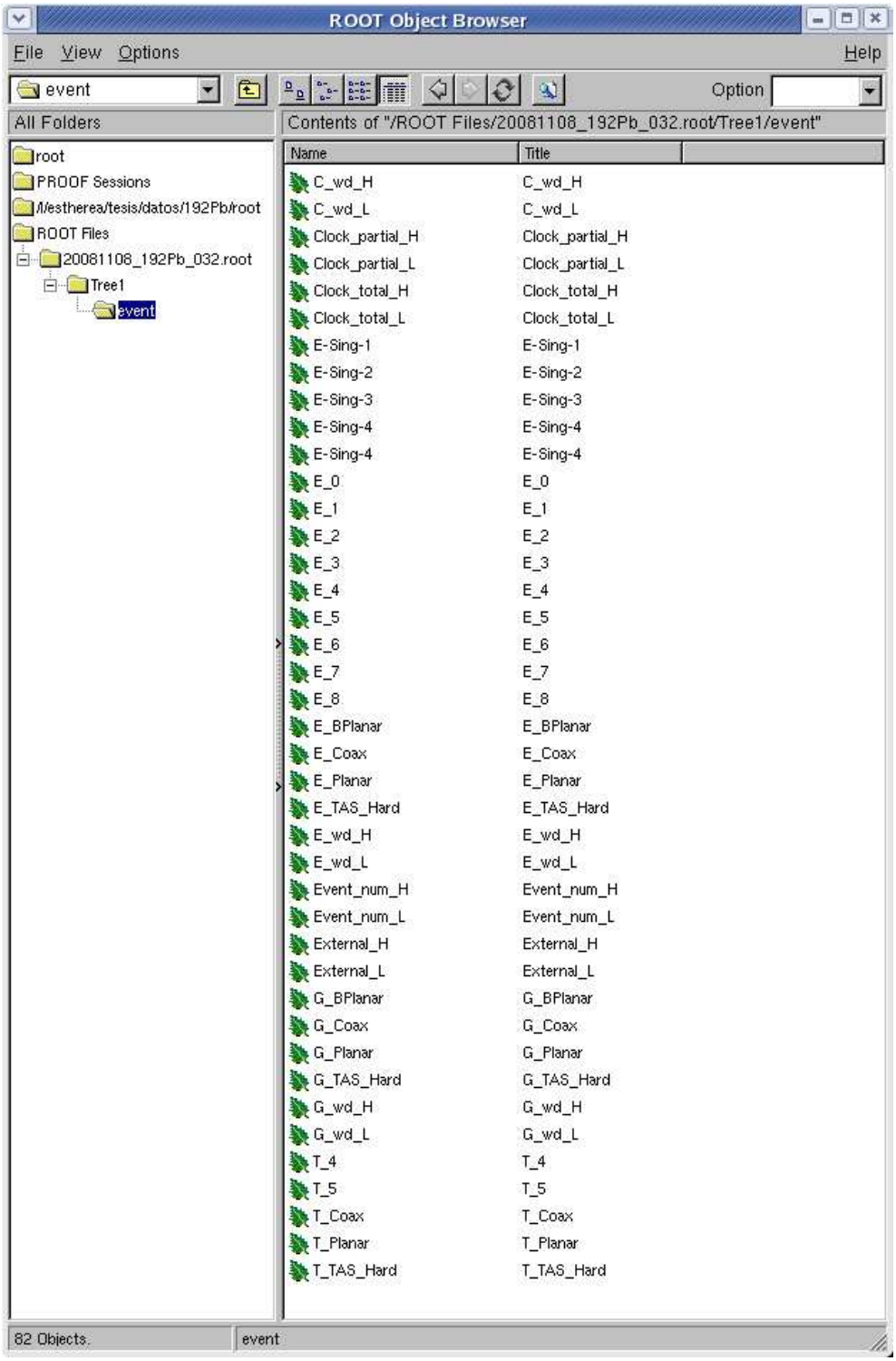

Figure C.1: Data structure of one of the ROOT files were the data was stored. This one is for run 32, when the ^{192}Pb was measured. From the leafs of interest, those whose name starts with E store the signals from the ADCs of 4k channels, and those starting with G, from the 8k ADCs. For more information about the experimental details see Chap. 8.

C.1. Alignment

During the measurements, there was a problem with the cooling system of the TAS setup. As a consequence, gain shifts appeared in the spectra. When plotting the TAS background spectra for every run, it was found that the centroid position of the potassium peak appears in a different position depending on the run number, as shown in Fig. C.2 a). That is, it changes with time: it seems to move to the left as the run number increases. The centroid of the potassium peak is plotted against the run number in Fig. C.2 b), to give a rough idea of the evolution of the gain change with time.

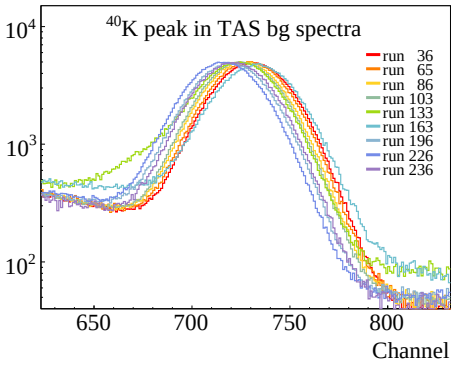

a) Raw TAS background spectra showing that the centroid position of the potassium peak is moving from run to run. These spectra are generated by reading all the statistics of the G_TAS_HARD leaf in the Tree structure shown in Fig. C.1 for each run of background measurements.

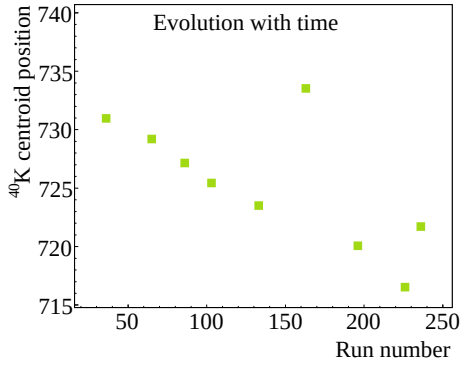

b) Evolution of the centroid position of the potassium peak with the run number. The points correspond to the plots of a). This plot gives a rough idea of the change of the gain with time.

Figure C.2: Gain drift of the TAS spectra.

This is an important observation, as the spectra must be generated with all the statistics of the measurement, and for this, the statistics of all the runs of a measurement have to be summed up. But if the spectra are misaligned it is not possible to add them, they must be corrected (aligned) first.

There is a LED connected to *Lucrecia*, triggered by a pulse generator. It monitors the crystal response stability, introducing a signal in the TAS spectra that was intended to help in the online stabilization of the photomultipliers. However, this signal was less stable than the TAS signal, as it moved even more than the latter, so it could not be used to align the spectra. Instead, a routine of the online software that controlled the DACQ system was used to monitor one peak of the TAS spectrum. This online control worked well but was still not enough to prevent the jumps in the gain.

The effect was corrected in the offline analysis. The idea is to move all the TAS spectra, so that the potassium peak appears in the same position for all the runs. This can be achieved by making a recalibration of each run's TAS spectrum with the program NRECALPOIS.F (introduced in Appendix A to make the measured sources match the calibration of the Monte Carlo simulated ones). In this way, one run is chosen as the reference, and the rest of the spectra are corrected to that run's gain. This step has to be done before the procedure described in Appendix A.

A fit of the potassium peaks of each run was made to obtain the position of their centroids. A typical TAS peak was modeled as a Gaussian profile, a Compton contribution and a background. The Compton contribution was described by a step function and the background by a linear function. The peaks were fitted to the function C.4 that is a combination of the three functions parameterized in Eqs. C.1, C.2 and C.3.

- **Step function:**

$$\begin{array}{rr|l} a_1 = & 0.34082 & p = 0.47047 \\ a_2 = & -0.09587 & \\ a_3 = & 0.74785 & arg = \frac{1}{\sqrt{2}}\frac{x-p_1}{p_2} \end{array}$$

(the values of these constant parameters are taken from [Abr64])

arg $<$ 0:

$$t = \frac{1}{1+p\cdot|arg|} \qquad \text{step} = 1 - \frac{1}{2}\left(a_1 + a_2 t + a_3 t^2\right) te^{-|arg|^2} \tag{C.1}$$

arg $\geq$ 0:

$$t = \frac{1}{1+p\cdot arg} \qquad \text{step} = \frac{1}{2}\left(a_1 + a_2 t + a_3 t^2\right) te^{-arg^2}$$

- **Gauss function:**

$$\text{gauss} = \frac{1}{\sqrt{2\pi}p_2}e^{-|arg|^2} \tag{C.2}$$

- **Linear function:**

$$\text{backg} = p_4 + p_5 x \tag{C.3}$$

- **Fit function:**

$$\boxed{\text{value} = p_0\text{gauss} + p_3\text{step} + \text{backg}} \tag{C.4}$$

where p_0 is the area of the peak, p_1 is the Gaussian's centroid, p_2 is the Gaussian's sigma, p_3 is the step height, p_4 is the offset and p_5 is the slope. The fit program needs starting values for at least p_0, p_1 and p_2, that can be easily obtained from the peak to be fitted. Starting values for the rest of parameters can also be provided.

This fit is robust, as changing these values does not have a large effect on the results or on the χ^2. Any time there were two peaks that were so close that could not be fitted separately (like for example, the peaks at 1332.5 and 1460.9 (^{40}K) in ^{60}Co), a slightly different fit function was used, which uses 2 step functions and 2 Gaussians. In Fig. C.3, the results of typical fits are shown.

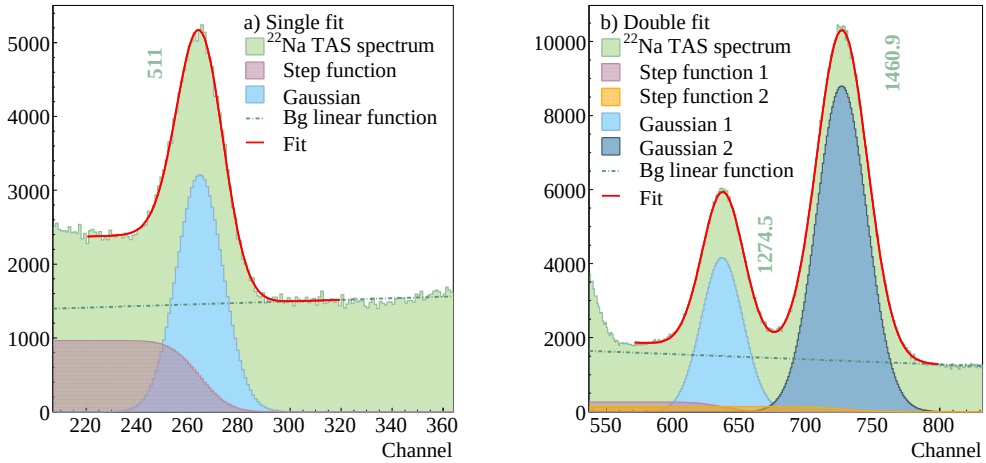

Figure C.3: Results of the fit of some peaks in the case of the ^{22}Na source: a) Single fit b) Double fit

Once the centroids of all the runs were calculated with this function, a recalibration was made for each TAS spectrum using a linear function with two points: zero and the potassium peak centroid position. The offset of this linear function is zero and the slope is the ratio between the centroid position calculated for the reference run and the centroid position calculated for the run to be recalibrated. The reference was run number 102, a background measurement coming after a relatively stable source measurement where the PMs were not apparently drifting. Using NRECALPOIS.F with

$$(I_0,\, I_1,\, I_2) = (0,\, \tfrac{p_1(run\ \ 102)}{p_1(run\ \ \sharp)},\, 0)$$

as the initial calibration coefficients and

$$(F_0,\, F_1,\, F_2) = (0,\, 1,\, 0)$$

as the final calibration coefficients, a recalibrated spectrum was obtained. At the end of this procedure there was one recalibration factor (or alignment factor)

$$\tfrac{p_1(run\ \ 102)}{p_1(run\ \ \sharp)}$$

associated with each run number.

In those cases where the fits were difficult because of the presence of nearby peaks or complicated backgrounds, the slopes ${}^{p_1(run\ 102)}/_{p_1(run\ \sharp)}$ were adjusted manually. Once the alignment was ready, meaning that the difference in the position of the centroids was less than 2 channels (∼4 keV, which is reasonable for the TAS detector), all the runs of each measurement were added. In the case of the gates, first the TAS gates for each run number were generated, then the recalibration was applied to each gate and finally they were added. In Fig. C.4 a comparison between the raw spectra and the aligned spectra is shown.

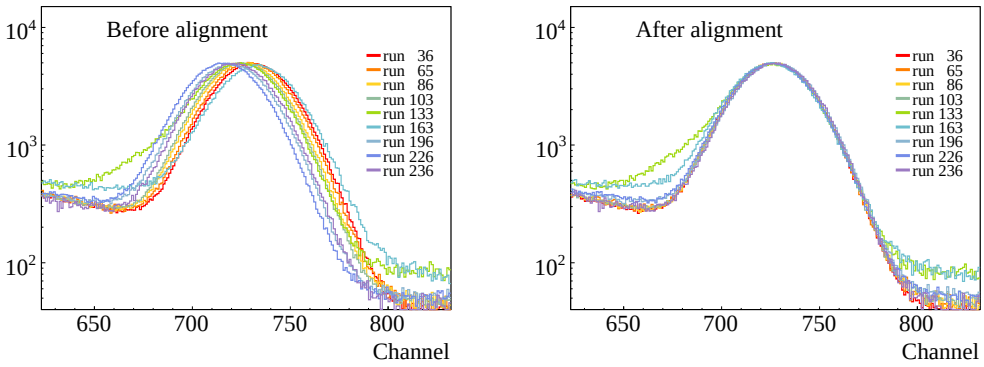

Figure C.4: Comparison between the raw spectra and the aligned spectra.

C.2. Calibrations

In this section the step 2 b) of the general summary of Appendix A is fully covered. The relevant information of the sources used in the analysis is presented in Table C.11 of Sec. C.4 (p. 182).

C.2.1. Energy calibrations

Sources:

In general, in the case of the *Lucrecia* detector, the sum peaks can not be used for the energy calibrations[2]. Also, the ${}^{40}K$ peak (as well as other background peaks like 511 and 1022 keV) where not used as we are not sure that they where emitted from the center of the TAS.

Since the ADC's are not linear at low energies, the spectra was divided in two calibration zones. The data was fitted to the function C.5:

$$E(x) = \begin{cases} a + bx + cx^2 & \text{if} \quad x < X_0 \\ n + mx & \text{if} \quad x > X_0 \end{cases} \tag{C.5}$$

[2] *Lucrecia* is made of NaI which suffers from a non proportionality in the light production, as mentioned in Sub. 2.2.2.

obeying:

$$a + bX_0 + cX_0^2 = n + mX_0$$

where x is the channel, X_0 is the channel that separates the two zones, (a, b, c) are the coefficients of the quadratic function, and (n, m) are the coefficients of the linear function. It is also possible to fit to one linear function, two linear functions, two quadratic functions, etc. but this is the combination that better reproduces most of the data (quadratic for low energies, linear for the rest).

To fit the peaks of the different sources, the same function of Sec. C.1 was used. In Table C.1 the peaks used for the energy calibration of the TAS detector are shown. The calibration coefficients can be found in Table C.5 and the fit in Fig. C.5 a).

Table C.1: Peaks used for the energy calibration of the TAS detector.

Source	Energy [keV]	Centroid [ch]
^{133}Ba	[a]80.997	49.3824
^{137}Cs	661.7	340.7
^{60}Co	1173.2	587.422
	1332.5	664.778
^{24}Na	1368.7	682.628
	2754.0	1352.39

[a] Complex peak, weighted sum of two close peaks: 79.6142(*12*) and 80.9979(*11.*)

The germanium detector was also calibrated in energy. A specific program (XTRACKN) developed by the Gamma Group of the Legnaro National Laboratory (LNL, INFN, Padova, Italy) was used for this purpose.

- For the calibration in energy of the planar detector the sources with low energy peaks ^{133}Ba, ^{137}Cs and ^{152}Eu were used.

- For the coaxial detector several calibrations were tested, the best one is shown in Table C.5. A calibration function for ^{152}Eu and ^{241}Am (which have a different gain) was also found. The peaks used for the energy calibration of the coaxial germanium are shown in Table C.3).

In Table C.5 the results obtained for the calibrations in energy are shown for all the detectors.

Table C.2: Peaks used for the energy calibration of the planar germanium.

Source	Energy [keV]	Centroid [ch]
^{133}Ba	30.973	414.0
^{137}Cs	32.194	430.5
^{133}Ba	34.987	468.0
^{137}Cs	36.378	487.5
	37.255	498.5
^{133}Ba	53.1625	712.0
	80.9971	1085.5
^{152}Eu	121.7817	1633.0
^{133}Ba	160.6109	2154.0
^{152}Eu	244.6975	3283.0
^{133}Ba	276.3997	3708.5
	302.8510	4063.5
^{152}Eu	344.278	4619.0
^{133}Ba	356.0134	4777.0
	383.8480	5150.5
^{152}Eu	411.115	5517.0
	443.975	5958.0

Table C.3: Peaks used for the energy calibration of the coaxial germanium.

Source	Energy [keV]	Centroid [ch]
^{133}Ba	80.997	160.5
	160.6109	319.5
	223.2373	444.0
^{228}Th	238.632	475.0
	240.986	480.0
^{133}Ba	276.3997	549.5
	302.851	602.5
	356.0134	708.5
	383.848	763.5
^{228}Th	510.77	1016.5
	583.187	1161.0
^{137}Cs	661.657	1317.0
^{228}Th	727.330	1449.0
	860.557	1715.0
^{60}Co	1173.228	2339.0
^{22}Na	1274.537	2542.0
^{60}Co	1332.508	2657.5
^{24}Na	1368.626	2729.0
^{228}Th	1620.5	3234.0
	2614.511	5223.0
^{24}Na	2754.007	5500.0

Monte Carlo:

For the calibration of the Monte Carlo simulation, γ rays of particular energies were simulated. They were launched from the center of the TAS detector and their energy deposition was tracked by the simulation code. Only a fit to the simulated TAS data was made (the energy spectra produced in the germanium detectors were not used). The fit of function C.4 provided poor results at low energies because of the fluctuations of the low energy tail of the peaks (see Fig. C.6), so a direct analysis was made with the function `getMean()` of the ROOT libraries [ROOT]. The peaks used for the calibration are presented in Table C.4.

In Table C.5 the coefficients of the calibration of sources and MC are shown.

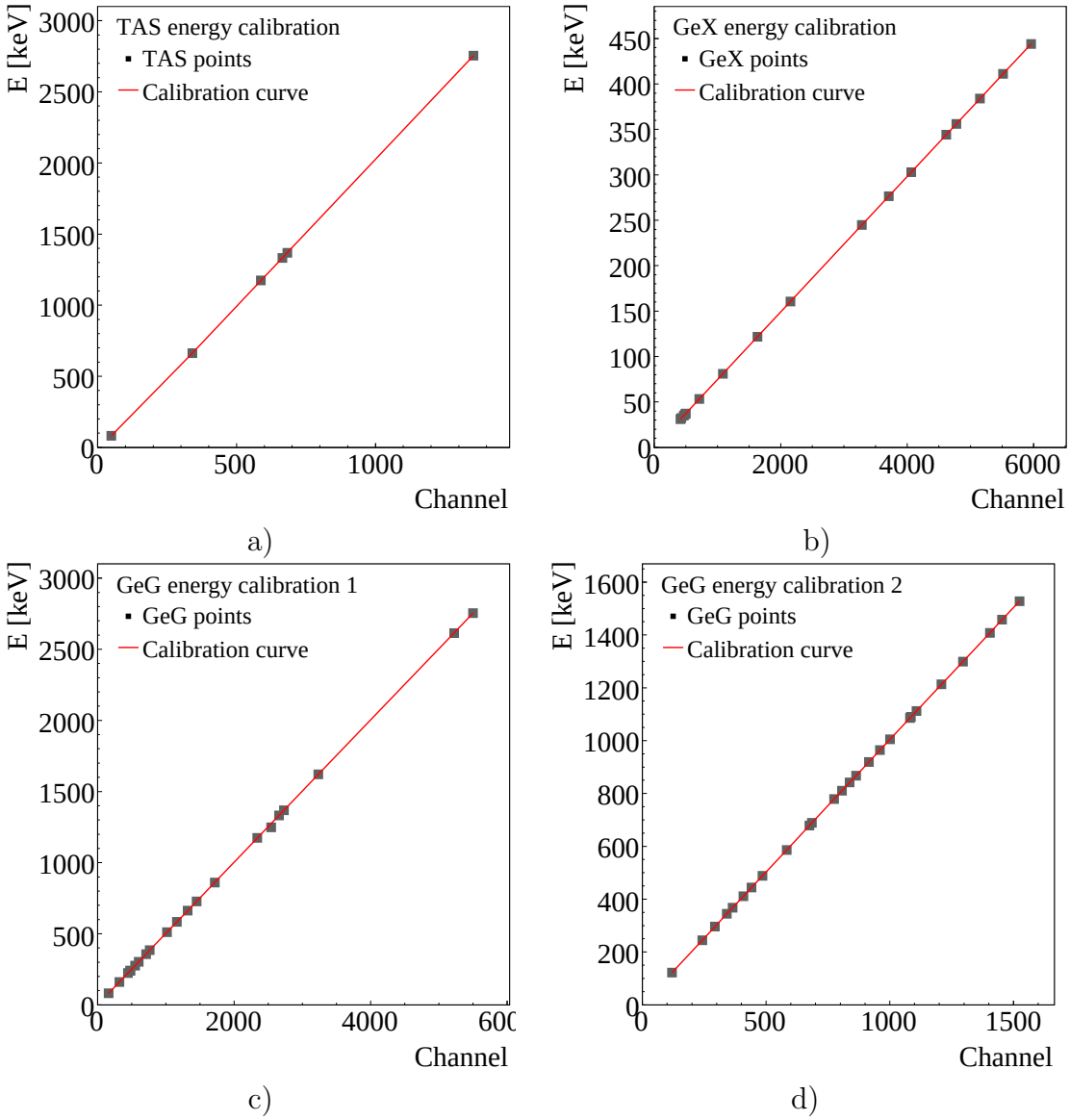

Figure C.5: Energy calibration plots for the different detectors used in the analysis. *a)* TAS. *b)* Planar germanium. *c)* Coaxial germanium. *d)* Coaxial germanium with half of the gain.

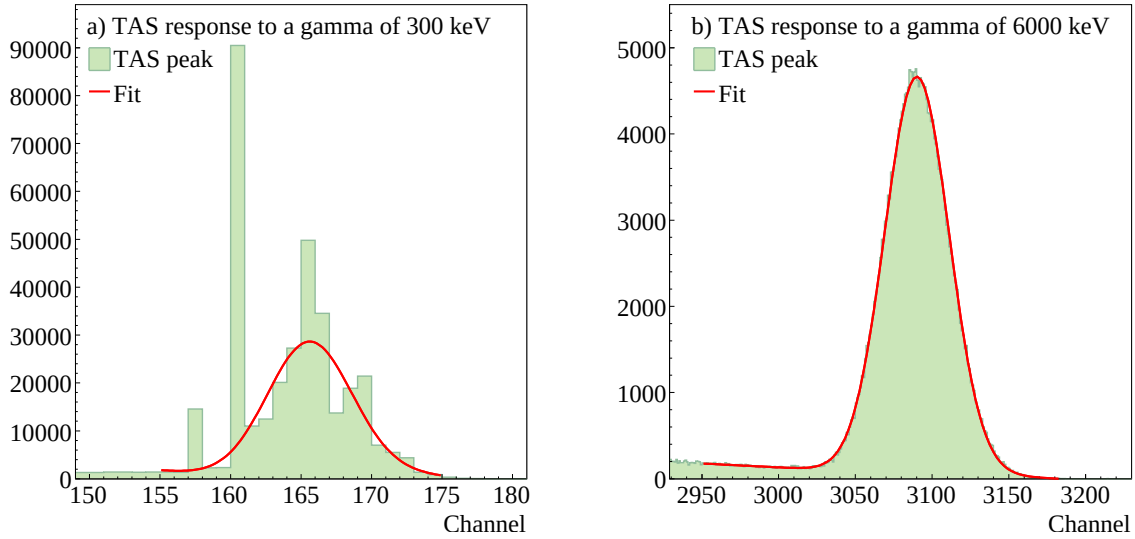

Figure C.6: Comparison of low and high energy MC peaks.

Table C.4: Peaks used for the energy calibration of the MC simulation.

Source	Energy [keV]	Centroid [ch]
Simulated	500	269.803
	800	425.735
	1022	539.975
^{60}Co	1173.2	617.585
^{22}Na	1274	669.55
^{60}Co	1332.5	699.248
^{24}Na	1368.7	717.771
Simulated	1500	785.094
	1785	931.329
	2000	1041.65
	2296	1193.46
^{24}Na	2754	1428.26
Simulated	3000	1554.51
	4000	2066.76
	5000	2578.51
	6000	3089.74

Table C.5: Calibration coefficients of Eq. C.5 for the experimental data of the different detectors used in the analysis and for the simulation. Ge Coaxial 1 stands for germanium coaxial detector normal calibration while Ge Coaxial 2 is the one obtained for the files with a factor 2 in the coaxial germanium gain. TAS is the calibration for the experimental TAS data and TAS MC for the simulated TAS data.

Detector	a [keV]	b $\left[\frac{keV}{ch}\right]$	c $\left[\frac{keV^2}{ch^2}\right]$	X_0 [ch]	n [keV]	m $\left[\frac{keV}{ch}\right]$
Ge Planar	-	-	-	-	0.121(7)	0.074500(2)
Ge Coaxial 1	0.6(8)	0.500(4)	0.000002(4)	993(100)	3(4)	0.50019(9)
Ge Coaxial 2	2.2(2)	1.002(1)	0.0000005(9)	863(70)	4.8(9)	0.9992(2)
TAS	-10(6)	1.8(1)	0.0004(3)	356(2)	-42(48)	2.067(2)
TAS MC	-15(3)	2(3)	0.00004(3)	649(124)	-33(2871)	2(3)

C.2.2. Width calibration

The width calibration was only made for the TAS detector, and not for the germanium detectors, since it is necessary for the MC spectra widening function calculation. To obtain the σ in energy units, the width in channels is transformed to energy using the parameters of Table C.5 with $a = n = 0$ and Eq. C.5.

The width calibration is in general well described for both MC and sources by:

$$\begin{aligned} \sigma^2(E) &= a_\sigma + b_\sigma E + c_\sigma E^2 \\ with : \sigma^2(0) &= a_\sigma = 0 \end{aligned} \tag{C.6}$$

where (a_σ, b_σ, c_σ) are the coefficients of the quadratic function, E is the energy, and $\sigma^2(E)$ is the squared width in units of energy. Both sets of data where fitted to the quadratic function C.6.

Sources:

The peaks used for the experimental width calibration are shown in Table C.6.

Monte Carlo:

In an analogous way to the case of the energy calibration (Sub. C.2.1), the function `getSigma()` was used to obtain the widths of the MC peaks, as the fit to the peaks at low energy was difficult. The peaks used for the MC width calibration are shown in Table C.7.

Table C.6: Peaks used for the width calibration of the experimental TAS spectra.

Source	Energy [keV]	Width [ch]
^{133}Ba	80.997	2.32615
^{137}Cs	661.7	10.4338
^{60}Co	1173.2	13.821
	1332.5	14.7797
^{24}Na	1368.7	15.2232
	2754	25.6614

Table C.7: Peaks used for the width calibration of the simulation.

Source	Energy [keV]	Width [ch]
Simulated	500	5.46961
	800	7.00069
	1022	7.71924
^{60}Co	1173.2	8.42502
^{22}Na	1274	8.73698
^{60}Co	1332.5	9.07931
^{24}Na	1368.7	9.34106
Simulated	1500	9.70469
	1785	11.0154
	2000	12.0387
	2296	13.1942
^{24}Na	2754	14.8381
Simulated	3000	15.4887
	4000	17.9811
	5000	19.7427
	6000	21.8614

Instrumental resolution distribution:

From the data of Tables C.6 and C.7 the coefficients of Table C.8 were found using the C.6 function.

Table C.8: Calibration coefficients of Eq. C.6 for the measured sources and for the MC simulations.

Set	b_σ	c_σ
TAS	0.45(4)	0.00020(2)
MC	0.25(1)	0.000009(2)

Once the calibrations in energy and width are obtained for both the simulation and the measured sources, the calibration that will widen the MC peaks to the experimental width can be calculated as the difference of the squared sigma of the sources and the MC squared sigma, that is, by means of a fit to the function C.7:

$$\begin{aligned} \sigma^2_{instrum.}(E) &= s_0 + s_1 E + s_2 E^2 = \sigma^2_{exp}(E) - \sigma^2_{MC}(E) \\ again: \sigma^2_{instrum.}(0) &= s_0 = 0 \end{aligned} \tag{C.7}$$

For the fit to function C.7, the experimental values of $\sigma^2_{exp}(E)$ and the values of $\sigma^2_{MC}(E)$ were used, instead of the values generated with Eq. C.6 and coefficients of Table C.8. The widening function obtained in this way is presented in Eq. C.8:

$$\boxed{\sigma^2_{instrum.}(E) = 0.25(2)E + 0.00017(1)E^2} \tag{C.8}$$

In Fig. C.7 the calibrations are shown. In Fig. C.8 the instrumental resolution distribution function is shown.

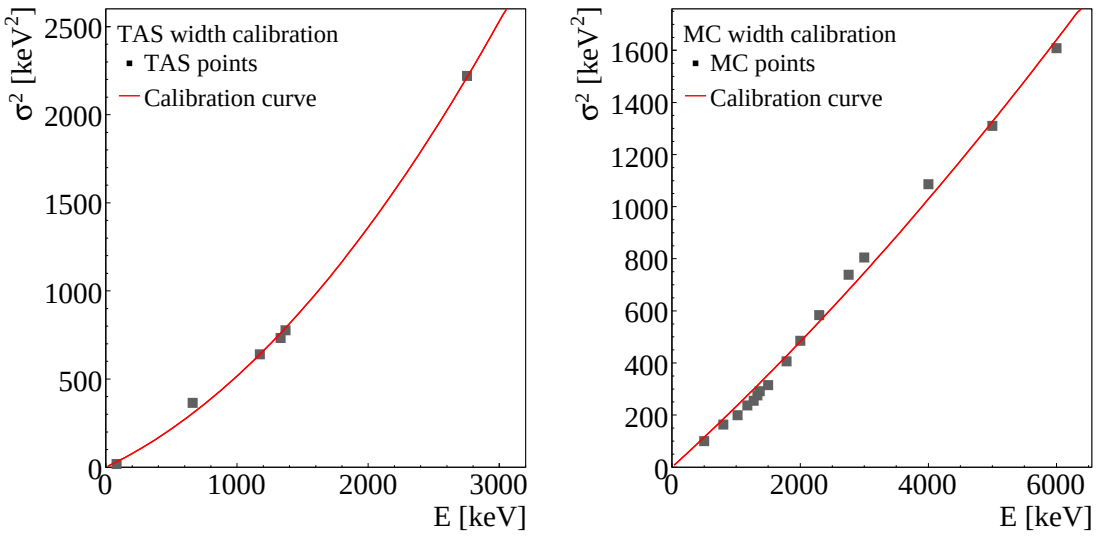

a) b)

Figure C.7: Width calibration plots. *a)* For TAS data. *b)* For MC simulation.

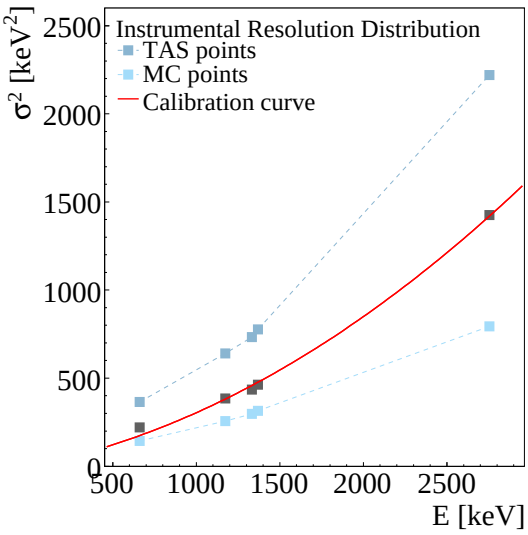

Figure C.8: Function for the instrumental resolution distribution $\Delta\sigma^2(E)$. For the fit, the points of $\sigma^2_{MC}(E)$ and the experimental points of $\sigma^2_{exp}(E)$ were used.

C.3. Efficiencies

For the calculation of the efficiencies of the germanium detectors, the XTRACKN program was used again, to obtain the area under the peaks. The available information of the ISOLDE sources is shown in Table C.11 p. 182. For the calibration in efficiency only the ^{152}Eu and ^{241}Am sources were used. These sources have a different calibration in energy that is labeled as "Ge Coaxial 2" in Table C.5.

The efficiency of the sources was calculated by means of Equation C.9.

$$\epsilon = \frac{Detected\ \ quanta}{Emitted\ \ quanta} = 100\frac{I_{peak}/\Delta t}{A(t_{meas.})br}. \tag{C.9}$$

were I_{peak} is the area under the peak, Δt is the measurement time, $A(t_{meas.})$ is the activity in the moment of the measurement $t_{meas.}$, and br is the intensity of the peak as it appears in the databases. The peaks used are shown in Table C.9.

Table C.9: Peaks used for the calibration in efficiency of the germanium detectors. Column *br* taken from the relevant Nuclear Data Sheets.

Source	Δt [s]	E [keV]	$I_{peak}/\Delta t$ [kBq]	br [%]	ϵ [%]
a) Planar Ge					
^{152}Eu	4440	121.7817	0.1315	28.67	4.2466
		244.6975	0.0082	7.61	1.0027
		344.2785	0.0205	26.60	0.7146
		411.1163	0.0012	2.24	0.4812
		433.965	0.0011	2.83	0.3728
^{241}Am	3240	26.3446	0.0399	2.27	4.3818
		59.5409	0.7533	35.90	5.2302
b) Coaxial Ge					
^{152}Eu	4440	121.7817	0.0103	28.67	0.3330
		244.6975	0.0058	7.61	0.7102
		344.2785	0.0170	26.60	0.5912
		411.1163	0.0012	2.24	0.4928
		433.965	0.0016	2.83	0.5202
		778.904	0.0043	12.98	0.3065
		867.373	0.0013	4.26	0.2903
		964.079	0.0042	14.65	0.2649
		1085.869	0.0026	10.24	0.2397
		1112.069	0.0036	13.69	0.2420
		1408.006	0.0046	21.07	0.2024

The efficiencies where fitted to the following function [Jac87]:

$$ln\epsilon(E_\gamma) + 25 = \left(a_0 + a_1 x + a_2 x^2\right) \frac{2}{\pi} \arctan\left(e^{a_3 + a_4 x + a_5 x^3}\right) \tag{C.10}$$

where $x = ln(E_\gamma)$. The first part describes the photopeak efficiency from $\sim$ 200 keV to $\sim$ 2500 keV and the arctan () function is introduced empirically to account for the sharp decrease of efficiency at low energies. In order to make a correct fit, at least 3 parameters have to be initialized. To have a rough idea of their order of magnitude, a first fit was made to a quadratic function and the values of the 3 parameters of this function were given as initial values for (a_0, a_1, a_2). In Table C.10 the parameters a_i obtained for the different detectors are shown.

Table C.10: Calibration coefficients of Eq. C.10 for the germanium detectors

Detector	a_0	a_1	a_2	a_3	a_4	a_5
Ge Planar	381(540)	-45(83)	0.5(3)	-2(1)	0.21(6)	-0.000112403(8)
Ge Coaxial	-132.0(3)	58.09(6)	-4.611(9)	3.95(1)	-0.935(2)	0.00743(3)

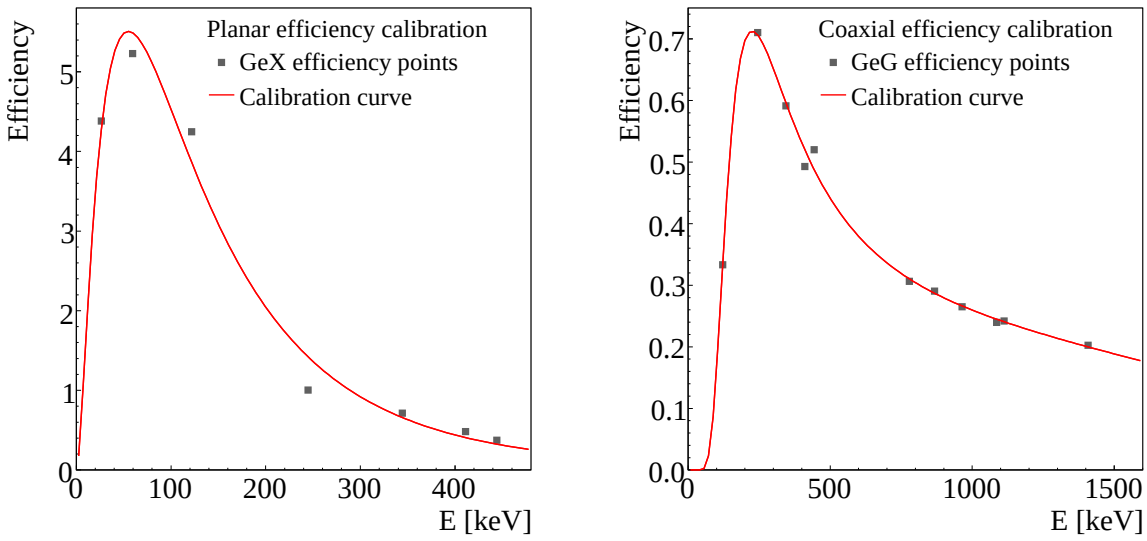

a) b)

Figure C.9: Efficiency calibration. a) For the planar germanium detector. b) For the coaxial germanium detector.

C.4. Sources

In this section a list of the sources that were measured at the experiment is presented (Table C.11), together with their de-excitation schemes (Figs.C.10, C.11, C.12, C.13, C.14 and C.15). The ^{24}Na source was produced during the measurements from a beam of 25 pulses of $5 \cdot 10^{12}$ protons, with a beam gate of 1.6 s. The TAS counting rate during this Na measurement was $\sim$ 5100 Hz.

Table C.11: Information available for the ISOLDE sources: $t_{1/2}$ is the half-life, A_t is the activity measured the 7/06/2010 and A_t is the activity in the moment of the measurements $t_{meas.}$.

CODE	Parent	Daughter	Decay Mode	$t_{1/2}$	$t_{meas.}$ (d / m / y)	A_t [kBq]	$A(t_{meas.})$ [kBq]
3607.7	^{22}Na	^{22}Ne	β^+	2.6027 y	11/11/2008	13.59	20.54
BEAM	^{24}Na	^{24}Mg	β^-	14.997 h	9/11/2008	-	5.1
2669 RP	^{60}Co	^{60}Ni	β^-	1925.28 d	9/11/2008	1.38	1.69
2668 RP	^{137}Cs	^{137}Ba	β^-	30.08 y	10/11/2008	20.83	31.69
2670 RP	^{152}Eu	^{152}Gd ^{152}Sm	β^- EC	13.537 y	11/11/2008	9.98	10.80
2666 RP	^{241}Am	^{237}Np	α	432.6 y	11/11/2008	40.02	40.12

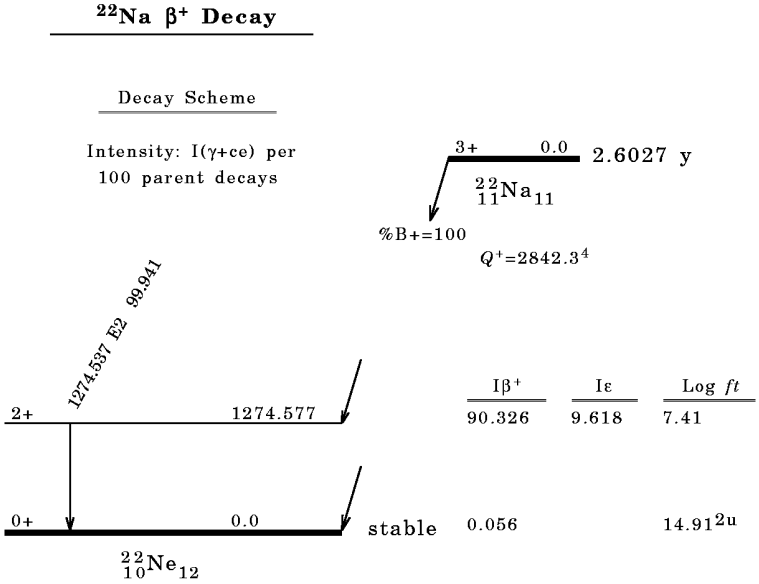

Figure C.10: ^{22}Na level scheme. Taken from [Fir05].

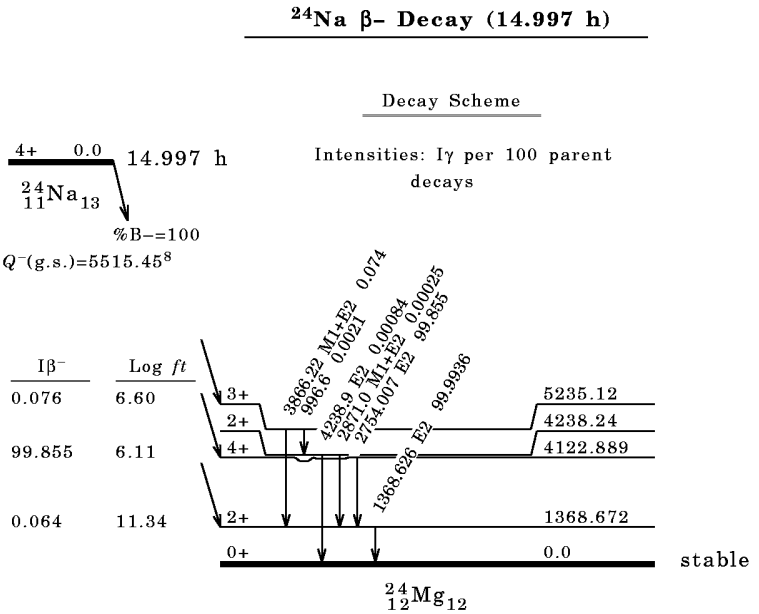

Figure C.11: ^{24}Na level scheme. Taken from [Fir07].

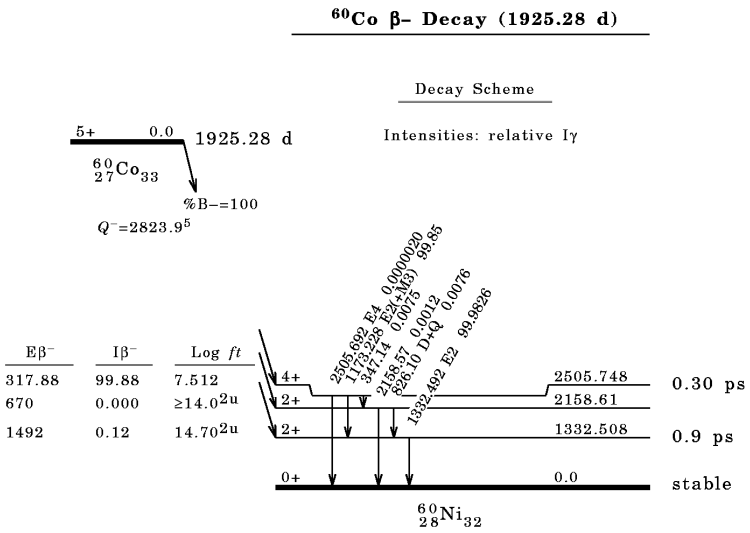

Figure C.12: ^{60}Co level scheme. Taken from [Tul03].

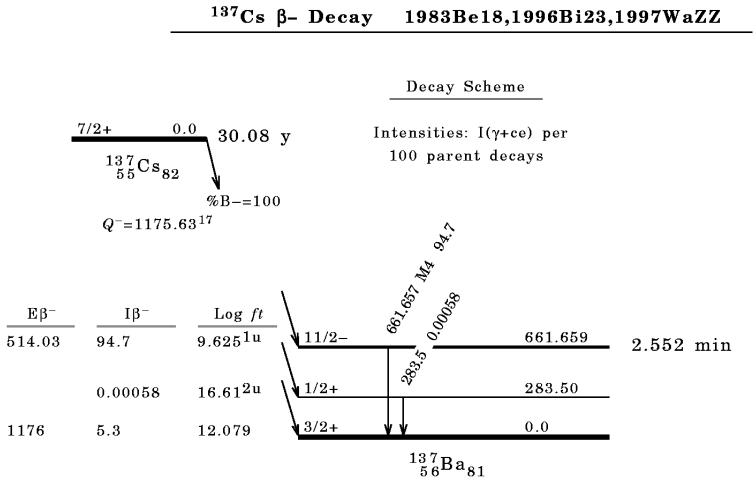

Figure C.13: ^{137}Cs level scheme. Taken from [Tul03].

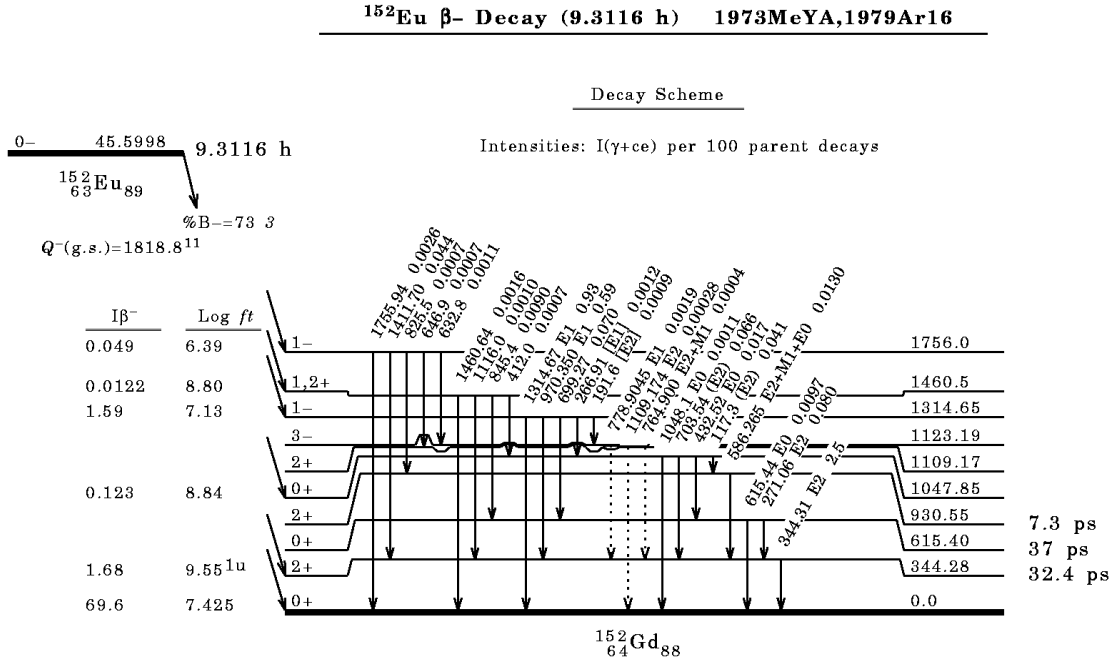

Figure C.14: ^{152}Eu level scheme, Gd branch. Taken from [Art96b].

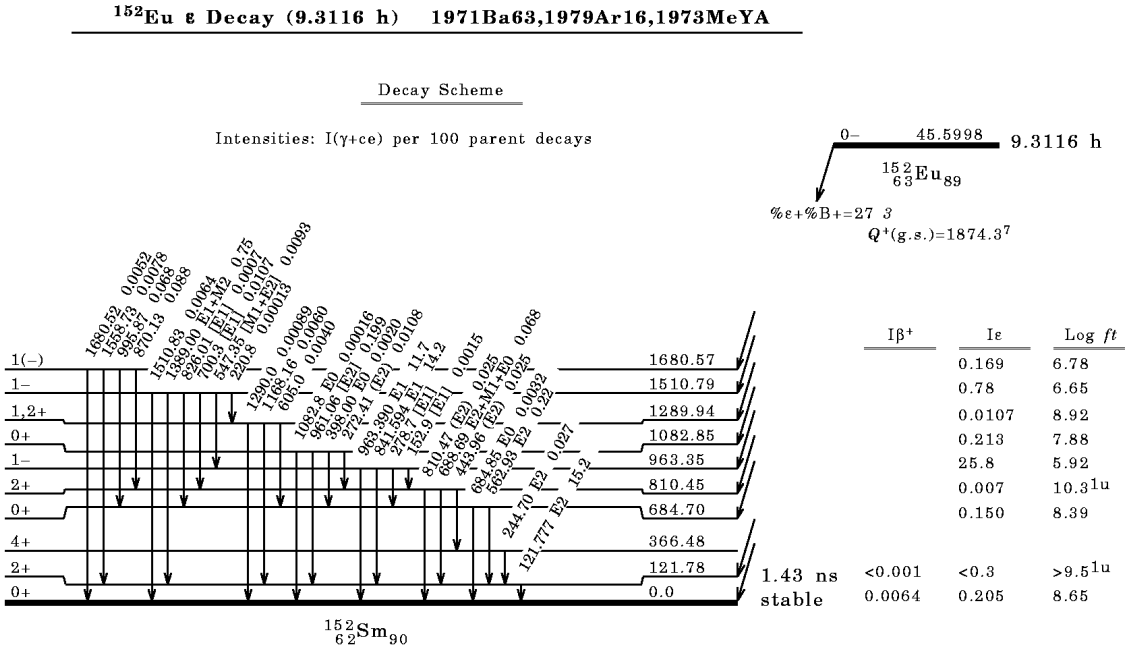

Figure C.15: ^{152}Eu level scheme, Sm branch. Taken from [Art96b].

References

[Abr64] M. Abramowitz and I. A. Stegun, "Handbook of Mathematical Functions with Formulas Graphs and Mathematical Tables" (1964) Dover, New York, isbn = "0-486-61272-4".

[Add10] Addendum to ISOLDE Experimental Proposal, CERN-INTC-2011-004, INTC-P-199-ADD-1, Spokespersons: A. Algora, B. Rubio, W. Gelletly.

[Agr11] J. Agramunt et al., in preparation.

[Ahm01] Q. R. Ahmad et al., Phys. Rev. Lett. 87 (2001) 7.

[Alg03] A. Algora et al., Phys. Rev. C 68 (2003) 034301.

[Alg04] A. Algora et al., Phys. Rev. C 70 (2004) 064301.

[And00] A. N. Andreyev et al., Nature 405, (2000) 430.

[Art96] A. Artna-Cohen, Nuclear Data Sheets 79 (1996) 1 and K. S. Toth et al. Phys. Rev. C 35 (1987) 310.

[Art96b] A. Artna-Cohen, Nuclear Data Sheets 79 (1996) 1.

[Aud03] G. Audi et al., Nucl. Phys. A 729 (2003) 337.

[Bag98] C. M. Baglin, Nuclear Data Sheets 84 (1998) 717, D. C. Sousa et al., Phys. Rev. C 24 (1981) 2245 and G. Audi et al., Nucl. Phys. A, Vol 595, 4 (1995) 409.

[Bag03] C. M. Baglin, Nuclear Data Sheets 99 (2003) 1.

[Ber05] J. Bernabéu et al., NIMA JHEP 12 (2005) 14.

[Ber09] J. Bernabéu et al., arXiv:0905.2913v1 [hep-ph] (2009).

[Cab78] N. Cabibbo, Phys. Lett. B 72, 3 (1978) 333, and J. Bernabéu, hep-ph/9904474v1 (1999).

[Can98] D. Cano-Ott, Trabajo de Investigación Tutelado (1998) Valencia.

[Can99a] D. Cano-Ott et al., NIMA 430 (1999) 333.

[Can99b] D. Cano-Ott et al., NIMA 430 (1999) 488.

[Can00] D. Cano-Ott, PhD Thesis (2000) Valencia.

[Dem01] P. Demetriou et al., Nucl. Phys. A 695 (2001) 95.

[Der95] E. derMateosian, NDS 75 (1995) 827 and K.S. Toth et al., Phys. Rev. C 35 (1987) 620.

[DeW07] H. De Witte et al., Phys. Rev. Lett. 98 (2007) 112502.

[Dil73] W. Dilg et al., Nucl. Phys. A 217 (2001) 269.

[Dug03] T. Duguet et al., Phys. Lett. B 559 (2003) 201.

[Egi04] J. L. Egido et al., Phys. Rev. Lett. 93 (2004) 082502, and M. Bender et al., Phys. Rev. C 69 (2004) 064303.

[Eng56] D. Engelkemeir, Rew. Sci. Instr. 27 (1956) 589.

[Eng73] J. Engler et al., NIM 106 (1973) 189.

[ENSDF] Evaluated Nuclear Structure Data File, http://www.nndc.bnl.gov/ensdf.

[Esp10] C. Espinoza, PhD Thesis (2010) Valencia.

[Fir05] R.B. Firestone et al., Nuclear Data Sheets 106 (2005) 1.

[Fir07] R.B. Firestone et al., Nuclear Data Sheets 108 (2007) 2319.

[Fra04] A. Frank et al., Phys. Rev. C 69 (2004) 034323.

[Fri95] F. Frisk et al., Phys. Rev. C 52 (1995) 2468.

[Fog11] G. L. Fogli et al., arXiv:1106.6028v1 [hep-ph] 29 Jun 2011.

[Fos03] R. Fossion et al., Phys. Rev. C 67 (2003) 024306.

[Geant] Geant4 libraries, http://geant4.cern.ch.

[Goo91] H. G. Essel et al., GOOSY Buffer Structures, http://www-linux.gsi.de/~goofy/goosy/goosy.php.

[Gor01] S. Goriely et al., Atomic Data Nuclear Data Tables 77 (2001) 311.

[Gri69] V. Gribov et al., Phys. Lett. 28B (1969) 7.

[GSI] GSI (*Gesellschaft für Schwerionenforschung*) GmbH, Planckstr. 1, 64291 Darmstadt. Phone: +49-6159-71- 0, http://www.gsi.de.

[Har77] L. C. Hardy et al., Phys. Lett. B71 (1977) 307.

[Hee93] J. Heese et al., Phys. Lett. B 302 (1993) 390.

[Hel96] O. Helene et al., NIM A 378 (1996) 624.

[Hey91] K. Heyde et al., Phys. Rev. C 44 5 (1991) 2216,

[ISO] ISOLDE, CERN, CH-1211 Geneva 23, http://isolde.web.cern.ch/ISOLDE.

[Jac87] B. Jäckel et al., NIM A 261 (1987) 543.

[Jul01] R. Julin et al., J. Phys. G: Nucl. Part. Phys. 27 (2001) R109.

[Kar97] M. Karny et al., Nucl. Instr. and Meth. B 126 (1997) 411.

[Kle88] P. Kleinheinz et al., KFA Annual Report (1988) 34 and P. Kleinheinz et al., Phys. Rev. Lett. 55 (1985) 2664.

[Kod01] K. Kodama et al., Phys. Lett. B 504 (2001) 218.

[Kop90] J. Kopecky, Phys. Rev. C 41, 5 (1990) 1941.

[Kos03] U. Köster et al., NIM B 204 (2003) 347.

[LOGFT] LOGFT, National Nuclear Data Center, Brookhaven National Laboratory, http://www.nndc.bnl.gov/logft.

[May77] F. R. May et al., Phys. Lett. B 68 (1977) 113.

[Mol95] P. Möller et al., Atomic Data Nuclear Data Tables 59 (1995) 185.

[Mor56] H. Morinaga, Phys. Rev. 101 (1956) 254.

[Mor06] O. Moreno et al., Phys. Rev. C 73 (2006) 054302.

[Nac04a] E. Nácher, PhD Thesis (2004) Valencia.

[Nac04b] E. Nácher et al., Phys. Rev. Lett. 92 (2004) 232501.

[Naz93] W. Nazarewicz, Phys. Lett. B 305 (1993) 195.

[Nic02] T. Niksic, Phys. Rev. C65 (2002) 054320.

[NDS] Nuclear Data Sheets, http://www.nndc.bnl.gov/nds.

[Nuc71] N.B Gove, M.J. Martin., Atomic Data Nuclear Data Tables 10 (1971) 205.

[Poi04a] E. Poirier et al., Phys. Rev. C 69 (2004) 034307.

[Poi04b] E. Poirier et al., PhD Thesis (2004) Strasbourg.

[Pro07] ISOLDE Experimental Proposal, CERN-INTC-2005-027, INTC-P-199, Spokespersons: A. Algora, B. Rubio, W. Gelletly.

[Pro12] ISOLDE Experimental Proposal, CERN-INTC-2012-012, INTC-P-328, Spokespersons: A. Algora, L. M. Fraile, E. Nácher.

[Rei03] C. W. Reich, Nuclear Data Sheets 99 (2003) 753 and R. L. Mlekodaj et al. Phys. Rev. C 27 (1983) 1182.

[RIL] Resonance Ionization Laser Ion Source (RILIS), http://isolde-project-rilis.web.cern.ch/isolde-project-rilis.

[RIPL] RIPL databases, http://www-nds.iaea.org/ripl2.

[ROOT] ROOT libraries, http://root.cern.ch/drupal.

[RRpc] R. Rodriguez, private communication.

[Sar01] P. Sarriguren et al., Phys. Rev. C 64 (2001) 064306.

[Sar05] P. Sarriguren et al., Phys. Rev. C 72 (2005) 054317.

[Sch11] T. Schwetz et al., 1103.0734v1 [hep-ph] 3 Mar 2011.

[Sin02] B. Singh, Nuclear Data Sheets 95 (2002) 387, K. S. Toth et al., Nuclear Physics A 356, Iss. 1 (1981) 26 and G. Audi et al., Nucl. Phys. A, Vol 595, 4 (1995) 409.

[Sin03] B. Singh, Nuclear Data Sheets 99 (2003) 275, Y. A. Ellis-Akovali et al., Phys. Rev. C 23 (1981) 480 and G. Audi et al., Nucl. Phys. A, Vol 595, 4 (1995) 409.

[Smi03] N. A. Smirnova et al., Phys. Lett. B 569 (2003) 151.

[Suh88] J. Suhonen et al., Phys. Lett B 202 (1988) 174.

[Tai07] J. L. Tain et al., NIM A 571 (2007) 719. J. L. Tain et al., NIM A 571 (2007) 728.

[Til95] D. R. Tilley et al., Nuclear Physics A 595 (1995) 1.

[Til02] D. R. Tilley et al., Nuclear Physics A 708 1, (2002) 3.

[Tot74] K. S. Toth et al., Phys. Rev. C 10, 6 (1974) 2550.

[Tot82] K. S. Toth et al., Phys. Lett 117B (1982) 11.

[Tow85] I. S. Towner et al., Nucl. Phys. A 444 (1985) 402.

[Tul03] J. K. Tuli et al., Nuclear Data Sheets 100 (2003) 347.

[Tul07] J. K. Tuli et al., Nuclear Data Sheets 108 (2007) 2173.

[Van84] P. Van Duppen et al., Phys. Rev. Lett. 52 (1984) 1974.

[Woo92] J. L. Wood et al., Phys. Rep. 215 (1992) 101.

[Zol80] D. R. Zolnowski et al., Phys. Rev. C 21, 6 (1980) 2556.

[Zuc02] P. Zucchelli et al., Phys. Lett. B 532 (2002) 166.